Sprites and their Parent Discharges

by

Mark Alan Stanley

Submitted in partial fulfillment
of the requirements for the degree of

Doctor of Philosophy in Physics

Department of Physics
New Mexico Institute of Mining and Technology
Socorro, NM

May 5, 2000

Abstract

A detailed analysis of sprites and their parent discharges is presented in this study. Observations at VHF of the 3-dimensional development of discharges in a mesoscale convective system (MCS) over central Florida showed that sprite-producing discharges usually began as ordinary bilevel intraclouds (ICs) within convective cells. The negative leaders in the upper portion of each IC dropped in altitude from ∼10–12 km above mean sea level (MSL) to 7–8 km MSL as they propagated out of the convective region into the stratiform region. These altitudes coincide with the upper positive charge layer in MCSs [*MacGorman and Rust*, 1998,pg. 267]. The average velocity of negative leader propagation was $\sim 1-2\times10^5$ m/s in the stratiform region, consistent with previous measurements of negative leader velocities in cloud-to-grounds (CGs) [*Uman*, 1987,pg. 83] and ICs [*Shao and Krehbiel*, 1996]. The negative leaders propagated a distance of about 40–60 km and filled a portion of the >20 dBZ reflectivity region at 7–8 km altitude prior to the occurrence of a +CG.

The sprite-producing +CGs removed positive charge from the 7–8 km MSL altitude of the upper positive charge layer in the stratiform region, consistent with previous multi-station electric field measurements of +CGs in a Florida MCS [*Krehbiel*, 1981]. The sprite-producing +CGs had average (downward) currents of ≃28-37 kA within the initial 1 ms post-return stroke interval and ≃13-16 kA within the initial 4 ms. The range of charge transfers to ground for these time intervals was ≃28-37 C and ≃52-64 C, respectively. A comparison of high-speed video of sprite development with ELF-based sferic measurements revealed that the charge moment required for sprite initiation was ≃300 C·km for delays of up to a few milliseconds after the +CG stroke, consistent with previous estimates of *Cummer and Inan* [1997] and *Huang et al.* [1999] as well as the charge moments based on static electric field changes presented in this work.

The sprite plan locations were only associated with the most recent (∼200-300 ms) portion of the discharges, suggesting that older channel segments had become resistive. The plan locations of most sprites were correlated with the apparent periphery of the parent discharges. Assuming that sprite initiation is correlated with local maxima in the electric field at high altitude, it is speculated that the +CG removes charge primarily from the periphery of the discharge in association with the advancement of negative leaders which supply the continuing current.

High-speed video revealed that the initiation altitude of nighttime sprites was 76±6 km MSL with a maximum density at ≃76-79 km MSL. The initiation altitude is consistent with conventional breakdown predictions [*Wilson*, 1925; *Fernsler and Rowland*, 1996; *Pasko et al.*, 1997b], though the measured charge moments were about 1.4–2.3 times less than required to initiate conventional breakdown in a homogeneously stratified atmosphere. Sprites developed bidirectionally upwards and downwards from the point of initiation, consistent with experimental and theoretical observations of positive and negative streamers which propagated in opposite directions away from an electron avalanche region in long air gaps [*Loeb and Meek*, 1940; *Dhali and Williams*, 1985]. The downward developing positive streamers in sprites typically attained peak velocities of $\sim 1 \times 10^7$ m/s, in agreement with the predictions of *Raizer et al.* [1998] for the observed charge moment changes in excess of 300 C·km.

Parent discharges with unusually large and rapid charge moment changes produced sprite halos consistent with the quasi-electrostatic heating of electrons [*Pasko et al.*, 1997b]. Angel (jellyfish) sprites initiated from enhanced luminous regions at the base of the sprite halos and the positive streamers propagated downwards at velocities which could exceed 3×10^7 m/s (10% of light).

On some sprites, inferred negative streamers were spawned from regions through which the positive streamers propagated previously. The negative streamers propagated and branched upwards and outwards, transforming the sprite from a columniform shape (with tendrils) to an upward-V, or "carrot", shape.

The measurements of sprites and their parent discharges were extended to the daytime via a unique sprite ELF signature which was used to detect the presence of daytime sprites. The charge moment threshold for daytime sprite initation was much higher than at night, consistent with the lower altitude of the base of the ionosphere and conventional breakdown theory [*Wilson*, 1925; *Fernsler and Rowland*, 1996]. The 6100 C·km charge moment change of the first daytime sprite-producing parent discharge, prior to the start of the sprite ELF signature, may have been sufficient for conventional breakdown below the base of the ionosphere at an altitude of ≃54 km, assuming an experimentally measured ion conductivity profile of *Holzworth et al.* [1985]. The daytime sprites themselves contained unusually large charge moment changes of ≃2800 C·km, ≃1200 C·km, and ≃910 C·km. These charge moments are larger than the largest nighttime sprite charge moment change published to date of ∼840 C·km [*Cummer and Stanley*, 1999].

Acknowledgements

There are many people who through their generosity and knowledge have made important contributions to this dissertation. It would be impossible to list everyone who contributed, or to adequately list the extent of the contributions for those who are mentioned.

First and foremost, I would like to thank my adviser, Paul Krehbiel, for the oustanding leadership and support that he provided over the past several years. Without his insightful direction, many of the results presented in this dissertation would not have been possible. I am also deeply grateful to Marx Brook for his diligent efforts to acquire and share sferics data as well as for the lenses and filters which he provided. He has shared many thought-provoking discussions with me and has instilled a sense of awe and wonder of the atmospheric electrical phenomena which surround us.

I would like to extend a special thanks to Steve Cummer of Duke University. All of the charge moment data based on extremely low frequency (ELF) measurements presented in this dissertation were calculated by him based on models and routines which he perfected over the past few years. Steve is beyond a shadow of a doubt the current "Jedi Master" of ELF. He has also shared valuable insights and other results with me on countless occassions.

I am deeply indebted to Bill Abrahams of Speed Vision Technologies, who loaned us the KODAK EktaPro High-Spec Motion Analyzer Model 1012 which was used in the high-speed video study of sprites. I am equally indebted to Bill Klein of Eastman-KODAK Company, who loaned us a replacement KODAK EktaPro Intensified Imager Model VSG on short notice.

I thank Chris Barrington-Leigh of Stanford University for providing the magnetic loop antenna in 1997. His detailed analysis of the events which recently were given the name "sprite halos" was a major step forward in our understanding of high altitude electrical phenomena. Furthermore, I am indebted to him for the numerous exchanges of ideas that we have shared.

I thank Bill Rison of New Mexico Tech for the design of the A/D boards which

acquired all of the sferic and interferometer data presented in this study. His mastery of electronic design continues to amaze us all. I'm also grateful to Ron Thomas of New Mexico Tech, who demonstrated his mastery of IDL programming by writing sferic analysis routines which enabled the processing of large volumes of sferic data.

A special thanks goes to Charles B. Moore of New Mexico Tech for providing VHS recording equipment and heavy-duty tripods which were invaluable in the sprite research. I also thank Otha H. Vaughan for loaning the normal speed low light level cameras to us.

I am indebted to Walt Lyons and Tom Nelson of FMA Research for providing the photometer data in early 1997 which provided conclusive evidence that sprites emit a unique ELF signature. Furthermore, we have shared many insightful results and illuminating discussions, and have even exchanged chilis and garlic. I can personally verify that Walt Lyons has the best and most complete selection of garlic products ranging from the ordinary to the exotic at *http://www.thegarlicstore.com/*.

Much of the hard work of transporting and securing observation equipment was performed by Gary Coppler of Langmuir Laboratory. I am indebted to him for his diligent efforts. I also thank Bill Winn of Langmuir Laboratory for his assistance. Bill also taught a "Spark Discharge" course in the fall of 1999 which had a significant influence on this dissertation. I am indebted to Sandy Kieft of Langmuir Laboratory for taking care of paper-work and other arduous tasks too numerous to mention.

I am indebted to Ken Cummins and John Cramer of Global Atmospherics, Inc. for providing stroke-level National Lightning Detection Network (NLDN) data of sprite-producing discharges. I also thank Dave Suszcynsky of Los Alamos National Laboratory for providing the photometer which was used in 1997.

Last, but far from least, I would like to thank my parents, Gerald and Ellen Stanley, as well as my brother, Randy Stanley, and his wife, Nicole Stanley, for the endless encouragement and support they have offered through the years. The strength of my family has been a tremendous boost to me. In recognition of this, I would like to dedicate this dissertation to my grandmother, Mary Alice Cook, and grandfather, Clifford Stanley, who both passed away while I was a graduate student at New Mexico Tech. Their work ethic, personal strength, and devotion to truth have been passed down from generation to generation through the eternal power of love.

Contents

1 Introduction **1**

1.1 Transient Luminous Events 1

1.2 Sprites and their Parent Discharges 3

1.3 Overview 5

2 Conventional Breakdown **7**

2.1 Introduction 7

2.2 Breakdown basics 7

2.2.1 Charge mobility and motion 7

2.2.2 E/N and electron energy, ε 8

2.2.3 Ionization, Recombination, and Attachment 9

2.2.4 Electron avalanche 10

2.3 Atmospheric Models 13

2.3.1 1976 U.S. Standard Atmosphere 13

2.3.2 Latitudinal and Seasonal Variation 14

2.4 Atmospheric Conductivity and Relaxation Time 16

2.4.1 Ion Conductivity 16

2.4.2 Electron Conductivity 16

2.4.3 Total conductivity 19

2.4.4 Relaxation Time 19

2.5 Sprite Initiation Threshold 21

2.5.1 Infinite images 21

2.5.2 Uniformly Charged Disk 23

2.5.3 Initiation Threshold vs. Height 27

2.6 Streamers 28

2.6.1 Formation 28

2.6.2 Propagation 29

3 Close Sprite-producing Discharges **32**
3.1 Introduction . . . 32
3.2 Instrumentation . . . 32
3.2.1 KSC LDAR . . . 33
3.2.2 NMT Interferometer . . . 34
3.3 Observations . . . 35
3.4 Storm development history . . . 35
3.5 Charge Moment Analysis . . . 39
3.6 01:42:57 UT Sprite-producer . . . 43
3.7 01:47:52 UT Sprite-producer . . . 53
3.8 01:51:02 UT Sprite-producer . . . 59
3.9 01:55:47 UT Sprite-producer . . . 67
3.10 02:15:19 UT Non-sprite-producer . . . 73
3.11 Summary . . . 79
3.12 Discussion . . . 80

4 ELF measurements **82**
4.1 Introduction . . . 82
4.2 Sprite Currents . . . 83
4.3 Daytime Sprites . . . 85
4.3.1 Instrumentation . . . 85
4.3.2 Experiment . . . 85
4.3.3 Results . . . 86
4.3.4 Relaxation Time during the Day . . . 91
4.3.5 Daytime Sprite Initiation Threshold . . . 93
4.4 Summary . . . 95
4.5 Discussion . . . 96

5 High-speed Video Observations of Sprites **97**
5.1 Introduction . . . 97
5.2 October 7, 1997 . . . 97
5.2.1 Storm Development . . . 97
5.2.2 Observations . . . 98
5.2.3 03:03:59 UT, 2000 frames/second . . . 101
5.2.4 03:40:37 UT, 1000 frames/second . . . 110
5.2.5 03:40:38 UT, 1000 frames/second . . . 112

5.3 October 6, 1997 116
5.3.1 Observations 116
5.3.2 04:37:05 UT, 2000 frames/second 116
5.3.3 04:45:48 UT, 2000 frames/second 119
5.4 Summary 122
5.5 Discussion 123

6 Conclusions **124**
6.1 Summary 124
6.2 Future Work 127

A Instrumentation **129**
A.1 High-speed Camera System 129
A.2 Data Acquisition System 130

B Calibration **133**
B.1 Introduction 133
B.2 Camera location 133
B.3 Camera orientation 134
B.3.1 Normal-speed camera 134
B.3.2 High-speed camera 136
B.4 Video timing 137
B.4.1 Normal-speed video 137
B.4.2 High-speed video 138
B.5 Refractive corrections 140
B.6 Electric Field Calibration 143
B.6.1 Local Calibration 143
B.6.2 Absolute Calibration 144

C Effect of Ionosphere on Static Field Measurements **151**

List of Figures

1.1 Electric field and electrical breakdown strength above a discharge. . . 4

2.1 Ionization and attachment of air versus E/N. 11
2.2 Electron avalanche in a laboratory experiment. 12
2.3 1976 U.S. Standard Atmosphere 14
2.4 1966 U.S. Standard Atmosphere Supplement 15
2.5 Model of atmospheric conductivity between 40-90 km altitude. 17
2.6 Simulated relaxation time profile just prior to sprite initiation 20
2.7 Calculated electric field at $Z = 78$ km vs. the number of images. . . . 22
2.8 Electric field at $Z = 78$ km as a function of disk radius and height. . . 26
2.9 The sprite initiation threshold for 70-81 km altitude. 28
2.10 Diagram of a positive streamer. 30

3.1 Storm development for 23-1 UT on June 21st-22nd, 1997 37
3.2 Storm development for 1-3 UT on June 22nd, 1997 38
3.3 Video sequence and NEXRAD radar for 01:42:57 UT event 45
3.4 Time series of 01:42:57 UT sprite-producing flash 47
3.5 Spatial development of 01:42:57 UT flash 48
3.6 Zoom of 01:42:57 UT sprite-producing CG 51
3.7 Height histogram of VHF sources for 01:42:57 UT flash 52
3.8 Video sequence of 01:47:52 UT sprite event 54
3.9 Time series of 01:47:52 UT sprite-producing flash 55
3.10 Spatial development of 01:47:52 UT flash 56
3.11 Azimuth and Elevation of 01:47:52 UT sprite event 57
3.12 Height histogram of VHF sources for 01:47:52 UT flash 58
3.13 Video sequence and NEXRAD radar for 01:51:02 UT event 60
3.14 Time series of 01:51:02 UT sprite-producing flash 61
3.15 Spatial development of 01:51:02 UT flash 63

3.16 Zoom of 01:51:02 UT sprite-producing CG 64
3.17 Height histogram of VHF sources for 01:51:02 UT flash 66
3.18 Video sequence and NEXRAD radar for 01:55:47 UT event 68
3.19 Time series of 01:55:47 UT sprite-producing flash 69
3.20 Spatial development of 01:55:47 UT flash 71
3.21 Zoom of 01:55:47 UT sprite-producing CG 72
3.22 Height histogram of VHF sources for 01:55:47 UT flash 73
3.23 Time series of 02:15:19 UT non-sprite-producing flash 75
3.24 Spatial development of 02:15:19 UT flash 76
3.25 Zoom of 02:15:19.419 UT +CG 77
3.26 Zoom of 02:15:19.51 UT non-sprite-producing +CG(s) 78

4.1 Sferics and photometry for sprite event at 05:38:00.77 UT, July 24, 1996. 84
4.2 Visible and infrared satellite images at 23:15 UT, August 14, 1998 . . 87
4.3 NLDN data for MCS on August 14, 1998 88
4.4 Electric field waveform of 23:19:48 UT +CG and daytime sprite. . . . 89
4.5 Largest charge moment change discharges on August 14, 1998 90
4.6 Profiles of n_e and τ_r on August 14, 1998. 92
4.7 Sprite initiation threshold for daytime sprites. 94

5.1 October 7, 1997, NLDN strokes for 01:30-4:30 UT. 99
5.2 Initial 4.5 ms of the October 7, 03:03:59 UT sprite cluster development. 102
5.3 Subsequent 4.5 ms of the October 7, 03:03:59 UT sprite cluster development. 103
5.4 Enhanced image sequence of the 03:03:59 UT sprite cluster's initial development. 104
5.5 Electric field and photometer data for the 03:03:59 UT event. 105
5.6 Formation of a carrot shape for sprite B of the 03:03:59 UT sprite cluster. 109
5.7 Development of the October 7, 03:40:37 UT sprite cluster. 111
5.8 Development of the October 7, 03:40:38 UT sprite cluster. 113
5.9 Electric field waveform and frame periods for the 03:40:38 UT sprite cluster 114
5.10 Correlated charge moment change and high-speed video of 04:37:05 UT sprite cluster. 117
5.11 Correlated charge moment change and high-speed video of the 04:45:48 UT sprite cluster. 120

A.1 VME Data Acquisition System 130

B.1 Star alignment for a normal-speed video image. 135
B.2 Normal-speed video timing via a Horita GPT-50. 138
B.3 Determination of high-speed video timing from LED transitions. . . . 139
B.4 Effect of refraction on height estimates. 142
B.5 The slow antenna calibrator. 143
B.6 Determination of magnetic loop orientation. 148
B.7 Calibration of E and B from NLDN data as a function of source azimuth. 149

C.1 Calculated electric field at $r = 80$ km vs. the number of images. 152
C.2 The effect of the ionosphere on the static electric field at 40-100 km range. 153

List of Tables

3.1 Charge Moment Measurements on June 22nd, 1997 42

A.1 VME system boards. 131

B.1 Example calculations for the high-speed video timing calibration. . . 140
B.2 Calibration of the electric field meter at KSC in 1997. 146

Notation

E_k	Electric field required for conventional breakdown of air
N	Number density of gas molecules
n_e	Number density of electrons
Q_d	Charge of disk
R_d	Radius of a disk
Z_d	Height of disk above ground
σ_d	Charge density on disk
μ_e	Mobility of electrons
ν_m	Effective collision frequency of electrons with neutral molecules and atoms
v_e	Net drift velocity of electrons
σ	Total conductivity
σ_e	Electron conductivity component
σ_i	Ion conducitivity component
τ_r	Relaxation time

Acronyms

CC	Continuing Current
+CG	Positive Cloud to Ground
-CG	Negative Cloud to Ground
ELF	Extremely Low Frequency
FA	Fast Antenna
IC	Intracloud
KSC	Kennedy Space Center
LDAR	Lightning Detection and Ranging
LMA	Lightning Mapping Array
MSL	Mean Sea Level
NLDN	National Lightning Detection Network
NMT	New Mexico Tech
RF	Radio Frequency
SA	Slow Antenna
STP	Standard Temperature and Pressure
TLE	Transient Luminous Event
VHF	Very High Frequency
VLF	Very Low Frequency

Chapter 1

Introduction

1.1 Transient Luminous Events

For at least a century there have been occassional eye-witness reports of transient optical flashes above thunderstorms. *Wilson* [1956] described discharges that he observed above a thunderstorm as "diffuse fan-shaped flashes of greenish colour extending up into a clear sky". There are numerous reports from pilots who have observed flashes extending above thunderstorms [*Vonnegut*, 1980; *Vaughan and Vonnegut*, 1989]. Many other observations of brief optical flashes above thunderstorms have been reported in the literature going back to 1885, as summarized by *Rodger* [1999].

The first official record of an optical discharge above a thunderstorm was obtained only relatively recently when, quite by accident, such an event was documented by a low-light-level camera during the SKYFLASH program in 1989 [*Franz et al.*, 1990]. Within only a few years, additional such discharges had been documented from the space shuttle [*Vaughan et al.*, 1992; *Boeck et al.*, 1995], from the air [*Sentman and Wescott*, 1993; *Sentman et al.*, 1995], and from the ground [*Lyons*, 1994; *Winckler*, 1995].

Various terms were first used to describe high altitude luminous flashes, such as "cloud-to-ionosphere" or "cloud-to-stratosphere" discharges. However, these terms implied vertical extents which were not accurately known in the earliest reports and also hinted at a direction-of-motion which could not be measured until recently. Consequently, the unassuming term "sprites" was adopted to describe the elusive and mysterious nature of the high altitude luminous structures [*Sentman et al.*, 1995].

The first color imagery and unambiguously triangulated extents of sprites were

obtained during the Sprites94 aircraft campaign by *Sentman et al.* [1995]. They found that sprites have a main red body located between $\sim$50–90 km altitude with faint bluish tendrils often extending to lower altitudes. During the Sprites94 aircraft campaign, *Wescott et al.* [1995] documented another type of optical emission which appeared to propagate upwards from the tops of thunderstorms at $\sim$20 km altitude to about 40–50 km altitude at an average velocity of 1×10^5 m/s. They termed these events "blue jets" due to their bluish color and development characteristics.

Similar to blue jets are "blue starters" [*Wescott et al.*, 1996]. Blue starters differ from blue jets only in their terminal altitude. *Wescott et al.* [1996] observed that blue starters propagated up from the tops of storms at 17–18 km altitude to a maximum altitude of only $\simeq$25 km. It is likely that most of the pilot reports [*Vonnegut*, 1980; *Vaughan and Vonnegut*, 1989] of discharges propagating up from the tops of storms were either blue starters or blue jets and not sprites, which appear nearly instantaneously at higher altitudes.

Boeck et al. [1992] observed a third major class of transient luminosity above thunderstorms. Using a Space Shuttle payload bay TV camera, they noted a significant brightening of the airglow layer at about 95 km altitude directly above a luminous discharge in a storm below. This brightening was attributed to the heating of nighttime ionospheric electrons and the increased ionization associated with the passage of an intense electromagnetic pulse (EMP), as described by *Inan et al.* [1991].

Theoretical models indicate that the peak emissions associated with the passage of an EMP pulse through the lower ionosphere would be between 85 and 95 km altitude [*Taranenko et al.*, 1992, 1993], which is similar to the altitude observed by *Boeck et al.* [1992]. These events were termed "elves", an acronym for "emissions of light and VLF perturbations from EMP sources". Observations from the ground showed that elves are horizontally extensive ($>$ 100 km) and have short durations ($<$ 1 ms) [*Fukunishi et al.*, 1996; *Inan et al.*, 1997]. Elves are correlated with large peak-current CGs ($>$ 100 kA) of both positive [*Fukunishi et al.*, 1996; *Lyons*, 1996; *Inan et al.*, 1997] and negative [*Barrington-Leigh and Inan*, 1999] polarities. All of these observations are consistent with an EMP-based mechanism.

Sprites, blue jets and starters, and elves all are examples of transient luminous events (TLEs) above thunderstorms. The remainder of this dissertation will focus on sprites and their parent discharges.

1.2 Sprites and their Parent Discharges

It has been known for about a century that the electric field required to produce breakdown scales as the air number density, N. *Wilson* [1925] insightfully realized that N would decrease at a rate faster than the decrease in E above a net charge in a thundercloud (e^{-z} vs. z^{-3}, respectively). He theorized that for a sufficiently large dipole moment of the charge and its below ground image, the electric field would exceed the "sparking limit" at high altitude.

The ionosphere is sufficiently conductive for electric fields to rapidly decay on submillisecond time scales. In the region just below the base of the ionosphere, the conductivity of the atmosphere is such that electric fields will decay on time scales of milliseconds. The electric field will take increasingly longer to decay at lower altitudes, but it is still sufficiently fast just above cloud tops (∼10 s) that any charge separation on the time scale between sprite-producing discharges (typically minutes) will be screened by charge motion in the atmosphere. Thus, the electric field above a storm and particularly at high altitude will only be of concern when charge is rapidly transported, such as during CG discharges. Figure 1.1 shows an example of how E would decrease above a CG, relative to the rapid decrease in the electrical breakdown strength of air, E_k, with increasing altitude. If the discharge was sufficiently energetic, E would exceed E_k below the base of the ionosphere, resulting in electrical breakdown.

Based on a self consistent model of conductivity, ionization, and electron heating, *Pasko et al.* [1995] predicted that optical emissions would extend down to sim65 km altitude for very large CG charge moment (charge times height) changes of 3000 C·km in 1 ms, corresponding to an exceptionally large average current of 300 kA. In order for there to be luminous sprite emissions below 50 km altitude, it was realized that space-charge field enhancements in the form of streamers would likely be involved [*Pasko et al.*, 1996; *Fernsler and Rowland*, 1996]. However, these early models lacked the fine spatial resolution needed to accurately model streamers and thus a minimum altitude could not be determined.

Streamers would be initiated below the base of the ionosphere from localized regions of breakdown (∼1–100 m wide) at altitudes of ∼70–80 km [*Pasko et al.*, 1998a; *Raizer et al.*, 1998]. The streamers would have radii of ∼100 m or less [*Raizer et al.*, 1998] below the base of the ionosphere, consistent with the observations of fine scale structure in sprites [*Stanley et al.*, 1996b; *Wescott et al.*, 1998]. It was also shown that streamers could propagate down to altitudes well below 50 km [*Raizer*

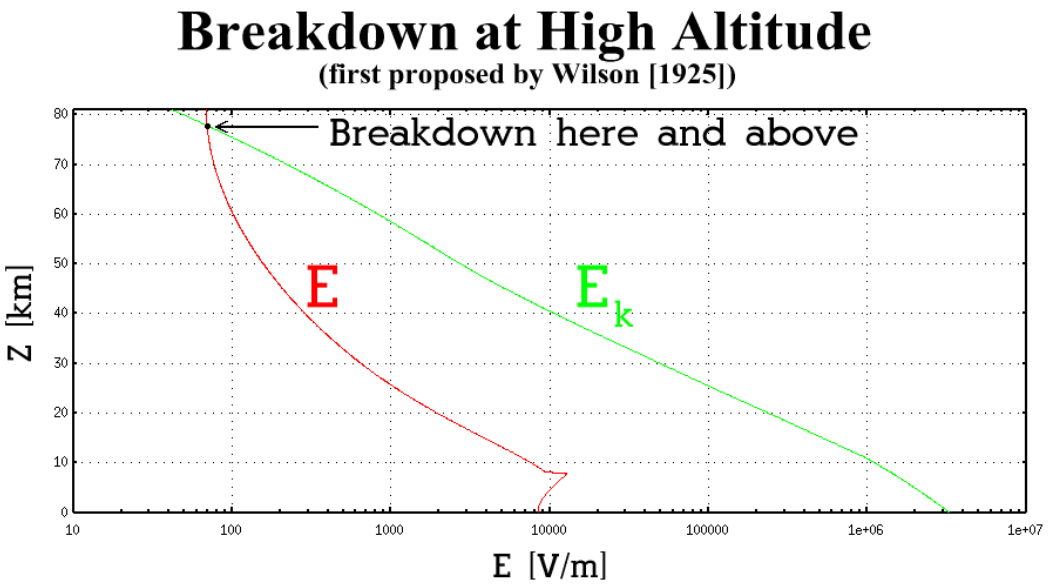

Figure 1.1: Charge at 8 km altitude is removed to ground by a CG discharge. As predicted by *Wilson* [1925], the electric field, E, decreases at a slower rate than the electrical breakdown strength of air, E_k, with increasing altitude. In this example, E exceeds E_k between an altitude of $\simeq$77 km and the base of the ionosphere at $\simeq$81 km, resulting in electrical breakdown in that altitude range.

et al., 1998; *Pasko et al.*, 2000], consistent with the observed lower terminal altitudes of sprites [*Sentman et al.*, 1995].

Early measurements of extremely low frequency (ELF) atmospherics ("sferics") showed that sprites were typically associated with positive cloud-to-ground (+CG) discharges which removed unusually large quantities of positive charge to ground [*Boccippio et al.*, 1995]. The apparent exclusive association of sprites with +CGs along with the detection of terrestrial gamma-ray flashes [*Fishman et al.*, 1994] led some researchers to theorize that sprite optical emissions were associated with an energetic upward runaway electron breakdown process [*Bell et al.*, 1995; *Taranenko and Roussel-Dupré*, 1996; *Roussel-Dupré and Gurevich*, 1996; *Yukhimuk et al.*, 1998].

Time resolved sprite imagery showed that sprites typically began 1.5-4 ms after the occurrence of the parent +CG [*Rairden and Mende*, 1995]. *Cummer and Inan* [1997] used ELF measurements to show that the charge moment changes of 6 sprite-producing discharges had each attained at least 250 C·km during the initial 5 ms. They noted that several of the charge moments were less than required to produce

significant optical emissions by the quasi-electrostatic heating or runaway electron breakdown models, suggesting that some other mechanism was involved.

Though the charge moment of sprite-producing discharges had been measured by remote ELF measurements, the height of the charge and hence the charge and current values could not be determined from this technique. Possible average charge heights used in the sprite literature range from 4 km to 10 km or even higher.

Numerous studies have shown that sprites occur only over large thunderstorm systems known as Mesoscale Convective Systems (MCSs) [*Lyons*, 1994; *Winckler*, 1995; *Boccippio et al.*, 1995; *Winckler et al.*, 1996; *Lyons*, 1996], MCSs are highly-organized storm systems with the upper-level anvil outflows from convective cells joined together into a solid cloud shield known as the "stratiform region" [*MacGorman and Rust*, 1998,p. 258]. Observations of sprites show that they occur primarily over the stratiform region of MCSs [*Lyons*, 1996]. Balloon soundings through the stratiform region and away from the "transition zone", which is near the convective region, show that there is a high-density of positive charge near the 0°C level at an altitude of $\simeq$4 km MSL [*Marshall and Rust*, 1993; *Stolzenburg et al.*, 1994]. Based on this and other measurements, *Williams* [1998] concluded that the altitude of positive charge removed by sprite-producing discharges would be at 4–6 km MSL.

1.3 Overview

Strong evidence for a conventional breakdown mechanism in sprite initiation will be presented in this dissertation. Chapter 2 presents a review of conventional breakdown in the form of electron avalanches and streamer processes. Profiles of conductivity and atmospheric number density are used to determine the altitudes and corresponding charge moment values of sprite initiation. These results are compared with previous estimates of the altitudes and charge moment thresholds required for sprite initiation. A uniformly charged disc model of the parent discharge is used to determine how the breakdown threshold depends on the horizontal extent and average height of charge removal in a discharge. This model is then used to assess the validity of the point dipole approximation for the measured sprite-producing discharge heights and extents presented in Chapter 3.

In Chapter 3, the 3D spatial and temporal development, broadband electric field, and VHF emissions of both sprite-producing and non-sprite-producing discharges are analyzed and compared. The data contains the first reported average height, charge,

and current values for several sprite-producing discharges. These results are compared with previous measurements of negative and positive CG discharge parameters. The charge moments are also compared with previous ELF-based estimates of the sprite initiation threshold as well as with theoretical predictions. The plan locations of the sprites are compared with discharge development up to the time of the sprites and inferences are made about the distribution of charge in the parent discharge. Also, evidence is presented which suggests the large and rapid charge transfers of sprite-producing discharges may often adversely affect tall metallic structures on the ground.

In Chapter 4, the comparison of photometry with ELF data of sprites is reviewed. These comparisons revealed that sprites emitted a unique ELF signature. The unique sprite signature was recently used in a collaborative effort to report the first detection of daytime sprites [*Stanley et al.*, 2000]. The charge moment changes of the parent discharges and the daytime sprites are presented. The charge moment changes of the parent discharges at the onset of the sprite ELF signatures are compared with conventional breakdown theory.

High-speed video of sprites is analyzed and correlated with the charge moment changes of the parent discharges (and sprites) in Chapter 5. The initial development of sprites based on the high speed video data was published [*Stanley et al.*, 1999] along with a comparison of sprite development with charge moments based on ELF measurements [*Cummer and Stanley*, 1999]. High speed video data obtained of sprite halos was recently compared with the theoretical predictions of *Pasko et al.* [1997a] by *Barrington-Leigh et al.* [2000]. Most of the data presented in this chapter are of sprites which were not included in the above papers. Some additional conclusions are drawn and the charge moment threshold and apparent altitude of sprite initation are compared with conventional breakdown theoretical predictions.

In Appendix A, the characteristics of the high-speed video system is shown. Also, the data acquisition system which was used to acquire broadband sferic data is described. The calibration of the various instruments is described in Appendix B. Finally, the effect of ionospheric images on static electric field measurements at ground-level is explored in Appendix C and these results were used to calculate the charge moments in Chapter 3.

Chapter 2

Conventional Breakdown

2.1 Introduction

The conventional breakdown mechanism will be reviewed in this chapter along with measurements of atmospheric density and conductivity. A possible relaxation time profile will be determined from the ion conductivity and electron density and mobility. The primary contribution of this chapter will be the application of a uniformly charged disc model to show how the breakdown threshold would depend on the height and dimensions of a discharge. The transition of breakdown to propagating ionization waves, or "streamers", will also be reviewed.

2.2 Breakdown basics

2.2.1 Charge mobility and motion

In the absence of an electric field, free electrons in a gas will move with a random thermal velocity of average magnitude $\bar{v}$. Because the motion is random, the net drift velocity $\langle v \rangle_t = 0$, where the angle brackets and subscript denote a time average. If an electric field $\vec{E}$ is applied, the electrons will acquire a net drift velocity $\vec{v}_e$ along the electric field lines but in the opposite direction to $\vec{E}$. $\vec{v}_e$ is directly related to $\vec{E}$ by:

$$\vec{v}_e = -\mu_e \vec{E} \,, \tag{2.1}$$

where μ_e is the mobility of electrons.

Electron mobility is a function of both the gas composition and density. It is also dependent on the magnitude of the applied electric field divided by the gas density

(see Section 2.4.2). Electron mobility is defined by the following relationship:

$$\mu_e = \frac{q_e}{m_e \nu_m} \tag{2.2}$$

where q_e is the electronic charge, m_e is the electron mass, and ν_m is the effective collision frequency of electrons with neutral molecules and atoms. A similar relation also applies for ions, though ion mobility will be very much less than that of electrons since $m_{ion} \gg m_e$.

The effective collision frequency ν_m is proportional to the number density of gas molecules (N), the thermal velocity of the electrons ($\bar{v}$), and the scattering cross section (σ_c) of the gas:

$$\nu_m \propto N \bar{v} \sigma_c \tag{2.3}$$

A rigorous relationship between the above quantities would include the mean scattering angle.

2.2.2 E/N and electron energy, ε

Equations 2.2 and 2.3 can be combined to show that the electron mobility is inversely proportional to the gas number density:

$$\mu_e \propto \frac{1}{N} \tag{2.4}$$

For low to moderate fields where $v_e \ll \bar{v}$, the proportionality relationship in Equation 2.4 can be combined with Equation 2.1 to produce the following relationship:

$$v_e \propto \frac{E}{N} \qquad \text{if} \quad v_e \ll \bar{v} \tag{2.5}$$

The above proportionality is not strictly true for larger v_e since $\bar{v}$ and hence ν_m will increase (Equation 2.3) leading to a decrease in μ_e (Equation 2.2). This decrease in μ_e will affect the relationship between v_e and E (Equation 2.1). However, it is generally true that $v_e = f(\frac{E}{N})$, since the increase in $\bar{v}$ is a function of E/N. It follows that the electron energy, $\varepsilon = \frac{1}{2} m v^2$, also follows the same similarity law:

$$\varepsilon = f(\tfrac{E}{N}) \tag{2.6}$$

This is a particularly important insight since the electron energy controls the breakdown physics, as will be reviewed in the next section. This fundamental property

of breakdown physics has been known since Townsend's pioneering work in the early 1900's.

2.2.3 Ionization, Recombination, and Attachment

An electrical discharge is produced when gas molecules or atoms are ionized by electron impact. In the absence of losses, the change in the electron density is given by:

$$\left.\frac{dn_e}{dt}\right|_i = \int_I^\infty N v \sigma_i(\varepsilon) n_e(\varepsilon)\, d\varepsilon = \nu_i n_e \ , \tag{2.7}$$

where the subscript i denotes that this is an electron density change due only to electron impact ionization, σ_i is the ionization cross section by electrons with energy ε, $n_e(\varepsilon)$ is the free electron density as a function of energy, I is the ionization potential energy, and ν_i is the ionization frequency (the average number of ionization events per electron per second). The ionization potentials for the two major constituents of air, N_2 and O_2, are 15.6 eV and 12.2 eV respectively.

Assuming that ν_i is constant, the solution to Equation 2.7 is

$$\left. n_e(t)\right|_i = n_o e^{\nu_i t} \ , \tag{2.8}$$

where n_o is the initial electron density. In the absence of losses, the electron density increases exponentially with time.

After an ionization event, a free electron can "recombine" with a positive ion. In the absence of other processes, the change in the electron density due to recombination is given by:

$$\left.\frac{dn_e}{dt}\right|_r = -\beta n_e n_+ \ , \tag{2.9}$$

where β is the electron-ion recombination coefficient, n_+ is the positive ion density, and the subscript r indicates that this is an electron density change due only to recombination. If one assumes that the plasma is neutral with only single ionization, then $n_e = n_+$. Substituting into Equation 2.9 and solving for $n_e(t)$ gives:

$$\left. n_e(t)\right|_r = \frac{n_o}{1 + \beta n_o t} \tag{2.10}$$

In addition to recombining with positive ions, electrons can also attach to neutral molecules if the gas has electronegative properties. Air is an electronegative gas

because of the electron affinity of O_2. Electrons can attach to oxygen either in triple collisions ($e + O_2 + M \rightarrow O_2^- + M$) or via dissociative attachment reactions ($e + O_2 + 3.6\ eV \rightarrow O^- + O$). The latter form of attachment dominates at E/N values near that of breakdown. The change in electron density due to attachment is:

$$\left.\frac{dn_e}{dt}\right|_a = -\nu_a n_e \ , \tag{2.11}$$

giving:

$$\left. n_e(t)\right|_a = n_o e^{-\nu_a t} \tag{2.12}$$

where ν_a is the attachment frequency.

At E/N values near breakdown, electron loss is due primarily to attachment processes and in particular to dissociative attachment [*Bazelyan and Raizer*, 1997,p. 24]. At a given E/N value, both the ionization and attachment frequencies will be proportional to the air number density, N, since the collision rate is proportional to N (see Equation 2.3). Figure 2.1 shows the density-normalized ionization frequency (ν_i/N) and attachment frequency (ν_a/N) plotted as a function of E/N in units of Townsends ($1\ \mathrm{Td} = 10^{-21}\ \mathrm{V\,m^2}$). For any given N, the ionization frequency will exceed that of attachment when $E/N \gtrsim 123$ Td. This is the basis for the breakdown strength of air at standard temperature and pressure (STP). An E/N of 123 Td corresponds to a breakdown field of $\simeq$3.3 MV/m at STP.

2.2.4 Electron avalanche

Equations 2.7 and 2.11 can be combined into a more general expression which can be solved to determine the change in electron density due to both ν_i and ν_a:

$$\frac{dn_e}{dt} = (\nu_i - \nu_a) n_e \tag{2.13}$$

$$n_e(t) = n_o e^{(\nu_i - \nu_a)t} \tag{2.14}$$

It is clear from Equation 2.14 that the electron density will increase exponentially if $\nu_i > \nu_a$. This occurs when $E/N \gtrsim 123$ Td in Figure 2.1. An exponential increase of electrons from one or more seed electrons is an electron avalanche.

An electron avalanche will develop at the electron drift velocity, $\vec{v}_e$. As it develops, the avalanche will expand due to diffusion and mutual electrostatic repulsion.

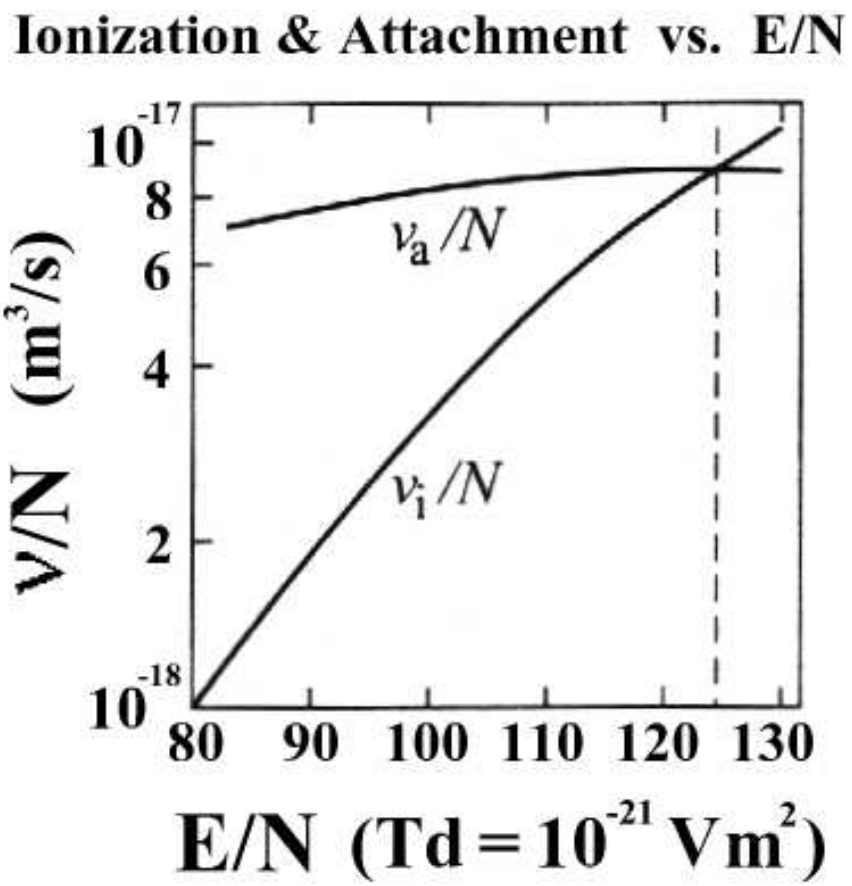

Figure 2.1: The ionization frequency (ν_i) and attachment frequency (ν_a) for air, divided by the air number density (N), are plotted against the electric field (E) divided by N. Electron avalanches can develop when $\nu_i > \nu_a$, which occurs for $E/N \gtrsim$ 123 Td. (From *Bazelyan and Raizer* [1997]).

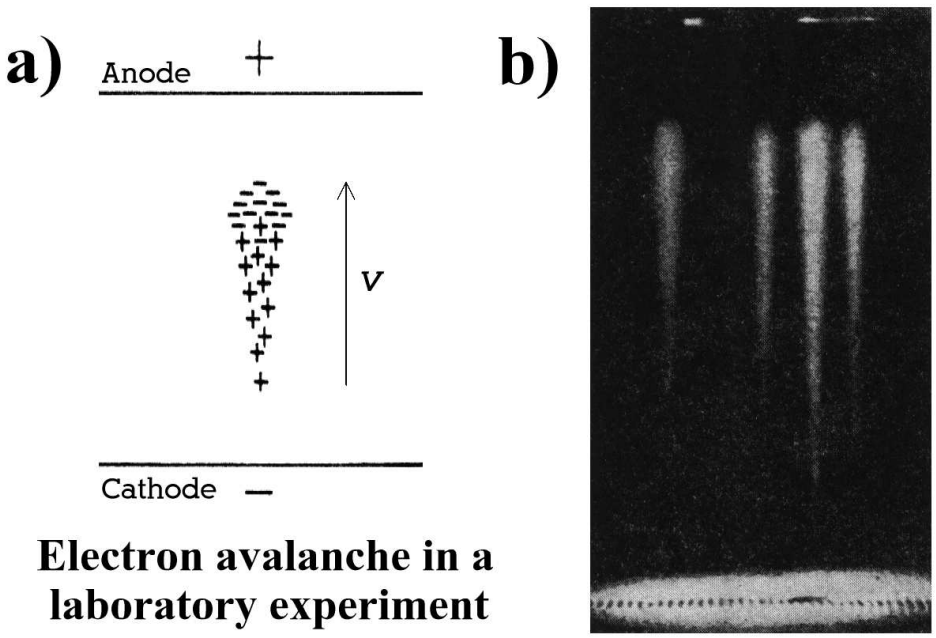

Figure 2.2: a) A schematic diagram of an electron avalanche. The electrons leave behind a trail of positive ions as they propagate towards the positively charged anode. b) An actual photograph of individual electron avalanches. (From *Raether* [1964]).

The diffusion expansion dominates during the initial stages while electrostatic repulsion dominates in the latter stages as a result of the growing number of electrons [*Bazelyan and Raizer*, 1997,p. 80]. An electron avalanche will also leave behind a trail of relatively immobile positively charged ions. A schematic illustration of an electron avalanche is shown in Figure 2.2a.

In a laboratory experiment where n_o is sufficiently small, electron avalanches starting from a single electron can be clearly distinguished on a photograph. Figure 2.2b shows a photograph from *Raether* [1964] of electron avalanches which began in this fashion. Electron avalanches can transition into streamers and are also a fundamental component of streamers, as will be discussed in Section 2.6. The relevance of electron avalanches and streamers to sprites will be shown in Chapter 5.

2.3 Atmospheric Models

2.3.1 1976 U.S. Standard Atmosphere

In 1953, the United States Committee on Extension to the Standard Atmosphere (COESA) was formed to assemble information on atmospheric parameters at altitudes traversed by suborbital rockets. One result of this effort was a mid-latitude (45° N) mean atmospheric profile published in *U.S. Standard Atmosphere, 1962.* COESA provided information, graphs, and tables of the latitudinal, seasonal, and diurnal variations of atmospheric parameters in *U.S. Standard Atmosphere Supplements, 1966.* The 1962 U.S. Standard Atmosphere model was updated when the United States National Oceanic sand Atmospheric Administration (NOAA) released *U.S. Standard Atmosphere: 1976.* The 1976 U.S. Standard Atmosphere is identical to the 1962 U.S. Standard Atmosphere for altitudes below 50 km, but differs for higher altitudes.

Fortran code for the 1976 U.S. Standard Atmosphere was obtained off of the web (*http://gate.cruzio.com/~pdas/atmosf90.htm*). The code was converted to Octave and IDL to interface with conventional breakdown (Section 2.5) and refraction (Appendix B.5) calculations respectively.

A critical atmospheric parameter for conventional breakdown models is the air number density, N, since the breakdown field, E_k, scales directly with N (see Sections 2.2.2 and 2.2.3). The scale factor relative to sea level will be the ratio of N to that at sea level, N_o. Figure 2.3a shows the 1976 U.S. Standard Atmosphere model of air density ratio as a function of height. The air density decreases exponentially with height.

The 1976 U.S. Standard Atmosphere model of temperature as a function of altitude is shown in Figure 2.3b. The approximate altitude range of the troposphere, stratosphere, and mesosphere are shown on the plot. Each successive layer alternates between polarities for the vertical temperature gradient. Above $\simeq$86 km altitude, the temperature slope becomes positive again (not shown), which corresponds with the approximate base of the thermosphere. The changes in temperature with respect to height produce small "wiggles" in the air-density ratio in Figure 2.3a, which otherwise would be a straight line.

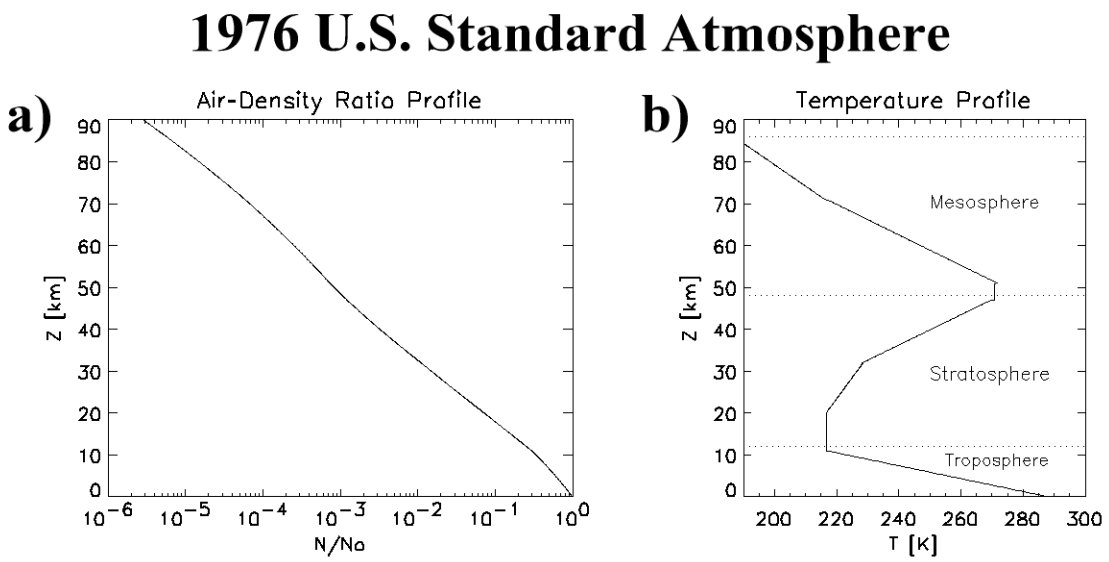

Figure 2.3: a) The ratio of the density of air to that at sea level is plotted as a function of height. b) The temperature is plotted as a function of height. The different atmospheric regions correspond to regions of increasing/decreasing temperature with respect to height.

2.3.2 Latitudinal and Seasonal Variation

An actual atmospheric profile can vary somewhat from the 1976 U.S. Standard Atmosphere. The amount of variation will depend on the latitude, day of the year, and even the time of day. Figure 2.4a corresponds to Figure 2.10 in *U.S. Standard Atmosphere Supplements, 1966*, which utilizes the 1962 U.S. Standard Atmosphere as the reference. The difference between the 1962 and 1976 models are small within the mesosphere, so the comparison also applies to the 1976 U.S. Standard Atmosphere.

Figure 2.4a shows how the air-density varies for 3 different latitudes as well as different times of the year. Generally, the higher the latitude, the more seasonal variation there will be.

Sprites within the U.S. are most numerous in July and August [*Lyons et al.*, 1999], which is near the time when the air density within the mesosphere is at a maximum (Figure 2.4a). This would imply that at any given altitude, the breakdown field, E_k, also increases during the summer. For instance, during the summer season E_k would be $\sim 20\%$ greater than in the spring and fall seasons and $\sim 40\%$ greater than in winter at 80 km altitude and 45°N latitude. However, the detailed comparisons

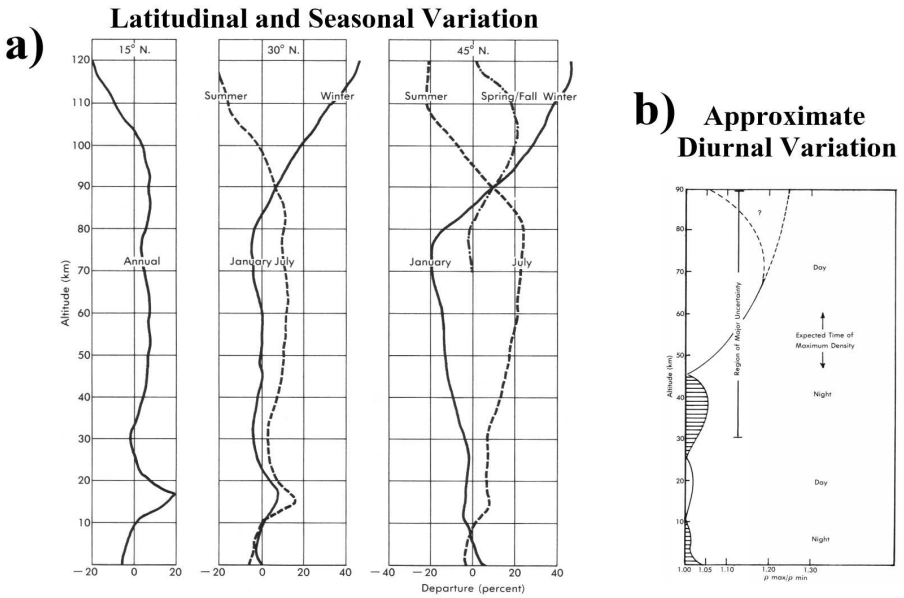

Figure 2.4: a) Typical percentage variations in air-density relative to the U.S. Standard Atmosphere are shown as function of altitude for different latitudes and times of year. b) The approximate diurnal variation in air-density is shown. The curves containing horizontal stripes correspond to density maxima which occur at night. Significant errors may exist in the diurnal density variation estimates above 40 km altitude. (From *U.S. Standard Atmosphere Supplements, 1966*).

of experiment with theory in this dissertation will focus primarily on sprites which occurred in the fall (see Section 5.3). The variation from the standard atmosphere for the fall season will be small, particularly in comparison to other sources of error.

The approximate diurnal variation of air density within the mesosphere is shown in Figure 2.4b. The nighttime air density near 80 km altitude can be as much as 25% less than the daytime density. However, nighttime rocket soundings conducted from White Sands, NM, (*U.S. Standard Atmosphere Supplements,* 1966, p. 31) measured air-densities at 60-80 km altitude to be between -3% to $+8\%$ of the standard atmosphere air densities. Thus, the 1976 U.S. Standard Atmosphere model should be adequate for theoretical calculations (Section 2.5) which will be compared with experimental observations from Langmuir Laboratory, NM.

2.4 Atmospheric Conductivity and Relaxation Time

2.4.1 Ion Conductivity

In situ measurements of nighttime polar (negative and positive) ion conductivity were performed by *Holzworth et al.* [1985]. The polar conductivity values were found to be nearly equal ($\sigma_+ \simeq \sigma_-$) at most altitudes. *Holzworth et al.* [1985] measured ion conductivities which were well fit by an exponential scale height of 8.0 km below 40 km altitude and 11.1 km between 40 and 56 km altitude. The total ion conductivity ($\sigma_i = \sigma_+ + \sigma_-$) at 40 km was measured to be $\simeq 4.0 \times 10^{-11}$ S/m.

Holzworth et al. [1985] found a significant departure from the 11.1 km scale height above $\simeq$56 km altitude with a significant drop in σ_+ measured at 65 km altitude. The σ_i profile above 56 km will be approximated by an exponential with the scale height determined from the measured σ_i values at or near the endpoints of 56 km and 72 km. The total ion conductivity at 56 km using Equation 2.16 is 1.69×10^{-10} S/m while that at 70 km was measured by *Holzworth et al.* [1985] to be $\simeq 4.0 \times 10^{-10}$ S/m. The exponential scale height based on these points would be about 16.3 km. The total ion conductivity profile is summarized in the equations below.

$$\sigma_i = 4.0 \times 10^{-11} e^{\left(\frac{z-40}{8.0}\right)} \quad \left[\frac{S}{m}\right] \qquad z < 40 \text{ km} \tag{2.15}$$

$$\sigma_i = 4.0 \times 10^{-11} e^{\left(\frac{z-40}{11.1}\right)} \quad \left[\frac{S}{m}\right] \qquad 40 \leq z < 56 \text{ km} \tag{2.16}$$

$$\sigma_i = 4.0 \times 10^{-10} e^{\left(\frac{z-70}{16.3}\right)} \quad \left[\frac{S}{m}\right] \qquad 56 \leq z < 72 \text{ km} \tag{2.17}$$

The dashed line in Figure 2.5 shows the ionic conductivity, σ_i, for 40-90 km altitude, based on Equations 2.15-2.17. Equation 2.17 was extended to altitudes above 72 km, even though *Holzworth et al.* [1985] did not obtain any measurements in that region. This extrapolation may be somewhat in error for altitudes of $\simeq$72-78 km. However, the increasing importance of the electron conductivity with increasing altitude will diminish the potential impact of such errors (see next section).

2.4.2 Electron Conductivity

The electron conductivity, σ_e, is related to the electron density, n_e, by:

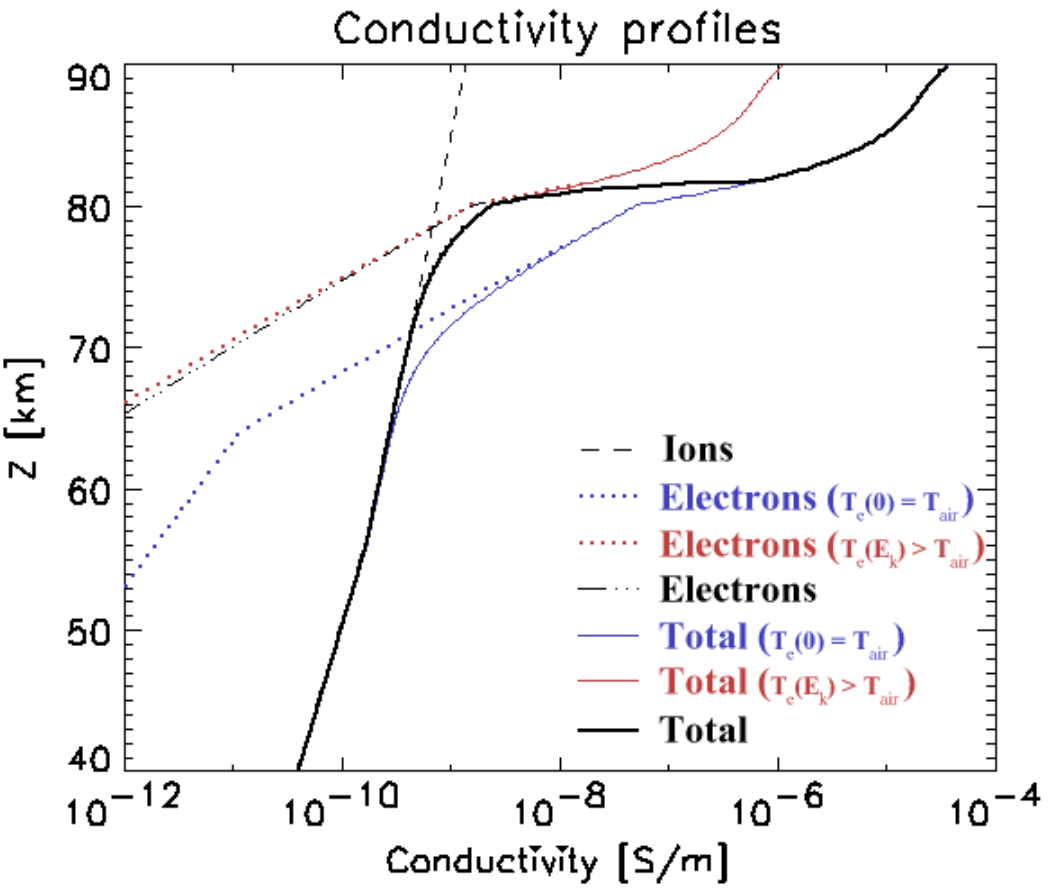

Figure 2.5: The ionic (dash), various electronic (dot and dash-dot), and corresponding total conductivities (solid) are shown in the graph above. An electron conductivity corresponding to: essentially "cold" electrons ($T_e \simeq T_{air}$) is drawn in blue, "hot" electrons immersed in a breakdown field of E_k ($T_e \gg T_{air}$) is drawn in red, and a realistic electron T_e based on a dipole field from the parent discharge, a near-breakdown field just below 80 km altitude, and a pre-existing relaxation time, is drawn in black (dash-dot). The corresponding total conductivities obtained by adding these electron conductivities with the ion conductivity is drawn with the same colors.

$$\sigma_e = q_e \mu_e n_e \tag{2.18}$$

where q_e is the fundamental unit of charge (1.6×10^{-19} C) and μ_e is the electron mobility. μ_e is a function of the air density (Section 2.2.2) and E/E_k (see below).

The electron mobility is inversely related to the effective collision frequency of electrons with neutrals, ν_m (Equation 2.2). ν_m is proportional to the thermal velocity of electrons, $\bar{v}$ (Equation 2.3). $\bar{v}$ can be expressed as a function of E/E_k according to the relationship $\varepsilon = \frac{1}{2}mv^2$ and Equation 2.6. As E/E_k is increased, μ_e will decrease as $\bar{v}$ and hence ν_m increases. This will decrease the electron conductivity, σ_e, according to Equation 2.18.

For altitudes of 64 km and below, an n_e profile identical to that of *Pasko et al.* [1997b] is used:

$$n_e = 8.0 \times 10^{-3} e^{(\frac{z-64}{10.1})} \quad [cm^{-3}] \qquad z < 64 \text{ km} \tag{2.19}$$

At altitudes of 80 km and higher, the IRI-95 model of electron density is used [*Rawer et al.*, 1978]. An IRI-95 profile was obtained from *http://nssdc.gsfc.nasa.gov/space/model/models/iri.html*. Input variables consist of latitude, longitude, date, and time. The location of Langmuir Laboratory (34.0° N, −107.2° W) was input into the model as well as a date and time of 1997, October 7, 4 UT. This particular time was chosen since it represents a reasonable average value for the high-speed video observations of sprites (Chapter 5). The IRI-95 model predicts that the electron density would be 3 cm^{-3} at 80 km altitude for the above input parameters. Changing the location and time inputs to correspond with particular high-speed video sprite events in Chapter 5 would result in an electron density at 80 km altitude which would be as high as 9 cm^{-3} at 3:03:59 UT (Section 5.2.3) or as low as 1 cm^{-3} for sprites which occur after 4:00 UT.

The value $n_e = 8.0 \times 10^{-3}$ cm^{-3} in Equation 2.19 at 64 km altitude and the IRI-95 model value of $n_e \simeq 3$ cm^{-3} at 80 km altitude were joined by assuming a constant exponential scale height increase of electron density between these altitudes. The exponential scale height for n_e between 64 km and 80 km altitude was only 2.65 km.

The dotted blue line in Figure 2.5 shows the electron conductivity component calculated with μ_e corresponding to essentially "cold" electrons with a temperature T_e the same as that of the air molecules, T_{air}. Once the breakdown field ratio, E/E_k, exceeds $\sim 5 \times 10^{-4}$ *Pasko et al.* [1997b], μ_e will decrease as ν_m increases (see previous discussion). The decrease in μ_e and hence σ_e (Equation 2.18) can be substantial

at $E = E_k$. This is shown by the dotted red line in Figure 2.5, which corresponds to the electron conductivity if somehow $E = E_k$ at all altitudes (corresponding to $T_e = T_e(E_k) \gg T_{air}$).

Neither the "cold" electrons, $T_e = T_{air}$, or "hot" electrons, $T_e = T_e(E_k) \gg T_{air}$, will correspond to the actual state of electrons at most altitudes. Rather, the actual T_e will likely lie somewhere in between for $E < E_k$. The dot-dash line in Figure 2.5 corresponds to conditions expected immediately after the onset of a sprite-producing CG with a maximum E/E_k of 0.8 at $\simeq$ 79 km altitude. Above 79 km altitude, the electric field is significantly attenuated by the larger conductivities (see Section 2.4.4). This causes the electron conductivity to rapidly cross from a "hot" profile to a "cold" one, resulting in a sharper conductivity ledge at the base of the ionosphere.

2.4.3 Total conductivity

The ionic and electronic conductivity components can be added together to determine the total atmospheric conductivity:

$$\sigma = \sigma_i + \sigma_e \tag{2.20}$$

In Figure 2.5, the total atmospheric conductivity profile which utilizes the "cold" electron profile is denoted by the solid blue line. The atmospheric conductivity for the $T_e(E_k)$ electron conductivity is denoted by the solid red line. The realistic total atmospheric conductivity profile which would likely exist immediately prior to sprite initiation is indicated by the solid black line.

2.4.4 Relaxation Time

The relaxation time, τ_r, is the amount of time it would take for an electric field to decay by $1/e$ in the absence of additional forcing. The relaxation time is related to the conductivity, σ, by the well known result: $\tau_r = \epsilon_o/\sigma$, where ϵ_o is the permittivity of free space.

The total conductivity profiles in Figure 2.5 were used to determine the corresponding relaxation times in Figure 2.6. Note that the effect of the change in the electron conductivity component due to electron heating just below the base of the conductitivy ledge increases the sharpness of the ionosphere conductivity "ledge". The relaxation time rapidly drops to less than 1 ms above $\simeq$ 81 km altitude. This height will be used in Section 2.5 as the base of the ionosphere.

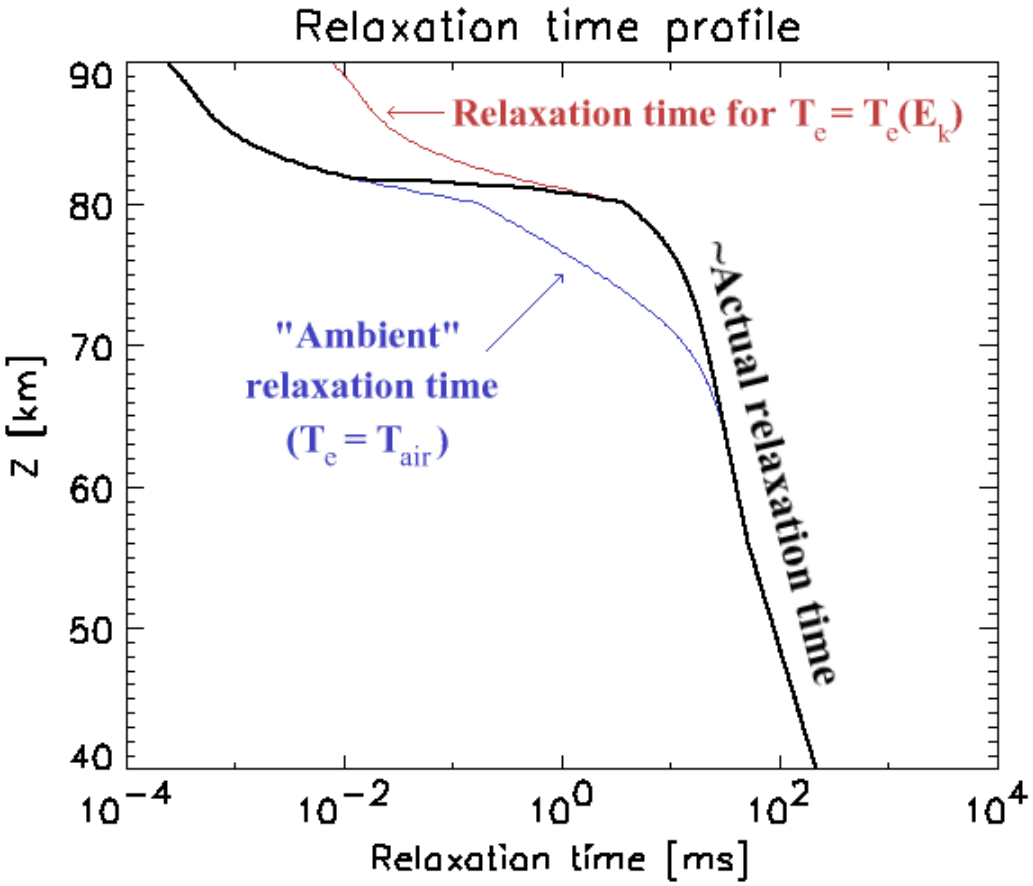

Figure 2.6: The blue and red lines plotted above are the relaxation time profiles corresponding to the total conductivities in Figure 2.5 with "quiescent" $T_e = T_{air}$ and $T_e = T_e(E_k) \gg T_{air}$ conditions respectively. The thick solid line is a best estimate of the relaxation time profile which would exist just prior to sprite initiation by a conventional breakdown mechanism at $E \geq E_k$.

2.5 Sprite Initiation Threshold

2.5.1 Infinite images

It is well known from electrostatic theory that a point charge placed above a conducting plane will cause charge to be redistributed on the plane's surface such that the potential will be constant there. Taking the potential to be zero on the surface, a charge of equal magnitude but of opposite sign to the source point charge can conceptually be placed an equal distance below the planar surface. The source charge and its image can be used to calculate the potential and hence the electric field vector anywhere above the conducting plane.

The situation becomes more complex when charge is placed between two parallel conducting planes. The charge will redistribute on the planes such that, conceptually, an image charge is formed behind each plane in the manner described previously. However, each plane will also respond to the redistribution of charge on the other plane and this will lead to the formation of "images of images" which are further displaced behind the respective conducting planes. The total number of images will be infinite, but the calculated electric field will be finite since each successive image charge is further away and the electric field contribution will decrease rapidly with distance.

A cloud-to-ground (CG) discharge will introduce a net charge at some average altitude Z. Figure 2.7a shows the index notation which is used in this work for the charge images. Assuming that a compact ("point") region of negative charge were placed at an altitude of $Z = 7.5$ km, surface charge rearrangement on the ground will lead to a positive image charge at $Z = -7.5$ km. It will be shown in Chapter 3 that 7.5 km is a reasonable approximation for the altitude of charge removal in sprite-producing discharges. The source charge and its immediate image correspond to $i = 0$ in Figure 2.7a.

Charge will rearrange on the nighttime ionosphere conductivity ledge at $Z \simeq 81$ km (see Section 2.4.4) in response to the source charge and its image. The result is the $i = 1$ image pair consisting of a positive image charge at $Z = 81 + (81 - 7.5) = 154.5$ km and a negative image charge at $Z = 81 + (81 + 7.5) = 169.5$ km. This, in turn, will lead to the $i = 2$ pair of negative and positive image charges at $Z = -154.5$ km and $Z = -169.5$ km, respectively, and so on. The effect of the ionosphere is to enhance the electric field above the source charge. However, the electric field at ground-level is decreased by the presence of the ionosphere, as will be shown in Appendix C. This

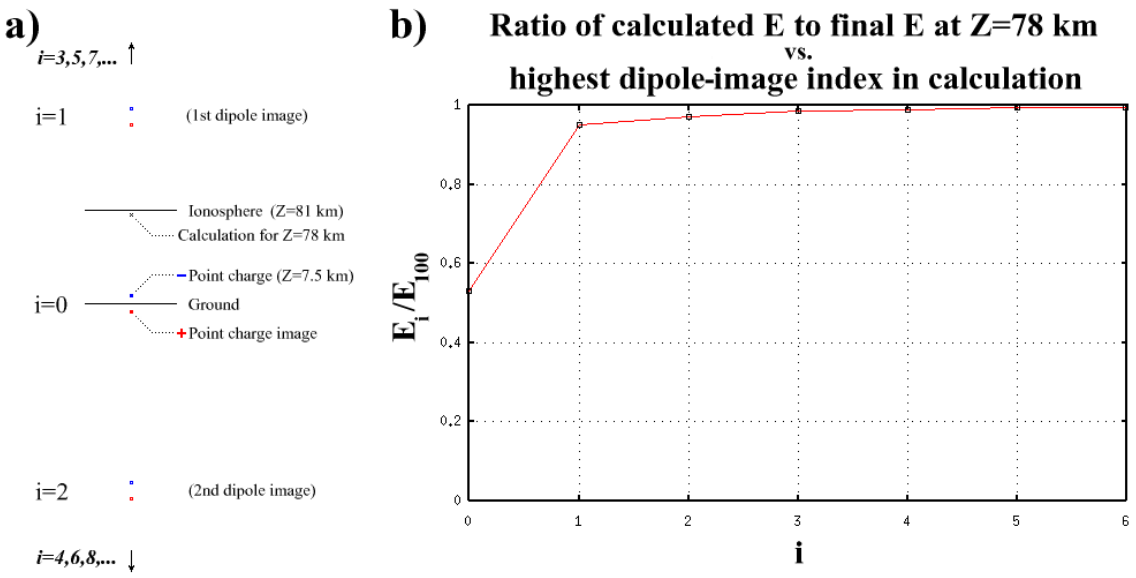

Figure 2.7: a) A schematic diagram of the infinite images formed by a negative point charge placed above the Earth's surface. The indices at left correspond to increasing image pairs (approximately dipoles) of positive and negative charges. b) The rate of convergence at $Z = 78$ km of the calculated electric field to a "final" electric field value is shown as a function of the number of successive image pairs included in the calculation (with $i = 0$ corresponding to a calculation based only on the source and its below-ground image). The "final" electric field was calculated for a summation up to $i = 100$.

latter effect will be important for calculations based on electric field measurements presented in Chapter 3.

It will be shown in Section 5.2.4 that sprites often appear to initiate at 77-78 km MSL altitude. Figure 2.7b shows how the calculated electric field at $Z = 78$ km varies with increasing image number in Figure 2.7a. The vertical axis is normalized such that a value of unity corresponds to the "final" electric field value, which was calculated for a summation up to the $i = 100$ image pair. By $i = 5$, the calculated electric field is within 1% of the "final" electric field value. The rate of convergence of E_i to E_{100} is sufficiently fast that a much larger "final" i value would not noticeably change the Figure 2.7b plot.

In this study, the theoretical electric field calculations for sprite altitudes implement a summation up to $i = 2$. The electric field calculated in this manner will only

be $\simeq 3\%$ less than that based on an infinite summation.

It should be noted that the appearance of each successive image pair will be delayed by the amount of time that it takes the electric field (propagating at the speed of light) to traverse the Earth-ionosphere distance, $\Delta t \simeq 81/300 = 0.27$ ms. As was shown by *Pasko et al.* [1999], the delayed appearance of the source charge's image below ground might significantly enhance electric fields aloft. For instance, if a charge were suddenly introduced at $Z = 7.5$ km, an observer far above the charge would at first only experience the effects of this monopole, for which the electric field falls only as r^{-2}, before a less intense dipole-like dependency of about r^{-3} appears due to the image. The time delay between the monopolar and dipolar field dependency would be twice the height of the charge divided by the speed of light (since the electric field must propagate down and then back up to the observer). For a charge at $Z = 7.5$ km: $\Delta t = 0.05$ ms. This time difference is not much less than the duration of the return stroke, which is typically $\sim$75-230 μs [*Uman*, 1987,pg. 124]. This retardation effect could significantly lower the sprite initiation threshold [*Pasko et al.*, 1999] from the quasi-electrostatic predictions of the following sections.

2.5.2 Uniformly Charged Disk

Sprites are primarily caused by +CGs which occur in the trailing stratiform region of mesoscale convective systems (MCSs) [*Boccippio et al.*, 1995; *Lyons*, 1996]. The sprite-producing +CGs may discharge horizontally-extensive positive charge regions which are known to exist near the 0°C isotherm within stratiform regions [*Marshall and Rust*, 1993; *Marshall et al.*, 1996].

In order to assess the possibility of conventional breakdown onset as a function of parent discharge charge height and horizontal extent parameters, a static field approximation identical to that of *Krehbiel et al.* [1996] is implemented. In this approximation, the parent discharge is modeled as a uniformly charged disk of total charge Q_d, radius R_d, and altitude of Z_d parallel to the ground. The electric field along the central axis above the disk can be readily determined, as shown below.

The solution to Poisson's equation ($\nabla^2 V = -\rho/\epsilon_o$) for a surface charge distribution is given by the formula:

$$V = \frac{1}{4\pi\epsilon_o} \int \frac{\sigma}{r}\, da$$

where r is the distance along a vector to the infinitesimal area, da, of local charge density σ.

Using cylindrical coordinates for the disk; $da = \rho\, d\rho\, d\phi$, where ρ is a radial distance from the disk center and ϕ is an angle around the disk. Assuming that V is measured along the central axis; $r = (\rho^2 + z^2)^{\frac{1}{2}}$, where z is the height above the disk. Since the disk is assumed to be uniformly charged, $\sigma \equiv \sigma_d =$ constant. Substituting,

$$\begin{aligned} V_d(z) &= \frac{\sigma_d}{4\pi\epsilon_o} \int_0^{R_d} \left(\int_0^{2\pi} \frac{\rho}{(\rho^2 + z^2)^{\frac{1}{2}}}\, d\phi \right) d\rho \\ &= \frac{\sigma_d}{2\epsilon_o} \int_0^{R_d} \frac{\rho}{(\rho^2 + z^2)^{\frac{1}{2}}}\, d\rho \\ &= \frac{\sigma_d}{2\epsilon_o} \left[(\rho^2 + z^2)^{\frac{1}{2}} \Big|_0^{R_d} \right. \\ &= \frac{\sigma_d}{2\epsilon_o} \left[({R_d}^2 + z^2)^{\frac{1}{2}} - z \right] . \end{aligned} \tag{2.21}$$

The electric field along the axis above the disk can be calculated from Equation 2.21 by using the electrostatic relationship $\vec{E} = -\nabla V$:

$$\begin{aligned} \vec{E_d}(z) &= -\frac{\mathrm{d}V_d}{\mathrm{d}z}\, \hat{z} \\ &= \frac{\sigma_d}{2\epsilon_o} \left[1 - \frac{z}{({R_d}^2 + z^2)^{\frac{1}{2}}} \right] \hat{z} \end{aligned} \tag{2.22}$$

where σ_d is the surface charge density on the disk,

$$\sigma_d = \frac{Q_d}{\pi R_d^2} , \tag{2.23}$$

which is assumed to be uniform.

Equations 2.22 and 2.23 provide a solution for $E_d(z)$ in terms of only Q_d, R_d, and the distance z along the central axis from the disk. As was shown in Section 2.5.1, the actual electric field $E(Z)$ at some height Z above the ground will be due to the source charge configuration and its multiple images. In this dissertation, the highest order disk-image pair used in the calculations corresponds to $i = 2$ in Figure 2.7a. Thus, the expression for the electric field as a function of height along the central axis will be:

$$\begin{aligned} \vec{E}(Z) \cong & \Big[E_d(Z - Z_d) - E_d(Z + Z_d) + \\ & E_d(2Z_{ledge} - Z - Z_d) - E_d(2Z_{ledge} - Z + Z_d) + \\ & E_d(Z_{ledge} + Z - Z_d) - E_d(Z_{ledge} + Z + Z_d) \Big] \hat{k} \qquad Z_d < Z < Z_{ledge} \end{aligned} \tag{2.24}$$

where Z_{ledge} is the altitude of the ionosphere conductivity "ledge". Equation 2.24 is valid only when the altitude of interest, Z, is greater than the altitude of the disk, Z_d.

It is well known in electrostatics that a dipole's field is proportional to the moment, $p = qd$, where q is the charge magnitude and d is the separation distance between the charges. The convention which is commonly used in sprite literature is to define the "charge moment" as the product of the total net charge with its mean height above ground, which would be one half the distance d between the charge and its image. This convention will also be adopted in this study. Thus, the charge moment of the disk will be $Q_d Z_d$.

Figure 2.8 illustrates how the horizontal dimensions of the source charge region would affect the value of the electric field just below the base of the ionosphere ($Z_{ledge} = 81$ km) at $Z = 78$ km. The charge moment, $Q_d Z_d$, was fixed for all of the plots. Thus, as R_d is increased, σ_d is decreased according to Equation 2.23) in order to keep Q_d constant for a given Z_d. In reality, however, σ_d may be somewhat fixed and thus more horizontally extensive discharges would produce a larger charge moment change, as was modeled by *Marshall et al.* [1996]. The main purpose in this section is to determine how accurately the electric field below the base of the ionosphere can be determined based on charge moment measurements in which the discharge dimensions are not known. The charge moment will be kept fixed while the discharge dimensions are varied to see what effect this has on the electric field at high altitude.

For a given charge moment, Figure 2.8 shows that a more horizontally extensive flash will be less effective at initiating conventional breakdown. However, if the horizontal dimensions are sufficiently small ($R_d < 20$ km), the decrease in electric field relative to the point charge approximation will be relatively minor ($< 10\%$). In Chapter 3, it is shown that sprite-producing discharges may often meet this criterion.

Three different disk altitudes, Z_d, which roughly correspond to the range of physically possible values are plotted in Figure 2.8. The 5 km altitude is close to that of the positive charge layer at or near the 0°C isotherm, typically between $4-5$ km altitude, within an MCS stratiform region [*Marshall and Rust*, 1993]. An altitude of 10 km is plotted since it has been used in the sprite-producing discharges modeled by *Pasko et al.* [1997b] and also represents a possible height of positive charge in a thunderstorm anvil [*Marshall et al.*, 1989]. An altitude of 15 km would correspond to the upper part of a thunderstorm turret and is plotted merely for the purpose of comparison.

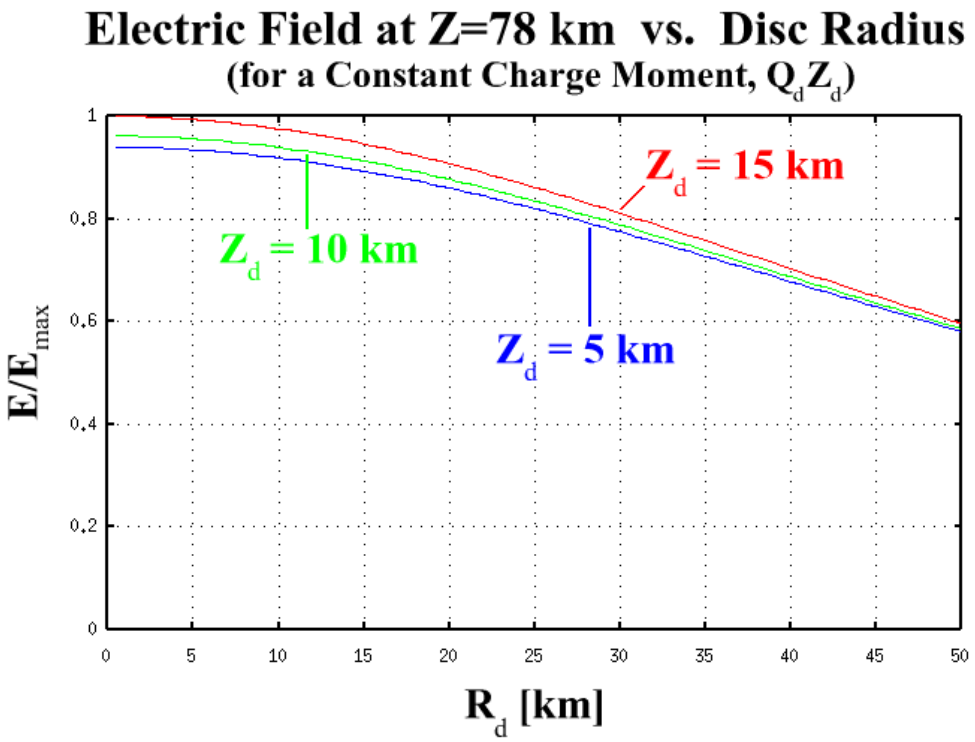

Figure 2.8: The variation of the electric field at $Z = 78$ km is shown as a function of disk radius, R_d, for a given charge moment, $Q_d Z_d$. The maximum electric field, E_{max}, corresponds to an extreme (and improbable) case of a point charge ($R_d = 0$) at $Z_d = 15$ km, the largest physically possible height (near the top of a convective turret). Larger R_d and lower Z_d will produce a smaller electric field ($E/E_{max} < 1$). However, decreasing Z_d has only a minor effect, especially for realistic Z_d of 5 and 10 km for which the electric field ratio differ by $\lesssim 3\%$ at each R_d.

For a given charge moment, Figure 2.8 shows that the electric field is only weakly dependent on mean charge altitude for realistic altitudes. The difference between the 5 and 10 km plots is less than 3% for all radii. This demonstrates the usefulness of the charge moment in assessing the likelihood of sprite initiation. One does not need to separate out the charge or height components. This will be fundamentally important for ELF measurements of sprite initiation thresholds (Chapters 4 and 5).

2.5.3 Initiation Threshold vs. Height

The earliest estimate of the charge moment required to reach a critical field, E_k, at high altitudes was made by *Wilson* [1925]. Wilson estimated that a charge moment of about 2800 C·km would be required to reach E_k at 60 km altitude, and that a moment about 1/10 of this ($\simeq 280$ C·km) would be required to reach E_k at 80 km altitude. However, Wilson's insightful early model didn't take a couple of factors into account. He did not incorporate the effect of an ionosphere, which nearly doubles the observed electric field at high altitudes (see Figure 2.7). Wilson also estimated an air density at 60 km which was only 64% of the 1976 U.S. Standard Atmosphere (Section 2.3.1). Fortuitously, the effect of these approximations almost cancels.

A more recent estimate was made by *Fernsler and Rowland* [1996] which incorporated the effects of a realistic ionosphere height between 80−85 km altitude. They estimated that the sprite initiation threshold would be 300 C·km at 80 km altitude and only 150 C·km at 85 km. They also estimated that a much larger charge moment change of 8000 C·km would be required to produce conventional breakdown at lower altitude during the daytime when the base of the ionosphere is lower (see Section 4.3). These charge moment estimates were based on the 1976 U.S. Standard Atmosphere and an assumption that $E_k/N = 100\ Td$.

The charge moment required to reach a breakdown condition of $E_k/N = 123\ Td$ (Section 2.2.3) is plotted in Figure 2.9 as a function of altitude. The height of the ionosphere, Z_{ledge}, was set to 81 km (Section 2.4.4). The moments were calculated based on electrostatics. Thus, the reduction in the electric field due to the relaxation time as well as the enhancement due to retardation effects *Pasko et al.* [1999] are not included.

Since the charge moment threshold depends somewhat on the source charge configuration (Section 2.5.2), the thresholds for different parent discharge geometries are plotted. As was discussed previously, a point charge at 15 km altitude represents an extreme and unlikely example, and is plotted merely as a limiting value.

Figure 2.6 shows that the relaxation time exceeds 1 ms for altitudes at and below 80 km. For a uniformly charged disk of radius $R_d = 10$ km and height $Z_d = 10$ km, the charge moment threshold would be $\simeq 360$ C·km for breakdown at $Z = 80$ km. If the disk's radius is increased to $R_d = 20$ km and the height decreased to $Z_d = 5$ km, the charge moment threshold criteria rises to $\simeq 390$ C·km. For breakdown at $Z =$ 78 km, the disk charge moment thresholds would be $\simeq 490$ C·km and $\simeq 530$ C·km, respectively. The initiation altitude of sprites will be determined in Chapter 5 and

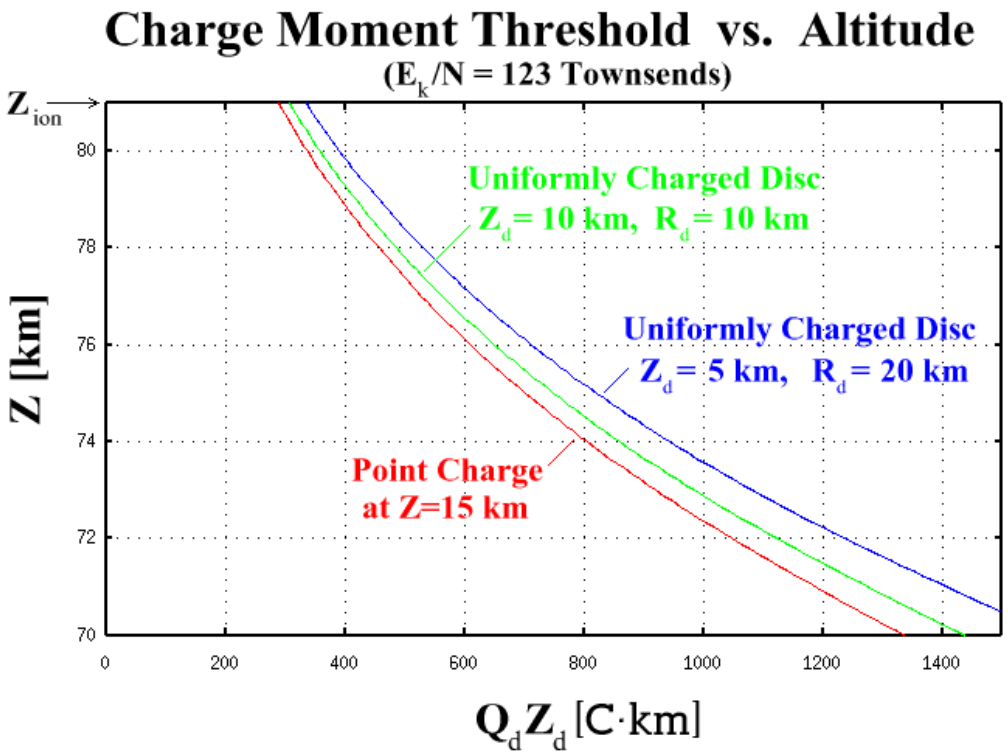

Figure 2.9: The charge moment threshold for sprite initiation is plotted as a function of altitude between 70 and 81 km for 3 different parent discharge configurations.

will be shown to be similar to the 78 km MSL altitude used here.

Pasko et al. [1997a] showed that discharges with charge moments exceeding the conventional breakdown threshold in a region below the base of the ionosphere would produce diffuse luminosity due to ionization within that region. Observations of these events will be presented in Chapter 5.

2.6 Streamers

2.6.1 Formation

It was shown in Section 2.2.4 that electron avalanches can form when the E/N ratio exceeds the breakdown threshold of air at $\simeq$123 Td. It was also demonstrated that the electrons will collectively drift under the influence of an external electric field and this cloud of electrons will expand (see Figure 2.2.4a) due to diffusion and mutual

electrostatic repulsion.

As the electron cloud expands and the number of electrons grows, the electric field produced by the electrons and positive ions will increasingly weaken the total electric field in the region between the electron and positive ion charge centers. In contrast, the electric field both ahead of the electron charge center and behind the positive ion charge center will be enhanced.

Figure 2.1 shows that the ionization and attachment frequencies (ν_i and ν_a) are strongly dependent on the E/N ratio. Thus, the alteration of the electric field by space charge in the electron avalanche can lead to a substantial alteration of the ionization rate, reducing the ionization rate in the region between the electron and positive ion charge centers and enhancing it ahead and behind of the respective charge centers. The enhanced ionization regions can develop and intensify into space charge waves which propagate in opposite directions away from the avalanche and have opposite polarities [*Loeb and Meek*, 1940; *Dhali and Williams*, 1985]. These space charge waves are commonly referred to as "streamers".

There is a minimum radius of the avalanche region which is required for the streamer transition, as was shown by *Pasko et al.* [1998a] and *Raizer et al.* [1998]. At 80 km altitude, the minimum radius is approximately 60 m [*Raizer et al.*, 1998].

2.6.2 Propagation

The streamer which develops from the positive ion region has a net positive charge in its tip and is referred to as a positive streamer. A schematic illustration of a positive streamer is shown in Figure 2.10. Multiple electron avalanches are produced by free electrons in the high electric field region ahead of the streamer tip. The avalanches fill in the positive tip, but also leave behind positive ions. These positive ions become the new streamer tip and the avalanche process can continue.

The avalanche process and resulting streamer motion will be continuous provided there are a sufficient number of free electrons ahead of the streamer tip and a sufficiently large external electric field. At tropospheric altitudes, the free electrons are generated by photoionization. At the altitudes of sprites within the mesosphere, enough free electrons may already be present for stable streamer propagation [*Raizer et al.*, 1998].

The minimum electric field, E_+, required for positive streamer propagation in air at standard temperature and pressure (STP) has been measured to be between 400 and 440 kV/m [*Loeb and Meek*, 1940; *Phelps*, 1974; *Allen and Ghaffar*, 1995],

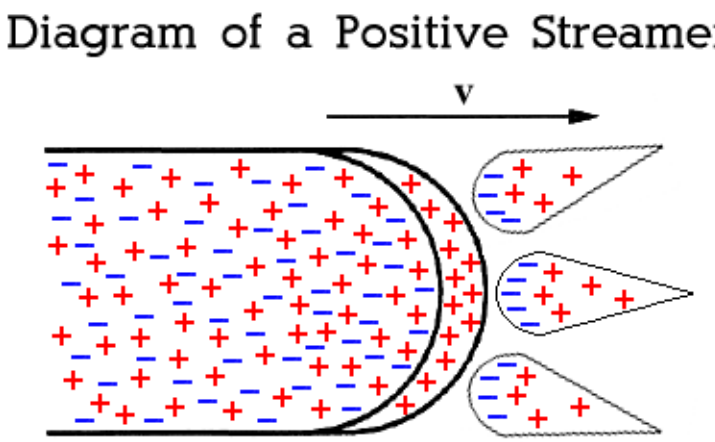

Figure 2.10: Schematic diagram of a positive streamer. A net concentration of positive ions in the streamer tip creates a strong electric field which produces electron avalanches. As the electron avalanches propagate into the net positive charge region, they leave behind positive ions which become the new streamer tip, advancing the streamer forward. Adapted from *Bazelyan and Raizer* [1997] Figure 3.1.

corresponding to an E_+/N of 15–16 Td. This is ∼8 times less than the breakdown threshold, E_k/N, of ≃123 Td (see Section 2.2.3).

Measurements of positive streamer propagation by *Griffiths and Phelps* [1976] show that E_+/N is not a constant, but actually diminishes with decreasing air density. Their measurements indicate that E_+/N decreases from ≃15 Td at 1000 mb (≃0 km MSL) to ≃9 Td at 300 mb (≃11 km MSL) and a constant temperature of 25°C. *Raizer et al.* [1998] noted that at higher altitudes and lower atmospheric densities, the attachment of electrons to oxygen loses importance due to the lower collision frequencies and the E_+/N value should approach that for molecular nitrogen (6 Td), a non-electronegative (non-electron-attaching) gas. They calculated that for a charge moment change of 350 C·km, a positive streamer would propagate from an altitude of 80 km MSL down to 48 km MSL, where it would terminate. Triangulated measurements of sprites show that they often extend down to 50 km or lower [*Sentman et al.*, 1995] while the charge moment changes of sprite-producing discharges have been measured to be ≳300 C·km [*Cummer and Stanley*, 1999; *Huang et al.*, 1999]. A charge moment analysis of several sprite-producing discharges is presented in Section 5.3.

Raizer et al. [1998] calculated that the velocity of the downward positive streamer propagation would maximize at $\simeq 1.2\times10^7$ m/s about 4 ms after it was initiated at an altitude of 80 km under the influence of a 350 C·km charge moment change. Actual measurements of maximum average positive streamer velocities in sprites will be presented in Chapter 5 and compared with theoretical predictions.

A schematic diagram of a negative streamer will differ from that of the positive streamer in that the tip of negative streamer will be negatively charged and the electron avalanches will point outward from the tip. As was discussed by *Pasko et al.* [2000], the minimum electric field, E_-, for negative streamer propagation is two to three times higher than for positive streamers and thus $-$CG sprites will tend to be less vertically extensive than +CG sprites.

Chapter 3

Close Sprite-producing Discharges

3.1 Introduction

In this chapter, the spatial and temporal development of several sprite-producing discharges will be analyzed as well as that of a non-sprite-producing discharge. All of the analyzed events were associated with a relatively small (∼50 by ∼100 km) mesoscale convective system (MCS) at less than 100 km distance over central Florida on June 22nd, 1997. The Kennedy Space Center Lightning Detection and Ranging system recorded the spatial development of the flashes. Electric field measurements associated with the New Mexico Tech Interferometer recorded the static electric field change as a function of time for the discharges. This, combined with range information, was used to estimate cloud-to-ground charge moment changes. Light-intensified video was obtained of the sprites and was used to estimate the positions of the sprites relative to the parent discharge. All of these results will be presented and interpreted in this chapter.

3.2 Instrumentation

The instruments which were commonly used to acquire data on or pertaining to sprites in this dissertation are described in Appendix A. However, much of the data presented in this chapter was acquired by instruments which were either not used elsewhere in this study (e.g. LDAR) or were operated in a different mode than elsewhere (e.g. NMT interferometer). These instruments and their operation will be briefly discussed below.

3.2.1 KSC LDAR

The Lightning Detection and Ranging (LDAR) system was developed at the Kennedy Space Center (KSC) in order to provide real time lightning safety information [*Maier et al.*, 1995a]. The LDAR is able to accurately locate lightning radiation sources in 3 spatial dimensions and time by measuring the arrival time of impulsive VHF events at seven stations.

The operating frequency of the LDAR is centered at 66 MHz with a 3 dB bandwidth of 6 MHz. The 66 MHz VHF signal at each station is logarithmically detected and transmitted to the central site via video microwave links. Each of the analog signals is sampled at the central site with a 100 MHz rate and with 8-bit resolution. The time and amplitude of the peak signal within an 81.96 μs window is determined for each channel every 100 μs. This data is output to a data computation system which determines 3D source locations for those points which are observed at the proper retardation times by at least 4 stations.

The stations are positioned such that they are approximately evenly-spaced from each other on the periphery of a circle $\simeq$10 km in radius, with one station at the center (see Figures 3.1-3.2). The median location error within the LDAR network is only $\simeq$50 m [*Maier et al.*, 1995a]. Outside the network, the 3D location errors are due primarily to radial errors which increase with range at a rate faster than the linearly increasing transverse errors due to a fixed bearing error of $\simeq 0.5^{\circ}$.

The individual flashes analyzed in this dissertation were reported by LDAR to be between 40-130 km range from the LDAR central station. The median radial error at 40 km was directly measured by *Maier et al.* [1995a] to be $\simeq$1 km for regular VHF pulses emitted from an aircraft which was equipped with a differential GPS navigational system. Assuming an approximate r^2 dependency of radial errors on range [*Boccippio et al.*, 1999], the median radial error at 130 km range would be $\simeq$10 km.

The detection efficiency of the LDAR instrument decreasees with increasing source range. Climatologically-averaged areal source density declines exponentially with ground range at an e-folding length of 39-50 km [*Boccippio et al.*, 1999]. Thus, the detection efficiency at 40-130 km range would be a factor of $\sim$3-30 less than within the LDAR network.

One effect of the rapid drop in detection efficiency is that sources which are closer than their calculated range will be overrepresented relative to sources which are further away, resulting in a net outward bias in radial locations. This will also result in

an upward bias in heights. Climatologically-averaged source density plots of LDAR heights with respect to range indicate that heights are "pushed up" at increasing range with an approximate r^2 dependency, though this effect is somewhat minor with only a $\simeq$1 km increase in height at 100 km range [*Boccippio et al.*, 1999]. Since most of the data points analyzed will be within 100 km range, the systematic increase in height will not be particularly important.

3.2.2 NMT Interferometer

The New Mexico Tech (NMT) interferometer maps lightning at 274 MHz (VHF) in 2 dimensions (azimuth and elevation) with high time resolution ($\sim$2 μs). The interferometer is able to map lightning by obtaining phase data from multiple pairs of antennas along orthogonal baselines [*Hayenga and Warwick*, 1981; *Richard and Auffray*, 1985; *Rhodes et al.*, 1994]. Prior to 1995, the interferometer antennas were confined to a horizontal plane and this limited the interferometer's ability to resolve flash structure beyond $\sim$20 km range [*Shao*, 1994]. In 1995, a vertical baseline was added to the interferometer which extended the interferometer's useful range to beyond 50 km. However, the vertical baseline's systematic errors have not yet been adequately determined and this limits its effectiveness in this study, particularly since the sprite-producing flashes were centered at or beyond 80 km range.

In addition to the phase data, log-RF and electric field data are sampled by the interferometer's data acquisition system (see Appendix A.2). Like the interferometer phase data, the log-RF is centered at 274 MHz with a 3 dB bandwidth of 6 MHz. The log-RF was sampled with 8-bit resolution.

The electric field data were acquired from a slow antenna (SA). Additional electric field data were sampled in the form of "fast antenna" (FA) data, which are amplified and high-pass-filtered SA data. Both the SA and FA were sampled at 12-bit resolution. The SA electric field data will be used in Section 3.5 to estimate the charge moment at various times after a return stroke for both sprite-producing and non-sprite-producing discharges.

The interferometer data acquisition system acquires data at a 500 kHz rate and can be armed in either an RF-threshold mode or in a FA-trigger mode. In the RF-threshold mode, a 100 μs data block of phase, log-RF, and FA data is acquired whenever a log-RF sample exceeds a user-specified threshold within a data block. The slow antenna data is sampled continuously at 5 kHz in this mode. In the FA-trigger mode, a user-specified FA threshold is used to trigger the system. A user-specifed pre-

and post-trigger length of phase, log-RF, and FA data is stored around the trigger. The SA data is also sampled and stored for the same time interval, albeit with a 10 kHz sample rate.

3.3 Observations

On June 22nd, 1997, the NMT interferometer was armed in an RF-threshold mode at 00:30 UT in support of a high-elevation (77°) Optical Transient Detector (OTD) overpass at 00:35 UT. The system continued to acquire RF-thresholded data after the overpass until about 01:48 UT, when the system was transitioned to a FA-threshold mode. The FA-threshold mode was activated at 01:50:20 UT and was not deactivated until an hour later at 02:50:25 UT, when the system was transitioned to a sferic-recording mode.

Video recording from a Xybion low light level camera began at 01:12:30 UT, a half hour before the first sprite was observed. Video was recorded continuously until 03:49 UT, which was more than an hour after the last sprite event had been observed. The Xybion camera was equipped with the widest angle lens available, a 12.5 mm lens, in order to cover the large angular region of sky above the close storm system. The field of view of the 12.5 mm lens was determined by a stellar fit (see Appendix B.3.1) to be $55.7° \times 45.6°$. The camera was pitched up to an elevation angle of $\simeq 43°$ above the horizon, which was high enough that sprites would appear near the center of the video image while the bright and potentially image-saturating "close" discharges would be below the field of view. In spite of this precaution, some of the discharges were still saturating the camera due to scattered light reflecting into the lens from the lens rim. To eliminate this scattered light, black electrical tape was placed on the lens rim at about 01:26 UT.

3.4 Storm development history

Figures 3.1-3.2 show the formation, maturation, and dissipation of a mesoscale convective system (MCS) over a time span of 4 hours between 23 UT on June 21, and 3 UT on June 22, 1997 (7-11 pm Eastern Daylight Time on June 21). The data points are 3D lightning VHF source locations determined by LDAR. These points are rainbow-colored with respect to time such that blue corresponds to VHF sources near the beginning, yellow is near the middle, and red is near the end of each 20 minute

time interval. The △ and + symbols correspond to –CG and +CG stroke locations, respectively, as determined by the National Lightning Detection Network (NLDN) [*Cummins et al.*, 1998].

In Figure 3.1a, a couple of isolated thunderstorms produced lightning throughout the 20 minute time interval. Towards the end of the time interval, a couple of new storms each produced their first intracloud discharge, as denoted by the clusters of red data points between and to the south of the active storms. Note the significant radial errors manifested by the spreading of the points along a radial line to the LDAR stations (□ symbols).

In Figure 3.1b, additional storm cells became electrified and these storms began to organize into a line. In the next time interval, the cell on the northern edge became inactive while the CG flash rate from the other cells intensified. In Figure 3.1d, new electrically active cells were evident on the southern edge. The MCS flash rate appeared to have reached a maximum between 00-01:00 UT (Figure 3.1d-f).

In Figure 3.2a, some discharges began to propagate into the region "behind" the northern half of the convective line. The horizontal discharges became more extensive with time, as evident in panel b). This pattern of increasing horizontal discharge dimensions was always readily evident 20 minutes or more prior to sprites, and turned out to be a good diagnostic for predicting where sprites might appear. In contrast, the CG strike locations indicated by NLDN did not provide any predictive lead time as to when and where sprites might occur. However, it should be noted that increasing horizontal discharge extent was not always followed by sprites, particularly if the discharges were somewhat 1-dimensional with a limited total area.

A large number of NLDN-indicated +CGs were associated with the active cell on the southern end of the storm line in Figures 3.2a-b. Almost all of these "+CGs" had NLDN signal strengths below 100 LLP units (< 18.5 kA peak current). An earlier unpublished study (by the author) of weak "+CG" sferic records indicated that such events were probably ICs, though this has not yet been quantified. A few NLDN-indicated +CGs were evident in the region of horizontally extensive discharges. All of these "+CGs" were also weak at under 150 LLP strength and may also have been ICs. The northermost "+CG" is known to be a false detection which followed less than 0.2 ms after a real –CG from the northernmost active convective cell.

Sprites were initiated by many of the +CGs associated with horizontally extensive discharges in Figure 3.2c. The sprite events were coincident on video with the +CGs at 01:42:57.172, 01:47:52.711, 01:51:02.762, and 01:55:47.956 UT. These sprite events

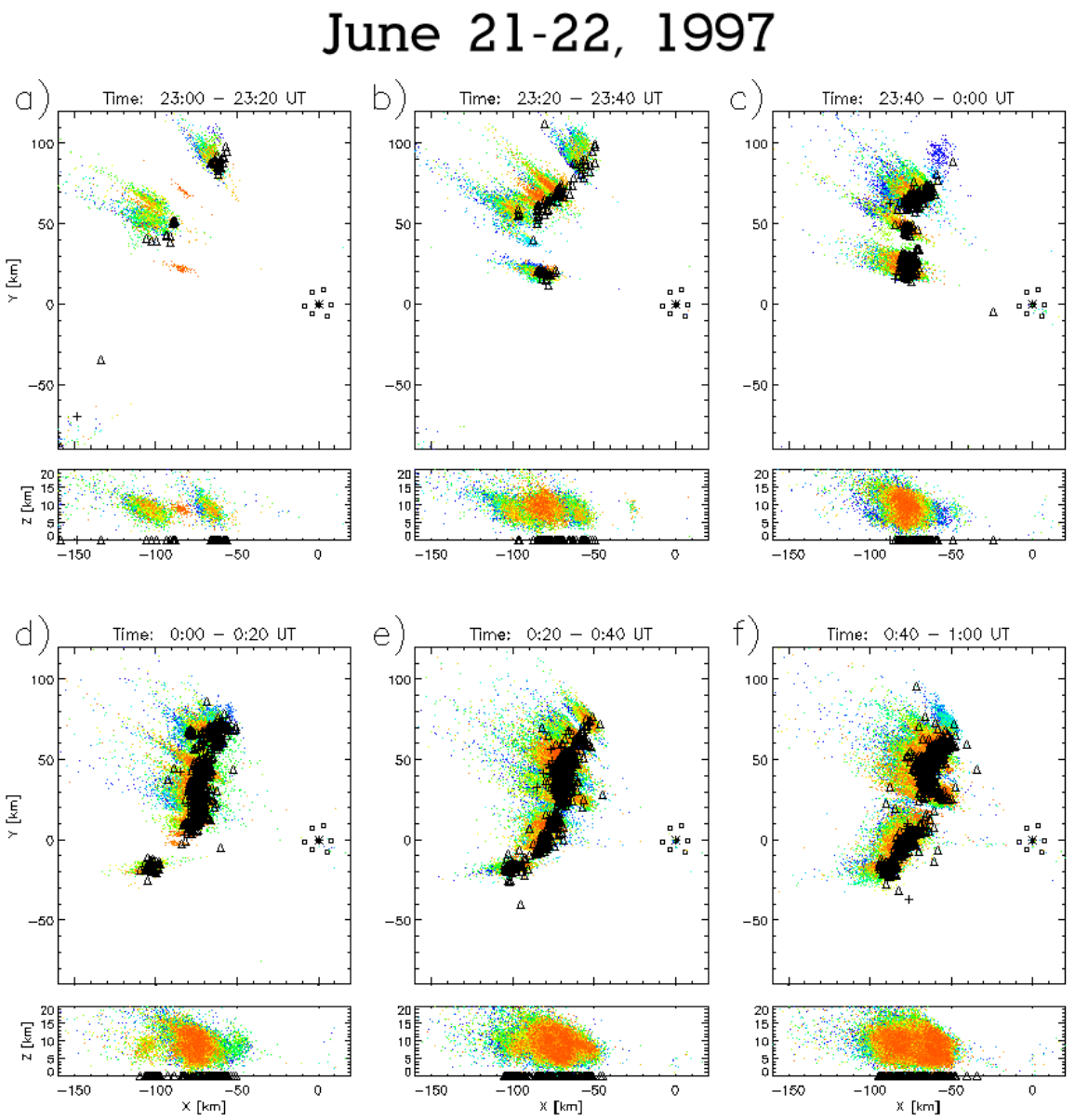

Figure 3.1: The formation of a mesoscale convective system (MCS) is shown in 20 minute intervals between 23 UT and 1 UT on June 21st and June 22nd, 1997. The Lightning Detection and Ranging (LDAR) data points are rainbow-colored from blue to red with respect to elapsed time within each interval. –CG stroke (△) and +CG stroke (+) locations were obtained from the National Lightning Detection Network (NLDN). The observation site (*) corresponds to $x = 0$, $y = 0$. The LDAR station locations (□) are also shown.

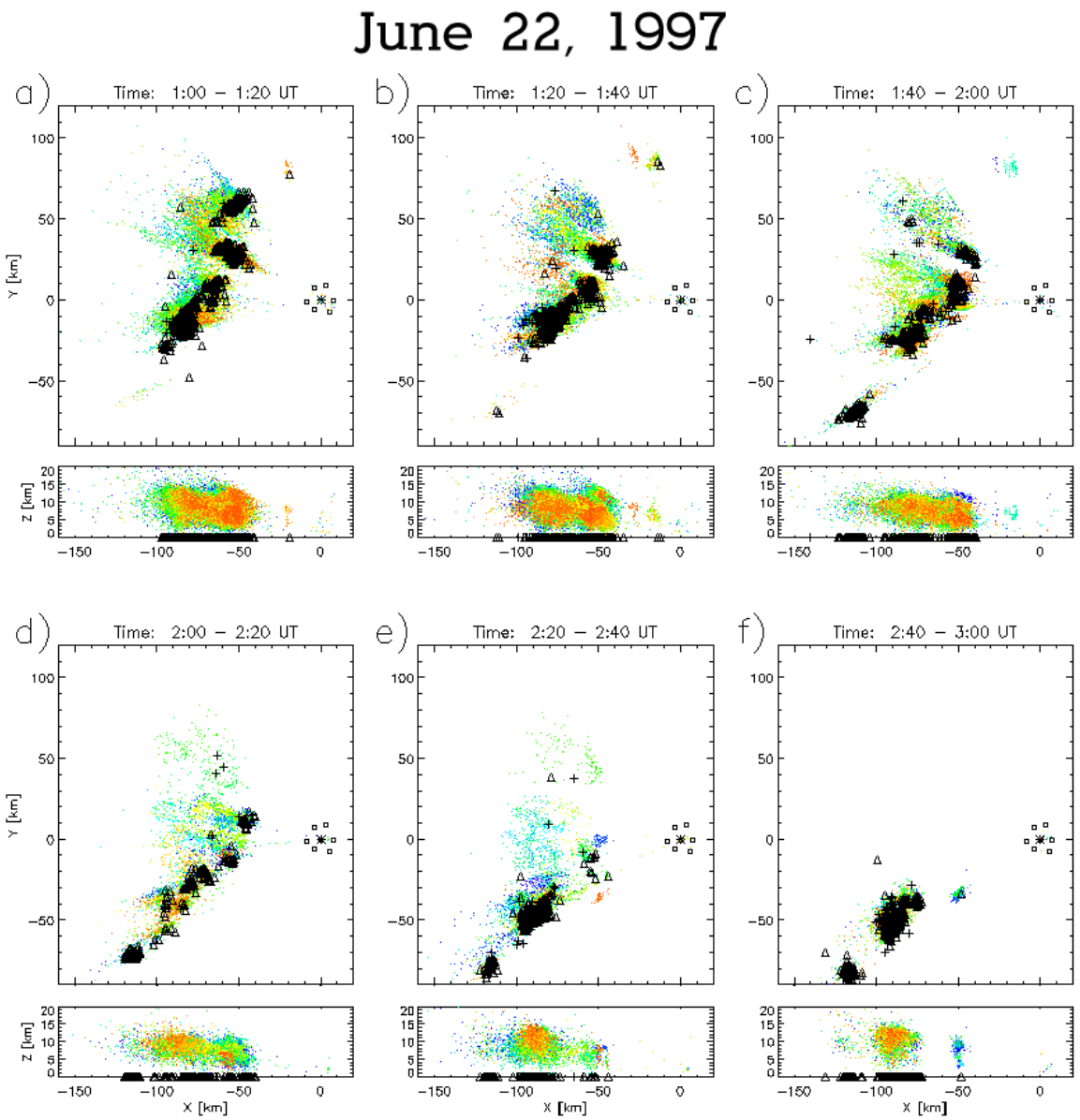

Figure 3.2: A continuation of Figure 3.1 for 1-3 UT on June 22nd, 1997. The MCS continued its southward advancement as new storm cells formed on the southern flank while older cells decayed on the northern flank. Sprites were associated with some of the +CGs produced by horizontally extensive discharges in panels c-e.

and their parent discharges are examined in detail later in this chapter. Additional sprite events occurred at 02:09:16.9, 02:09:17.1, and 02:27:21.3 UT in Figures 3.2d-e. Unfortunately, the interferometer system failed to trigger for these events.

The storm system continued to advance southward as new cells formed at the southern edge. However, it is clear that the convective line lost its cohesion in Figure 3.2. The storm complex eventually subsided within a few hours and no sprites were observed after the 02:27 UT event.

3.5 Charge Moment Analysis

The charge moment is defined in this study to be the product of the charge magnitude and its average height above ground. It was shown in Chapter 2 that the charge moment magnitude is the fundamentally important parameter in conventional breakdown models of sprite initiation. The quantity being measured is the moment due to the removal of charge to ground by a CG discharge. This corresponds to a "charge moment change". Since the electric field produced by intracloud charge transfers will decrease with range at a rate greater than cloud-to-ground transfers (r^{-4} versus r^{-3}, respectively), the electric field below the base of the ionosphere will primarily be produced by the charge moment change of the CG, provided also that the interstroke interval is much longer than the local relaxation time.

The average charge moment of –CG strokes has been known for nearly a century. *Wilson* [1925] stated that the mean charge moment of lightning discharges was 50 C·km. *Pierce* [1955] measured the charge moment change of –CG strokes to be typically about 30 C·km while *Brook et al.* [1962] measured an average charge moment change of about 22 C·km per stroke with an average charge transfer of about 2.6 C. *Krehbiel et al.* [1979] measured –CG stroke charge transfers between 1 C (or less) and 20 C in four multi-stroke flashes in New Mexico. They found that the negative charge was removed from altitudes of 4.5–6 km above the ground, which was at 1.8 km MSL. The charge moment changes for the strokes was between <5 C·km and ≃120 C·km. Numerous studies indicate that the negative charge region in storms is centered roughly on the altitude of the −15°C isotherm [*Krehbiel*, 1986], which is at ≃7 km MSL during the midlatitude summer.

Typical +CG parameters were determined more recently. *Berger* [1972] measured the current at instrumented towers struck by lightning. He found that +CGs sustained high currents for a much longer period of time than their –CG counterparts

and that 95% of the +CGs reached a peak current within 200 μs compared to only 18 μs for 95% of the –CGs [*Fisher*, 1988]. The +CG charge transfers measured by *Berger* [1972] were as large as 450 C.

Krehbiel [1981] used multiple station electric field measurements at KSC to determine the altitude and quantity of charge removed by three different +CGs. The +CGs were associated with horizontally extensive discharges in the stratiform region of a large storm system. *Krehbiel* [1981] determined that the +CGs removed about 14–45 C of charge to ground within the initial 3 ms from average altitudes of 6.7–10.8 km MSL ($\pm$2 km) and with average currents of 5–18 kA. The +CG charge moment changes were 130–430 C·km within 3 ms after the stroke onsets. These +CG charge moments were much larger than the charge moment changes typically attained by -CGs.

Brook et al. [1982] were able to locate and measure the charge transferred to ground by several +CGs produced by winter storms in Japan. They found +CG charge transfers as large as 300 C in only 4 ms with a correspondingly large charge moment change of $\simeq$900 C·km. *Brook et al.* [1982] found that all the +CGs analyzed for a couple of storms exceeded 300 C·km in only a few milliseconds, while the +CGs from another couple of storms were 100 C·km or less on the same time scale. More recently, charge moment estimates of +CGs have been obtained by remote ELF measurements [*Cummer and Inan*, 1997; *Bell et al.*, 1998], which are in general agreement with the above measurements.

The charge moment change will be estimated for all of the +CG waveforms as well as some –CG waveforms which were successfully acquired within the 50 minute time interval between 01:40 UT and 02:30 UT on June 22nd, 1997. This time interval corresponds to the sprite-producing phase of the MCS. An electric field change (ΔE) threshold of $\pm$2 V/m was used as a minimum requirement to minimize errors due to the $\pm$0.3 V/m noise level of digitized slow-antenna data.

A "positive-z" convention will be used for the electric field observations. Thus, a net increase in the negative charge overhead would produce an increase in the electric field. However, the "negative-z" convention will be adopted for the peak-current and charge moment measurements since it is more commonly used in the literature for such measurements. Since a +CG lowers positive charge to ground, the current and charge moment change of a +CG will be indicated as positive.

Table 3.1 shows charge moment (QZ) estimates based on the cumulative quasistatic electric field change at 1 and 4 ms after the onset of the return stroke. These

time delays were chosen based on earlier measurements of 1.5 to 4 ms delays to sprite onset [*Rairden and Mende*, 1995]. The CG was approximated by a dipole in the charge moment calculations. The error introduced by this approximation will be small ($< 4\%$) since the ranges to the charges are much greater than their average heights, which were on the order of 7 km.

The QZ values were calculated based on the range to the NLDN stroke as well as a range to the center of the flash as indicated by LDAR. The effect of ionospheric images as a function of range was also included in the calculations (see Appendix C).

The LDAR-based range was calculated from the average LDAR VHF source location for the time interval extending from 250 ms before the stroke to 10 ms afterwards. The pre-stroke time interval of 250 ms was chosen somewhat arbitrarily, but should give a reasonable approximation to the extent of the removed charge. If a longer time interval corresponding to the flash duration prior to the stroke had been used instead, then older channels which have decayed will unneccessarily bias the range towards the point of origin in a convective cell. If a much shorter time interval was used, then the horizontal development would likely be under-represented.

In order to reject outliers due to mislocation or the rare case of a coincident flash, points were rejected if they were more than three times the average VHF source distance from the calculated average VHF source location. The average VHF source location was then recalculated along with a new average distance, R_d, which corresponds to the approximate "radius" of the discharge. If there were fewer than 4 VHF sources used to calculate the final center location and radius R_d, the results were rejected as being statistically insignificant.

Table 3.1 supports the previous observations that +CGs usually transfer considerably more charge than −CGs on millisecond time scales. The charge moment changes are consistent with previous measurements discussed earlier. The +CG discharges also had a much greater horizontal extent (larger R_d) than the −CG discharges, as was previously observed by *Krehbiel* [1981]. The larger charge removal of the +CGs relative to −CGs may simply be a result of the larger horizontal extent.

The sprite-producing +CGs, which are denoted by a bold font, produced larger NLDN range-based charge moments than the non-sprite-producing +CGs at 02:15:19.51 UT. It is not known if the 02:15:19.4189 UT +CG produced sprites since the video image was saturated by the +CG. However, no luminous persistence indicative of sprites was seen after saturation (see Section 3.10).

The +CG at 02:15:19.5112 was followed a little over 4 ms later by another +CG

Charge Moment calculations for 1997, June 22, 1:40-2:30 UT											
Time [UT]		LDAR		NLDN, $t=0$		$t = 1$ ms			$t = 4$ ms		
H:MM	Seconds	Range [km]	$\sim R_d$ [km]	Range [km]	I_{peak} [kA]	ΔE [V/m]	Q Z [C·km] LDAR	NLDN	ΔE [V/m]	Q Z [C·km] LDAR	NLDN
1:42	**57.4092**	**82.9**	**15.0**	**71.1**	**50.2**	**6.2**	**265**	**154**	**10.0**	**478**	**265**
1:51	**2.7627**	**86.1**	**13.4**	**82.1**	**61.3**	**4.3**	**213**	**179**	**7.1**	**393**	**325**
1:55	**47.9570**	**83.8**	**11.5**	**83.1**	**85.5**	**6.3**	**281**	**272**	**8.2**	**408**	**393**
1:56	36.9219	-	-	50.4	-46.1	-3.1	-	-24	-3.3	-	-26
1:58	19.0034	-	-	50.5	-51.6	-2.8	-	-22	-2.7	-	-21
	19.0557	-	-	50.4	-47.8	-3.2	-	-24	-3.1	-	-25
	19.1108	55.1	3.4	53.1	-13.7	-2.5	-25	-22	-2.2	-23	-20
1:59	38.4795	50.5	1.0	49.5	-37.3	-3.3	-25	-24	-3.3	-26	-25
	38.9351	50.4	2.2	49.8	-40.5	-3.5	-27	-26	-3.7	-29	-28
2:00	13.9844	50.0	1.8	49.1	-30.1	-2.5	-19	-18	-2.8	-22	-20
2:03	54.7979	47.4	2.2	45.4	-27.7	-5.0	-32	-27	-5.9	-38	-33
2:04	51.2842	51.4	1.0	47.3	-44.9	-4.0	-33	-25	-4.1	-34	-26
	51.6587	-	-	47.1	-28.7	-3.9	-	-24	-5.7	-	-36
	51.7808	-	-	47.3	-19.0	-3.0	-	-19	-3.6	-	-23
2:06	21.3560	-	-	47.2	-49.6	-5.2	-	-33	-5.8	-	-37
	21.4175	49.9	1.3	48.6	-17.4	-4.1	-31	-29	-4.7	-36	-33
2:07	20.8521	49.0	0.9	47.5	-35.3	-3.4	-24	-22	-3.9	-28	-26
	20.8853	48.9	0.8	48.0	-20.5	-2.3	-16	-15	-2.1	-15	-14
	20.9297	48.9	0.8	47.2	-38.9	-3.9	-27	-24	-3.6	-26	-23
	20.9976	48.9	0.8	48.7	-17.3	-2.2	-15	-15	-2.1	-15	-15
	21.1348	49.6	1.3	47.8	-24.8	-2.7	-20	-18	-3.4	-25	-22
2:15	19.4189	71.1	9.9	52.4	78.7	15.3	381	136	25.7	683	234
	19.5112	71.4	14.6	74.6	29.4	3.7	93	109	7.0	187	222
	19.5156	71.4	14.6	75.6	4.9	2.5	63	77	3.2	86	108
2:16	40.9277	-	-	55.3	-33.2	-3.1	-	-32	-3.5	-	-38
2:19	50.7617	-	-	57.4	-60.1	-4.4	-	-53	-5.1	-	-63
	50.8408	56.7	2.0	56.6	-20.0	-2.1	-23	-23	-2.5	-29	-29
	51.1572	58.8	3.3	56.9	-18.7	-2.1	-27	-25	-3.0	-41	-36
2:22	22.0957	-	-	53.2	-98.3	-6.2	-	-57	-6.8	-	-65
	22.1514	59.2	1.0	56.1	-54.1	-3.5	-46	-38	-3.7	-50	-42
	22.1904	59.2	1.8	56.1	-27.1	-2.2	-29	-24	-2.8	-38	-31
2:24	15.5098	-	-	60.9	-64.6	-4.2	-	-62	-4.8	-	-72

Table 3.1: The cumulative charge moment change at 1 and 4 ms post return-stroke delays is calculated for a dipole at an LDAR-indicated range as well as the NLDN-indicated range. The strokes shown in bold produced sprites.

according to the NLDN. Whether or not this was a real +CG is not clear from the electric-field data (see Figure 3.26). In any case, the video record indicates that no sprites were produced by the +CG(s), in spite of a charge moment change well in excess of that typically observed for −CGs. This suggests based on the LDAR-derived charge moments at $t = 4$ ms in Table 3.1 that the charge moment threshold for sprite initiation is probably between $\simeq 200$ and $\simeq 400$ C·km. This estimate is consistent with a previous ELF measurement of at least 250 C·km attained by sprite-producing discharges within the initial 5 ms.

A static field calculation such as in Figure 2.9 indicates that 400 C·km would be sufficient for conventional breakdown at $Z \gtrsim 79$ km. The relaxation time (τ_r) should exceed 1 ms just above 80 km altitude and will be several milliseconds at 79 km altitude according to Figure 2.6. Thus, the charge moment measurements here provide some evidence that sprites may develop when a conventional breakdown threshold is reached. A more precise answer to this question requires that the time of sprite onset be measured in relationship to the parent discharge charge moment change. Such observations will be presented in Chapter 5.

3.6 01:42:57 UT Sprite-producer

The first sprite cluster was observed at 01:42:57 UT, about a half-hour after video observations began. The development of the sprite cluster is shown in Figure 3.3. The light integration period for the first image began at 160±4 ms and ended $1000/60 = 16.7$ ms later at 177±4 ms after 01:42:57 UT.

A single sprite appeared in the first video field in Figure 3.3, one field before the remaining 3 sprites. The first sprite bloomed in the next field. This indicates that it was still in the process of developing at the end of the first video field. A 50.2 kA +CG had occurred at 171.7 ms and 71.1 km range. From the video frame timing, the sprites visible in the second field developed no sooner than 1 ms after the +CG and no later than 9 ms afterwards. As Table 3.1 shows, the cumulative charge moment change increased significantly from 1 to 4 ms after the return-stroke onset. Unfortunately, there were ±4 ms timing errors due to the image saturation by the LED which made it difficult to pinpoint the time of an LED transition (see Appendix B.4.2 for an example of how video timing is determined from LED transitions). These timing errors made it impossible to determine a possible sprite initiation threshold with greater accuracy than derived earlier in Section 3.5.

All of the sprites reached maximum brightness in the second video field. The sprites faded into the third video field and continued to fade until they were barely visible in the fifth field. The total optical duration of the sprite event was ∼70 ms.

The 3-dimensional development of the 01:42:57 UT sprite-producing flash relative to NEXRAD radar reflectivity contours is shown in the lower half of Figure 3.3. The NEXRAD radar was based in Melbourne, Florida, to the southeast of the MCS. The displayed elevation scan corresponded to an altitude of ∼5 km on the southeast side of the storm, and increased to ∼8 km on the northwest side. The contours are incremented at 10 dBZ intervals starting at 0 dBZ.

The higher reflectivity regions occurred along a southwest-northeast line on the southern edge of the MCS are the convective cores. The stratiform region trails behind the northern edge of the line while new cells formed on the southern edge, as shown in Figure 3.2. This asymmetric development pattern is identical to that of asymmetric Oklahoma MCSs which are known to be more likely to produce tornadoes and hail than their symmetric counterparts [*Houze et al.*, 1990].

It is known from laboratory experiments that electrical discharge propagation is spatially correlated with the locations of space charge regions [*Williams et al.*, 1985]. Thus, lightning channels mapped by the KSC LDAR should give an indication of charge location.

The flash began in a high reflectivity region of ∼40 dBZ (at ∼5 km altitude) within a convective cell on the eastern edge of the MCS. It then propagated into the lower reflectivity stratiform region. The flash was mostly confined within the $\gtrsim$20 dBZ reflectivity region, but did not traverse the entire $\gtrsim$20 dBZ region. The flash development relative to radar reflectivity was very similar to that documented by the KSC LDAR for smaller Florida storms [*Maier et al.*, 1995b; *Stanley et al.*, 1996a].

The temporal and spatial development characteristics of the sprite-producing flash are shown in Figures 3.4 and 3.5. The duration of the flash was about 1.3 s. The electric field was measured at the interferometer site by a slow antenna with a long relaxation time of ∼10 s. The log-RF at 274 MHz is shown in 8-bit digital units in Figure 3.4. The noise level of the log-RF is at ∼10 units. The dropouts in log-RF data are due to the RF-thresholded data acquisition mode which was in effect for this flash.

The initial upward deflection of the electric field was caused by the upward (and possibly towards the observer) transport of negative charge during the initial portion

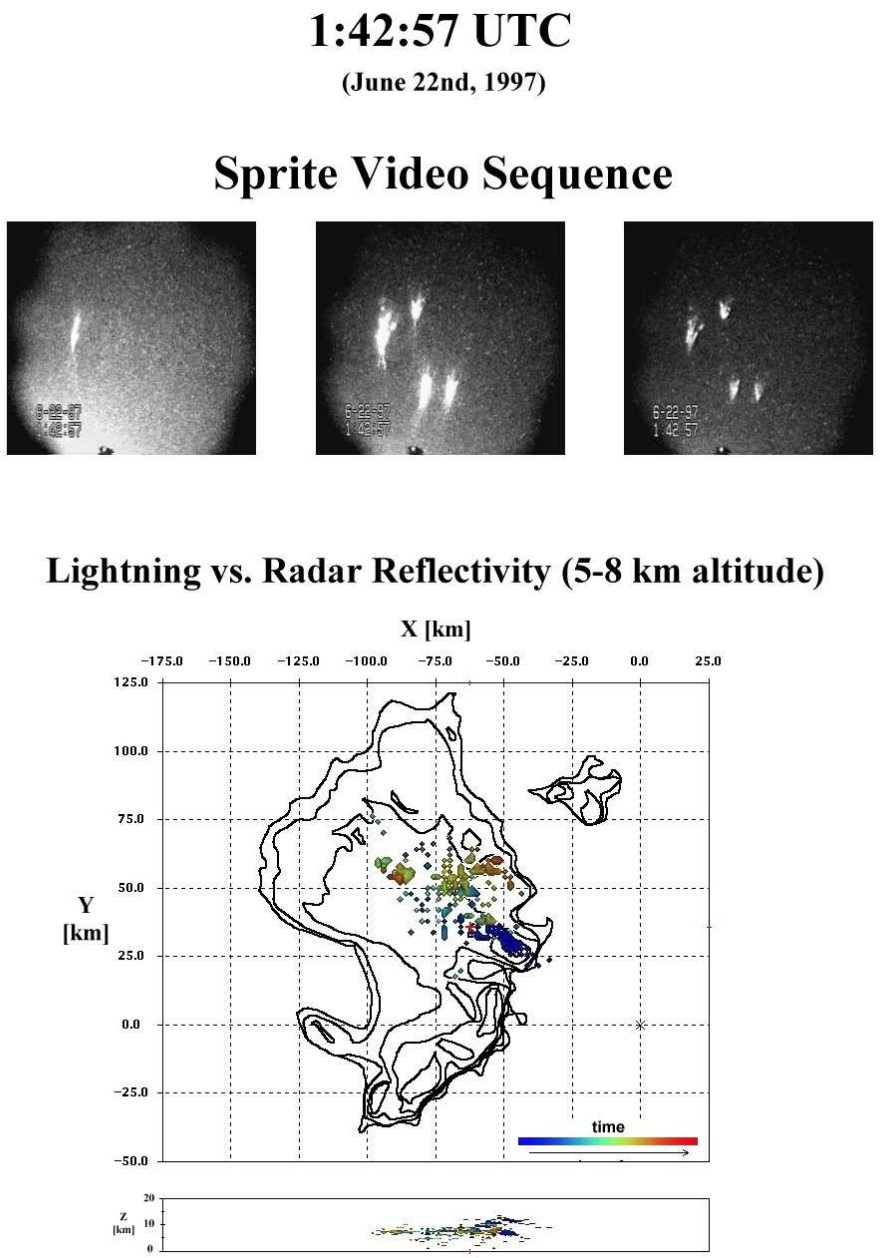

Figure 3.3: The temporal development at 17 ms intervals of the 01:42:57 UT sprite cluster is shown at top as seen through a wide angle lens. The LDAR data is plotted on top of NEXRAD reflectivity at bottom and is rainbow-colored from blue to red with respect to time. The reflectivity is contoured at 10 dBZ intervals starting with 0 dBZ. Note that the flash is mostly confined within 20+ dBZ reflectivity, but does not traverse the entire 20+ dBZ region.

of the intracloud discharge. This transport of negative charge by negative leaders propagating into the upper positive charge region of the convective cell makes negative charge more "visible" to distant ground observers, thus increasing the vertical electric field at a distance. This initial portion of the flash is designated as interval "t1".

The subsequent downward deflection of the electric field in interval t2 of Figure 3.4 was due to the transport of negative charge out into the positively charged anvil in a direction away from the slow antenna. The outward motion is clearly evident in Figure 3.5b by the temporal development of inferred negative leaders away from the interferometer and observation site at $[x, y]=[0, 0]$, as indicated by the rainbow-color progression from blue (sooner) to red (later). The flash developed over a $\simeq$40 km distance in the 170 ms interval of t2. This corresponds to an average negative leader velocity of 2.4×10^5 m/s, which is consistent with negative leader velocities in ordinary ICs [*Shao and Krehbiel*, 1996], spider-lightning discharges, [*Mazur et al.*, 1998], and –CGs [*Uman*, 1987,pg. 83].

The negative breakdown developed into a region of 20-30 dBZ reflectivity within the stratiform region, as indicated by Figure 3.3. The decrease in altitude of the negative breakdown at the start of interval t2 in Figure 3.4 is in excellent agreement with the decrease in average positive charge altitude from $\simeq$11 km in an MCS convective core to $\simeq$8 km in the stratiform region [*MacGorman and Rust*, 1998,pg. 267]. A horizontally extensive flash observed by the New Mexico Tech Lightning Mapping Array also developed in a similar fashion within an MCS in Oklahoma [*Krehbiel et al.*, 2000].

A bilevel structure in the IC flash is clearly evident in Figure 3.4 for time intervals t1 and t2. The initial development and bilevel nature are consistent with previous VHF observations of IC flashes with the upper level corresponding to the positive charge region and the lower level to the negative charge region [*Shao and Krehbiel*, 1996]. The lower level VHF sources may correspond to negative polarity recoil events which delineate the tracks of positive leaders [*Mazur and Ruhnke*, 1993]. Support for this comes from VHF measurements which have failed to detect positive leaders from close triggered lightning, though negative polarity breakdown events propagating back along the inferred positive leader channel locations are readily detected [*Krehbiel et al.*, 1994; *Stanley et al.*, 1994; *Shao et al.*, 1996].

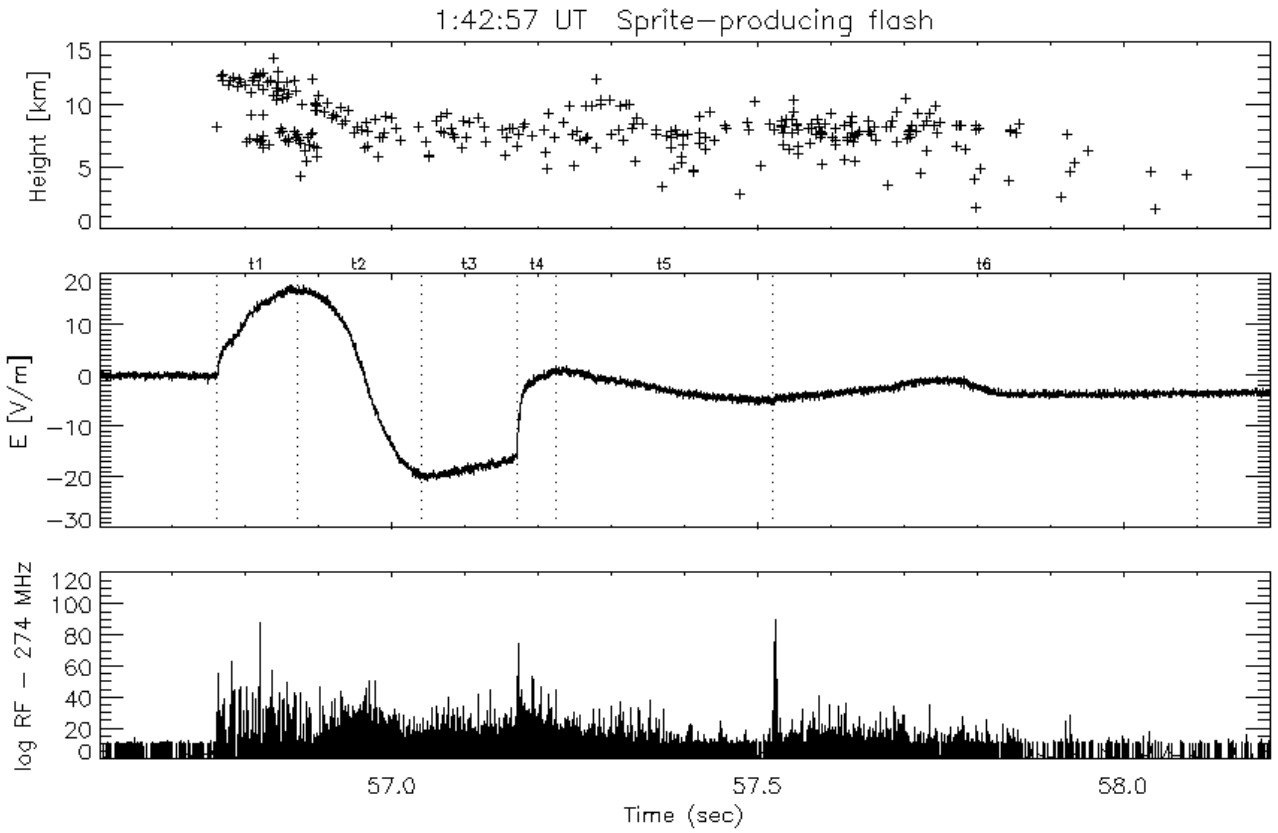

Figure 3.4: The VHF source height, electric field, and log-RF strength at 274 MHz as a function of time for the 01:42:57 UT sprite-producing discharge. The electric field is divided into time intervals t1-t6 primarily according to the slope of the field change. The sudden upward deflection at the start of interval t4 corresponds to the sprite-producing +CG.

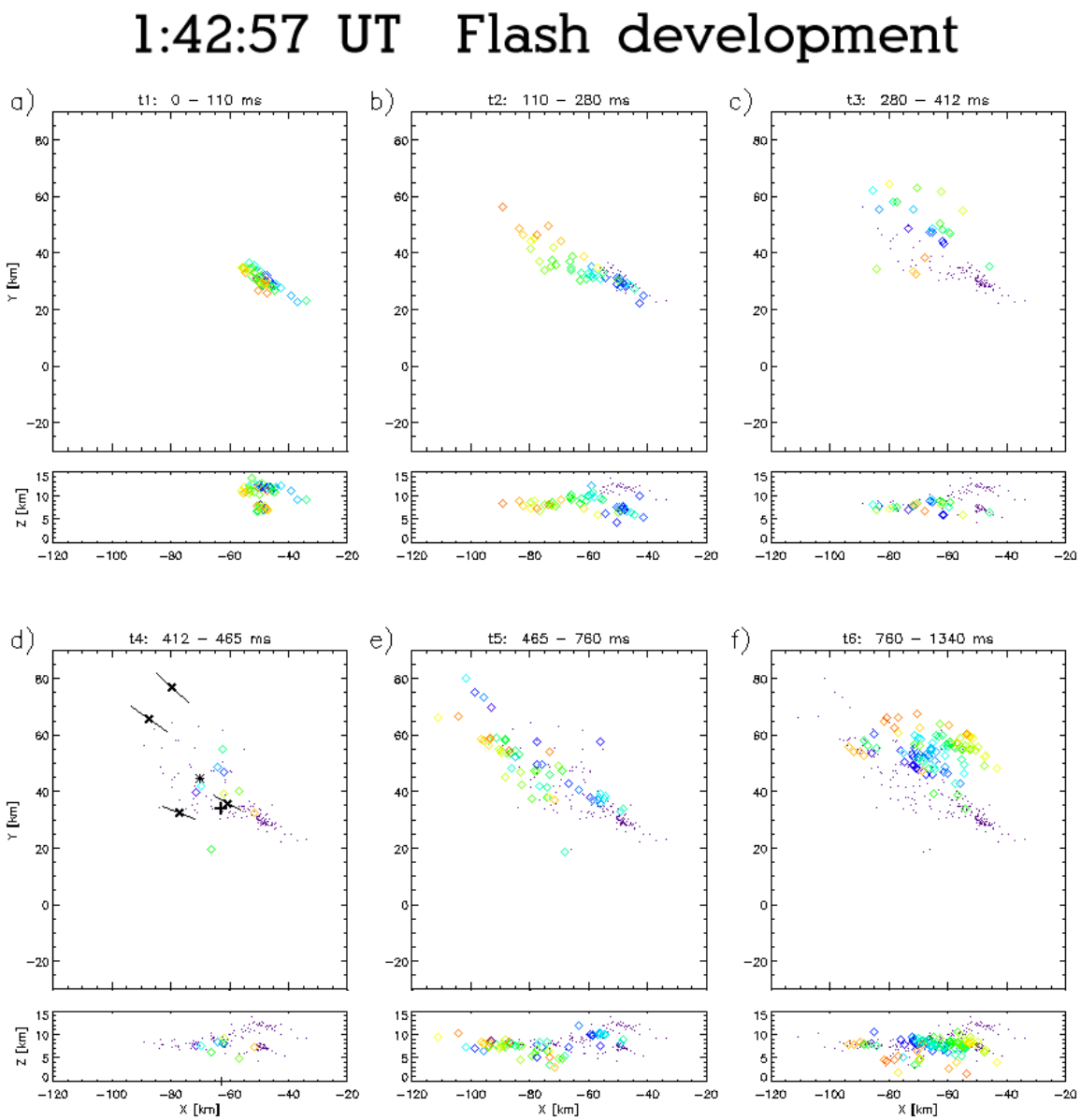

Figure 3.5: The spatial development of the 01:42:57 UT sprite-producing discharge as a function of time. The VHF sources ($\Diamond$) are rainbow-colored from blue to red according to elapsed time within the respective time interval. VHF sources from previous intervals ($\cdot$) are purple. The +CG location ($+$), LDAR-indicated sprite-producing discharge center ($*$), and sprite locations ($\mathbf{x}$) are shown within time interval t4. The maximum range error estimates for the sprite locations are indicated with lines. Note that many of the sprites appear to lie at the periphery of the parent discharge.

The VHF activity in the lower level of the bilevel IC flash appeared to stop near the beginning of time interval t2. This may indicate that the positive leaders have stopped propagating. However, the relationship of VHF source occurrence to positive leader propagation is poorly understood at the present time. Thus, it is not clear when, or even if, the positive leaders have ceased, though the lack of VHF sources suggests that they have ceased. Figure 3.5c shows that only a single VHF source occurred in the lower level in time interval t3.

The recovery of the electric field in interval t3 is partly due to the "right-turn" and tangential-motion taken by the negative leaders in Figure 3.5c. This recovery is also the strongest evidence that older channel segments became resistive, consistent with the interpretation that the positive leaders had stopped propagating. If the entire channel structure was still conductive, the outward transport of negative charge through the closer channel structure would have continued to decrease the electric field at the observation site.

The horizontal extent of the flash did not grow much beyond interval t3, as an inspection of Figure 3.5d-f shows. This indicates that the negative leaders essentially stopped near the periphery of the 20 dBZ reflectivity region, as was discussed earlier. The sources at the end of the interval t3 occurred on the southern end of the horizontally expansive region near the +CG strike point. The significance of this is not understood.

The +CG occurred at the start of interval t4. There is no clear indication in the LDAR data that the positive leader to ground was detected, particularly since there were no data points below ~6 km up to the time of the +CG. This is not unexpected, since previous measurements of +CG leaders at VHF by the interferometer show that they radiate only weakly [*Mazur et al.*, 1998].

Initial triangulation studies of sprites indicated that the upper terminal height was 88±5 km [*Sentman et al.*, 1995]. Triangulation of numerous columniform sprites by *Wescott et al.* [1998] determined that their average upper terminal height was 87 km, but could range from 81-89 km. To determine the locations of these sprites, a terminal height of 87±6 km was used. The camera orientation was determined precisely based on stellar locations (see Appendix B.3.1). Thus, the location errors will primarily be range errors due to ±6 km height errors. Since the elevation angle to the top of the sprites was on the order of 45°, the range errors will be approximately the same as the terminal height errors.

The most probable locations of the sprites is shown in Figure 3.5d along with a

range error estimate for the locations. Surprisingly, the plan position of two sprites appear to lie at the periphery of the discharge while the northernmost sprite appears to lie just beyond the apparent discharge boundary. The fourth sprite was almost directly over the +CG strike point. The first sprite which appeared in Figure 3.3 was located west of the +CG along the southern edge of the discharge.

Figure 3.6 shows an expanded plot of the electric field and 274 MHz log-RF around the time of the +CG. The LDAR data is not shown since there were too few data points within the time interval. The electric field was obtained by de-drooping the fast antenna data (which has a higher sample rate than the slow antenna) so that the static field change component of the slow antenna was accurately reconstructed for the time intervals around the +CGs shown in this work. The 60 Hz AC and higher harmonics were (incompletely) subtracted from the final waveform.

A sudden increase in the electric field occurred about 200 μs after the return stroke according to Figure 3.6. The electric field increased with a substantial slope and noisy bursts superimposed until about 2 ms after the return stroke. This phase of the discharge was accompanied by strong VHF radiation. After 2 ms, the electric field continued to increase due to a persisting intense continuing current until $\sim$10 ms after the discharge, when the slope became more gradual. The more gradual slope may correspond to only horizontal movement of charge after the cessation of continuing current or could be due to a significantly weakened continuing current.

The log-RF activity is enhanced throughout the entire interval after the +CG. It is the negative leader activity which supplies the current during the continuing current phase of the discharge, so this is expected.

The LDAR-indicated charge center used in Table 3.1 was near the middle of the sprite cluster and is much closer to the cluster center than to the location of the +CG. The charge moment change based on this charge location was 265 C·km at 1 ms. Figure 3.6 shows that most of this charge moment change occurred within the initial $\sim$200 μs, thus retardation effects will be important and the electric field will be briefly higher than expected from quasi-electrostatic theory (see Section 2.5.1). However, it is not clear how this could produce the observed pattern of sprite initiation, particularly since the field from a monopole has a weaker radial dependency than a dipole and seemingly would be even less likely to produce high fields near the periphery of the discharge.

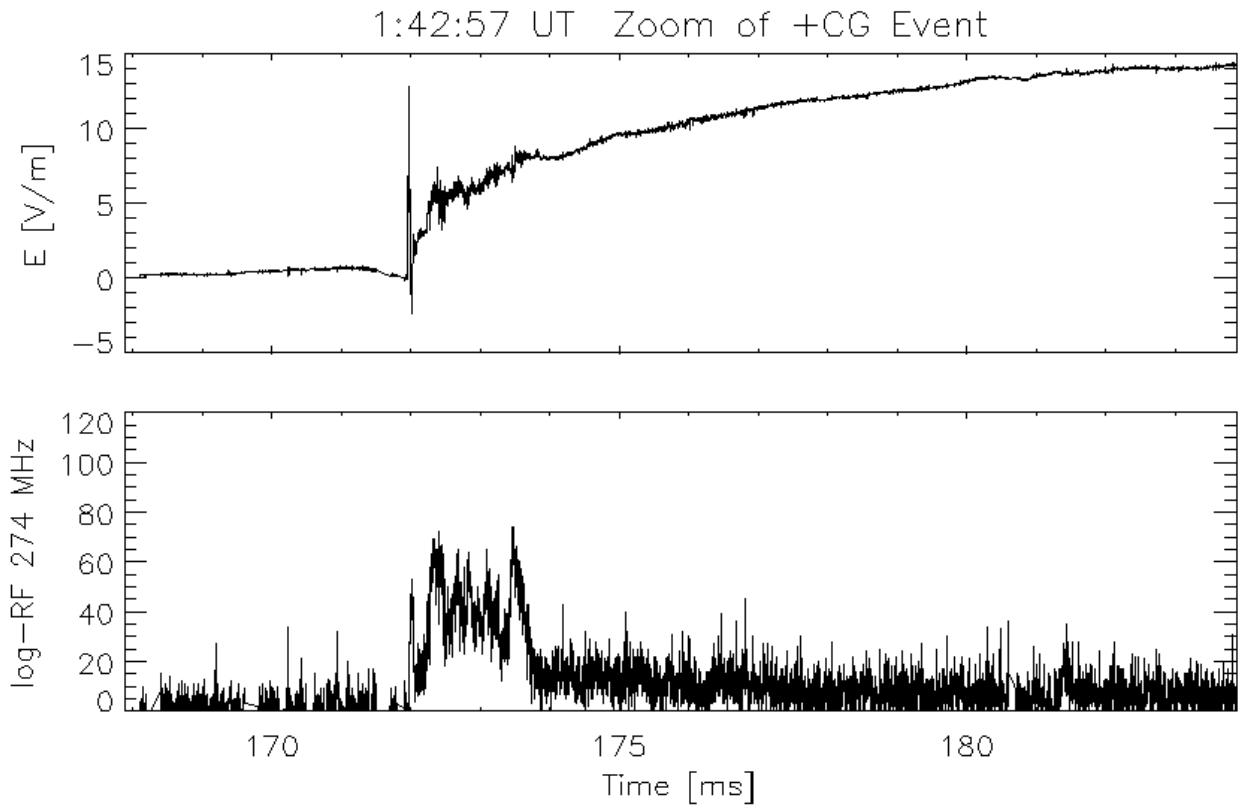

Figure 3.6: The 01:42:57 UT sprite-producing +CG electric field waveform as well as the log-RF strength at 274 MHz. An intense current and log-RF phase lasts for almost 2 ms after the return stroke onset, with the most intense current occurring within the initial $\sim$200 μs. The steady upward slope which is readily evident up to $\simeq$10 ms after the return stroke is probably due to a large continuing current.

Figure 3.5 shows the remaining development of the flash in intervals t5 and t6. The x-z plots indicate that many of the VHF sources were associated with channels which propagated down from ≃8 km altitude to ≃4 km altitude, or to about the height of the 0°C isotherm. The lower altitude sources were likely associated with spider-lightning discharges, which can be observed to "crawl" below cloud base or just above cloud-base [*Marshall et al.*, 1989]. Such spider-lightning discharges typically propagate at about 4 km altitude, presumably through a stratified positive charge layer, and are composed of negative leaders [*Mazur et al.*, 1998].

The measurements presented here indicate that the charge removed for this sprite-producing +CG was associated with positive charge higher up in the stratiform region, rather than near the 0°C isotherm. The average height of the charge region according to Figure 3.7 was ∼7.5 km MSL. Based on the LDAR range-based charge moments (Table 3.1), the charge transferred to ground would have been 35 C at 1 ms and 64 C at 4 ms after the return stroke. The average current for these intervals would have been 35 kA and 16 kA respectively. Such high average currents are not unusual for +CGs, as indicated by current [*Berger*, 1972] and multi-station electric field [*Krehbiel*, 1981; *Brook et al.*, 1982] measurements.

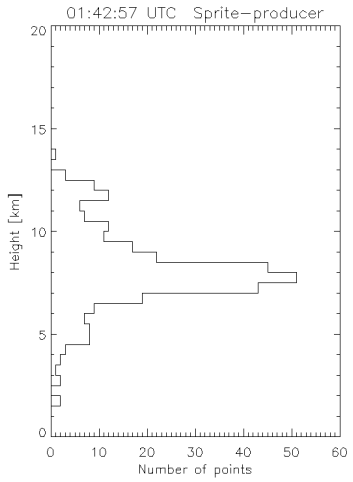

Figure 3.7: The density of VHF sources in 500 m height bins is shown above for the 01:42:57 UT flash. The VHF sources above 10 km altitude were associated with the initial IC development while those below 6 km occurred later in the flash, after the sprites. Factoring in a small systematic error which increases the heights by <1 km (Section 3.2.1), the average charge removal height of the sprite-producing +CG was between 7-8 km altitude.

3.7 01:47:52 UT Sprite-producer

The second sprite event of the June 22nd storm was associated with a 83.7 kA +CG at 01:47:52.7112 UT. The video sequence of the sprite cluster is shown in Figure 3.8. The sprite reached maximum brightness in its first frame and then faded into the next 3 frames until it was at the limit of detectability.

A large number of IC and CG flashes occurred in the intervening time between the first and second sprite-producing flashes. However, none of these flashes developed very far into the stratiform region.

The 01:47:52 UT flash began as an ordinary –CG discharge. A -31.2 kA –CG occurred at 01:47:51.4763 UT, about 0.3 s after the start of the flash, according to Figure 3.9. Only a single data point was located by LDAR in the subsequent 0.3 s, though the interferometer log-RF record indicates that there was activity throughout this interval. Figure 3.10a shows that the VHF sources within interval t1 were relatively localized.

The flash developed horizontally outward into the stratiform region during interval t2 (Figure 3.10b). The lateral extent grew to ∼64 km in ∼1 s during interval t2, corresponding to a progression velocity of 6.4×10^4 m/s. This is somewhat less than typically observed for negative leaders, but is not unrealistically low.

The NLDN indicated that a 9.7 kA +CG occurred at 01:47:52.3209 UT about 5 km west of the earlier –CG. The "weak" current (relative to ordinary +CGs) indicates that this was probably an IC event, as discussed earlier in Section 3.4. Unfortunately, the interferometer buffer filled up due to an excessive number of RF-triggers during the flash. This resulted in the loss of all fast antenna, log-RF, and phase data for the remaining flash activity, starting at ≃0.24 s prior to the weak +CG. The slow antenna data, which is stored in a separate buffer, was also affected by the lock-up and was lost for the entire flash.

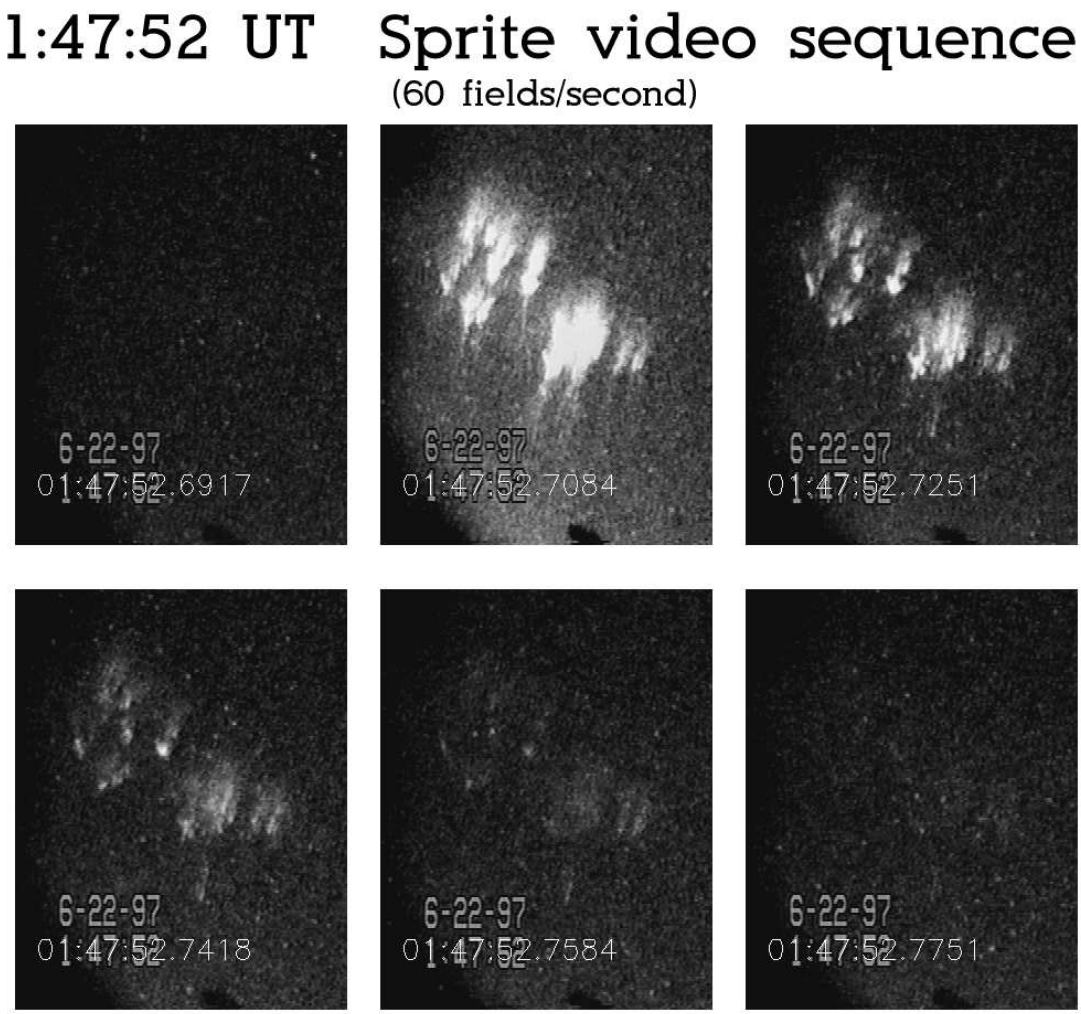

Figure 3.8: The video sequence of the 01:47:52 UT sprite cluster. The sprites reached maximum brightness within the first frame. They then faded over the next 3 frames to the limit of detectability. Scattered light from the parent discharge can be seen in the lower portion of the final 5 frames. Note that the first frame was relatively dark, which suggests that there was relatively little breakdown activity in the parent discharge prior to the +CG. The start time of each video field, accurate to ± 5 ms, is shown at the bottom of each image.

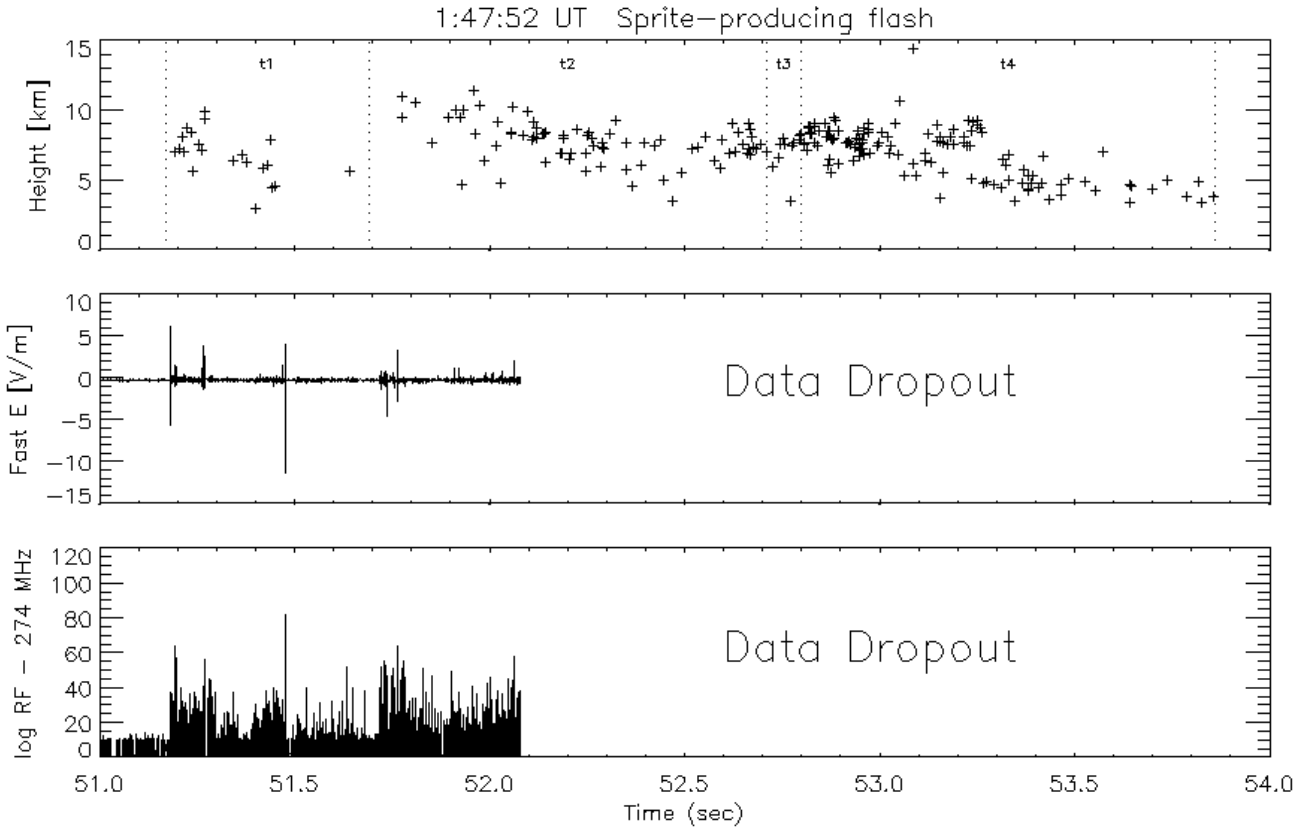

Figure 3.9: The VHF source height, fast antenna electric field, and log-RF strength at 274 MHz as a function of time for the 01:47:52 UT sprite-producing discharge. The LDAR data is divided into time intervals t1-t4 according to spatial development characteristics as well as the time of the sprite-producing +CG (start of t3). A buffer full condition in the interferometer's RF-thresholded acquisition program caused the data dropout prior to the sprites.

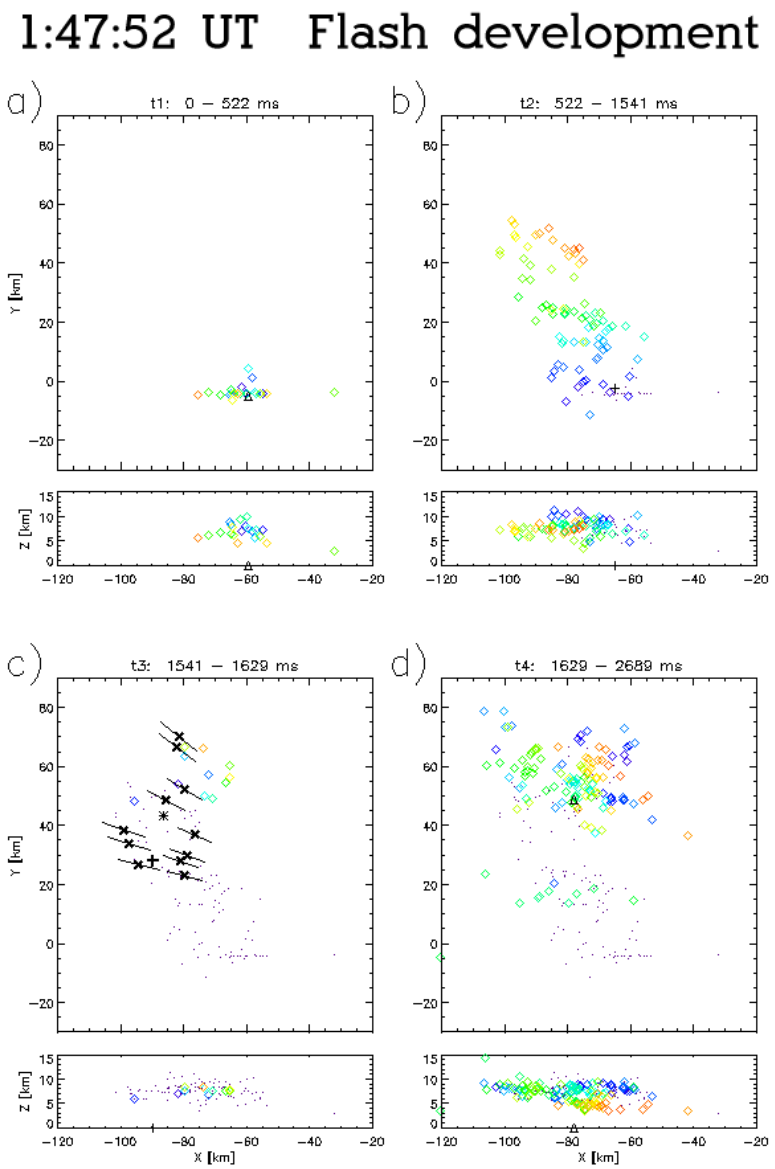

Figure 3.10: The spatial development of the 01:47:52 UT sprite-producing discharge as a function of time. The flash produced a –CG (△) in the first time interval (t1) and then developed horizontally outward through the anvil in the second (t2). A weak ≃10 kA "+CG" (intracloud?) was indicated by the NLDN in interval t2. The sprite-producing +CG's location (+), LDAR-indicated sprite-producing discharge center (*), and sprite locations (**x**) are shown within time interval t3. As before, many of the sprites were near the periphery of the discharge. The NLDN detected a –CG beneath the discharge in the final interval, t4.

A 83.7 kA +CG occurred at the start of interval t3 and was concurrent with the appearance of sprites on video (Figure 3.8). The sprite positions were determined in the same way as before; the maximum sprite altitude was assumed to be 87±6 km. Figure 3.10c indicates that many of the sprites occurred near the periphery of the discharge, as in Figure 3.5d.

However, two of the sprites occurred to the north of the apparent northern periphery of the discharge. The discharge appeared to extend further northward during interval t3 only after the sprites appeared. Figure 3.11 shows that these sprites were tilted somewhat from vertical. The direction of the tilt (away from the center of the overall activity) is qualitatively consistent with what would be expected due to a somewhat nonvertical electric field below the ionosphere at a significant distance from the parent CG charge center. Sprites at significant tilt angles have been observed previously by *Winckler et al.* [1996].

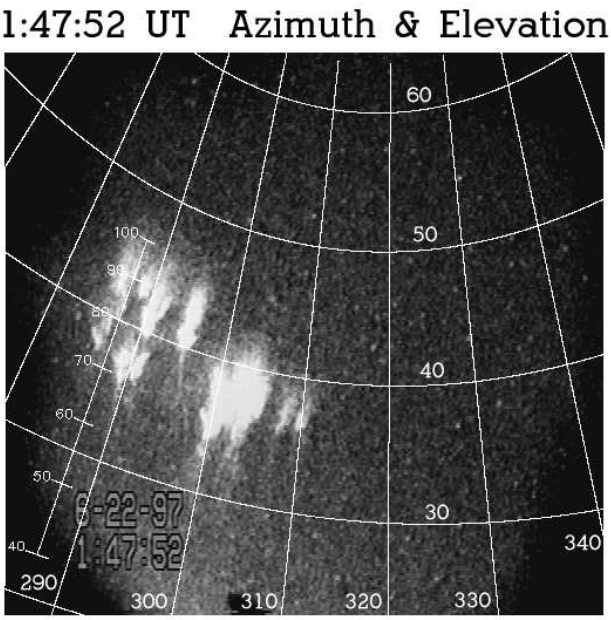

Figure 3.11: The azimuth and elevation orientation of the camera is shown for the 01:47:52 UT sprite event. The same camera orientation was used for the other sprite events up to ∼2 UT. Most of the sprites were vertically oriented, with the notable exception of the slanted pair of sprites at ∼310° azimuth. The slanted sprites occurred north of the apparent northernmost extent of the flash at the start of interval t3 in Figure 3.10c.

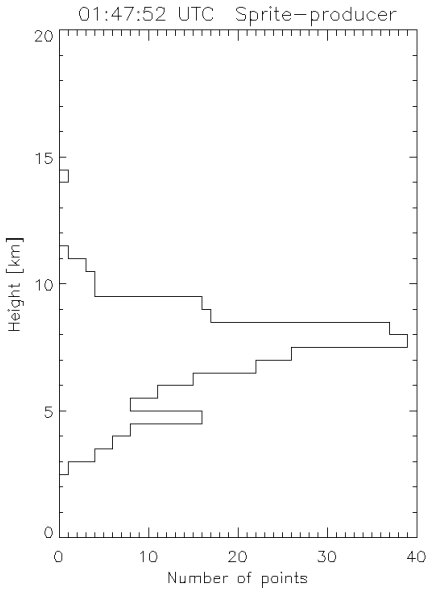

Figure 3.12: The density of VHF sources in 500 m height bins for the 01:47:52 UT flash. Two peaks in density are evident at just below 8 km altitude and just below 5 km altitude, near the 0° C isotherm. The former likely corresponds to the altitude of charge removal for the sprite-producing +CG while the latter was due primarily to development in the late phase of the flash after the sprites had decayed.

During the final time interval, numerous VHF sources were observed to descend to 4-5 km and to propagate at that altitude. As was noted for the previous flash, these sources were likely associated with negative leaders (spider lightning) propagating through the positive charge layer near the 0°C isotherm. These sources produced a significant secondary maximum below 5 km in the height distribution of VHF sources (Figure 3.12). The primary maximum in the VHF source distribution just below 8 km altitude should correspond to the average height of charge removal for this sprite-producing discharge. The total duration of the flash was about 2.7 s, nearly twice that of the previous sprite-producing discharge.

An interesting feature of time interval t4 is that the NLDN detected a –CG stroke emanating from underneath the horizontally expansive discharge. The –CG may have been produced by a negative leader spawned from the parent discharge. However, another possible origin will be discussed in Section 3.8, in which several –CG strokes were observed beneath another sprite-producing discharge.

3.8 01:51:02 UT Sprite-producer

The third sprite event occurred at 01:51:02 UT. The video sequence of the sprite event is shown in Figure 3.13. The sprite cluster was the brightest of the night. The heads of the sprites saturated the first frame. Tendrils were readily visible and numerous below the sprite heads. Light integration for the first frame began at 01:51:02.748 UT and lasted for 16.7 ms.

Figure 3.13 shows that the flash originated in a convective cell between the cells where flashes 01:42:57 and 01:47:52 UT originated. The temporal development of the flash was very similar to that of the 01:42:57 UT flash, as Figures 3.14 and 3.15 show. The flash developed vertically as a bilevel IC in time interval t1. The negative leaders in the upper level then propagated horizontally outward away from the slow antenna in interval t2. The flash covered a horizontal distance of $\sim$55 km in $\sim$0.35 s during interval t2. The average speed of development was $\sim 1.6 \times 10^5$ m/s. This speed is consistent with that normally observed for negative leaders, as discussed in Section 3.6.

The electric field deflected dramatically upward at the beginning of interval t3 and maintained a constant slope throughout (see Figure 3.14). This is difficult to understand based solely on the negative leader activity, which produced only a few data points primarily near the start of the interval and on the upper right quadrant of the discharge.

Conceptually, an upward deflection of the electric field would be produced by the onset of positive leader activity which was propagating downwards or away from the observation site. It is interesting to note that a single data point in interval t3 appeared at 4-5 km altitude almost directly above the +CG location of interval t4. If a positive leader was propagating uniformly downwards from $\sim$7.5 km altitude over the $\simeq$0.11 s duration of interval t3, the average downward propagation speed would be $\sim 6.8 \times 10^4$ m/s. The progression speed would be greater if the leader took a tortuous path to ground, as leaders often do. A positive leader may also be responsible for the less dramatic electric field increase during time interval t3 of the 01:42:57 UT flash (Figure 3.4).

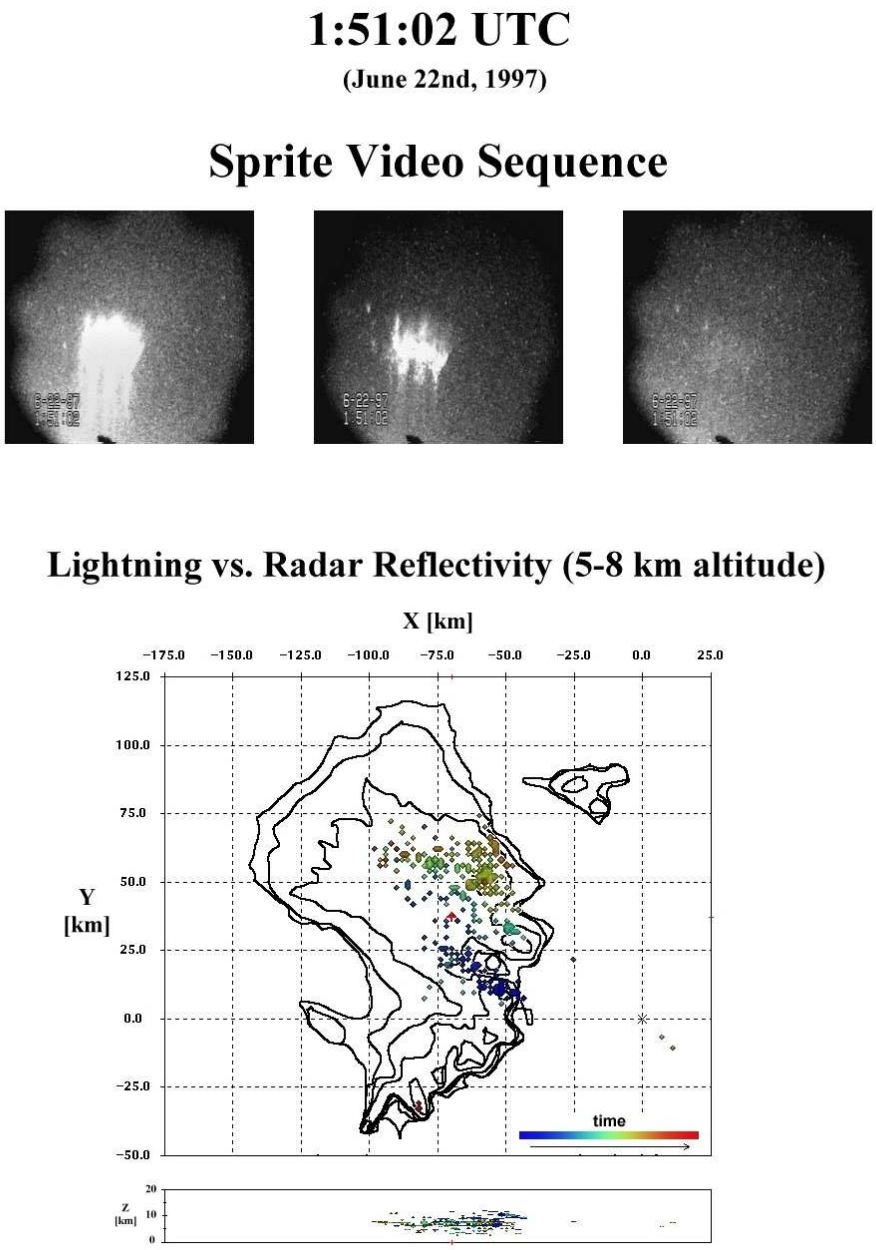

Figure 3.13: The temporal development at 17 ms intervals of the 01:51:02 UT sprite cluster (top) as seen through a wide angle lens. The LDAR data are plotted on top of NEXRAD reflectivity (bottom) and follows a rainbow-sequence from blue to red with respect to time. The reflectivity is contoured at 10 dBZ intervals starting with 0 dBZ. As before, the flash is mostly confined within 20+ dBZ reflectivity, but does not discharge the entire 20+ dBZ region.

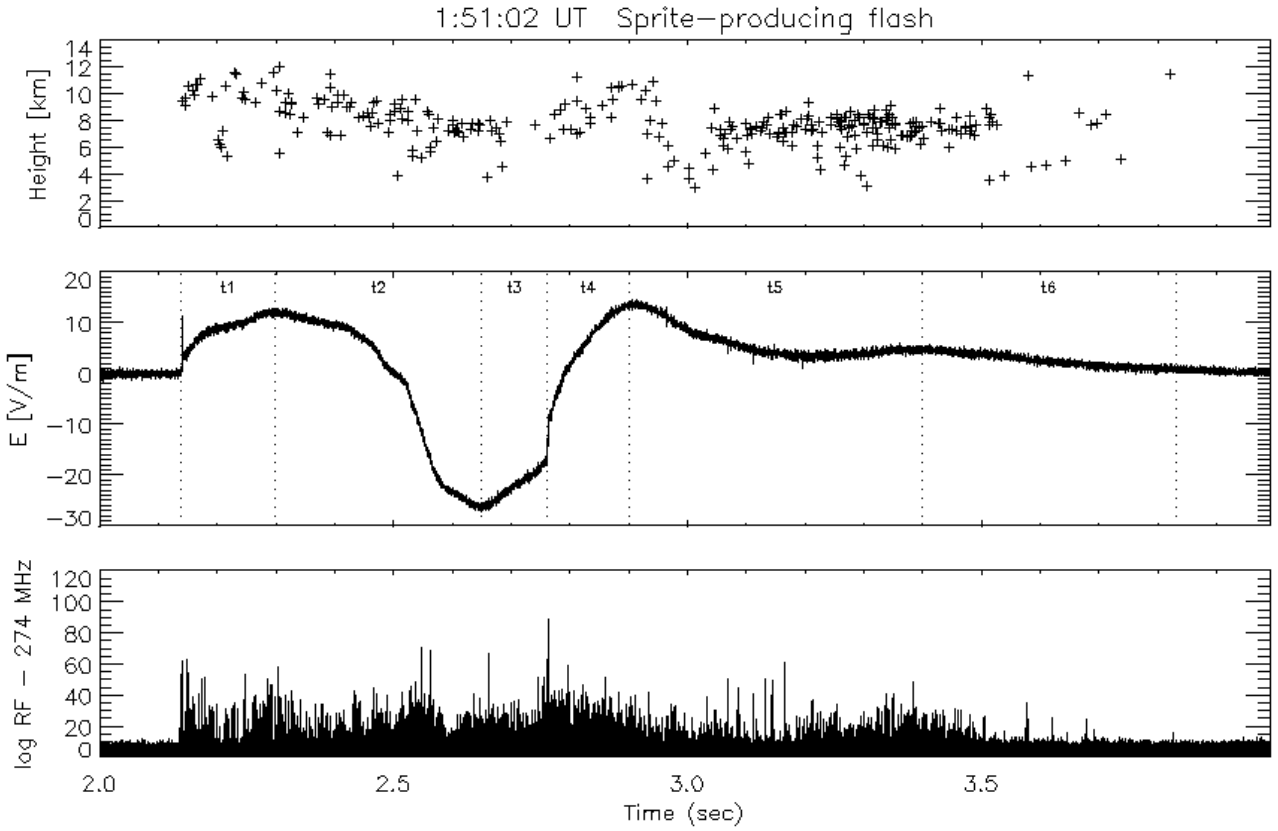

Figure 3.14: The VHF source height, electric field, and log-RF strength at 274 MHz as a function of time for the 01:51:02 UT sprite-producing discharge. The electric field is divided into time intervals t1-t6 primarily according to the prevailing slope polarity or characteristics. The sudden upward deflection at the start of interval t4 corresponds to the sprite-producing +CG.

A 61.3 kA +CG occurred at 01:51:02.762 UT and marks the start of interval t4. The brightness of the sprite cluster in Figure 3.13 makes it difficult to locate individual sprites. The azimuth extent of the sprite cluster on video was obtained and the heights of the sprites at each azimuth extrema were used to estimate the distance to the sprite cluster "center". The sprite cluster is drawn as a circle in Figure 3.15d.

The actual shape of the sprite cluster is unknown for the "back" side, since it is obscured by the foreground sprites. Regardless, the portion of the sprite cluster which can be seen appears to be associated with the periphery of the discharge, as with the previous sprite events. Also like the previous sprite events, the +CG occurs on the side of the sprite cluster in the opposite direction of the preceeding negative leader propagation. Not surprisingly, the LDAR-indicated charge center appears to be a better, if still imperfect, approximation of the sprite cluster plan location than the CG.

The de-drooped fast electric field waveform for the +CG stroke is shown in Figure 3.16 along with the log-RF strength. The static electric field grew most rapidly during the initial ∼300 μs. A substantial electric field change occurred at ∼300 μs and is accompanied by intense log-RF at 274 MHz. This field change appearred to have been inductive in nature as it does not produce much of a static field change. The static electric field continued to increase dramatically for ∼4 ms, at which point it increased at a slower rate. The bulge at ∼4 ms may be due to current flowing in the sprite itself. The presence of significant sprite currents will be discussed in Chapter 4.

The flash activity after interval t4 was arbitrarily divided into intervals t5 and t6. As was observed for previous sprite-producing flashes, the majority of VHF sources observed below 6 km altitude appeared after the sprite event. What is particularly interesting about interval t5 is that there was a tight cluster of 3 –CG strokes which appeared below the horizontally extensive discharge.

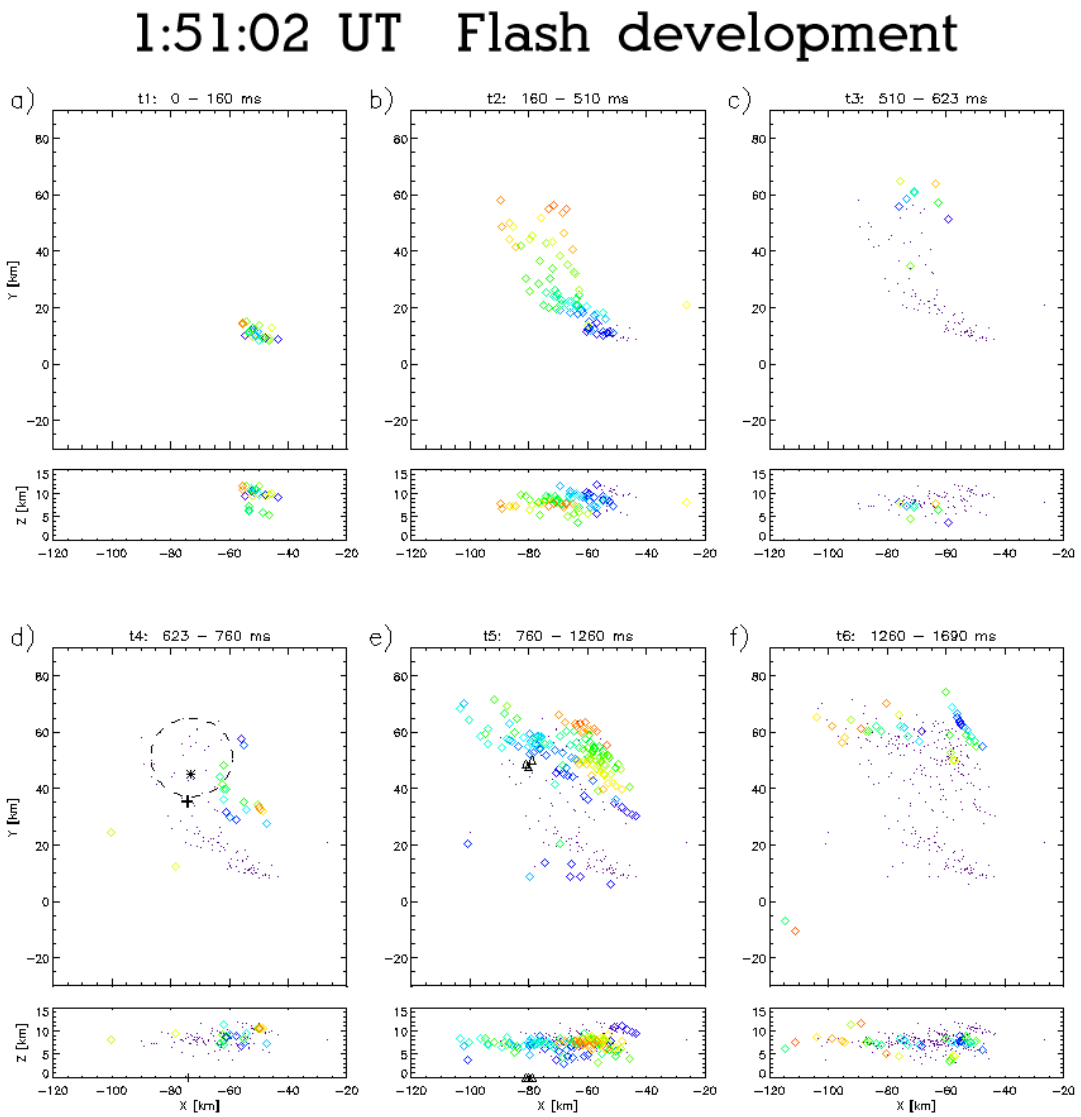

Figure 3.15: The spatial development of the 01:51:02 UT sprite-producing discharge as a function of time. The VHF sources ($\Diamond$) are rainbow-colored from blue to red according to elapsed time within the respective time interval. VHF sources from previous intervals ($\cdot$) are purple. The +CG ($+$) and –CG stroke ($\triangle$) locations are plotted within their respective intervals. The LDAR-indicated sprite-producing discharge center ($*$) and sprite region (dashed circle) are also plotted. Note that the edge of the sprite region corresponds with the periphery of the preceeding discharge activity and that the +CG occurred below the edge of the sprite cluster; as with the earlier sprites.

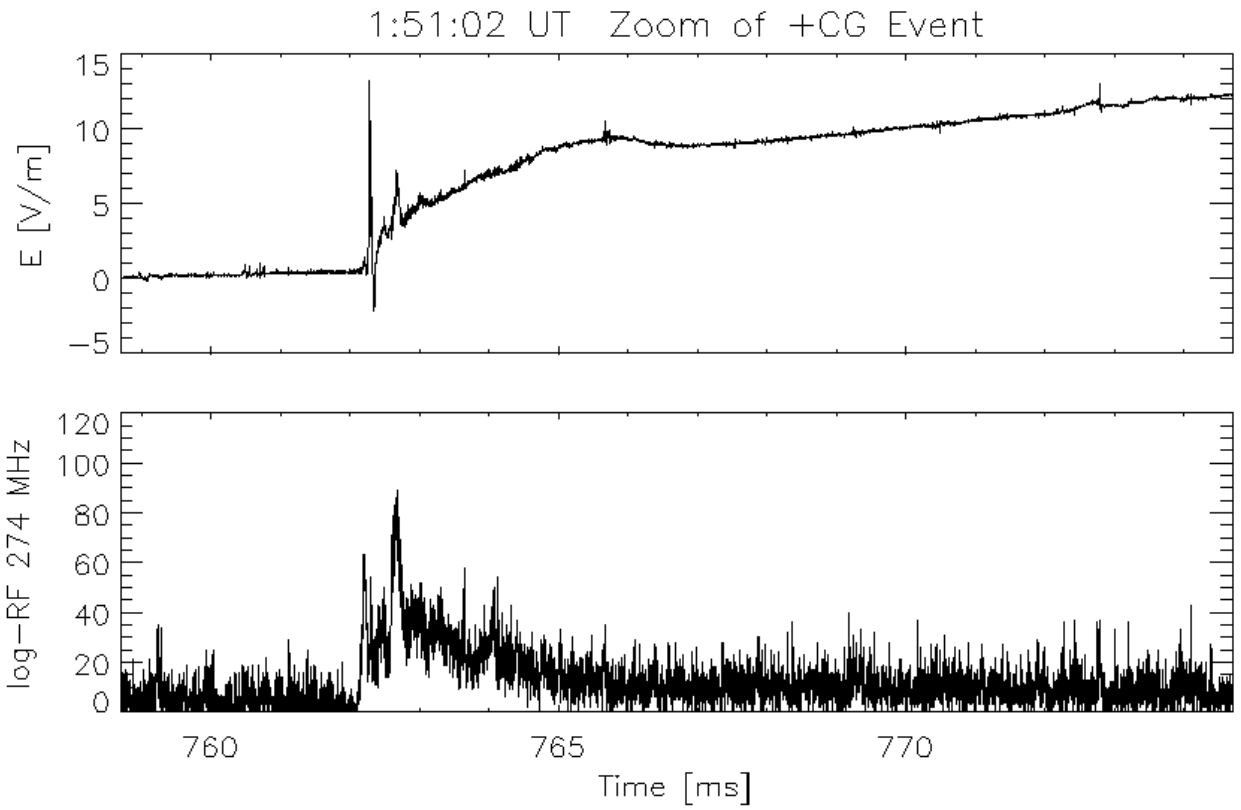

Figure 3.16: The 01:51:02 UT sprite-producing +CG electric field waveform as well as the log-RF strength at 274 MHz. A large electric field pulse and log-RF burst occurs at a delay of ∼300 μs. The continuing current appears to persist for the entire duration of the interval, with the most intense current within the initial 4 ms following the return stroke. Note the mysterious broad bulge in the electric field at 4 ms. A possible explanation for this bulge will be discussed in Chapter 4.

It is conceivable that the –CG strokes were produced when one or more negative leaders from the sprite-producing flash struck the ground. However, it is far more likely that they were part of a separate discharge initiated by the +CG. From Table 3.1, the +CG produced a charge moment change which at 4 ms post-return stroke delay was ∼20 times larger than normally observed for –CGs. The electric field beneath the discharge would also have been similarly enhanced, with the actual enhancement factor dependent on discharge geometry.

The electric field at the top of a tall metallic structure such as a radio and communications tower might have exceeded the electrical breakdown strength of air while subjected to the strong electric field. This could have resulted in the formation of an upward-developing positive leader. This process would be essentially identical to that of ordinary triggered lightning, with the only difference being that the conductor is fixed within a very rapidly growing field (∼milliseconds) as opposed to rapidly extending (∼seconds) through a fixed electric field. It is well known that ordinary triggered lightning can produce return strokes 10's or 100's of milliseconds after trigger initiation.

The –CG strokes were in the same location as the –CG observed for the previous sprite-producing discharge. These –CGs were in the vicinity of Florida Hills, which is slightly elevated above the surrounding terrain and is in a strategic position for radio broadcasts to both Orlando and Daytona Beach. Whether or not radio towers were located at the –CG strike positions is not known by the author, but this will be examined in the future.

The height distribution of VHF sources for the 01:51:02 UT flash is shown in Figure 3.17. The density peak at 7-8 km altitude corresponded to the average charge removal height of the +CG. Assuming an average height of ∼7.5 km altitude and the LDAR-indicated charge moment change in Table 3.1, the charge transferred to ground (-Z direction) would have been 28 C at 1 ms and 52 C at 4 ms. The average current to ground for these intervals would have been 28 kA and 13 kA respectively.

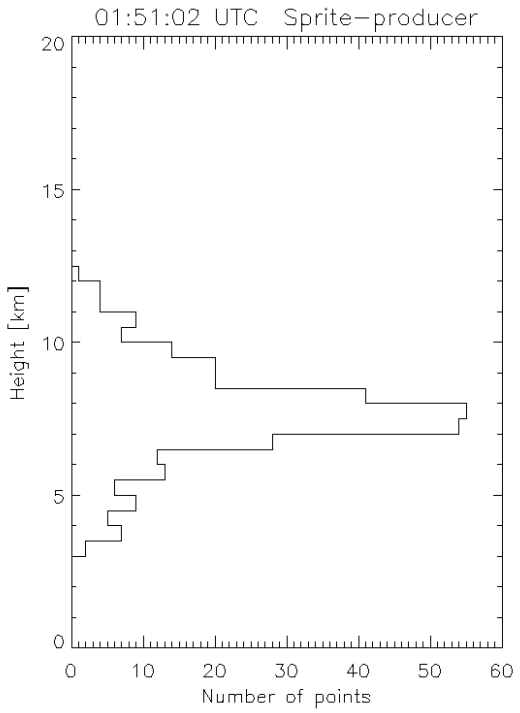

Figure 3.17: The density of VHF sources in 500 m height bins for the 01:51:02 UT flash. The peak at 7-8 km altitude corresponds to the average altitude of charge removal for the sprite-producing +CG.

3.9 01:55:47 UT Sprite-producer

The fourth sprite-producing discharge occurred at 01:55:47 UT. The video sequence for this event is shown in Figure 3.18. This sprite cluster was not as bright as the previous one, but the heads of the sprites still saturated the camera. A few small sprites are also visible on each side of the bright sprite cluster. The first video frame began at 1:55:47.953 UT, $\sim$3 ms before the occurrence of the +CG stroke.

Figure 3.18 shows that the flash originated in a convective cell immediately to the southwest of the convective cell which initiated the 01:47:52 UT flash. Thus, it appears that all of the sprite-producing discharges up to and including this discharge originated in a different convective cell. In spite of this, all of the flashes propagated into the same charge region within the stratiform region.

The temporal development of the flash is detailed in Figures 3.19 and 3.20. The initial increase in the electric field in interval t1 was due to the vertical development of the IC flash. The magnitude of this increase was less than that shown for previous sprite-producing flashes due to the greater range.

The negative leaders propagated outward through the stratiform region for $\sim$20 km during interval t1, but the electric field did not change significantly since the motion was primarily tangential relative to the slow antenna. The negative leaders continued their northward progression during interval t2 and the electric field decreased due to a net outward motion of negative charge away from the slow antenna. The average negative leader speed during interval t2 was $\sim 1.1 \times 10^5$ m/s.

The electric field stabilized during interval t3 and even increased towards the end of the interval. Figure 3.20c indicates that the negative leaders were still progressing outwards throughout the interval, so one would expect the electric field to have decreased. It is possible that a vertical moment due to "VHF quiet" positive leaders propagating at lower altitude is responsible for the discrepancy.

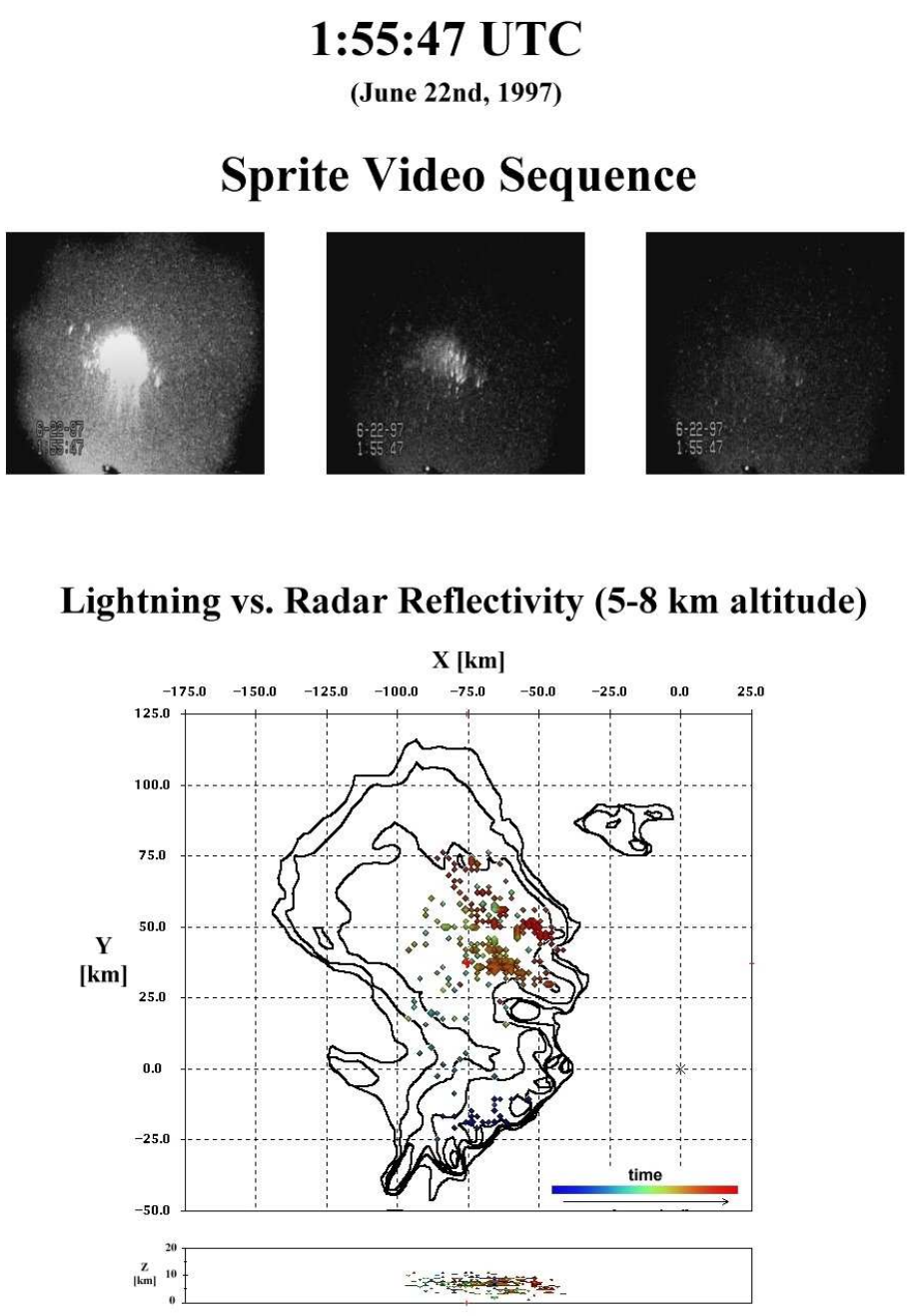

Figure 3.18: The temporal development at 17 ms intervals of the 01:55:47 UT sprite cluster (top), as seen through a wide angle lens. The LDAR data are plotted on top of NEXRAD reflectivity (bottom) and follows a rainbow-sequence from blue to red with respect to time. The reflectivity is contoured at 10 dBZ intervals starting with 0 dBZ.

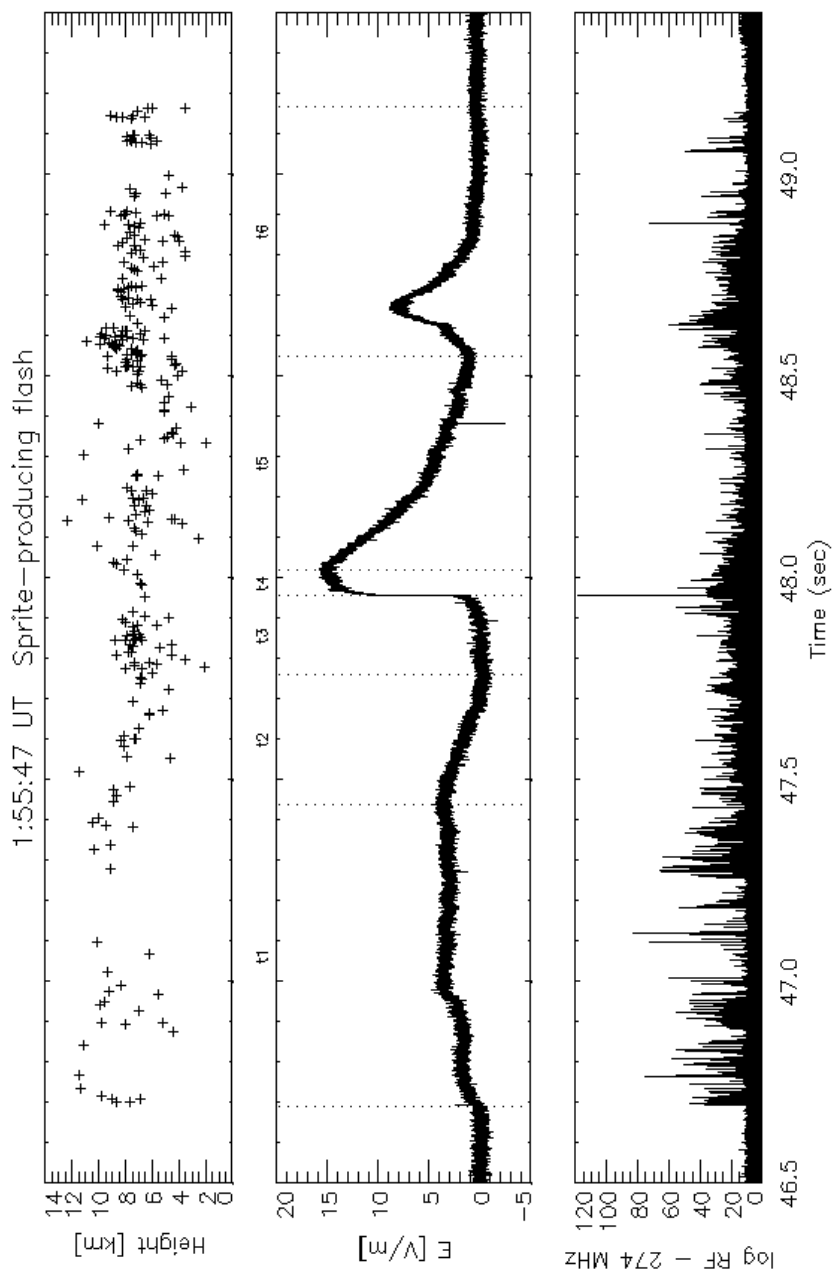

Figure 3.19: The VHF source height, electric field, and log-RF strength at 274 MHz as a function of time for the 01:55:47 UT sprite-producing discharge. The electric field is divided into time intervals t1-t6 primarily according to the prevailing slope polarity or characteristics. The sudden upward deflection at the start of interval t4 corresponds to the sprite-producing +CG.

A 85.5 kA +CG occurred at 01:55:47.9564 UT, the start of interval t4. The sprite cluster location was determined in the same way as the 1:51:02 UT sprite cluster (see Section 3.8). The sprite cluster was well correlated with the most recent negative leader activity as well as with the LDAR-indicated charge center derived from that activity. As with all previous sprite events, the +CG was displaced from the center of sprite activity in the direction opposite of the negative leader advancement. Several of the individual sprites were near or just beyond the periphery of the discharge, though one sprite was almost directly over the +CG.

The electric field waveform of the +CG is shown in Figure 3.21 along with the log-RF at 274 MHz. The most dramatic increase in electric field occurred within the initial $\sim$300 μs after the return stroke onset. Continuing current was readily evident up to about 2.5 ms after the return stroke, at which point the electric field increased more gradually.

This +CG is unusual in several respects compared to the others. First, there was a field change resembling a return stroke $\simeq$180 μs after the +CG. The delay was too short and the slant angle to the ionosphere was too great for this to have been an ionospheric reflection. The cause of this field change is unknown. Second, the +CG was preceeded for a full millisecond by stepped leader pulses, as evidenced by the log-RF bursts and noisy electric field prior to the +CG. The pulses were not located by LDAR. Finally, the log-RF within the initial millisecond was stronger than that of the other sprite-producing +CGs, possibly indicating that there was unusually vigorous negative leader activity. This shows that there can be significant differences between sprite-producing +CGs, the interpretation and effects of which are not yet understood.

The post-sprite development of the flash (Figure 3.20e-f) was similar to that of previous sprite-producing flashes. The slow electric field change at the start of interval t6 (see Figure 3.19) was due to negative breakdown which first propagated towards the slow antenna and then away, as evidenced by the blue data points in Figure 3.20f. Comparison of Figures 3.18 and 3.3 shows that the forward (towards) motion of the negative breakdown was directed into the convective cell which initiated the 01:42:57 UT sprite-producing flash.

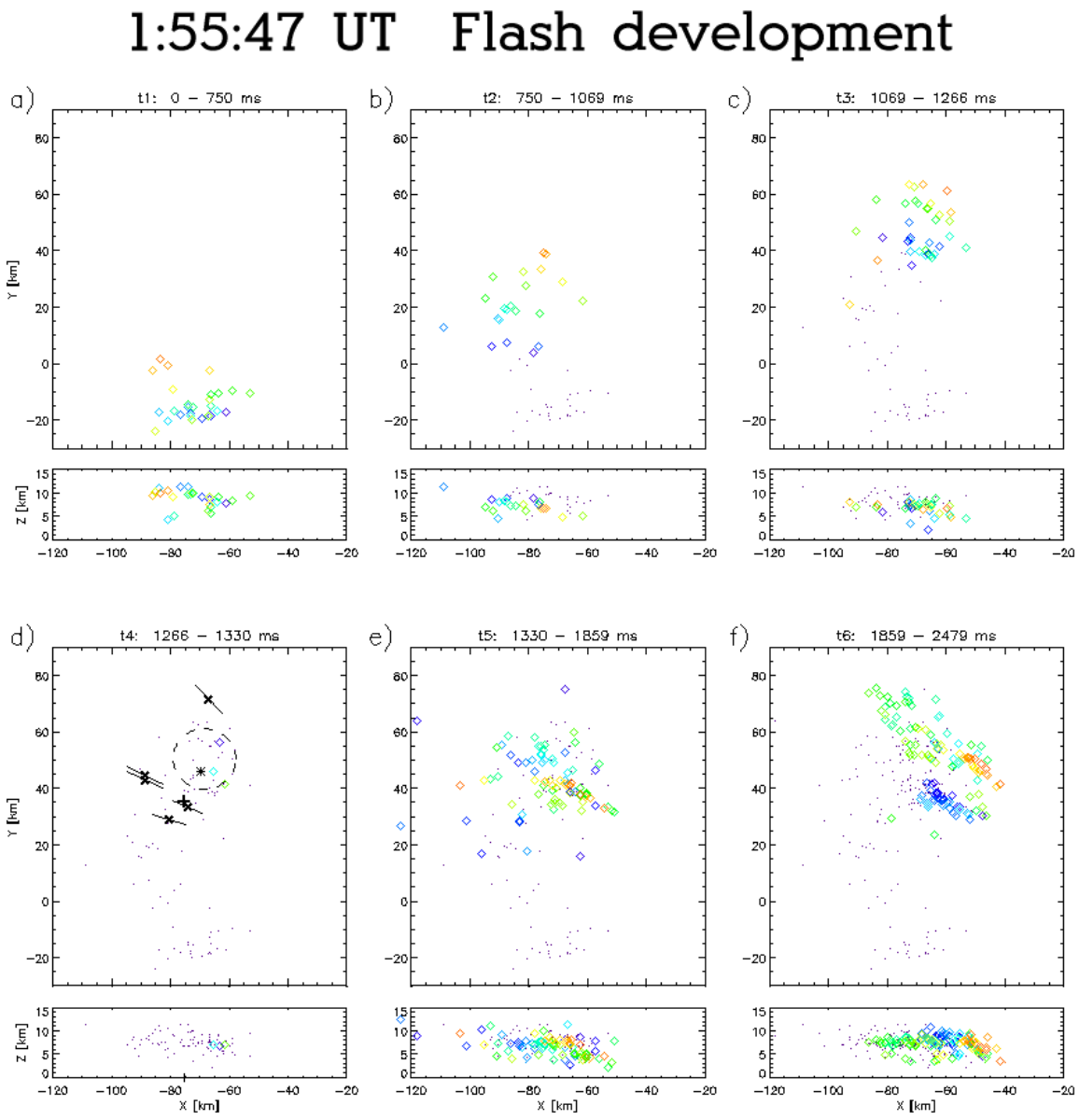

Figure 3.20: The spatial development of the 01:55:47 UT sprite-producing discharge as a function of time. The VHF sources ($\Diamond$) are rainbow-colored from blue to red according to elapsed time within the respective time interval. VHF sources from previous intervals ($\cdot$) are purple. The +CG ($+$), LDAR-indicated sprite-producing discharge center ($*$), sprite region (dashed circle), and individual sprites ($\mathbf{x}$) are shown in interval t4.

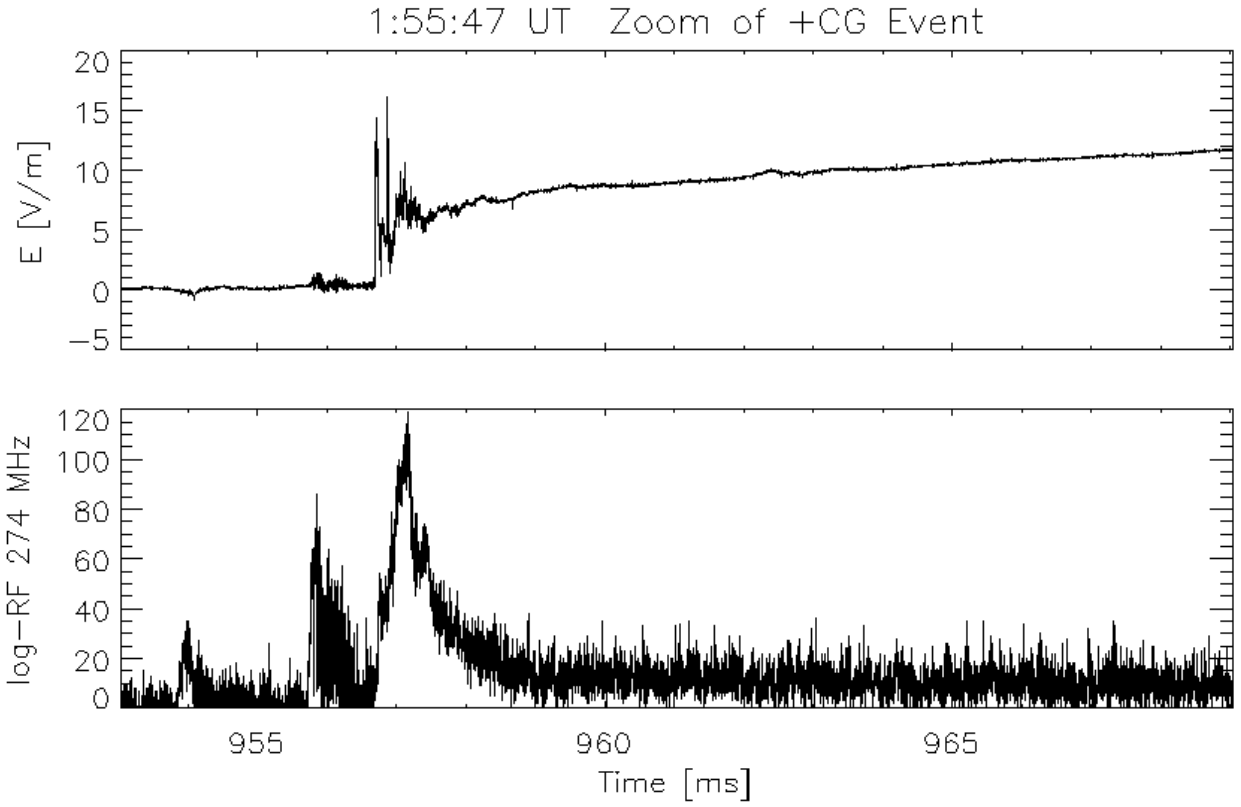

Figure 3.21: The 01:55:47 UT sprite-producing +CG electric field waveform as well as the log-RF strength at 274 MHz. The log-RF and electric field activity following the return stroke was unusually active for this CG. A return stroke-like pulse follows $\simeq$180 μs after the main return stroke. Note the "loud" and impulsive RF bursts associated with leader pulses starting $\simeq$1 ms prior to the +CG. These pulses were not located by LDAR.

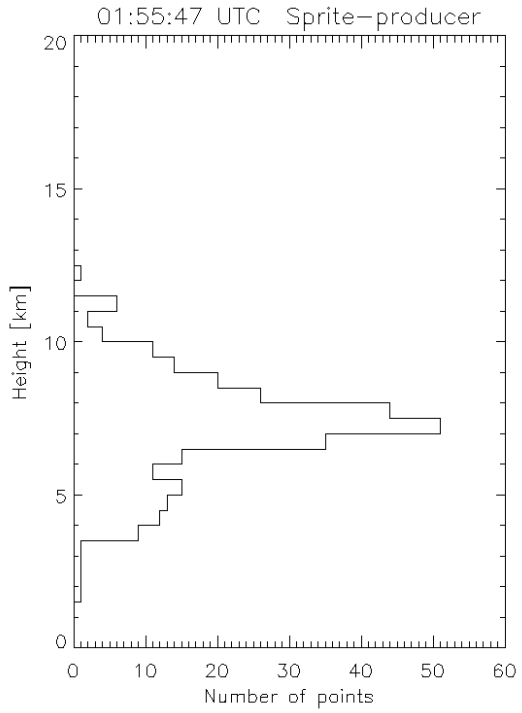

Figure 3.22: The density of VHF sources in 500 m height bins for the 01:55:47 UT flash. The peak at 7-8 km altitude corresponds to the average altitude of charge removal for the sprite-producing +CG.

The height distribution of VHF sources for the 01:55:47 UT flash is shown in Figure 3.22. The density peak at 7-8 km altitude corresponded to the average charge removal height of the +CG. Assuming an average height of ∼7.5 km altitude and the LDAR-indicated charge moment change in Table 3.1, the charge transferred to ground (-Z direction) would have been 37 C at 1 ms and 54 C at 4 ms. The average current to ground for these intervals would have been 37 kA and 14 kA respectively.

3.10 02:15:19 UT Non-sprite-producer

A 78.7 kA +CG occurred at 02:15:19.4192 UT. No sprites were seen in association with this +CG, though the image was saturated in the first field and was nearly saturated in the second by the bright parent discharge. Since sprites typically persist for at least 2 video fields, the lack of any structure in subsequent images suggested that no sprites were associated with this +CG, though this is not certain. The video

clearly indicated that the subsequent +CG(s) of the same flash at 2:15:19.51 UT did not produce any sprites.

The temporal and spatial development of the flash is shown in Figures 3.23 and 3.24. The initial development of the flash during the first 2 time intervals was similar to the sprite-producing flashes, with the notable exception of a significantly smaller areal extent.

The first, most energetic, +CG occurred at the start of interval t3. This +CG differed from the previous sprite-producing +CGs in several respects. The most obvious discrepancy was its location, which was directly below the convective cell where the IC initiated (see Figure 3.24c). Another difference was that the electric field did not deflect upwards prior to the +CG. In previous discharges, the upward deflection was speculatively attributed to the net upward transport of negative charge by positive leaders propagating at/to lower altitude, after a significant portion of the discharge between the convective cell and the negative leaders had become nonconductive. The lack of this upward deflection suggests that the horizontal channels never became resistive. The net outward motion of negative charge throughout interval t2 was maintained right up to the moment of contact of a positive leader with the ground.

If the channels were still conducting along the full extent of the discharge, then the LDAR-indicated charge center location might have been a reasonable approximation to the average charge distance. If this were the case, then this +CG would have produced the largest charge moment change of the +CGs listed in Table 3.1. It would be surprising if there were no sprites initiated by such a large charge moment change. The factor of $\sim$3 difference between the charge moment calculated from the NLDN and LDAR data illustrates how important an accurate determination of range is, particularly for closer flashes where a given uncertainty in range will comprise a bigger percentage of the total range. It is possible that the electric field increase was dominated by one or more negative leaders which were much closer than the others.

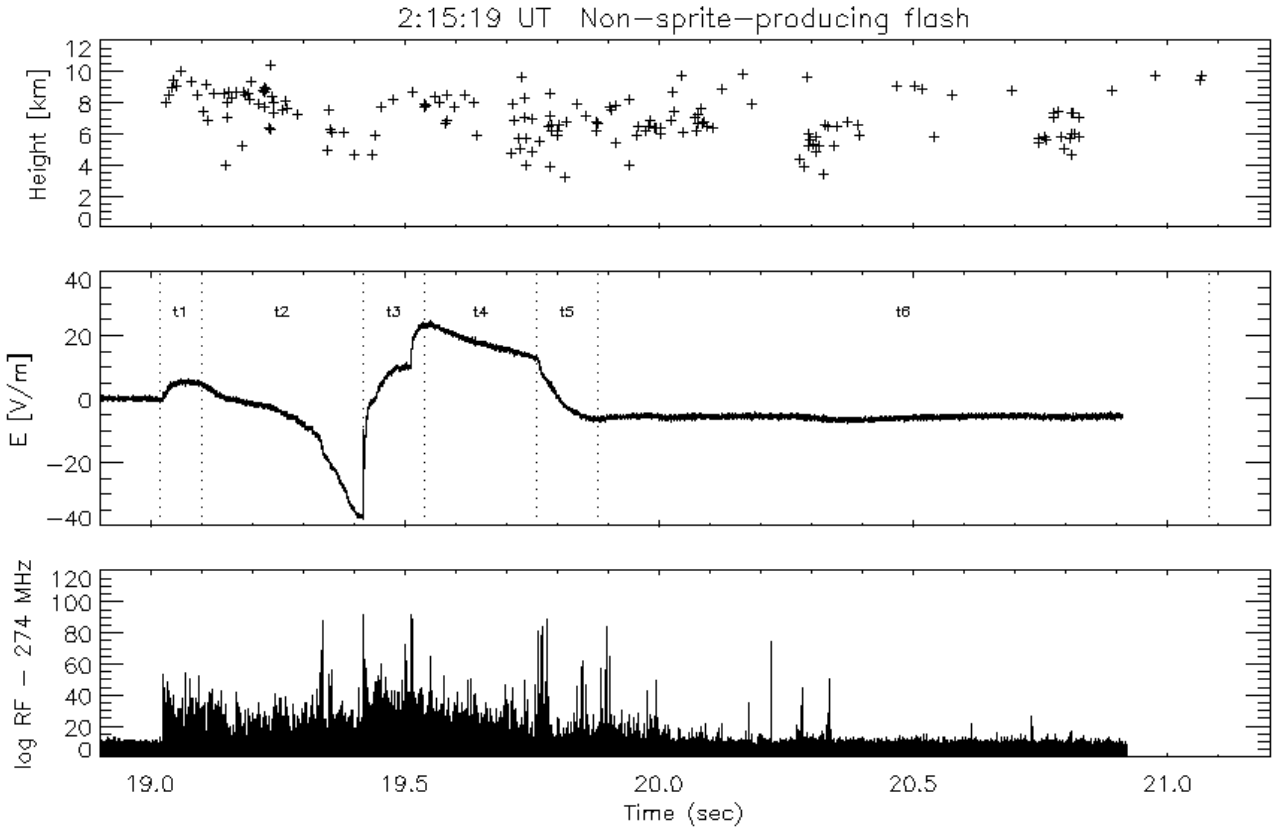

Figure 3.23: The VHF source height, electric field, and log-RF strength at 274 MHz as a function of time for the 02:15:19 UT non-sprite-producing discharge. The electric field is divided into time intervals t1-t6 primarily according to the prevailing slope polarity or characteristics. At least 2 +CG's occurred during interval t3, as evidenced by the upward steps in the electric field.

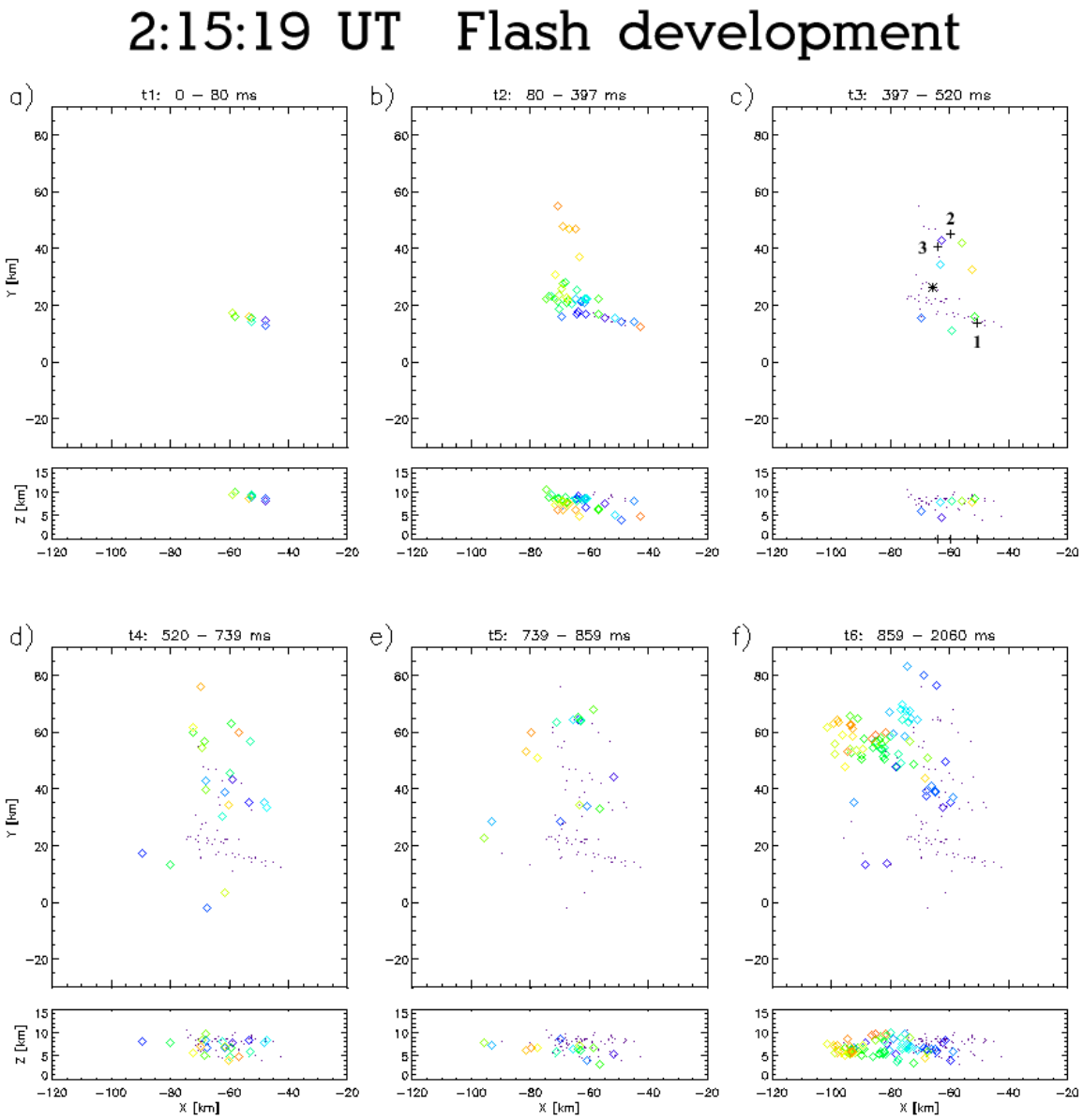

Figure 3.24: The spatial development of the 02:15:19 UT non-sprite-producing discharge as a function of time. The VHF sources (◊) are rainbow-colored from blue to red according to elapsed time within the respective time interval. VHF sources from previous intervals (·) are shown in purple. The NLDN-indicated +CGs (+) are numbered according to the order in which they occurred within interval t3. The LDAR-indicated charge center (*) was essentially the same for each of the three +CGs.

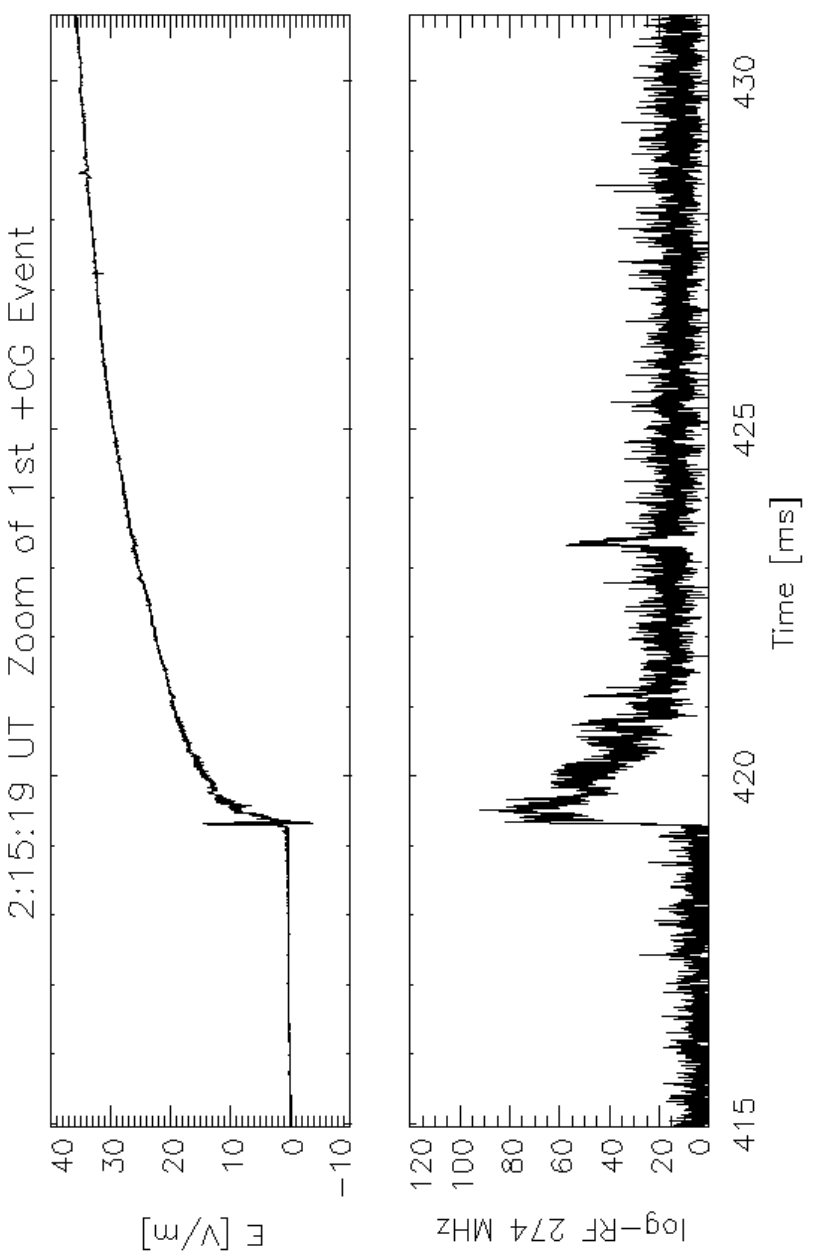

Figure 3.25: The 02:15:19.419 UT +CG electric field waveform and log-RF strength at 274 MHz. The large amplitude of the electric field change relative to other +CGs from the storm was at least partly due to its closer range, though the actual range to the charge center is uncertain (see text).

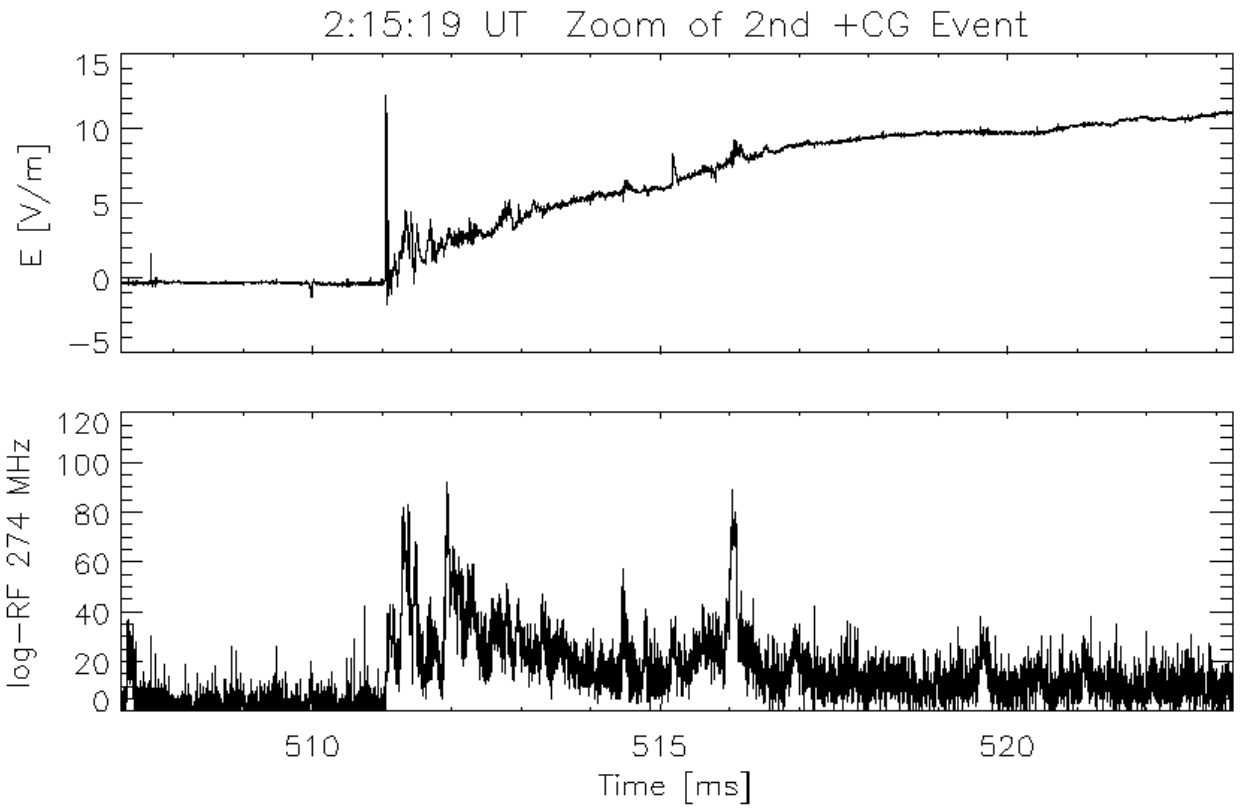

Figure 3.26: The 02:15:19.511 UT +CG electric field waveform and log-RF strength at 274 MHz. The NLDN also indicated a +CG 4 ms later at 515 ms. It is not clear from the plots whether or not this latter event was a real return stroke, though it was followed by what appears to be an increase in the continuing current. The electric field leveled off at $\simeq$518 ms, suggesting that the continuing current died out after $\simeq$7 ms.

The electric field waveforms for the 02:15:19 UT +CGs are shown in Figures 3.25 and 3.26. As was discussed previously, the first +CG at 02:15:19.419 UT was much closer than the others and this at least partly explains its larger magnitude.

The waveforms of the 02:15:19.51 UT non-sprite-producing +CG(s) are shown in Figure 3.26. The 29.4 kA +CG at 511 ms was followed by a continuing current, which like the other +CGs, had noisy impulsive events superimposed. The continuing current persisted until at least 0.5 ms before the NLDN-indicated subsequent 4.9 kA +CG stroke at 515 ms. If the continuing current was still in effect, then this can not be a return stroke. A subtle but real increase in the overall slope of the electric field apparently followed the NLDN-indicated "stroke".

3.11 Summary

In this chapter, relatively close sprite-producing discharges at <100 km range have been analyzed. The 3-dimensional development of the flashes was observed at VHF using time-of-arrival LDAR system. The flash development was compared with slow antenna measurements of the electric field, and with NEXRAD radar reflectivity data. The plan locations of the sprites were estimated from video observations and compared to the flash location and dimensions up to the time of the sprite event. A non-sprite-producing flash was also analyzed. The key results are as follows:

- A comparison of charge moment changes during a 4 ms interval after the RS for both sprite-producing and non-sprite-producing discharges indicates that the charge moment threshold for sprite initiation is probably between 200-400 C·km. This is consistent with ELF-based estimates [*Cummer and Inan*, 1997; *Cummer and Stanley*, 1999; *Huang et al.*, 1999].

- As was already observed by *Berger* [1972], *Krehbiel* [1981], and *Brook et al.* [1982], the +CGs sustained large currents of >10 kA magnitude much longer than the −CGs. The sprite-producing discharges had average downward (−z direction) currents of ≃28-37 kA within the initial 1 ms post-return stroke interval and ≃13-16 kA within the initial 4 ms. The range of charge transfers to ground (-z direction) for these time intervals was ≃28-37 C and ≃52-64 C, respectively. The source of the general discrepancy between +CG and −CG sustained currents may simply be that all of the +CGs were associated with horizontally extensive discharges while the −CGs were not.

- The positive charge lowered to ground by the sprite-producing discharges was located at an average altitude of 7-8 km within the stratiform region of the MCS. This is in agreement with previous multi-station electric measurements of +CG charge removal altitudes within the stratiform region of an MCS [*Krehbiel*, 1981], but contradicts numerous predictions that the sprite-producing CGs would discharge a portion of the positive charge layer at or just below the 0° C isotherm at ≃4.5 km altitude.

- The electric field and VHF source pattern are consistent with the interpretation that +CGs within the stratiform region of an MCS are produced after horizontally extensive channels become "cutoff" (nonconducting), as was proposed by *Krehbiel* [1981].

- The sprites occurred primarily above the periphery of the most recent (∼200-300 ms) portion of the discharge. This most recent discharge section was almost entirely located between the +CG and the negative leader advancement front. This provides further evidence for the channel cutoff hypothesis.

- Surprisingly, the plan locations of most sprites were correlated with the periphery of the above mentioned discharge section. The sprites might, in essence, provide a crude outline of the horizontal extent of charge removal.

- In two of the sprite-producing flashes, the +CGs were followed by one or more –CG strokes which occurred underneath a region of rapid charge removal. I speculate that these –CG flashes were separate discharges initiated from the top of one or more tall structures due to the influence of the +CG's charge removal.

3.12 Discussion

A correlation between the sprites and the apparent periphery of the discharge would be surprising if the charge distribution throughout the flash were somewhat uniform, as assumed in the uniformly charged disk models of Section 2.5.2. The electric field will, of course, be maximized directly over the center of a uniformly charged disk. It was also shown in Section 2.5.2 that the electric field below the base of the ionosphere varies little for disk radii of 15 km or less for a given charge moment. This implies

that the electric field is insensitive to the actual charge distribution for such small radii.

In order to produce sprites with plan positions near the periphery of the discharge in a purely quasi-electrostatic approximation, two things must both be true: 1) the charge must be localized at or just beyond the plan positions of the sprites 2) The horizontal dimensions must be sufficiently large so that the charge regions do not produce a high-altitude electric field maximum near the center of the charge distribution.

It should be stressed that the exact plan location of the sprites relative to the discharge boundary is unknown for several reasons:

1. The detection efficiency of the LDAR drops off rapidly with range (see Section 3.2.1)

2. The LDAR did not adequately detect the negative leader activity following the +CG. This leader activity will extend the horizontal dimensions of the discharge.

3. The sprite locations were obtained by assuming the uppermost luminous emissions were at 87 km altitude. This introduces an uncertainty of at most ±6 km in the plan location, as discussed in Section 3.6.

4. The range errors in LDAR locations are on the order of a few kilometers at the distance of the sprite discharges.

The second point is particularly important for the localization of charge near the discharge periphery, since it is the outward propagation of the individual leaders which supplies the current, and hence the new charge regions, following the return stroke process. Optical measurements indicate that the two-dimensional return stroke velocity of natural positive return strokes is $0.9 \pm 0.4 \times 10^8$ m/s and does not change with height [*Mach and Rust*, 1993]. Thus, it should take a return stroke $\sim$300 μs to propagate to the end of a $\sim$30 km channel length which might be typical of the sprite-producing discharges. Thus, the dramatic increase in electric field after the initial $\sim$300 μs ramp would be due to new charge near the periphery of the discharge. This charge would be relatively localized since the leader velocities would be very much less than that of the return stroke. Even if the negative leader velocities were as high as 2×10^6 m/s ($\sim$10 times the average shown earlier), they would only advance $\sim$8 km in 4 ms.

Chapter 4

ELF measurements

4.1 Introduction

Extremely low frequency (ELF) radio waves (3 Hz-3 kHz) can propagate for long distances within the earth-ionosphere waveguide due to a weak $\propto R^{-1/2}$ dependency of amplitude on range, R [*Greifinger and Greifinger*, 1976]. This enables measurements to be made of CG current moments (current times height) at ranges well in excess of 1000 km. Numerous ELF measurements indicate that sprites are primarily correlated with positive cloud-to-ground (+CG) strokes that have slow tails produced by large continuing currents [*Boccippio et al.*, 1995; *Reising et al.*, 1996; *Cummer and Inan*, 1997; *Sukhorukov and Stubbe*, 1997; *Bell et al.*, 1998; *Marshall et al.*, 1998; *Reising et al.*, 1999; *Huang et al.*, 1999; *Cummer and Stanley*, 1999].

In his landmark paper which predicted the existence of sprites, *Wilson* [1925] also predicted that "The discharges above the cloud would doubtless give rise to atmospherics". There were several limited searches for these "sprite sferics" prior to 1996 [*Franz et al.*, 1990; *Winckler*, 1995; *Winckler et al.*, 1996]. These studies failed to provide significant evidence that sprites produce detectable electric field waveforms. On the basis of photometer to VLF comparisons, *Winckler* [1995] concluded that there was no unambiguous evidence that sprites emit sferics, but admitted that the simultaneous presence of coincident sferics from intracloud or cloud-to-ground discharges made it difficult to address that question.

Farrell and Desch [1992] attempted to explain the apparent lack of VLF emissions by resorting to a longer time scale for sprite development. Their model placed the peak emission below ~50 Hz; well into the ELF region of the spectrum. At the AGU Fall Meeting in 1996, New Mexico Tech (NMT) researchers reported slow (~500 Hz)

electric field changes which were correlated with bright sprites on video but were temporally distinct from +CG slow tails. These slow field changes were unique in that they were not immediately preceded by the VLF radiation produced by a CG's return stroke. NMT researchers attributed these isolated slow field changes to vertical charge transfer within sprites and this was subsequently confirmed by photometric measurements which showed that the slow field changes were directly correlated with spatially-integrated sprite light output [*Brook et al.*, 1997; *Cummer et al.*, 1998; *Reising et al.*, 1999]. Examples of this correlation will be shown in this chapter and in Chapter 5.

When video is available at night, the isolated slow field changes have always been found to be correlated with bright sprite events and this correlation enables the detection of bright sprite events via ELF measurements when video is not available [*Brook et al.*, 1997]. Daytime sprite events were detected on August 14, 1998, via their ELF "fingerprint". These events were analyzed and published by the author [*Stanley et al.*, 2000]. The content of this published work is included in this chapter, along with some additional figures that were excluded from the original paper due to length constraints.

The lightning current moment (current times vertical channel length) for the daytime sprite events was extracted quantitatively by a technique described in detail by *Cummer and Inan* [2000]. This technique had been used previously for sprite-producing discharges of both positive [*Cummer et al.*, 1998; *Cummer and Stanley*, 1999] and negative polarities [*Barrington-Leigh et al.*, 1999]. In order to separate the probable lightning and sprite current (i.e., the second peak), it is assumed that the lightning current moment varies linearly after the first few milliseconds of the discharge. The charge moment changes were obtained by integrating the respective current moments according to: $M_q(t) = \int_0^t M_i(\tau)d\tau$.

4.2 Sprite Currents

At 5:38:00.77 UT on July 24, 1996, a bright sprite event was observed on video from both Langmuir Laboratory, New Mexico and Yucca Ridge, Colorado. A slow field change recorded at Langmuir was coincident with the sprite appearance in video. Red and blue photometery of the sprite event was recorded by Walt Lyons and Tom Nelson at Yucca Ridge. The position of the sprite was triangulated from the video observations. The light propagation delays to each site was subtracted from the

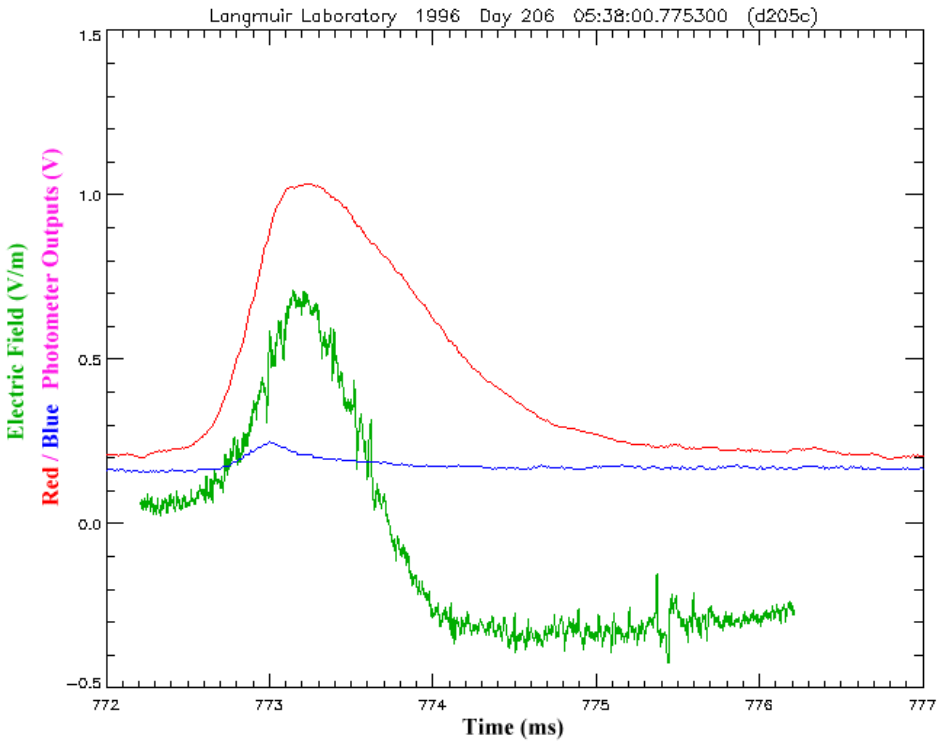

Figure 4.1: An isolated slow electric field change recorded at Langmuir Laboratory is compared with the red and blue photometry observed from Yucca Ridge. The waveforms were temporally aligned to the triangulated position of the sprite event. The red luminosity from the sprite is strongly correlated with the electric field signature, thus proving that the sprite produced the slow field change.

corresponding waveforms and the result is shown in Figure 4.1.

The distance between the sprite and Yucca Ridge was sufficiently great (>500 km) that the parent discharge was well below the horizon and thus could not significantly contaminate the photometer signal. The strong correlation between the sprite's light output and the electric field change provides clear evidence that the sprite, not the parent discharge, was the source of the field change.

The peak in the blue photometer signal leads that in the red. This may be due to millisecond-scale timing errors which affected the blue channel (T. Nelson, personal communication, 1997). However, other measurements [*Armstrong et al.*, 1998; *Suszcynsky et al.*, 1998] have shown that blue emissions lead those of the dominant lower energy red emissions, indicating that significant ionization occurs during sprite gener-

ation. The identity and nature of the ionization mechanism is disclosed in Chapter 5.

Cummer et al. [1998] independently confirmed the correlation of the photometer signal with the sprite field change for 3 sprite events. Using an ELF propagation model and a vertical sprite extent of ∼30 km, they estimated that the sprites had peak currents (integrated across their horizontal extent) of 1.6-3.3 kA and total charge transfers of 5-42 C. *Reising et al.* [1999] observed that the sprite charge moment change was linearly related to the total sprite luminosity. They also noted that ∼20% of sprite events are accompanied by an ELF pulse. The author's observations also support this estimate.

4.3 Daytime Sprites

4.3.1 Instrumentation

The GPS-based New Mexico Tech (NMT) interferometer/atmospheric (sferic) data acquisition system (see Appendix A.2) was used to acquire very broadband (<1 Hz - 250 kHz) electric field data. A sensitive bipolar trigger setting was used on August 14, 1998 was used to acquire CG and IC sferics. The sensitive setting made it possible to unambiguously discriminate between slow tails which are associated with CGs and delayed slow field changes associated with sprites. The pre- and post-trigger lengths were set to 2 and 6 ms respectively on August 14, 1998.

The NMT sferic system was located on a mountain ridge at Langmuir Laboratory, NM. In order to determine the electric field intensification due to the ridge, sferics at >800 km range were compared between the NMT sferic system and an electric field sferic system located ≃30 km away on level terrain operated by Marx Brook. This comparison revealed that the ridge intensified the electric field by a factor of 1.9±0.2. The NMT system's electric field values were converted to flat terrain values and these were used for the ELF propagation model.

4.3.2 Experiment

On August 14, 1998, the sferic system was armed between 23:07-23:42 UT (6:07-6:42 pm CDT). During this time interval, there was a large mesoscale convective system (MCS) over southern Texas not quite 2 hours remaining before local sunset after 8 pm CDT (see Figure 4.2). NEXRAD radar data (not shown) indicated that the areal coverage of base reflectivity (>15 dBZ) for this MCS was >66,000 km^2,

which exceeds the mean of ≃50,000 km^2 for nighttime sprite-producing MCSs [*Lyons et al.*, 1999]. Figure 4.3 shows National Lightning Detection Network (NLDN) data for southern Texas during the time period that the sferic system was armed. A horizontal bipolar pattern is clearly evident, which is a common feature of nighttime sprite-producing MCSs [*Boccippio et al.*, 1995; *Lyons*, 1996].

4.3.3 Results

Starting at 23:19:48.535 UT, the electric field system was triggered in 3 consecutive time intervals. The broadband electric field data, sampled at 500 kHz, is shown in Figure 4.4. A –CG field change precedes a +CG field change with a large slow tail. The slow tail is followed by a large and isolated slow field change with a waveshape very similar to that produced by energetic nighttime sprites [*Brook et al.*, 1997; *Cummer et al.*, 1998; *Reising et al.*, 1999; *Cummer and Stanley*, 1999]. The +CG had a peak current of 70.9 kA and occurred in the MCS over southern Texas (see Figure 4.3) while the –CG was produced by an unrelated small storm in central Wyoming. The onset of the sprite field change occurred 13.2 ms after the +CG onset.

The charge moment change of the 23:19:48 UT parent +CG discharge and sprite event are shown in Figure 4.5. The charge moment change of the +CG at the onset of the sprite field change was 6100 C·km. In contrast, the onset of nighttime sprite ELF signatures occurred at +CG charge moment changes well below 1100 C·km [*Cummer and Stanley*, 1999]. Charge moment changes exceeding 6000 C·km may be exceptionally rare since *Huang et al.* [1999] found no charge moment changes larger than ≃5000 C·km across the entire globe during an ≃18 day observation period in the summer of 1997.

The charge transferred to ground by the parent +CG can be estimated by assuming that the average charge height was no lower than ≃4 km, which is the base altitude of a significant positive charge layer in stratiform regions [*Marshall et al.*, 1996], and no higher than the maximum cloud top height of ≃15 km indicated by infrared satellite measurements of cloud top temperature (Figure 4.2). From the charge moment change, the total charge transferred to ground would therefore have been between 410 C and 1500 C prior to the onset of the sprite field change. The largest directly measured total charge transfer that the authors are aware of is ≃450 C (also associated with a +CG) [*Berger*, 1972], which further attests to the highly energetic and unusual nature of this event.

The sprite event added ≃2800 C·km to the total charge moment change, as in-

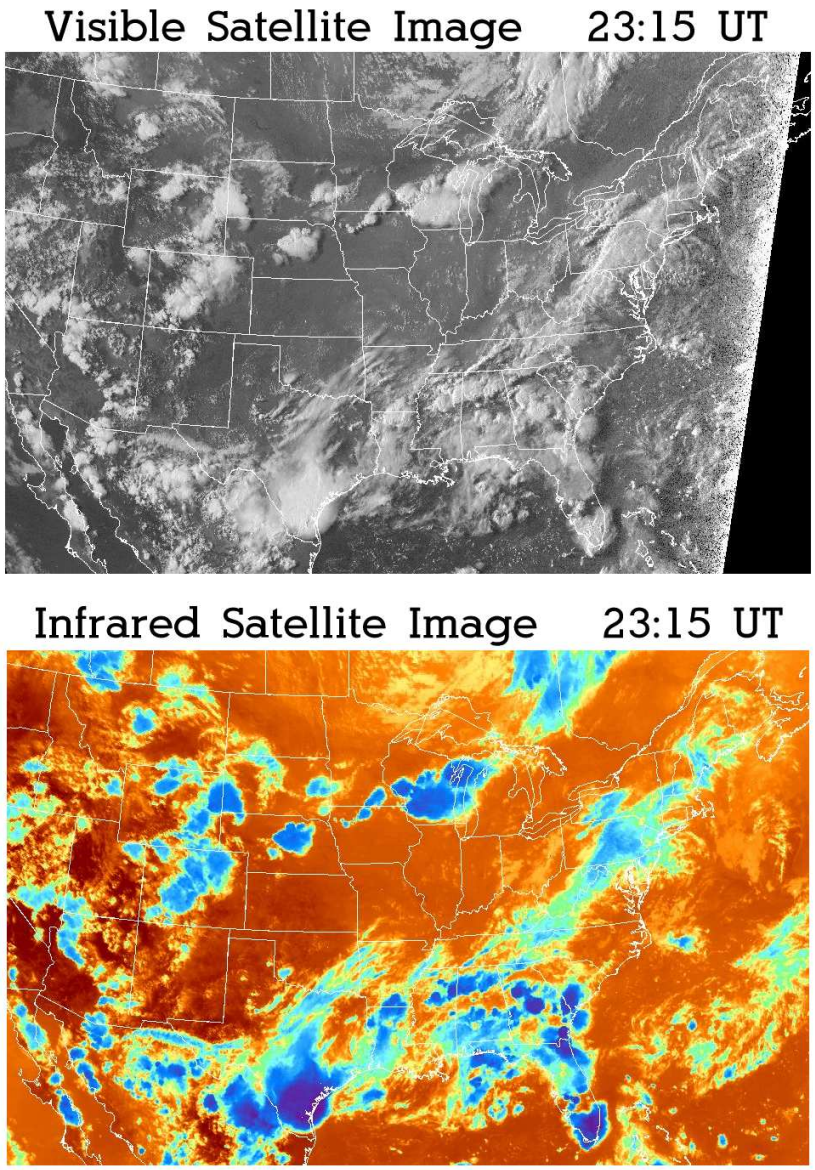

Figure 4.2: The GOES-8 visible satellite image of the United States (top) at 23:15 UT, August 14, 1998, ∼5 min prior to the first sprite event. The diagonal line over the Atlantic Ocean on the right side of the image is the terminator, or "sunset" line. The GOES-8 infrared satellite data is shown at the bottom for the same time and region. The darkest blue colors correspond to cloud tops of about −65° C. A large MCS over southern Texas is evident in both pictures, with the infrared indicating an average cloud top temperature below −60° C over a large area. The images were obtained from *http://www.rap.ucar.edu/weather/satellite.html*.

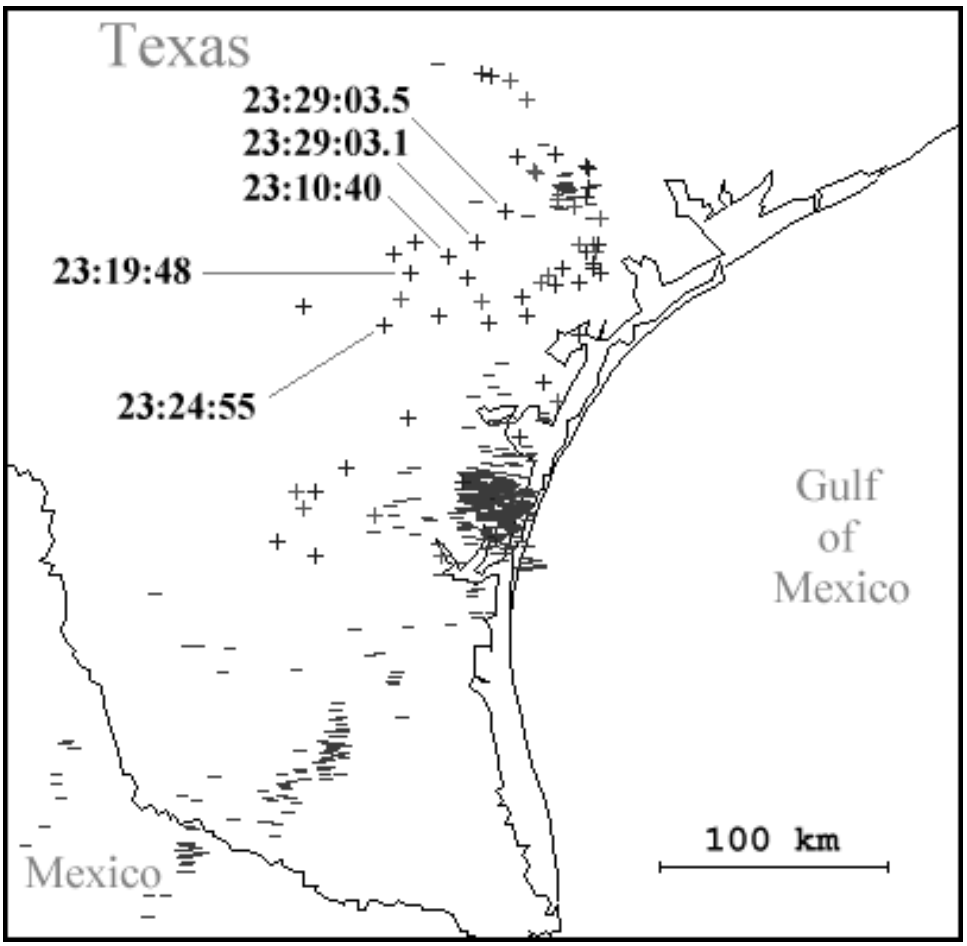

Figure 4.3: National Lightning Detection Network (NLDN) data for a Mesoscale Convective System (MCS) over southern Texas is displayed for the time period 23:07-:42 UT on August 14, 1998. The five energetic +CGs discussed in this section are labeled.

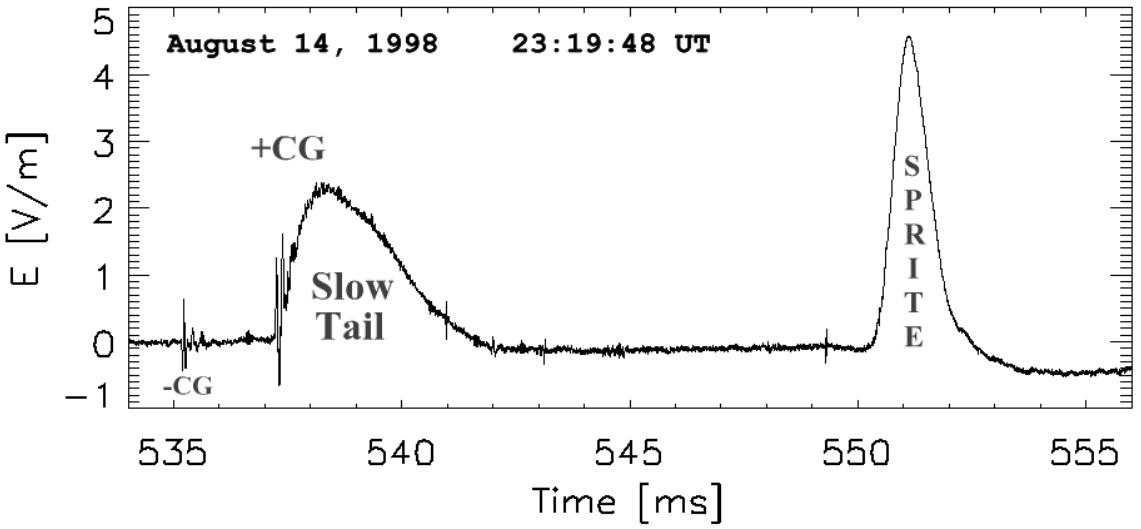

Figure 4.4: VLF radiation from a +CG return stroke followed by a large slow tail indicative of a large continuing current. More than 13 ms after the return stroke, a large slow field change occurred which is not immediately preceded by VLF radiation. The slow field change was likely produced by an energetic sprite event.

dicated in Figure 4.5 by the separation between the total charge moment change (solid line) and the estimated parent discharge charge moment change component (dashed line) for the 23:19:48 UT event. To put this into perspective, the largest sprite charge moment change found by *Cummer and Stanley* [1999] for 11 nighttime sprite events was ∼840 C·km (see Section 5.3.3) while *Reising et al.* [1999] found no sprite charge moment changes larger than ≃380 C·km for 81 nighttime sprite events. Since nighttime sprite charge moment changes are known to be linearly correlated with spatially-integrated sprite brightness *Reising et al.* [1999], it is likely that this daytime sprite event was unusually bright.

Five minutes later at 23:24:55.658 UT, another +CG occurred within the same region of the storm as the first (Figure 4.3) and produced the second sprite field change. The onset of the sprite field change occurred after 11.0 ms had elapsed when the parent discharge charge moment change had reached 4300 C·km (Figure 4.5). Although this was less than the threshold for the previous sprite ELF signature onset, it is still far in excess of that observed for nighttime sprites. The sprite event added ≃1200 C·km to the total charge moment change.

At 23:29:03.129 UT, the third consecutive +CG to strike within the same general

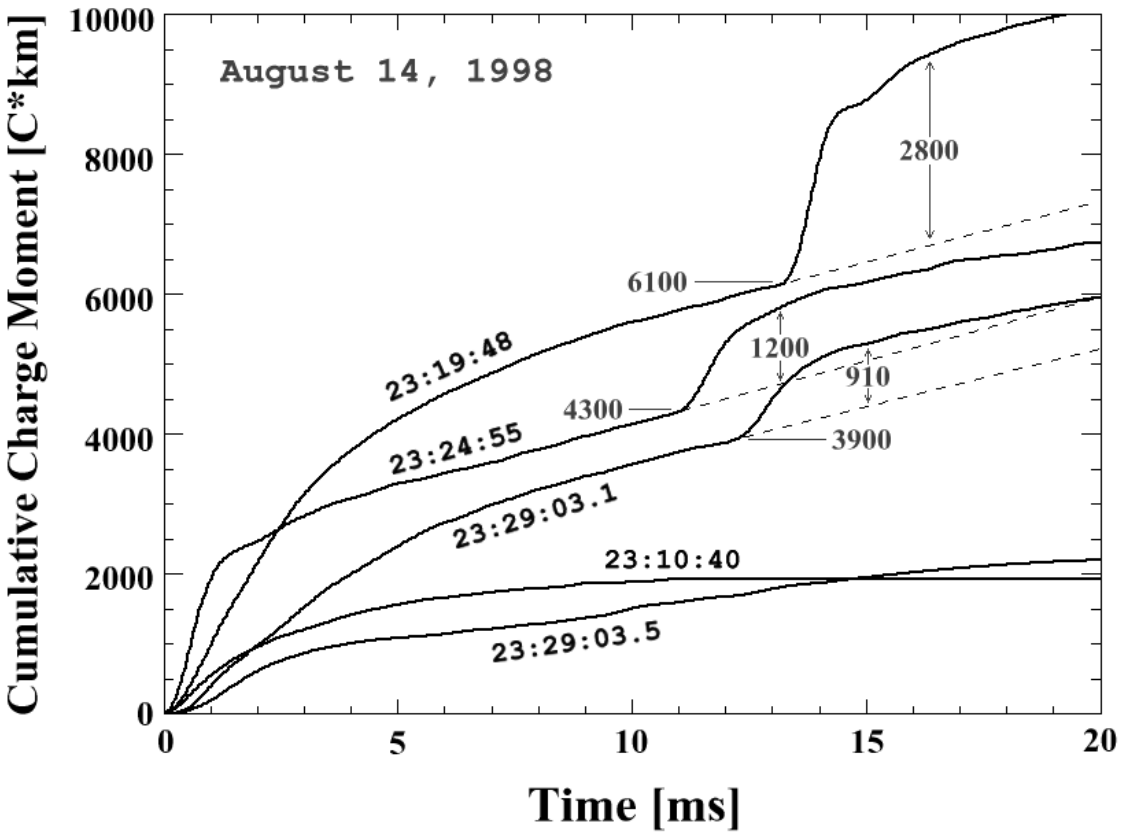

Figure 4.5: The cumulative charge moment changes of the five +CGs which produced the largest such changes (within 20 ms of the return stroke) during the data acquisition period. The three most energetic discharges produced sprite events having charge moment changes of 910-2800 C·km, as shown by the separation between the total charge moments (solid lines) and the estimated parent discharge components (dashed lines).

region as the previous sprite-producing discharges produced the third (and final) sprite field change. Figure 4.5 shows that the charge moment change of the parent discharge for the onset of this sprite field change was 3900 C·km after 12.3 ms had elapsed. The sprite event added ≃910 C·km to the total charge moment change.

There were other +CGs during the 35 min data acquisition period which also produced large slow tails but were not accompanied by isolated slow field changes. The two such discharges with the largest charge moment changes occurred at 23:10:40.964 UT and at 23:29:03.532 UT, and their charge moment changes are shown in Figure 4.5. The larger of these +CGs produced a charge moment change of 2200 C·km in 20 ms, which was either insufficient to initiate a sprite or, more specifically, a sprite with a detectable ELF signature.

4.3.4 Relaxation Time during the Day

The nighttime relaxation time profile was derived and shown in Section 2.4.4. In this section, we will estimate τ_r as a function of height around the time of the daytime sprites. The results will then be used in the next section to estimate the initiation altitude of the sprites.

Figure 4.6a shows the IRI-95 model [*Rawer et al.*, 1978] of electron number density (n_e) relative to local ground-level sunset over South Texas on August 14, 1998. The base altitude of the model output is 65 km for daylight hours and 80 km for night. A significant change in n_e occurs within ±3 hours of sunset, with the greatest change being at sunset when the change in incident solar flux is greatest. The dashed line in Figure 4.6a is the IRI-95 n_e profile at 23:19:48 UT, the time of the first sprite event. The solid line in Figure 4.6b shows τ_r based on the IRI-95 n_e profile and a "cold electron" assumption (see *Pasko et al.* [1997b]) for 65-70 km altitude at 23:19:48 UT. Note that although n_e at the time of the sprites was significantly less than at midday, the corresponding τ_r was still very small.

The thick dashed line in Figure 4.6b shows the IRI-95 τ_r extrapolated down to 60 km altitude using the τ_r scale height at 65 km altitude. Below 60 km, ion conductivity begins to dominate over the electron conductivity [*Reid*, 1986]. The thin dashed line (profile A) in Figure 4.6b below 60 km is based upon combining the IRI-95 electron conductivity extrapolation with the experimentally measured ion conductivity of *Holzworth et al.* [1985]. The dot-dash line (profile B) in Figure 4.6b is an interpolation between the IRI-95 τ_r profile and Hale's mid-latitude τ_r profile for 53 km altitude and below [*Hale*, 1994]. The vertical dotted lines in Figure 4.6b denote the range of

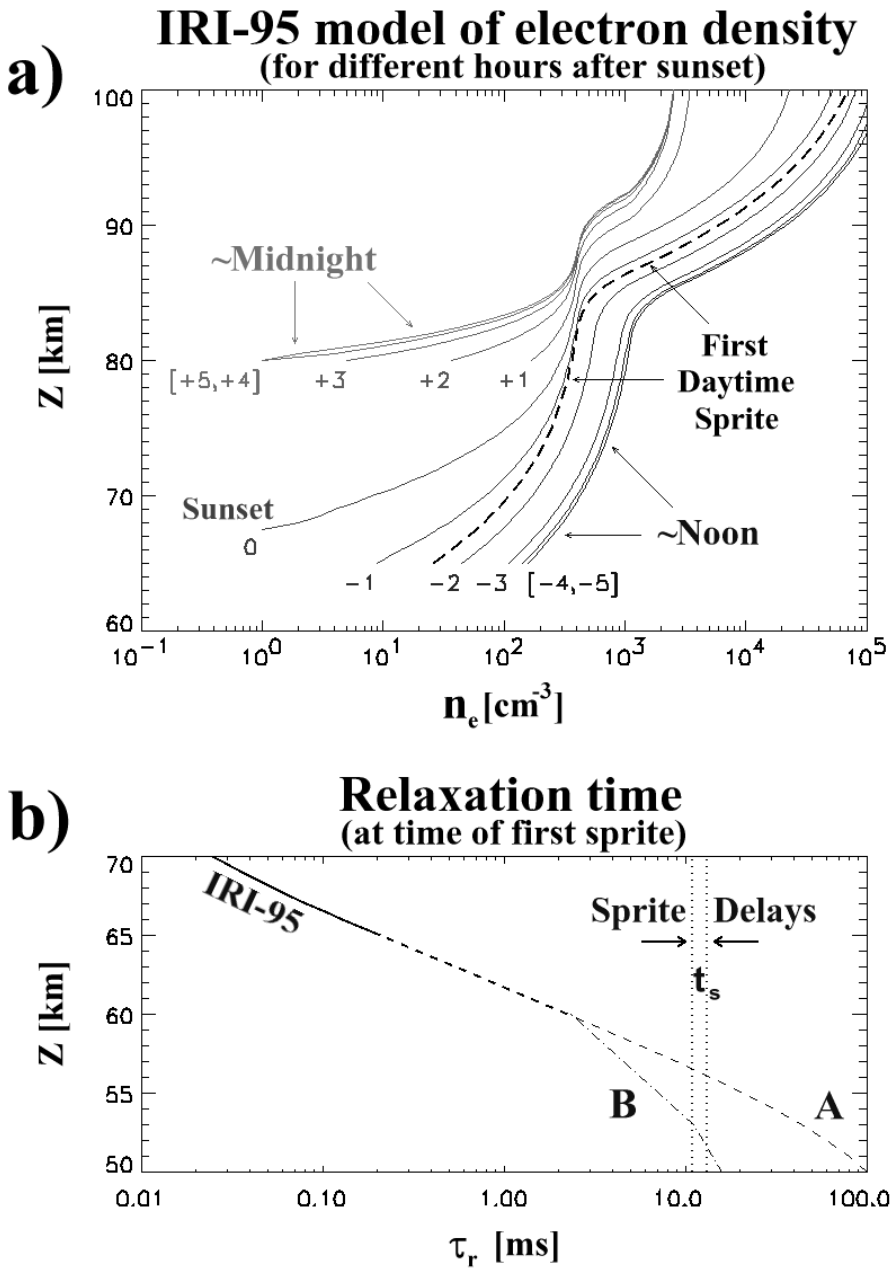

Figure 4.6: a) The IRI-95 model of electron density (n_e) as a function of time in hours relative to sunset over S. Texas on August 14, 1998. The dashed line shows the IRI-95 n_e at the time of the first sprite. b) The relaxation time (τ_r) at the time of the first sprite, with the IRI-95 model (thick solid line) extrapolated below 65 km (thick dashed line) and incorporating the effects of different ion concentrations of *Holzworth et al.* [1985] (Profile A) and *Hale* [1994] (Profile B) below 60 km. The vertical dotted lines show the range of daytime sprite delays (t_s).

daytime sprite initiation time delays (t_s: 11.0-13.2 ms) reported in this study. Note that τ_r exceeds all t_s below $\simeq$56 km altitude for Profile A but does so only below $\simeq$51 km altitude for Profile B.

4.3.5 Daytime Sprite Initiation Threshold

It has been estimated that a parent discharge charge moment change of 8000 C·km would be required to initiate a daytime sprite at 50 km altitude [*Fernsler and Rowland*, 1996]. In order to better assess the possibility of conventional breakdown onset as a function of charge height and horizontal extent parameters, the parent discharge is modeled as a uniformly charged disk of radius R_d, height Z_d, and total charge Q_d. This static field approximation is nearly identical to that used in Section 2.5.2 for nighttime calculations, with the main difference here being that the base of the ionosphere is approximated as 62 km altitude (where $\tau_r \lesssim 1$ ms) instead of 81 km.

Figure 4.7a shows that conventional breakdown ($\frac{E}{E_k} \geq 1$) probably would have occurred at 54 km altitude (where $\tau_r \gg t_s$ for profile A of Figure 4.6b) for $Q_d Z_d = 6000$ C·km (ie, the first sprite-producing discharge) if $R_d < 25$ km. Table 3.1 shows that R_d is typically < 25 km for nighttime sprite-producing +CGs, which supports the possibility that the radius of even this unusually energetic flash might have been small enough to produce conventional breakdown for Profile A. However, it is clear from Figure 4.7b that the first sprite-producing discharge would probably not have been able to initiate conventional breakdown at altitudes where $\tau_r > t_s$ in Profile B.

The charge moment changes at the onset of the second and third sprite field changes was shown to be 4300 C·km and 3900 C·km, which would have been insufficient to initiate conventional breakdown at 54 km according to Figure 4.7b. One speculative possibility is that the conductivity above 54 km altitude had somehow been decreased by the energetic first sprite event on the time scale of minutes, leading to a higher initiation altitude and hence lower initiation threshold.

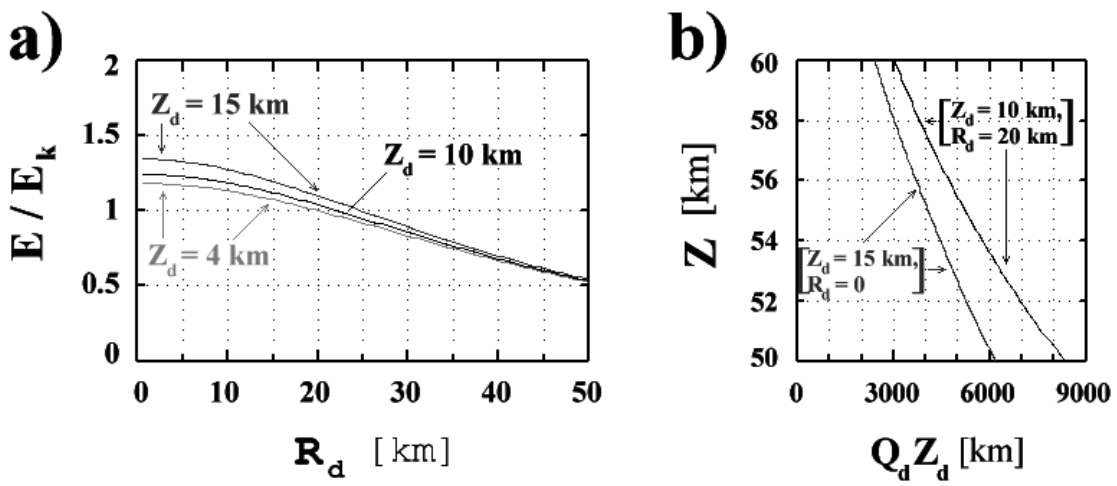

Figure 4.7: A static field approximation for a uniformly charged disk of radius R_d and height Z_d along with an ionosphere conducting plane at $Z = 62$ km is used to calculate a) The ratio of the electric field to the breakdown field at $Z = 54$ km due to a total charge moment ($Q_d Z_d$) of 6000 C·km. b) The minimum $Q_d Z_d$ required to initiate breakdown for a $Z_d = 15$ km point charge and a more realistic example of $R_d = 20$ km and $Z_d = 10$ km.

4.4 Summary

As discussed in this chapter and in the papers by *Cummer et al.* [1998]; *Pasko et al.* [1998b]; *Reising et al.* [1999]; *Cummer and Stanley* [1999], sprites can emit ELF radiation. The ELF sprite emissions are separate and distinct from the ELF slow tail which often follows sprite-producing CGs. This "sprite signature" was used to detect the presence of daytime sprites. An ELF propagation model was applied to the observed electric field waveform in order to determine the charge moment change of the daytime sprite-producing discharges and sprites. The key results of this study are summarized below:

- The slow field changes attributed to sprites by New Mexico Tech Researchers were found to be well correlated with spatially-integrated sprite light output [*Brook et al.*, 1997; *Cummer et al.*, 1998; *Reising et al.*, 1999]. This proved that sprites are the source of the slow field changes which are temporally distinct from the ELF slow tail of a parent discharge. This "sprite signature" can be used to detect the presence of sprites when video is not available.

- Three different sprite events were detected during the daytime on August 14, 1998, by virtue of their ELF signature. All three slow field changes had unusually large amplitudes. The onset of the sprite ELF signatures was delayed by 11.0-13.2 ms from +CGs which had unusually large slow tails. All of the parent CGs occurred beneath the stratiform region of a large MCS in southern Texas.

- The charge moment changes of the parent discharges, in chronological order, were 6100, 4300, and 3900 C·km at the onset of the sprite ELF signatures. A charge moment change of 6100 C·km may have been sufficient for conventional breakdown at $\simeq$54 km altitude, assuming an experimentally measured ion conductivity profile of *Holzworth et al.* [1985]. However, the other parent discharges would have been unable to initiate conventional breakdown unless the conductivity of the atmosphere had somehow been altered by the first sprite event.

- The daytime sprites themselves produced unusually large charge moment changes of $\simeq$2800 C·km, $\simeq$1200 C·km, and $\simeq$910 C·km. These charge moments are larger than the largest nighttime sprite charge moment change published to date ($\sim$840 C·km by *Cummer and Stanley* [1999] and shown in Section 5.3.3). This

suggests that daytime sprites dissipate much more stored electrical energy on average than their nighttime counterparts, consistent with the much larger charge moment threshold for daytime sprite initiation.

4.5 Discussion

Several attempts were made in 1997 to detect daytime sprite signatures. In spite of this, no such signatures were detected. The fortuitous observation in 1998 of the three daytime sprite events presented in this chapter are the only such events detected to date. As was noted earlier, daytime sprite events are expected to be rare since the charge moment threshold for sprite initiation is very much higher during the day than at night.

Observations of nighttime sprites indicate that their bases are typically located at ∼50 km altitude, but can be as low as ∼31 km or lower *Sentman et al.* [1995]; *Winckler* [1995]; *Lyons* [1996]. It will be shown in Chapter 5 that the tendril region of sprites is composed of downward-developing positive streamers. Theoretical models of positive streamer development under the influence of a 350 C·km (+CG) parent discharge predict a terminal altitude of ∼48 km [*Raizer et al.*, 1998]. Increasing the charge moment change to 1000 C·km results in a lower terminal altitude of ∼40 km *Pasko et al.* [2000]. These altitudes are in rough agreement with those observed. The terminal altitude of streamers will, of course, be even lower under the influence of the much larger daytime charge moment changes.

Assuming that the minimum altitude drops at least another 10 km when the charge moment change is increased from 1000 C·km to 3900 C·km (corresponding to the weakest event), then the vertical extent of the sprite will be at least 32 km for an ionosphere height of 62 km. Thus, the maximum charge transfers within the 2800, 1200, and 910 C·km sprite events would be 88, 38, and 28 C respectively. These charge transfers are much larger than the 5-6 C previously estimated for a couple of nighttime sprite ELF signatures, but are comparable to the ∼42 C estimated for an unusual long-duration nighttime sprite ELF signature [*Cummer et al.*, 1998].

Chapter 5

High-speed Video Observations of Sprites

5.1 Introduction

In early October 1997, a high-speed light-intensified camera system was operated at Langmuir Laboratory, NM to observe sprite phenomena. Frame rates of either 1000, 2000, 3000, or 4000 s^{-1} were used to capture the development sequence of 42 separate sprite clusters at estimated ranges of 200-900 km. Electric field, magnetic field, and photometric data were obtained of the parent discharges and the sprites.

The characteristics of the initial 2-3 ms of sprite development observed on high-speed video were summarized by *Stanley et al.* [1999]. The total charge moment change calculated from magnetic field measurements was compared with high-speed observations of sprite development by *Cummer and Stanley* [1999]. Finally, the spatial development of diffuse luminous events observed on high-speed video was compared with theoretical predictions of quasi-electrostatic heating by *Barrington-Leigh et al.* [2000]. The primary purpose of this chapter is to document high-speed video results in more detail (and for more examples) than was possible in the above publications.

5.2 October 7, 1997

5.2.1 Storm Development

Shortly after 18:00 UT on October 6, 1997, scattered thunderstorm cells formed along a roughly north-south corridor to the east of the Rio Grande in central New

Mexico. Some of the cells clustered together, particularly in southern New Mexico, but the storms were not well organized as a whole. The storms in southern New Mexico organized into a mesoscale convective system (MCS) after 23:00 UT. The line of convection advanced eastward and was still active at 01:30 UT on October 7, as shown in Figure 5.1 by the line of –CG activity.

Figure 5.1 shows that the convective line became less active after 02:30 UT with only infrequent –CG strokes occuring by 04:30 UT. In contrast, the +CG activity increased after 02:30 UT, particularly in the region behind the northern half of the line where significant –CG activity was located much earlier (not shown). These +CGs were centered ∼300 km away from the observation site at Langmuir Laboratory. The weak amplitude +CGs prevalent throughout the time period are probably IC events, as discussed in Section 3.4.

It was shown in Chapter 3 that sprite-producing +CGs were situated near the periphery of a sprite cluster in a Florida MCS. The center of the sprite clusters were generally located at a greater plan distance from the convective cells than were the +CGs, a fact which was attributed to the outward motion of the negative leaders and the decay of older channels. Thus, one can obtain a rough estimate of where the sprite clusters will be located in relation to their parent +CGs by comparing the +CG locations with the convective cell locations indicated by the −CG activity. The sprite-producing flashes analyzed here occurred between 03:00 and 04:00 UT. The +CGs were situated primarily to the northwest of the convective line. The observation site at Langmuir Laboratory was situated to the west-northwest of the +CGs, so it follows that the sprites will tend to appear both to the left of the +CGs and at a closer range. This latter effect will result in a systematic increase in height estimates obtained from the plan location of the NLDN CG data, relative to actual heights. This will be further demonstrated in this section by comparing sprite terminal altitudes estimated from the NLDN plan location with previous triangulated measurements of terminal altitudes.

5.2.2 Observations

Normal-speed low-light-level video recordings began at 02:24:24 UT. The sferic data acquisition system started recording at 02:25:04 UT. The 3-channel sferic data was comprised of 8-bit magnetic field, 12-bit photometer, and 12-bit fast antenna electric field data sampled at 500 kHz. A bipolar-amplitude threshold on the fast antenna data was used to trigger the system. The pre- and post-trigger lengths were set at 3

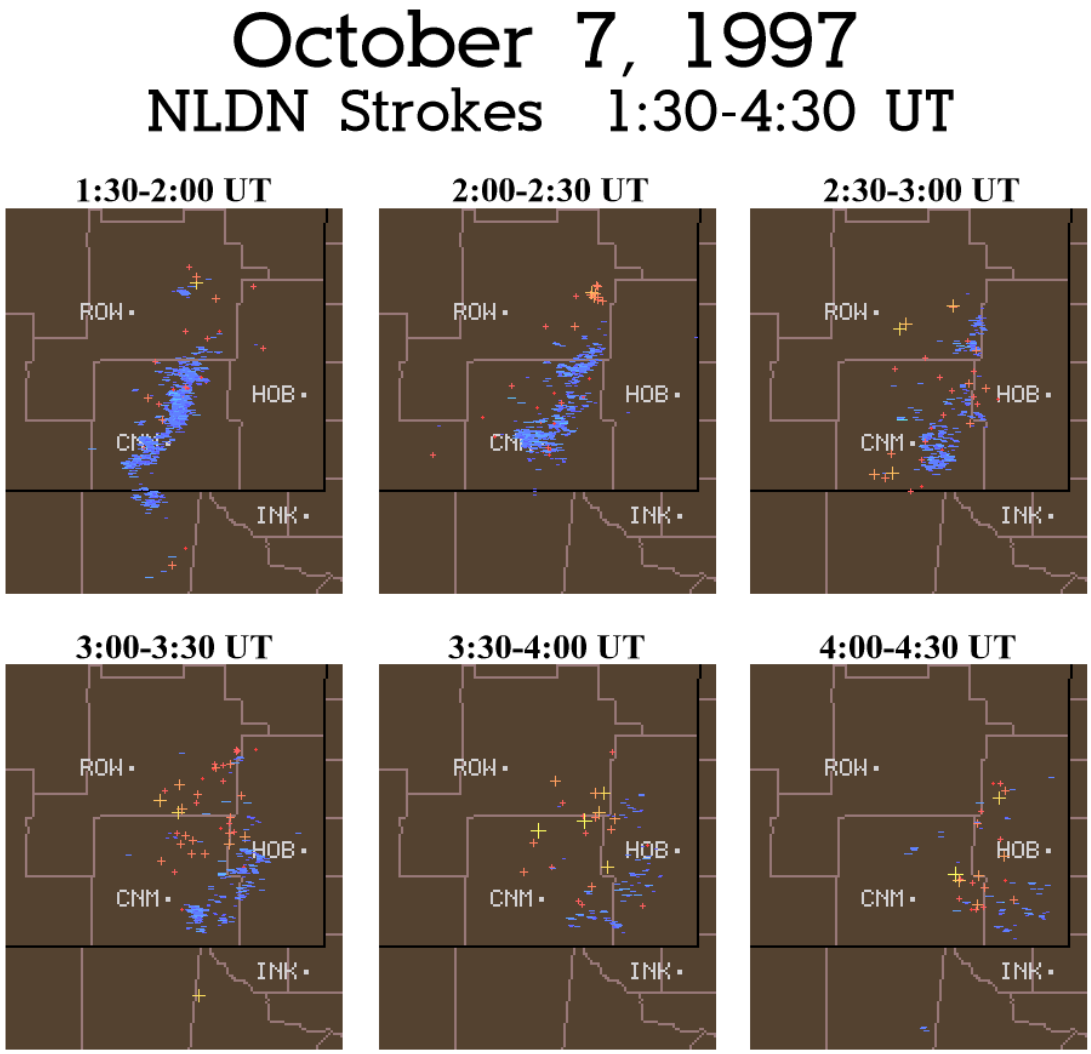

Figure 5.1: NLDN stroke data for southeast New Mexico between 01:30 and 4:30 UT on October 7, 1997. A line of convective cells, marked by –CG activity, decayed throughout the time interval. A significant number of sprite events were associated with the +CGs which trailed primarily behind the northern half of the convective line after 02:30 UT. The brighter colors and larger symbols correspond to larger peak current magnitudes.

and 9 ms respectively. The data were also recorded continuously at 10 kHz.

Unfortunately, the magnetic loop antenna was not oriented to the proper azimuth for an optimal signal-to-noise level for the sprite-producing +CG activity. Rather, the loop remained in an orientation used on the previous day for +CGs to the south-southwest (see Section 5.3). Since the +CGs on this day were situated to the east-southeast, they were close to the null in the loop's reception pattern. The adverse effect of the improper orientation was alleviated by the fact that the vertical electric field is proportional to the magnetic field tangential to a circle around the source at long distances (within the "radiation zone") and thus provides the same information. The magnetic field instrument had a better signal-to-noise ratio at low frequencies when it was properly oriented (due, perhaps, to the lack of static field contamination from local space charge which effects only the electric field). Charge moment change measurements derived from ELF magnetic field data are shown in Section 5.3 for sprite events on another day.

The photometer monitored a wide region of sky above the MCS. The photometer was high-pass filtered above $\sim$600 nm in order to improve the signal-to-noise ratio for the sprites relative to the parent discharge by capturing the dominant sprite emissions from N_2 first positive bands between 600-760 nm [*Mende et al.*, 1995; *Hampton et al.*, 1996]. The signal-to-noise ratio was further improved by positioning a horizontal slit in front of the photometer so that the sprites would be observed through the slit while light escaping from the thundercloud would be rejected. In spite of these precautions, light scattered through the atmosphere from the discharge still reached the photometer, though the scattering was greatly reduced from what it would have been.

The high-speed video system was armed shortly after the sferic system began recording. The high-speed video system was manually triggered after sprite events were observed on normal-speed video. A total of 23 triggers were obtained with the first being at approximately 02:39:56 UT and the last at 04:50:57 UT. Of these 23 high-speed video records, just over half (12) were obtained at 2000 frames/second while the remainder were obtained at 1000 frames/second. Seven of the 23 video records did not contain sprites due to improper camera orientation, a late manual trigger, or perhaps unusually dim sprites. Of the remainder, some contained multiple sprite clusters. The total number of sprite clusters observed on October 7 was 24, which is over half of the 42 total sprite clusters observed by the high-speed camera in this work.

5.2.3 03:03:59 UT, 2000 frames/second

The fourth high-speed video trigger on October 7 was obtained at 03:03:59 UT. It was also the first trigger on the 7th to successfully capture a sprite. The observations were of a cluster of carrot sprites at a video rate of 2000 frames/second. The sprites were associated with a 30 kA +CG at 332 km range. Development of the cluster is shown in Figures 5.2-5.3.

The start of light integration for the first frame (Figure 5.2a) was at 03:03:59.8067 UT. The integration of light in the frame is not performed simultaneously, as discussed in Appendix B.4.2. Rather, a video frame recorded at 2000 frames/second is composed of 6 horizontal blocks each of which is integrated discretely.

Figure 5.4 shows the first four frames of the sprite cluster development (Figures 5.2a-d) with the pixel intensities stretched such that faint sprite features are readily visible. The horizontal lines correspond to the location of block boundaries, with the uppermost block (block 1) excluded from the images. The block boundary locations will factor into the velocity estimates of vertical sprite development, since the time elapsed between frames depends on the block number. The start and stop times of light integration for the high-speed video blocks is shown in Figure 5.5 relative to electric field and photometer data. Frame *a* is delayed by $\simeq$4 ms after the +CG.

Seven distinct sprites formed within the first four frames. The sprites are labeled from left to right in frame *d* of Figure 5.4. The vertical bar denotes altitude in kilometers MSL directly above the parent +CG stroke with the tick marks indicating 10 km height intervals.

Sprite D apparently formed first, as evidenced by the single sensor pixel illuminated in the first frame. If the plan distance to the sprite were the same as to the parent +CG, then this luminous spot would have been at an altitude of 79.3 km MSL. The maximum altitude of sprite D would have been $\simeq$98 km MSL (see frame h of Figure 5.2) if the sprite was located at the same plan location as the +CG. Triangulation studies of sprites indicate that the maximum altitude generally does not exceed $\simeq$93 km MSL [*Sentman et al.*, 1995]. Thus, it is likely that the plan location of sprite D was closer than that of the +CG. In Chapter 3, an upper terminal altitude of 87 km MSL was used to determine the most likely range of sprites. The 03:03:59 UT sprites were brighter than average, so the terminal altitude was probably higher than 87 km. Unless stated otherwise, the height and velocity estimates in this section will be based on the assumption that the terminal altitude of each sprite was

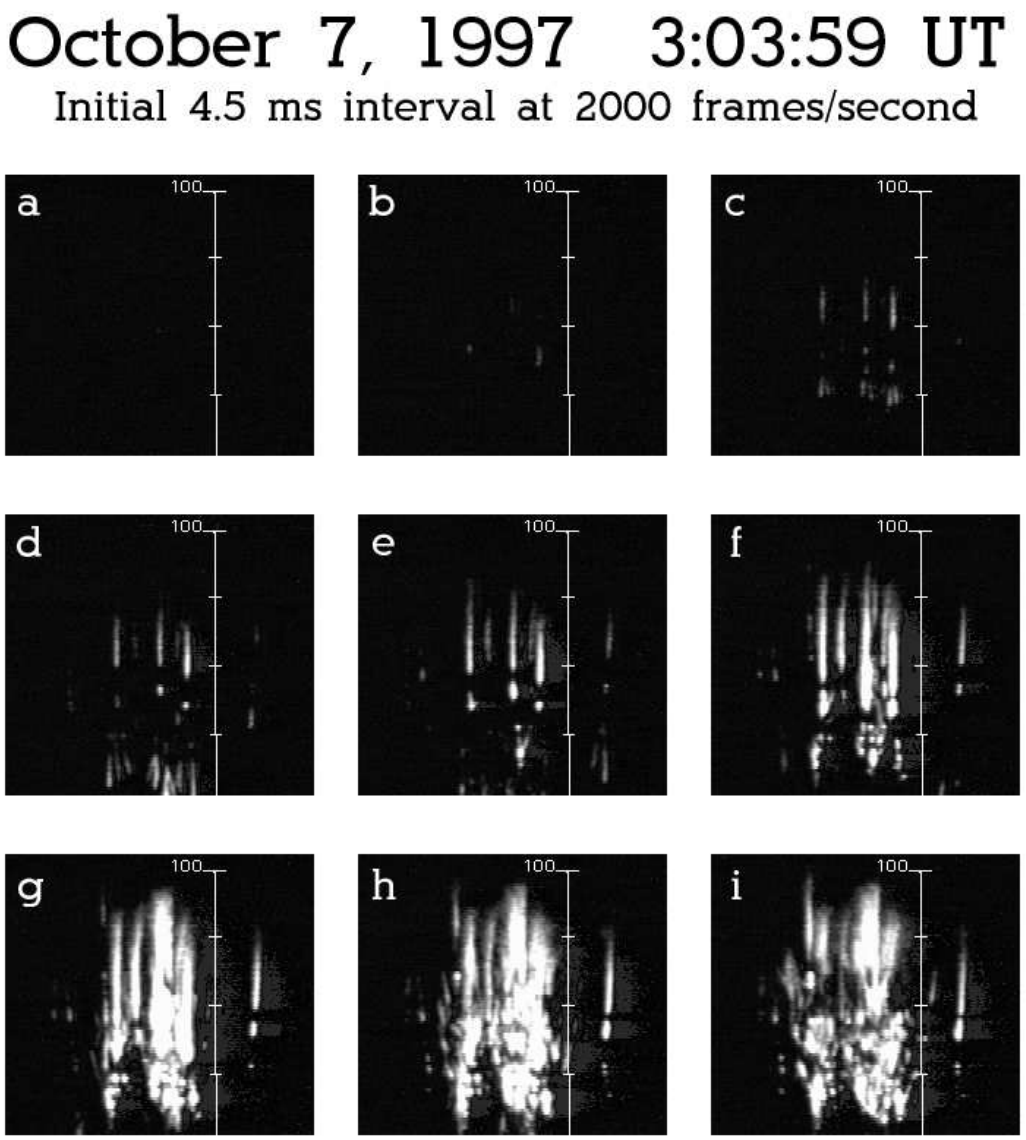

Figure 5.2: Initial development of a cluster of carrot and columniform sprites, at a speed of 2000 frames/second. The sprites initiated at different times within the first several frames and all began with a columniform shape, the downward (positive streamer) portion of which often split into tendrils. An upward divergent carrot shape began to emerge in some of the sprites as negative streamers were initiated in the latter frames from regions through which the positive streamers propagated. The vertical bar denotes the altitude in kilometers directly above the parent +CG, with tick marks corresponding to 10 km height intervals.

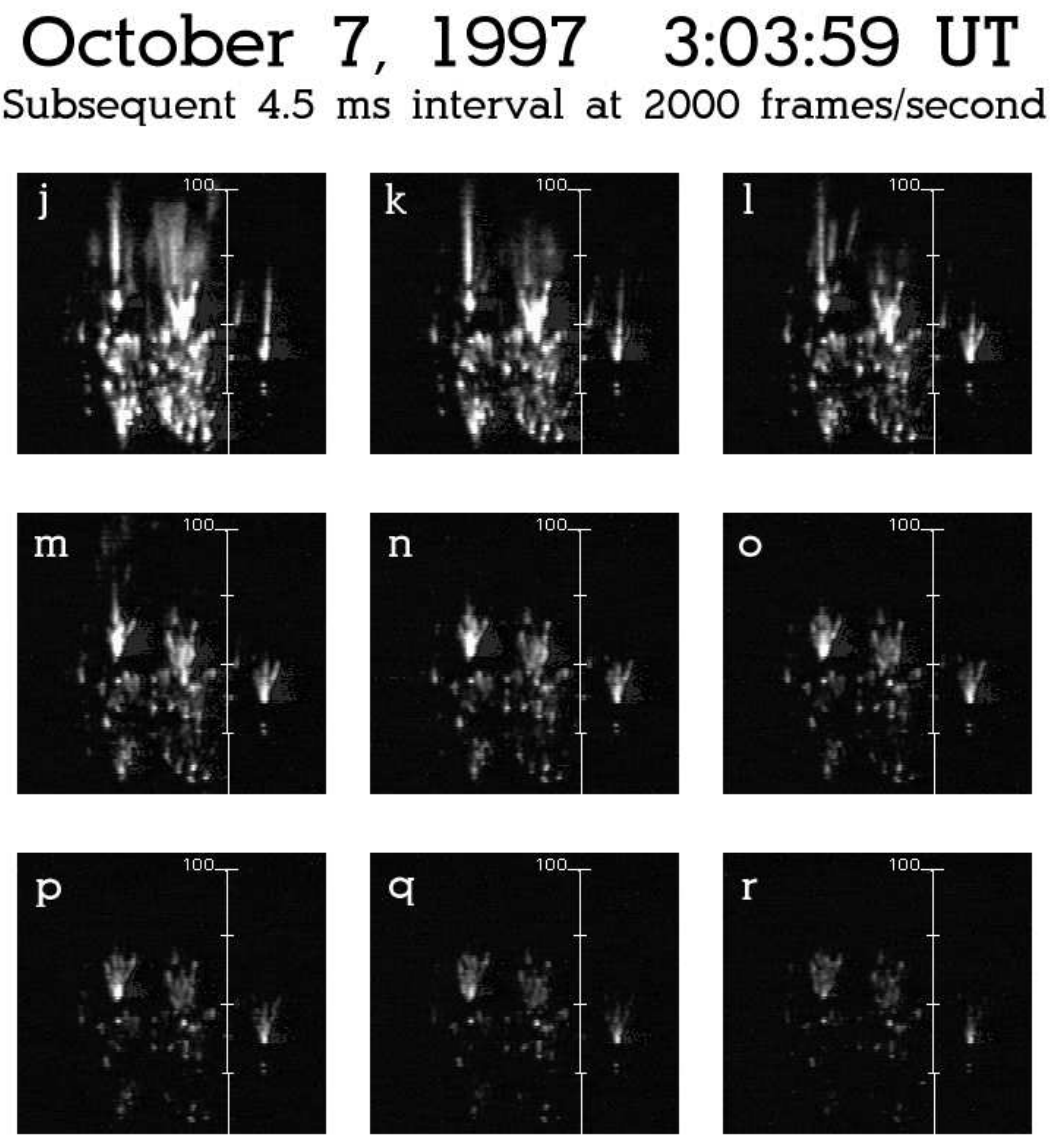

Figure 5.3: Continued development of the carrot and columniform sprite cluster of Figure 5.2. Additional upward developing streamers are evident in frames j-m. All of the sprites gradually decayed after frame m.

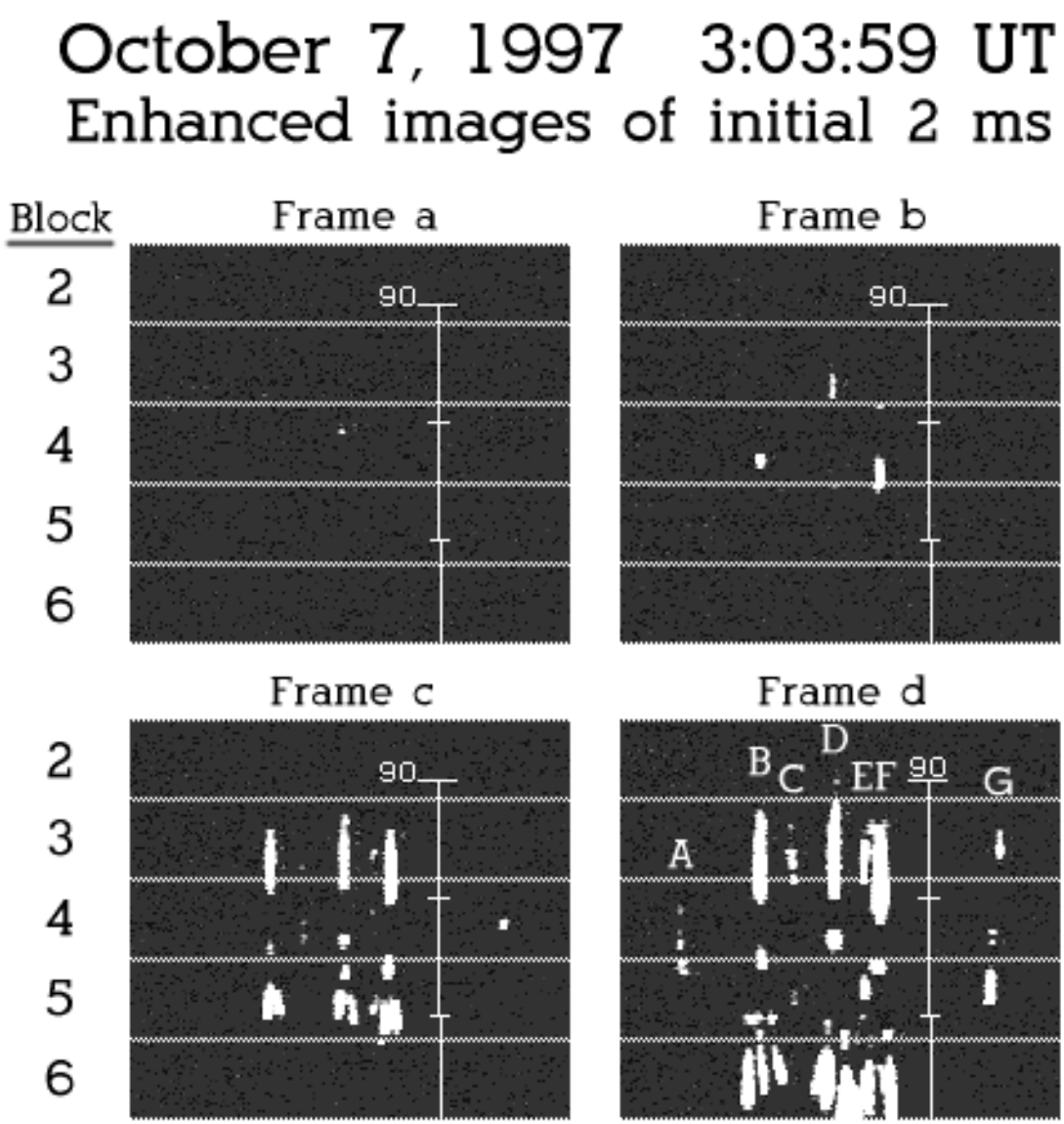

Figure 5.4: Image sequence corresponding to Figures 5.2a-d, with the pixel intensity modified to emphasize fainter features. The block boundary locations are indicated by the horizontal bars. The seven sprites which are visible by frame *d* are denoted with letters. The center sprite, D, was the first to form, as evidenced by the single camera pixel illuminated in frame *a*. All of the sprites developed simultaneously upwards and downwards, and tendrils branched downwards from sprites B, D, and F.

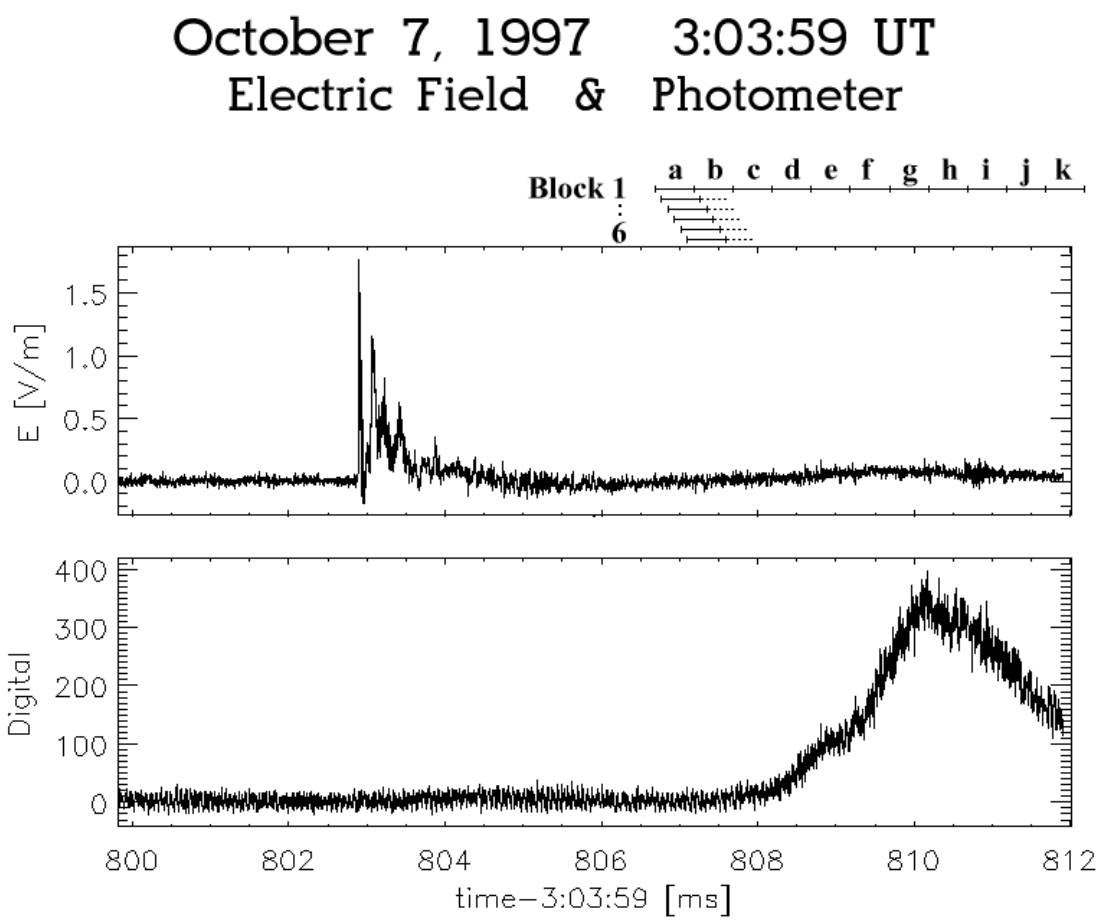

Figure 5.5: The electric field and photometer data for the 03:03:59 UT event. The photometer signal is coincident with a small-amplitude slow electric field change. The start and stop times are shown for the different light-integration blocks (see Appendix A.1) of frames in Figures 5.2-5.3.

$\simeq$90 km MSL.

The range to sprite D would have been 306 km for a 90 km MSL terminal altitude. With this assumption, the plan location of the sprite would have been at least 26 km away from the parent +CG stroke location. This is a reasonable distance since triangulated measurements of sprites show that their plan location can be as far as $\simeq$50 km away from the parent +CG [*Lyons*, 1996; *Wescott et al.*, 1998] (also see Chapter 3).

The initial luminosity from sprite D was at $\simeq$72.9 km MSL altitude. The sprite developed both upward to $\simeq$78.0 km MSL and downward to $\simeq$68.4 km MSL in frame *b* with the minimum altitude barely visible as a single illuminated sensor pixel at the top of block 5. The maximum altitude of the sprite in frame *b* was one block higher than the starting point in frame *a*. Thus, the time elapsed for the upward development was $((6-1)/6) \times 0.5 = 0.417$ ms. The average upward development velocity of sprite D in frame *b* was therefore $((78.0-72.9) \times 10^3)/(0.417 \times 10^{-3}) = 1.2 \times 10^7$ m/s. The minimum altitude was one block lower than the starting point with a time elapsed for downward development of $((6+1)/6) \times 0.5 = 0.583$ ms. The average downward development velocity of sprite D in frame *b* was therefore $((72.9-68.4) \times 10^3)/(0.583 \times 10^{-3}) = 0.77 \times 10^7$ m/s.

Sprite D continued to develop bidirectionally into frame c, extending up to about 80.0 km MSL altitude and down to about 63.7 km MSL in the right tendril branch (about 64.1 km MSL for the left). Sprite D's average upward development velocity in frame *c* was therefore 0.40×10^7 m/s while its average downward velocity was 0.94×10^7 m/s. The average downward velocity estimate does not factor in the slight non-vertical motion of the tendril, the radial component of which can not be determined without triangulation.

The average downward velocity increased from frame *b* to frame *c* while the average upward velocity decreased by a factor of three. The increase and magnitude of the downward velocity is roughly consistent with the theoretical predictions of positive streamer velocities in sprites by *Raizer et al.* [1998] for a similar altitude extent.

In frame *d*, sprite D extended up to $\simeq$82.8 km MSL altitude while the right main branch of tendrils had extended below the field of view at $\lesssim$56.6 km MSL altitude. The average downward velocity for the right main branch of tendrils would have been $\gtrsim 1.2 \times 10^7$ m/s. The average downward velocity for the left main branch of tendrils, which was still completely in the field of view, was 1.2×10^7 m/s. Thus, the right main branch of tendrils may have extended only slightly below the field of view. The

average downward velocity in frame *d* was greater than in frame *c* and is the same as the maximum velocity of 1.2×10^7 m/s predicted by *Raizer et al.* [1998] for a similar total altitude extent.

Sprite B developed in a similar fashion as sprite D. Sprite B was first visible as three illuminated pixels in a vertical column in frame *b*. The altitude extent of this region was $\simeq$72.6-73.6 km, consistent with the $\simeq$72.9 km MSL origin of sprite D which was also determined on the assumption of a $\simeq$90 km MSL terminal altitude. In contrast, the altitude derived from the range to the +CG would have been 76.2-77.2 km MSL, at least 2 km lower than the sprite D origin of 79.3 km MSL based on the same range.

The upward developing component of sprite B reached $\simeq$81.8 km in frame *c* with an average velocity of 2.0×10^7 m/s, significantly faster than the average initial upward velocity of sprite D in frame *b*. The downward-developing component of sprite B reached $\simeq$66.5 km MSL altitude on the left tendril branch in frame *c* with an average downward velocity of 1.0×10^7 m/s. This velocity is comparable to the average downward velocity of sprite D (0.94×10^7 m/s) in the same frame, in spite of the delayed appearance by one frame of initial luminosity for sprite B relative to sprite D.

In frame *d*, the upper extent of sprite B was at $\simeq$83.4 km altitude while the lower extent was at $\simeq$59.3 km. The corresponding average velocities were 0.32×10^7 m/s and 1.2×10^7 m/s, respectively. The downward development velocity was essentially identical to that of sprite D in the same frame.

The pattern of development of the other sprites was similar to sprites B and D. All of the sprites appeared to develop bidirectionally from the first frame to the next. This development pattern is consistent with bidirectional streamer growth observed in laboratory experiments and predicted by theory (see Section 2.6.1).

The downward development velocites were similar for all of the sprites and did not exceed 1.2×10^7 m/s. The maximum velocity was consistent with the theoretical predictions of *Raizer et al.* [1998] for the maximum velocity of a downward-developing positive streamer under the influence of a 350 C·km parent discharge. The downward developing tendrils also exhibited short persistence between adjacent frames. The short persistence will be explored in more detail in Section 5.2.5 for a sprite cluster with unusually bright tendrils.

The maximum upward average velocity of sprite bidirectional development was usually obtained in the second frame (the first possible frame for an average velocity

measurement). These initial upward development velocities varied considerably from sprite to sprite, as was already demonstrated by intercomparing sprites B and D. The upward development velocity slowed down considerably after attaining an altitude of ~81 km, which is consistent with the predicted altitude for the base of the ionosphere (Section 2.4.4). However, the continued advancement above this altitude is difficult to understand conceptually, particularly in light of the significant minimum electric field required to sustain negative streamer propagation (see Section 2.6.2).

The spatially-integrated luminosity of initial sprite development in frames *a* and *b* was below the detection threshold of the photometer (Figure 5.5). This demonstrates that a photometer may not give a reliable estimate of when sprites are initiated. This difficulty is further compounded by the fact that sprites within a sprite cluster often do not appear simultaneously. Rather, sprite appearance can be spread out over several milliseconds, as was the case here. Another (initially faint) sprite appeared in frame *e* to the left of sprite A while two more sprites appeared in frame *f*, one just to the left of sprite B while the other was between sprites F and G. There may also have been additional sprites which formed behind the main cluster of sprites (B-F) after frame *d*.

The tendrils of sprites B, D, and F propagated downward out of the field of view in Figure 5.2e. A tendril segment above a branch point brightened significantly in frame *e* on sprite D's right main tendril branch. The lower columnar portion of sprite B brightened and also bulged outward on the right side. This bulge probably was the beginning of an inferred negative streamer which propagated upward and to the right in frame *f*.

Additional tendril segments brightened in frame *f*. A striking feature is that the brightening occurred in the form of regularly spaced beads. Such beads were previously observed on tendrils by *Mende et al.* [1999]. The tendril segments which brightened first on sprites B, D, and F were also the segments which propagated the furthest downward in frame *d* relative to other segments associated with the same sprites (Figure 5.2d). A speculative possibility is that the lower altitudes (and faster propagation speeds) of the positive streamers were also associated with higher currents in the channels and this led to the subsequent brightening. However, it is not known how this could have produced a regular spacing of beads.

The development of sprite B through frames *e*-*j* is shown in Figure 5.6. In this sequence, sprite B transitioned from a columniform sprite with tendrils to a carrot sprite, which is characterized by an upward-divergent "V" shape above downward-

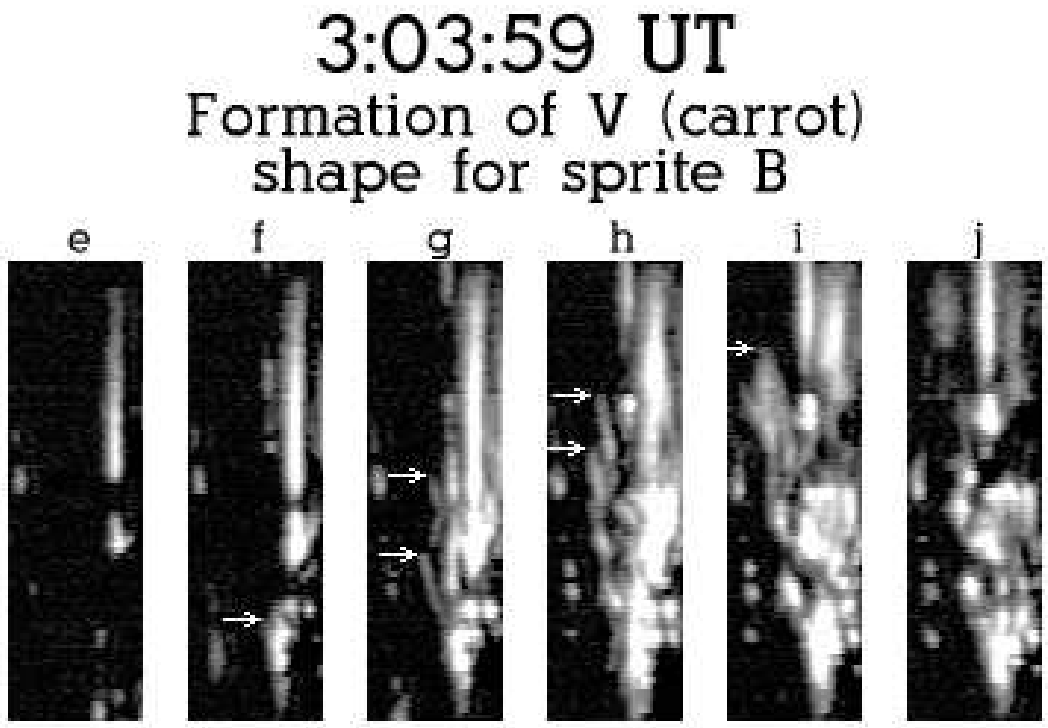

Figure 5.6: The formation of a V (carrot) shape for sprite B (see Figure 5.4). Inferred negative streamers are spawned from regions through which positive streamers propagated earlier. The upward-development of a couple of negative streamer groups for which average velocities (see text) were obtained are denoted with arrows.

divergent tendrils. The sequence shows primarily the development on the left side of sprite B, since sprite C obscures much of the development on the right.

In frame f of Figure 5.6, an inferred negative streamer began its upward-propagation from the left tendril branch of sprite B. The arrow in frame f denotes the streamer's tip location, which was at $\simeq$65.5 km MSL altitude. The streamer propagated up to $\simeq$69.9 km MSL (lower arrow) in frame g at an average angle of 24° from vertical. The corresponding average velocity of propagation was 0.97×10^7 m/s if there was no radial component. The average velocity would have been somewhat greater if there was a radial component. This streamer continued its upward propagation in frame h at a reduced angle relative to vertical and had split several times. The uppermost tip is denoted by the lower arrow in frame g at an altitude of $\simeq$76.8 km MSL. The corresponding average velocity of upward-propagation was 1.7×10^7 m/s, which was significantly greater than the average velocity in the previous frame.

The negative streamer continued its upward-development into frame i to an altitude of $\simeq$84.2 km MSL (see arrow). The average streamer velocity of 1.8×10^7 m/s in frame i was only slightly greater than in frame h. The width of the streamer increased noticeably in frame i and this is even more pronounced in frame j. This expansion may be associated with penetration of the streamer into the ionosphere above $\simeq$81 km MSL. The streamer reached a terminal altitude of $\simeq$89.8 km MSL in frame j with an average velocity which would have been greater than 1.3×10^7 m/s.

The inferred negative streamer which presumably originated within the column reached an altitude of $\simeq$75.0 km MSL (upper arrow) in frame g. The point of origin is difficult to determine due to the development of foreground tendrils from a sprite which originated in frame f just to the left of sprite B. However, the point of origin is likely correlated with the bulge at $\simeq$70.7 km MSL. This bulge is opposite the origin of the inferred negative streamer which originated in frame e and propagated to the right and upwards. The leftward streamer propagated up at an average angle of 35° relative to vertical and an average velocity which would have been greater than 1.3×10^7 m/s. This streamer continued up to an altitude of $\simeq$80.9 km MSL (upper arrow) in frame h at an average velocity of 1.4×10^7 m/s and terminated at a slightly higher altitude in frame i.

Numerous negative streamers initiated and developed in frames e-m of Figures 5.2-5.3. The formation of negative streamers in each sprite was not simultaneous across the cluster, but was staggered in rough accordance with the different initiation times. The negative streamer velocities were similar to those reported above.

5.2.4 03:40:37 UT, 1000 frames/second

A 42.5 kA peak-current +CG occurred at 3:40:37.832 UT. Figure 5.7 shows the development of a cluster of columniform sprites which were produced by the +CG. The apparent initiation of a couple of sprites in frame a was delayed by $\simeq$ 2-3 ms after the +CG. Based on the height above the +CG (shown in 10 km increments), the sprite 2 luminosity in frame a was between 77.3 and 78.2 km MSL altitude. Sprite 2 appeared to reach an upper terminal altitude of about 88 km in frame d based on the height above the +CG. Assuming an upper terminal altitude of $\simeq$ 87 km [*Wescott et al.*, 1998] would shift the apparent initiation altitude down by only $\simeq$ 1 km to 76-77 km.

Sprite 1 reached an apparent upper terminal altitude of about 94 km MSL in frame d based on the height above the +CG. Assuming an upper terminal altitude of $\simeq$ 87 km MSL, the initial luminosity of sprite 1 in frame a was between 78.1 and

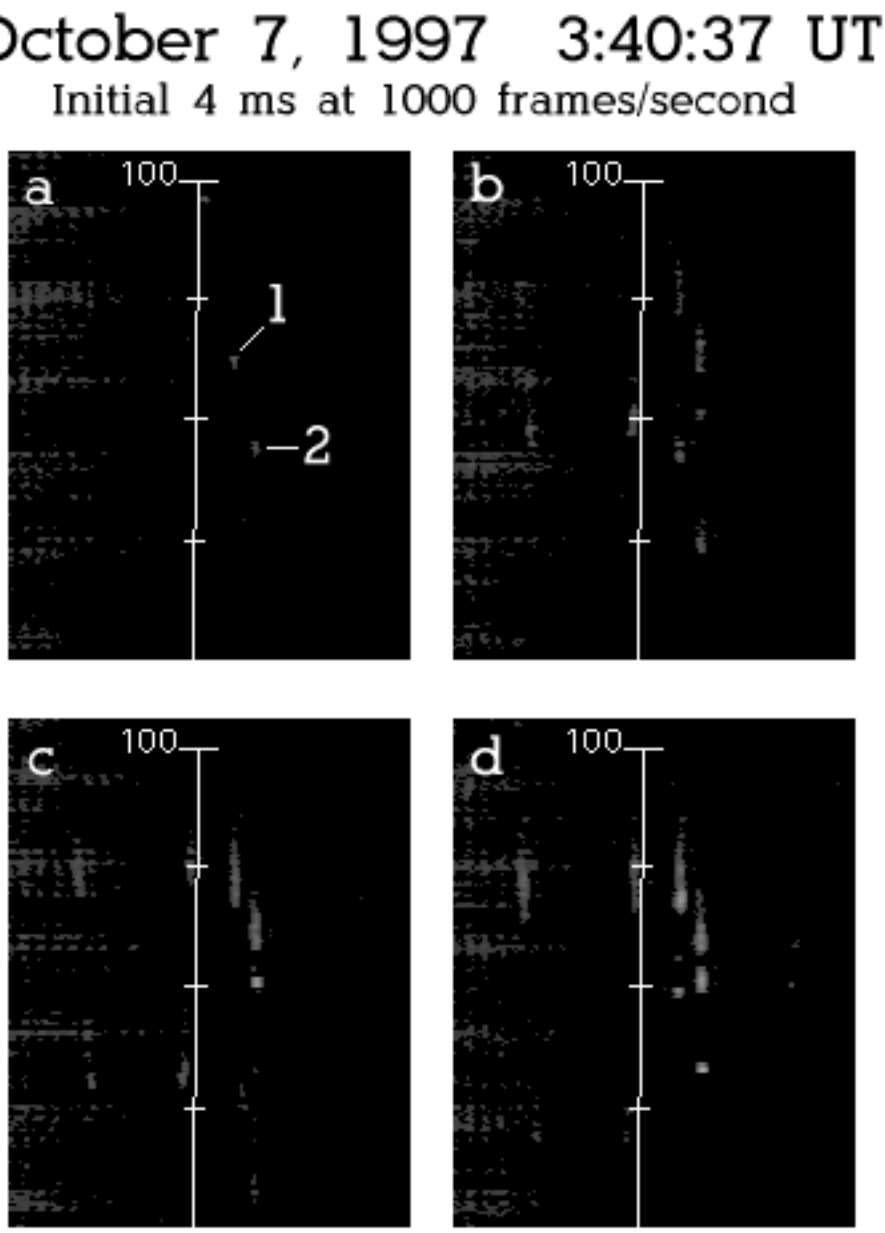

Figure 5.7: Initial 4 ms of the development of a cluster of columniform sprites. A couple of sprites initiated in the first frame and extended bidirectionally upward and downward in the second frame. The horizontal streaks at left are artifacts at the left edge of the camera sensor.

79.0 km MSL altitude. This is about 2 km higher than the initial luminosity of sprite 2 (for the same terminal altitude). However, the heights based on an upper terminal altitude of 87 km for the sprites are in better agreement than the heights obtained relative to the +CG, which differ by about 7 km. An initiation height of 76–79 km MSL was found to be typical of most sprites in this study.

Sprite 2 developed downward to 69.5 km MSL altitude in frame *b* at an average velocity of 0.72×10^7 m/s. It developed further downward to a lower terminal altitude of 62.8 km MSL in frame *c*. The minimum downward velocity in frame *c* was 0.62×10^7 m/s. The downward velocities of the other sprites in the cluster were very similar. These velocities are less than predicted by *Raizer et al.* [1998] and were also less than the average velocities shown for the 3:03:59 UT sprite cluster, which appeared to initiate at a lower altitude of about 73 km MSL (Section 5.2.3).

5.2.5 03:40:38 UT, 1000 frames/second

Figure 5.8 shows high-speed video observations obtained at 1000 fps of a cluster of columniform and angel sprites that occurred at 03:40:38 UT. These sprites were associated with a 116 kA peak-current +CG at 298 km range. The +CG was probably associated with the same flash which produced the 03:40:37 UT +CG and sprite cluster. The vertical bar in Figure 5.8 is plotted directly above the +CG location and shows the height in km above sea level. The height estimates may be somewhat in error because the radial distance of the sprites from the CG plan location is not known. A radial displacement of 40 km would result in a vertical error of about 10 km.

From the time-correlated field change measurements, the beginning of the frame (top block) in Figure 5.8a was 0.44±0.05 ms prior to the arrival time of the return stroke pulse at the observation location (see Figure 5.9). Several luminous regions and columns, many of which are paired, are visible in the first frame at inferred heights between 70 and 88 km.

The column pair just left of the height bar in Figure 5.8a have vertical extents of about 8 km. Taking into account the time it takes the return stroke field change to arrive at the altitude of the top of the columns ($\frac{85\ km}{3\times10^5\ km/s} \simeq 280\ \mu s$), the longer line-of-sight light travel time from the sprites than from the return stroke ($\frac{\sqrt{298^2+85^2}-298\ km}{3\times10^5\ km/s} \simeq 40\ \mu s$), and the video scan information (the top of the columns are within the 5th video block, the start of which is delayed by (5-1)×83 μs $\simeq$ 330 μs from the start of the uppermost video block), the columns were initiated within

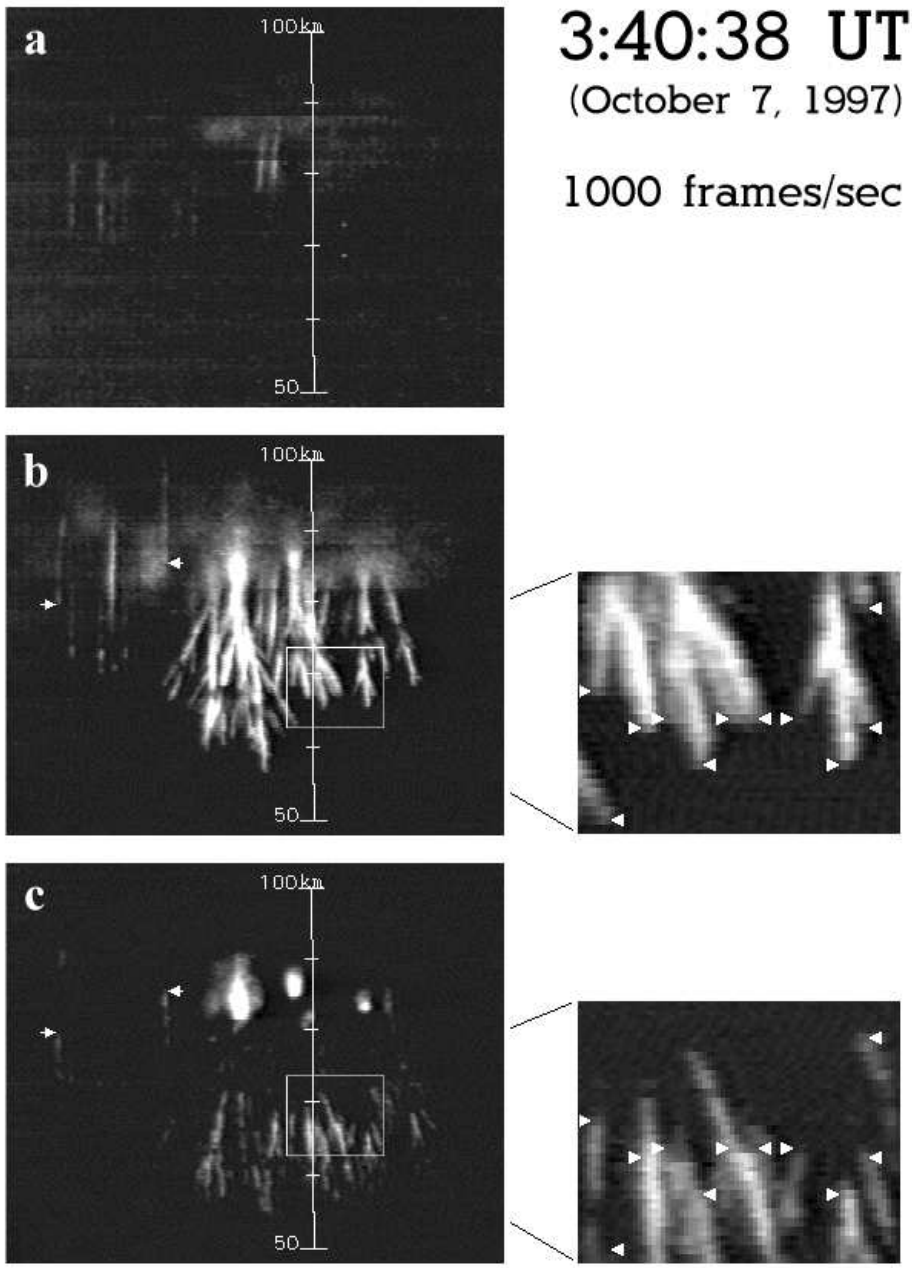

Figure 5.8: Initial frames of 1000 fps sequence for a cluster of angel and columniform sprites. The short persistence indicative of emissions dominated by electron impact ionization in streamer heads is evident for both the columns and tendrils which propagated downwards between frames, as denoted by the arrows in both the overall sequence (left) and expanded images (right). The limiting horizontal and vertical resolution is 400 m.

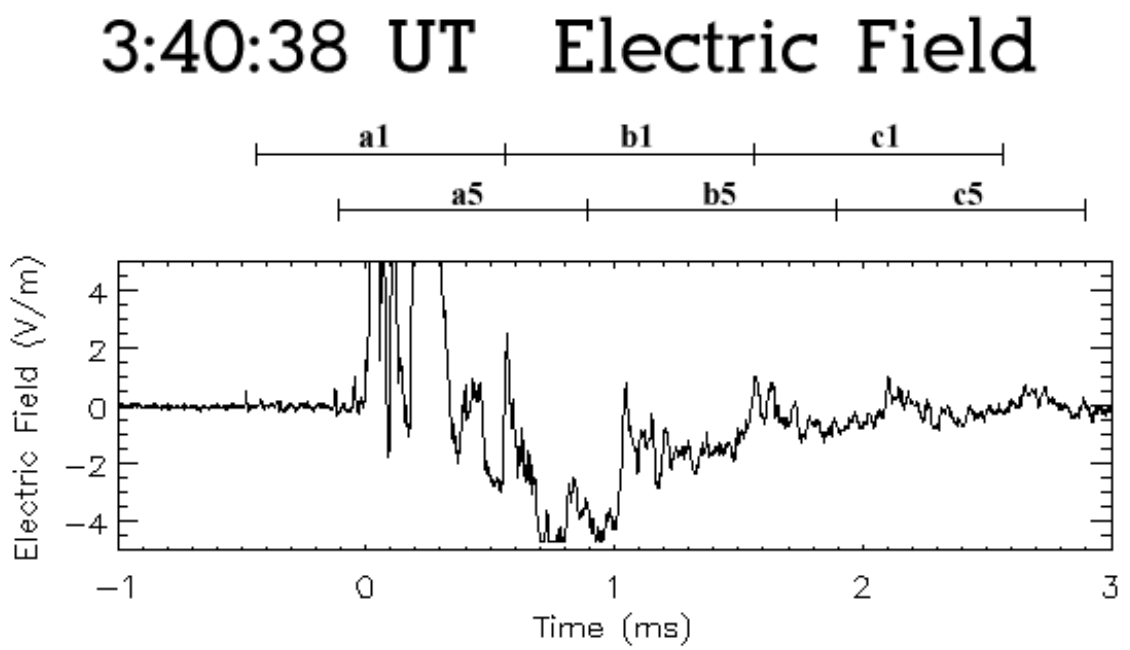

Figure 5.9: The 03:40:38 UT +CG electric field waveform. The horizontal bars correspond to the light integration periods for the 1st and 5th video blocks in the first three frames.

$(-0.44+1)+0.33-0.28-0.04 \simeq 0.57$ ms of the arrival of the return stroke pulse at altitude. Since the base of the columns extend down into the next video block, the minimum speed for purely downward development would be about $\frac{8\ km}{(570+83)\mu s}$ = 1.2×10^7 m/s. The minimum speed would be somewhat higher for upward development (due to the video scan nature) and less for the upward and downward components of bidirectional development. The similarity of the minimum velocity estimate to other velocity estimates presented in this work may indicate that the initiation of the sprites in Figure 5.8a occurred well within 0.57 ms of the return stroke.

The columns seen in the first video frame (Figure 5.8a) were in some instances brighter in the second frame (Figure 5.8b) and showed some downward development. However, the well-developed angel sprites of the second frame were not associated with detectable columns in the first frame. Rather, at least two of the angel sprites developed downwards from enhanced luminous regions visible in the first frame.

The surrounding diffuse luminosity is probably a diffuse sprite caused by conventional breakdown, as will be shown in Section 5.3.3 for a similar sprite cluster.

Further evidence for this is provided by velocity measurements which will be shown below. The enhanced luminous regions may have been enhanced ionized regions with a sufficient density and geometrical separation of space charge required for streamer formation as described by *Raizer et al.* [1998].

In the third video frame (Figure 5.8c), the heads of the angel sprites are still luminous while the tendrils are only luminous in their downward-developing lower extremities. An expanded view of the base of the tendrils in the boxed region is presented to the right of Figure 5.8b-c. The arrows denote the lower extent of each tendril for the second frame. All but two of the tendrils propagated downward during the third frame with no significant persistence indicated at the 400 m vertical resolution of the camera system, while the two exceptions appear to be accompanied by minor persistence (these may also be a chance superposition of a foreground and background tendril). A general lack of persistence can also be seen in the overall picture of Figure 5.8b-c for the lower portion of a couple of downward developing columns (arrowed). On sufficiently short time scales, a streamer's luminosity will be dominated by emissions associated with electron impact ionization in the propagating tip [*Pasko et al.*, 1998a; *Raizer et al.*, 1998]. The lack of persistence clearly indicates that both tendrils and the lower part of sprite columns are propagating events with visual characteristics identical to that of streamers. The downward direction of development would be in the same direction as the quasi-electrostatic field created by a positive CG (which, in effect, places negative charge into the cloud) and hence the streamers would be of positive polarity.

The most developed of the angel sprites in the second frame had a vertical extent of about 28 km and developed at an apparent minimum velocity of 2.0×10^7 m/s. This velocity is much greater than the average velocities reported for the tendrils of the 03:03:59 UT sprite cluster. The higher velocities would be consistent with a larger charge moment change parent discharge [*Raizer et al.*, 1998], which provides further evidence that the diffuse luminosity may be due to conventional breakdown at high altitude.

The brightness of the head of the sprites at an inferred altitude of 80-90 km underwent a gradual decay into later frames (not shown). This decay was observed for about 53 milliseconds.

5.3 October 6, 1997

5.3.1 Observations

Early on October 6, 1997, a horizontally-extensive region of thunderstorm activity was producing frequent -CG activity over Mexico. Significant +CG activity was noted at ∼02 UT and persisted for several hours until ∼06 UT. Initially, the +CG activity was at a range of ∼650 km, but the range increased to ∼900 km by 05 UT. The first high speed video trigger of a sprite event was obtained at 02:20 UT while the last was obtained at 05:55 UT. The high speed video camera was initially operated at 2000 frames/second. The frame rate was increased to 3000 frames/second prior to a 04:52 UT trigger and was further increased to 4000 frames/second prior to a 05:11 UT trigger.

A total of 16 sprite clusters, some less than a second apart, were sucessfully captured by the high speed video camera on October 6. Of the 16, 10 were obtained at 2000 frames/second, 4 were at 3000 frames/second, and 2 were at 4000 frames/second.

Normal-speed low-light-level video recordings began at 02:23:40 UT. Unfortunately, the VHS tape on which the recordings were made reached its end at 03:15:45 UT and this was not noticed until over an hour later. During this time period, the orientation of the high speed video camera could not be determined (see Appendix B.3). At 04:25:25 UT, normal-speed operations were continued and persisted throughout the remaining time period of high-speed video recordings.

The sferic data acquisition system started recording at 02:25:04 UT and continued recording for the duration of the observations. The 3-channel sferic data had the same composition as was used on October 7 (see Section 5.2.2). The trigger lengths were somewhat shorter with a pre-trigger of 2 ms and a post-trigger of 8 ms.

5.3.2 04:37:05 UT, 2000 frames/second

Figure 5.10 shows a high-speed video sequence obtained at 2000 frames/second of a cluster of carrot and columniform sprites. The grey-scale was stretched somewhat so that fainter features would be more visible. The charge moment change of the parent +CG discharge was determined from magnetic-field ELF measurements by a technique identical to that used in Chapter 4 (see Section 4.1). The NLDN detected the +CG, but could not give an accurate estimate of its location or peak-current magnitude.

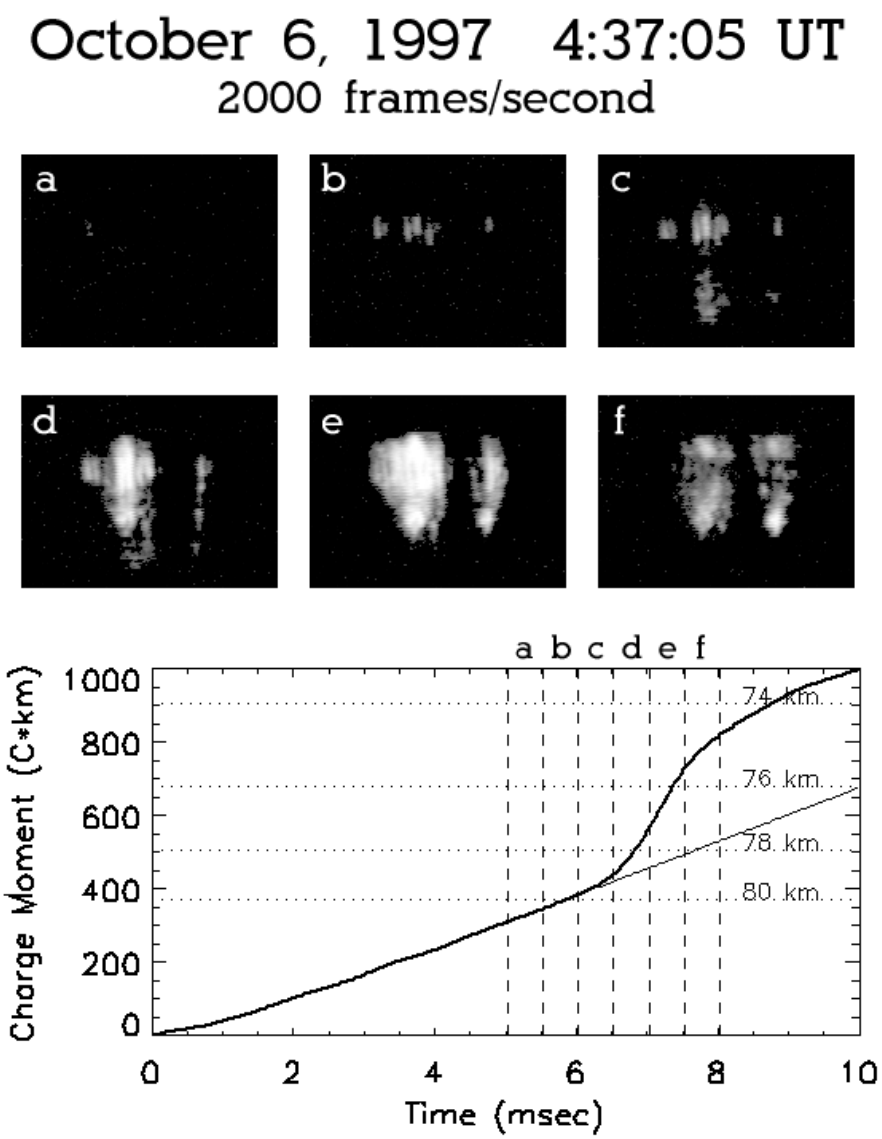

Figure 5.10: The high-speed video sequence of the 04:37:05 UT sprite cluster is correlated with the charge moment change following the parent +CG. The horizontal lines correspond to conventional breakdown thresholds between 70-80 km MSL altitude, assuming a uniformly-charged disk with $Z_d = 7.5$ km and $R_d = 15$ km (see Section 2.5.2) and an ionosphere conducting ledge at 81 km MSL. A sprite began in frame a at $\simeq$330 C·km. The sprite cluster produced a significant charge moment change, as shown by the separation between the total charge moment change (thick line) and the parent discharge charge moment change (thin line). The charge moment curve was provided by Steve Cummer.

The approximate light integration periods of frames *a*-*f* are bounded by vertical dashed lines in the charge moment plot of Figure 5.10. As discussed in Appendix A.1, the high-speed video frame is integrated in horizontal blocks. The light integration periods correspond to that of the 3rd block down from the top, since this is the block in which the sprites first appeared in frames *a* and *b*.

A single sprite column is visible in frame *a*, just over 5 ms after the onset of the +CG. The +CG's cumulative charge moment change was 310-350 C·km during frame a. Additional sprite columns appeared in frame *b*. It was shown in Section 5.2.3 that the onset of sprites can be at the limit of detectability at $\sim$300 km range. It follows that sprite onset may have been undetected at the $\sim$900 km range to this sprite cluster. As Figure 5.2 demonstrated, sprites usually brightened dramatically in the initial frames, so the initiation of these sprites probably occurred not much more than one frame earlier than the first detected luminosity. Thus, the charge moment threshold for sprite initiation was $\simeq$300 C·km. A similar threshold was observed for other sprite clusters in this study.

A 300 C·km sprite-initiation threshold is consistent the 200-400 C·km estimate based on static-field measurements presented in Chapter 5. This threshold is also consistent with earlier ELF measurements of the minimum charge moment change associated with sprite-producing discharges [*Cummer and Inan*, 1997; *Huang et al.*, 1999]. Based on an assumption of a breakdown threshold of 100 Td, *Fernsler and Rowland* [1996] predicted that 300 C·km would be sufficient to initiate conventional breakdown at 80 km altitude. The threshold at 80 km calculated in this work (see Figure 2.9) is somewhat larger than 300 C·km since a value of 123 Td was used for the breakdown threshold, as discussed in Section 2.2.3.

In Section 5.2.4, it was shown that sprites typically initiated at 76-79 km MSL altitude. Based on a uniformly charged disc model presented in Section 2.5.2 with R_d = 15 km and Z_d = 7.5 km MSL, corresponding to measurements presented in Chapter 3, the charge moment threshold for conventional breakdown is $\simeq$430 C·km at 79 km MSL and $\simeq$680 C·km at 76 km MSL. Thus, the measured charge moments for sprite initiation were 1.4–2.3 times less than required to initiate conventional breakdown in a homogeneously stratified atmosphere. Significant spatial variation in conductivity might enhance the electric field in localized regions to the point of breakdown. Such conductivity inhomogeneities might be produced by radiated fields from the lightning discharge [*Valdivia et al.*, 1998].

5.3.3 04:45:48 UT, 2000 frames/second

Figure 5.11 shows the development of an angel sprite cluster at 04:45:48 UT. The sprite event was associated with an unusually energetic 165 kA +CG at 891 km range. The vertical bar in the figure shows the altitude in kilometers above the +CG. The error in height of the sprites would be $\sim$6 km for a 40 km radial displacement from the +CG location.

Figure 5.11 shows that the charge moment change of the parent discharge rose very rapidly. Within the initial millisecond, the charge moment exceeded the conventional breakdown threshold between the base of the ionosphere ($\simeq$81 km MSL) and $\simeq$75 km MSL altitude. This should have resulted in a diffuse luminous region due to large-scale ionization (referred to as a "sprite halo" in *Barrington-Leigh et al.* [2000]), as was indeed observed in frame *a*. The shape and altitude extent of the sprite halo is consistent with the theoretical predictions of *Pasko et al.* [1997b].

The dashed vertical lines in Figure 5.11 correspond to the light-integration periods of the second horizontal sensor block from the top of the high-speed imaging sensor (see Appendix A.1). This block was chosen because all but the lowest portion of the sprite halo was within this block. There was an apparent delay between the first appearance of the sprite halo, which occurred in frame *a*, and the onset of conventional breakdown at 80 km according to the calculated charge moment change. The apparent delay was due to the additional path length required for the electric field from the parent discharge to propagate upwards to produce the sprite halo before luminosity could propagate outwards to the observer along a similar path length taken by the sferic. This additional propagation path would result in emissions which were delayed by approximately the propagation speed of light up to 80 km altitude. This delay was $80/300 = 0.27$ ms, which would result in conventional breakdown first appearing in frame a, as is observed.

The sprite halo reached a lower altitude of $\simeq$71 km MSL in frame *a*. However, by the end of frame *a*, the charge moment change had only exceeded the threshold at 76 km MSL altitude ($\simeq$700 C·km) according to the calculations based on an ionosphere conductive ledge at 81 km MSL and the geometric considerations discussed above. The source of this discrepancy is partly due to the choice of the ledge altitude. The breakdown will greatly enhance the ambient conductivity and this will drop the altitude of the ledge. Conceptually, the electric field will be enhanced at a given altitude and charge moment change if the conducting ledge is lowered, since the distance to the images above the ionosphere will decrease. This will reduce the

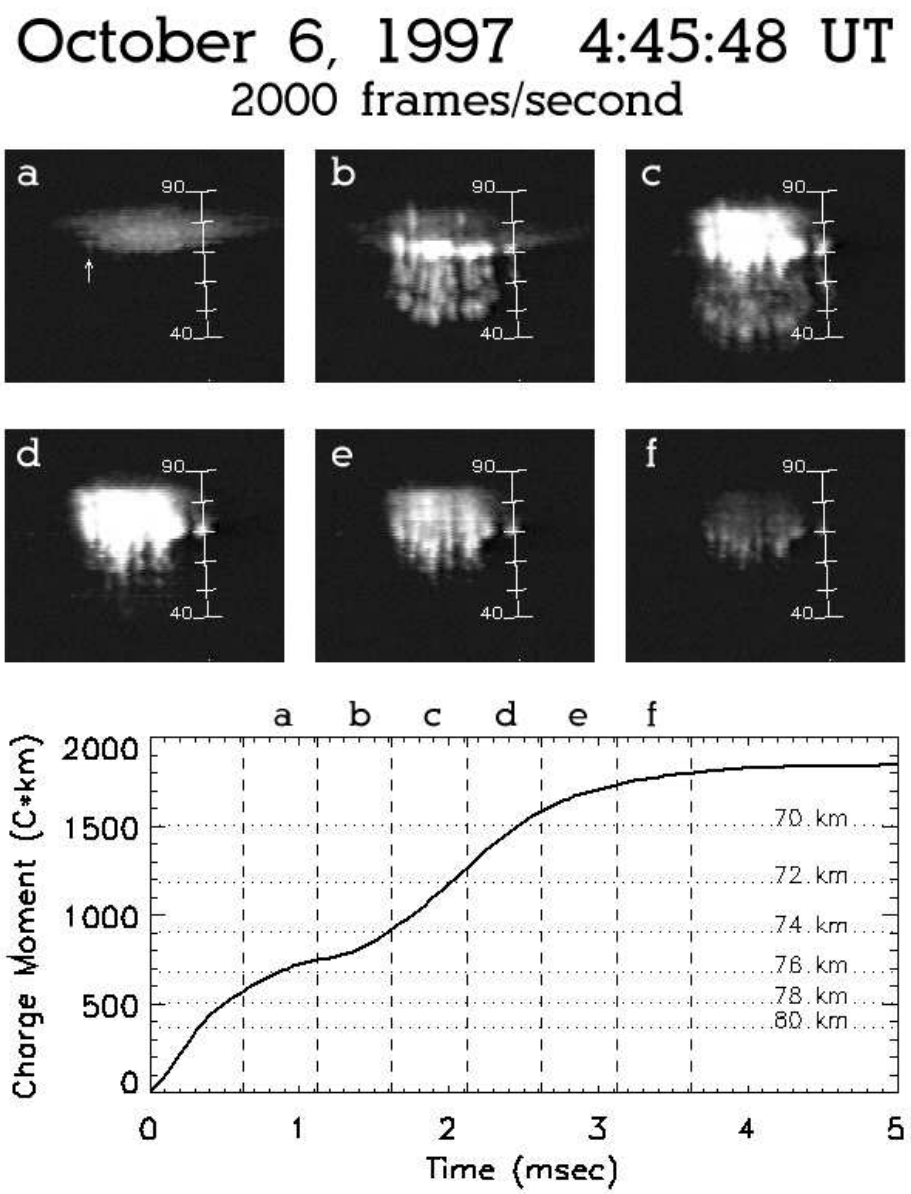

Figure 5.11: The correlated high-speed video sequence and charge moment change of the 4:45:48 UT sprite event. The horizontal lines are the same as before (see Figure 5.10 caption). The parent +CG's charge moment change exceeded the conventional breakdown threshold above $\simeq$75 km MSL altitude within the first frame and this produced diffuse luminosity consistent with the theoretical predictions of *Pasko et al.* [1997b]. Angel sprites developed downward at unusually high velocity in frame *b*. The sprite cluster produced a large charge moment change in frames c-d. The charge moment curve was provided by Steve Cummer.

breakdown threshold at any given altitude. This demonstrates the importance of self-consistently modeling breakdown and relaxation-time parameters, as was shown by *Pasko et al.* [1997b].

Dropping the ledge from 81 km MSL altitude to just above 74 km MSL will reduce the altitude of breakdown shown in the charge moment curve for frame *a* from $\simeq$76 km MSL to $\simeq$74 km MSL. If the center of the sprite halo was located at a range of $\sim$20 km beyond the +CG, then a feature at 74 km MSL altitude would have appeared to have been at 71 km MSL. However, the lower extent may also have been associated with local regions of enhanced breakdown which developed into streamers, as discussed next.

An enhanced luminous region which extended below the base of the sprite halo is shown by an arrow in frame *a*. A positive streamer developed (and split) downwards in frame *b* from the enhanced luminous region at an average velocity of 3.4×10^7 m/s (>10% the velocity of light). The velocity of the positive streamers in the angel sprites were much faster than in carrot and columniform sprites (see Sections 5.2.3 and 5.2.4). The higher velocities are roughly consistent with the larger charge moment change and the theoretical model of tendril velocities put forth by *Raizer et al.* [1998]. Several of the other angel sprites in frame *b* were also preceeded by enhanced luminosity at the base of the sprite halo in frame *a* and this is consistent with the development of angel sprites shown in Section 5.2.5.

A few of the tendrils of the angel sprites reached a lower terminal altitude of $\simeq$36 km MSL in frame *c*. *Pasko et al.* [2000] predicted that the tendrils would terminate at $\simeq$38 km under the influence of a 1000 C·km parent discharge, which is roughly consistent with the cumulative charge moment change in frame *c*.

A second hump in the charge moment began in the latter part of frame *b* and was likely correlated with current in the sprite, as discussed in Chapter 4. The magnitude of the sprite charge moment change is difficult to separate from the parent discharge charge moment since the latter may still have been varying. An extrapolation of the parent discharge slope at 1.2 ms reveals that the sprite charge moment may have been as large as 840 C·km, which would be the largest charge moment change ever indicated for a nighttime sprite. As was shown in Section 4.3, daytime sprites can produce significantly larger charge moment changes than even this extreme event.

5.4 Summary

High-speed video observations of sprites were analyzed in this chapter. The approximate initiation altitude, development sequence, and average velocities were presented for several sprite clusters. The charge moment change of the parent discharge was also correlated with the initiation and development of some sprite clusters. The key results of this analysis are summarized as follows:

- The initiation altitude of all sprites was 76±6 km MSL with most sprites initiating at 76–79 km MSL. The initiation altitude is roughly consistent with conventional breakdown predictions. The initiation altitudes were based on fixing the terminal altitude of the brightest carrot sprites at 90 km MSL and the moderate-brightness columniform sprites at 87 km MSL.

- Sprites were initiated when the charge moment change of the parent discharge exceeded $\simeq$300 C·km. This is consistent with previous ELF-based estimates [*Cummer and Inan*, 1997; *Huang et al.*, 1999] and with the 200-400 C·km estimate based on static-field measurements presented in Chapter 5. Using an E/N breakdown threshold of 100 Td (compared to 123 Td used in this study), *Fernsler and Rowland* [1996] predicted that 300 C·km would be sufficient to initiate conventional breakdown at 80 km MSL altitude. The result that initiation heights appear to be below 80 km MSL, compared with the compact origin of most sprites, suggests that significant conductivity inhomogeneities may locally intensify the electric field to produce breakdown at lower altitudes.

- Most sprites developed bidirectionally upward and downward from the point of initiation. The initial development characteristics are consistent with experimental observations [*Loeb and Meek*, 1940] and theoretical predictions [*Dhali and Williams*, 1985] of bidirectional streamer development in long air gaps. In sprites produced by +CGs, the upward component would be a negative streamer while the downward component would be a positive streamer.

- Parent discharges having unusually large and rapid charge moment changes produced sprite halos, consistent with the theoretical predictions of *Pasko et al.* [1997b]. Angel sprites were observed to initiate from enhanced luminous regions in the sprite halos.

- The average velocity of the inferred positive streamers which propagated downward could exceed 1×10^7 m/s, consistent with the predictions of *Raizer et al.* [1998]. The average velocities of the positive streamers of angel sprites were as fast as 3.4×10^7 m/s, which is significantly faster than that of other types of sprites.

- During some sprites, apparent negative streamers were spawned from regions through which the positive streamers propagated previously. The negative streamers propagated and branched upwards, transforming the sprite from a columniform shape (with tendrils) to an upward-V, or "carrot", shape.

5.5 Discussion

The observed initiation altitudes (76±6 km MSL) of sprites are roughly consistent with conventional breakdown predictions, although the measured charge moment changes appear to be insufficient for sprite initiation at these altitudes if the atmosphere were homogeneously layered. Significant variations in the conductivity may arise from electromagnetic pulse fields creased by a horizontal lightning discharge [*Valdivia et al.*, 1998]. Variations in air density may arise from gravity waves [*Pasko et al.*, 1997a], though recent observations show no obvious connection between gravity waves and sprite locations [*Sentman et al.*, 1999].

The plan location of the sprites could not be determined precisely, but could only be estimated based on previous measurements of sprite terminal altitudes. Thus, the altitudes of sprite features were somewhat uncertain. As was shown in Figure 2.9, the charge moment threshold is sensitive to the initiation altitude. Because of the uncertainty in altitude, one can not make a definitive statement as to the degree of inhomogeneity which is required for conventional breakdown onset.

Chapter 6

Conclusions

6.1 Summary

Sprites and their parent discharges were analyzed in this study. The 3 dimensional and temporal development of discharges was observed with the Kennedy Space Center Lightning Detection and Ranging (KSC LDAR) instrument. A pattern of increasing horizontal dimensions of discharges which propagated into the stratiform region of MCSs was readily evident at least 20 minutes prior to the production of sprites.

Most of the sprite-producing discharges began as relatively ordinary bilevel intracloud (ICs) similar to those documented by *Shao and Krehbiel* [1996]. However, one of the sprite-producing discharges began as a more complex hybrid IC and negative cloud-to-ground (-CG) discharge. The negative leaders in the upper level portion of the ICs dropped in altitude from 10–12 km to 7–8 km MSL as they propagated away from the convective region into the stratiform region. The leaders then propagated horizontally through the stratiform region at average speeds of about $1 - 2 \times 10^5$ m/s while maintaining an altitude of 7–8 km MS. The altitude of the leaders is in excellent agreement with the altitude of the upper positive charge layer in stratiform regions [*MacGorman and Rust*, 1998,pg. 267].

The horizontal development of the negative leaders away from the convective region either stopped or was redirected after propagating a distance of about 40–60 km to near the periphery of the 20 dBZ reflectivity region at 7–8 km MSL. The outward propagation was followed by a steady static electric field change which was consistent with the downward propagation of one or more positive leaders. These leaders were poorly located with often not more than one VHF source located above the subsequent strike location.

The sprite-producing +CG discharges removed positive charge from 7–8 km MSL altitude, corresponding to the upper positive charge layer in the stratiform region. This altitude range is consistent with multi-station electric field measurements of +CG charge heights in MCSs [*Krehbiel*, 1981]. The height of the charge removed by the +CG is similar to the ≃7 km MSL altitude of negative charge removed by −CGs in the midlatitude summer [*Krehbiel*, 1986], indicating that neither (stratiform) +CGs nor −CGs have the "upper hand" in the generation of a charge moment from a given amount of charge. The idea that sprite-producing discharges remove charge from the lower positive charge layer near the 0°C in the stratiform region [*Williams*, 1998] is not supported by these measurements. Rather, negative leaders were observed to propagate into the lower positive charge region primarily during the subsequent IC portion of the discharge after the sprites had faded.

The sprite-producing +CGs had average downward (−z direction) currents of ≃28-37 kA within the initial 1 ms post-return stroke interval and ≃13-16 kA within the initial 4 ms. The range of charge transfers to ground for these time intervals was ≃28-37 C and ≃52-64 C, respectively. The non-sprite-producing CGs of both polarities had smaller average currents and charge removals for the post-stroke time intervals. These CGs also had smaller horizontal extents of charge removal compared to the sprite-producing CGs.

The charge moment threshold for sprite initiation was found to be ≃300·km for delays of up to a few milliseconds after the +CG stroke. This threshold is similar to previous estimates based on ELF measurements [*Cummer and Inan*, 1997; *Huang et al.*, 1999]. Most sprites were located above the approximate periphery of the parent discharge. Since the +CG continuing current is produced by the propagation of negative leaders at the end of the channels, much of the charge removed by the +CG will likely be located at the discharge periphery. Thus, the sprites may be initiating in regions of local quasi-static electric field maxima. However, there were also a few sprites which appeared to be located beyond the discharge periphery where the quasi-static field should have been smaller.

The sprites were only associated with the most recent (∼200-300 ms) portion of the discharge. Also, the +CG location was usually located under the periphery of the sprite cluster in the general direction away from the previous negative leader propagation. These characteristics suggest that the older (>300 ms) portion of the discharge had "cutoff" (become nonconducting). The cutoff of a channel might have produced enough electrical stress at the conducting end opposite of the negative

leader(s) for the generation of a positive leader, as suggested by [*Krehbiel*, 1981].

Two of the sprite-producing +CGs were followed by one or more −CG strokes which occurred underneath the region of rapid charge removal. The locations of the −CGs for the different discharges were nearly identical, while the +CGs struck at different locations. I speculate that these −CG flashes were not produced by negative leaders from the horizontally extensive flash, but were instead initiated from the top of one or more tall structures under the influence of the large and rapidly increasing electric fields produced by the +CGs.

The initiation altitude of nighttime sprites is 76±6 km MSL with a maximum density at ≃76-79 km MSL. The initiation altitude is consistent with conventional breakdown predictions, though the measured charge moments were about 1.4–2.3 times less than required to initiate conventional breakdown in a homogeneously stratified atmosphere. Significant spatial variation in conductivity might enhance the electric field in localized regions to the point of breakdown. Such conductivity inhomogeneities might be produced by radiated fields from the lightning discharge [*Valdivia et al.*, 1998].

Most sprites developed bidirectionally upwards and downwards from the point of initiation. The bidirectional development is similar to that of breakdown initiated in long air gaps in which positive and negative streamers propagate in opposite directions away from an electron avalanche region [*Loeb and Meek*, 1940; *Dhali and Williams*, 1985]. The downward developing positive streamers typically attained peak velocities of $\sim 1 \times 10^7$ m/s, consistent with the predictions of *Raizer et al.* [1998] for the observed charge moment changes in excess of 300 C·km.

Parent discharges with unusually large and rapid charge moment changes produced sprite halos, consistent with the theoretical predictions of *Pasko et al.* [1997b]. Angel (jellyfish) sprites initiated from enhanced luminous regions at the base of the sprite halos. Positive streamers propagated downwards from the initiation regions at velocities well in excess of more typical sprite positive streamers initiated by less energetic discharges. The angel sprite positive streamer velocities could exceed 3×10^7 m/s (10% of light).

On some sprites, inferred negative streamers were spawned from regions through which the positive streamers propagated previously. The negative streamers propagated and branched upwards, transforming the sprite from a columniform shape (with tendrils) to an upward-V, or "carrot", shape. In normal speed video, the apparent vertex of a carrot sprite at ∼65 km altitude (or lower) can appear to be the initia-

tion point for the upward and downward branching streamers. The high-speed video observations clearly show that the actual initiation altitude is always higher than the apparent vertex of carrot sprites.

A unique sprite ELF signature was used to detect the presence of daytime sprites. During the day, the base of the ionosphere is located at a lower altitude resulting in a higher charge moment threshold for conventional breakdown. The charge moment changes of the parent discharges, in chronological order, was 6100, 4300, and 3900 C·km at the onset of the sprite ELF signatures. In contrast, the onset of nighttime sprite ELF signatures occurred at +CG charge moment changes well below 1100 C·km [*Cummer and Stanley*, 1999]. The 6100 C·km charge moment change of the first parent discharge may have been sufficient for conventional breakdown below the base of the ionosphere at an altitude of ≃54 km, assuming an experimentally measured ion conductivity profile of *Holzworth et al.* [1985].

The daytime sprites themselves contained unusually large charge moment changes of ≃2800 C·km, ≃1200 C·km, and ≃910 C·km. These charge moments are larger than the largest nighttime sprite charge moment change published to date of ∼840 C·km [*Cummer and Stanley*, 1999] (see Section 5.3.3).

6.2 Future Work

The sprite-producing discharges analyzed in Chapter 3 were well outside of the LDAR network. The radial errors and reduced detection efficiency outside of the network (see Section 3.2.1) made it difficult to resolve channel structure in the discharges. The New Mexico Tech Lightning Mapping Array (NMT LMA) was based on the KSC LDAR [*Rison et al.*, 1999], but improves upon the LDAR in that it can be deployed across a wider area, resulting in smaller radial errors as a function of distance from the center of the network. The ability of the NMT LMA to accurately resolve structure in horizontally extensive discharges was recently shown by *Krehbiel et al.* [2000] for a discharge with a 75 km horizontal extent in Oklahoma.

The NMT LMA will be deployed across eastern Colorado and western Kansas during the STEPS 2000 campaign (May 22 – July 16, 2000) and beyond. Large sprite-producing MCSs are not uncommon in this region during the summer months *Lyons et al.* [1999]. Sprite observations will be conducted from Yucca Ridge, Colorado both during and after the STEPS campaign. These measurements, along with possible triangulation data from another observation site, will provide an opportunity

to exam in detail the relationship between the parent discharge and the sprites. A network of DC field mills, slow antennas, and a few fast antennas will provide detailed information about the electrical dynamics of the storm system and the discharges.

The New Mexico Tech Interferometer will be deployed in STEPS 2000 near the center of the LMA network and will be operated by the author. Of particular interest will be a comparison of the interferometer data with LMA data for the same discharges. The recent observation by the LMA that VHF source powers are systematically less in the inferred positive portion of the discharge relative to the negative portion [*Thomas et al.*, 2000] raises the possibility that the LMA may be able to directly map positive leader propagation rather than only map negative polarity breakdown, which can occur back along decaying positive leader channels [*Ogawa and Brook*, 1964; *Mazur*, 1989] in the form of K-changes which are bright at VHF [*Shao and Krehbiel*, 1996]. The interferometer will be used to explore the temporal and spatial development of K-changes relative to the positive discharge development shown by LMA data in order to better understand what physical processes are seen by the LMA. This will result in a better understanding of lightning processes as well.

Appendix A

Instrumentation

A.1 High-speed Camera System

A KODAK EktaPro High-Spec Motion Analyzer Model 1012 with a KODAK EktaPro Intensified Imager Model VSG was used to acquire the high speed video imagery of sprites. The pixel array size of the imager sensor was 239x192. The operational wavelength region was 440-700 nm at 50% sensitivity and 350-800 nm at 10% sensitivity. The system was capable of 1000 frames per second (fps) using the full sensor area and higher rates using correspondingly fewer horizontal scan lines. The frame start times were accurate to within 50 μs as determined by GPS timing (see Appendix B.4.2).

The high-speed camera's pixel sensor was scanned out in blocks of 16 rows each for a total of $192/16 = 12$ blocks (at 1000 fps). This scanning proceded downward from the top of the sensor's active area. Each block had integration start and end times that were delayed by $1\ ms/12 = 83\ \mu s$ from the block immediately above. The lowest block of the frame preceded the top block of the next frame by 83 μs. This timing information was utilized in analyzing the images, and into the velocity estimates.

The light integration period was configurable, but was always set to match the duration of the individual blocks within a frame. There was a short period during a block's read-out interval when light could not be integrated. The duration of the scan-out interval was $\approx$1 μs, which was too small to have a noticeable effect on the images.

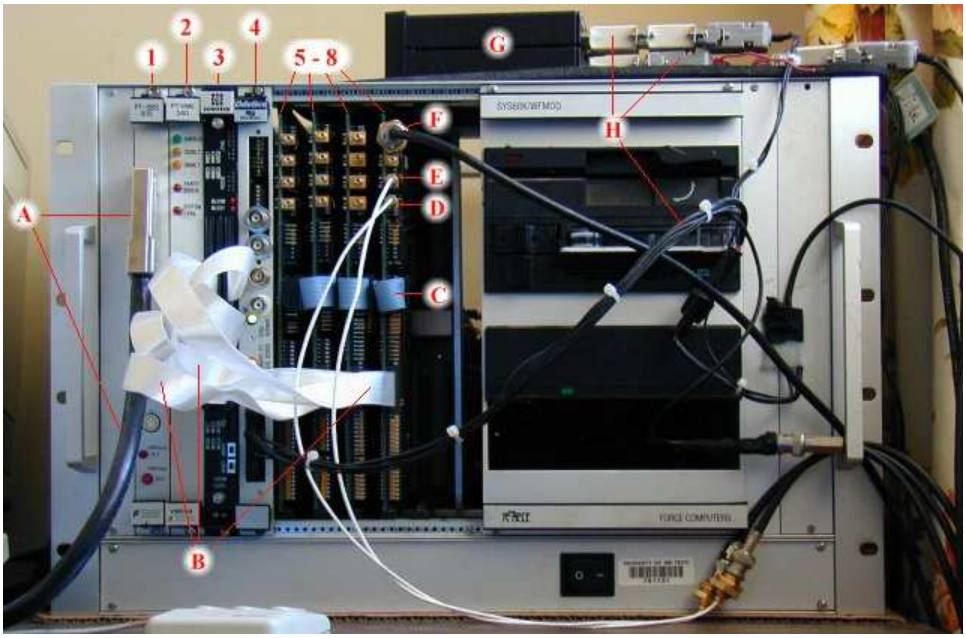

Figure A.1: The VME-based data acquisition system. The various boards are designated with numbers while some of the cables, ports, and peripherals are shown with letters. The identity and function of the various boards is described in Table A.1.

A.2 Data Acquisition System

The data acquisition system was composed of a VME-based digitizing and processing system linked to a Sun IPC host computer. A photograph of the VME system is shown in Figure A.1. The VME boards are numbered in the figure and are described in Table A.1. The digitizer cards were specially designed for the system by W. Rison. The data acquisition software was developed by the author.

Cable "A" in Figure A.1 links the VME system to the host Sun IPC unit. Prior to acquiring data, a program is run on the Sun which downloads an executable program to the DSP board (3) in the VME system. The program first resets the A/D boards and then continuously processes data received from the boards through the cables marked with "B" in Figure A.1. Cable "C" interconnects the A/D boards and allows a single chip on a "master board" to control and synchronize the data sampling on the other boards. A jumper on the master board allows one to configure the sampling rate at either 500 kHz or 1 MHz. Each card can be jumpered to sample four 8-bit channels simultaneously, or one 8-bit and two 12-bit channels. The former has been the preferred mode for sampling interferometer phase data while the latter is used for

VME Boards		
Board	Manufacturer & Model No.	Description
1	Performance Technologies PT SBS-915	Interfaces the VME system with the host.
2	Performance Technologies PT VME-240	32 MB memory board. It is currently used only by the interferometer trigger mode.
3	Sonitech International SP-40 VME Dual DSP	The dual DSPs continuously receive and process all of the data from the A/D boards.
4	KSI Odetics GPS VME	Produces GPS-based timing which is integrated into the data stream by the A/D boards.
5-8	New Mexico Tech (custom design)	A/D boards. Board no. 8 is used to acquire sferics.

Table A.1: The identity and function of the VME boards numbered in Figure A.1 are described here.

sampling log-RF (8-bit) and sferics data (12-bit).

All four A/D boards are utilized when interferometer data is acquired. However, when the picture in Figure A.1 was taken, only sferics were being acquired. Log-RF data was input into the 8-bit channel F while 12-bit slow and fast antenna data were input into the 12-bit channels E and D respectively.

The black box at top (G) is the Horita unit (viewed side on) which is used for normal-speed video timing, as described in Appendix B.4.1. GPS timing information is input into the Horita unit and the VME system via the cables marked with "H".

Appendix B

Calibration

B.1 Introduction

Calibration of instruments is a vital part of any scientific experiment. An important experiment can be rendered useless or worse; produce false results, if the instruments were not properly calibrated. In this section, the calibration procedures which were utilized to produce the results in this dissertation are shown.

One of the key parameters in sprite measurements is the height of sprite features. As was shown in Chapter 5, sprite heights can be estimated from NLDN CG locations or from a presumed sprite maximum altitude. Sprite heights can also be accurately determined from triangulation studies. Fundamental to all of these techniques is that the location and orientation of the camera must be accurately known. The video timing also needs to be accurately known.

B.2 Camera location

The camera location consists of 3 independent parameters: 1) latitude, 2) longitude, and 3) height above sea-level. At Langmuir Laboratory, New Mexico, there were 2 primary observation sites: 1) the Balloon Hangar in 1996 and 1997 and 2) the Annex patio in 1998. In both instances, the camera location was obtained by using a nearby theodolite stand as a reference. For the balloon hangar, the cameras were usually situated about 50 m away from the theodolite stand and the location of the camera was corrected for this (even though this is a small correction for sprite measurements). At the annex, the cameras were located close enough to a theodolite stand that no correction was necessary.

At the Kennedy Space Center in 1997, the location of the camera was determined by using the nearby LDAR central station as a reference and correcting for the estimated range and direction of the camera from the station.

B.3 Camera orientation

The camera orientation consists of 3 independent parameters: 1) azimuth 2) elevation 3) rotation angle. The azimuth is essentially a measure of the where the camera is pointing relative to the cardinal directions: north, south, east, and west. The azimuth is measured with 0° azimuth corresponding to due north and progressing clockwise to the east at 90° azimuth and so on until arriving back at the north.

The elevation angle is a measure of how the camera is tilted in the vertical. A 0° elevation angle would correspond to a level orientation with the horizon near the center of the field of view. An elevation angle of 90° would correspond to the zenith, which is directly overhead.

Ideally, the camera should be mounted in such a way that the bottom is level with the ground. In this case, one only needs to know the camera azimuth and elevation. In actuality the camera is usually not perfectly level but is at least slightly rotated about the axis normal to the focal plane. Not correcting for this in the images can introduce significant errors, particularly near the periphery of the image.

Finally, the field of view of the camera must also be known. The field of view is measured in angular width units for both the X and Y directions. This only has to be determined once for a given lens or lens setting (for a zoomable lens).

B.3.1 Normal-speed camera

The orientation of the normal-speed camera was determined by using stars within the field of view. The actual azimuths and elevations of stars can be calculated for any location on the globe once the date and time of the observation are known.

Prior to 1998, the camera orientation was determined by guessing an azimuth, elevation, and rotation angle and then outputting a stellar image from a software program called "Sky Map" for this guess. The stellar image was then rescaled so that the star pattern had the same 2-dimensional size as the actual image and the two images were then digitally combined so that the stars overlapped. If there was no significant rotation angle, then the center azimuth and elevation of the image could be obtained directly from this procedure as well as the field of view (if it

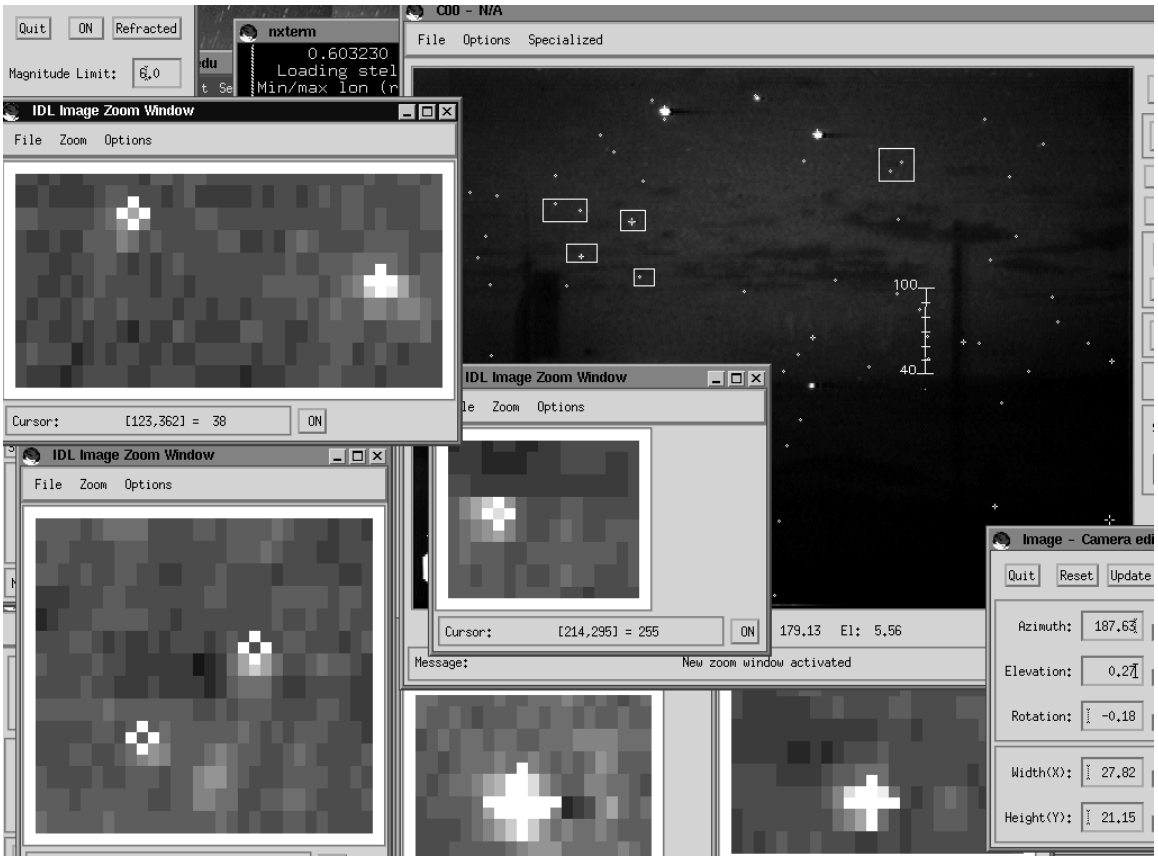

Figure B.1: Screen capture of the star alignment procedure used on actual data. The azimuth, elevation, rotation-angle, and field of view could be varied in the window at lower right. Altering these settings changed the location of the calculated star positions, as indicated by the crosses.

wasn't already known). However, if there was a significant rotation angle, multiple such image overlays might have to be attempted until both the angle and the proper image resizing could be accurately determined. This procedure was very tedious and could easily take several hours per camera orientation.

In early 1998, Christopher Barrington-Leigh of Stanford University adapted some astronomical routines to Matlab for the purpose of predicting the azimuth and elevation of stars for a given location, date, and time. These routines were adapted to IDL by the author and were integrated into the author's IDL sprite analysis software. The routines also incorporated refractive corrections developed and written by the author (see Section B.5).

Figure B.1 shows how the camera orientation is determined. A normal-speed

video image is displayed within the large window in the upper right. The image is the average of several frames. By averaging frames, the signal to noise level is improved. This results in more stars being visible as well as better highlighting of any cloud boundaries.

The white crosses on the image are the calculated star positions according to the camera orientation settings, camera field of view, camera location, date, and time. The size of a given cross is an indication of the apparent brightness of the star, with bigger crosses corresponding to brighter stars. The goal of the star alignment procedure is to adjust the camera orientation settings (and field of view settings, if not already set) until an optimal alignment is achieved between the calculated star positions and actual star positions. Once the optimal alignment is found, the camera settings were stored in a configuration file for future use. The same camera settings were also used for other video sequences if the camera was pointing in the same direction with the same lens settings.

The error in the final azimuth and elevation of the camera orientation was sub-pixel if there were many stars in the field of view, but was more typically on the order of a pixel. The angular size of a pixel depended on the lens, but was $\simeq 0.04^\circ$ in width and height for the 25 mm lens which was used for most of the normal-speed sprite video shown in this dissertation.

B.3.2 High-speed camera

Only the brightest stars in the sky will appear on high-speed image-intensified video since the light-integration period is very much less than that of the normal-speed image-intensified video. More often than not, no stars were visible in a high-speed video image sequence. Consequently, it was not possible to determine the high-speed video camera's orientation directly from the stars.

Fortunately, the sprites themselves could be used to determine the camera orientation. This was done by determining the azimuth and elevation angles of sprite features in a calibrated normal-speed video image and then adjusting the high-speed camera orientation parameters (and field of view, if not already set) to produce the correct azimuth and elevation values for the same sprite features. The error in this technique is estimated to be typically no more than a few hundredths of a degree above that introduced by the normal-speed video stellar alignment procedure.

B.4 Video timing

Accurate timing of video is necessary to determine which parent discharge produced the sprites. The onset of the parent discharge can be determined to microsecond accuracy by the GPS-based data acquisition system (see Appendix A.2). High-speed video must be timed precisely to determine sprite initiation times relative to the time of cloud-to-ground strokes.

B.4.1 Normal-speed video

Prior to the sprite campaign conducted at Langmuir Laboratory in 1997, normal-speed video timing was obtained by placing one or more LEDs within the field of view and connecting the LED(s) to a calibrated GPS-based signal(s). The UTC time in hours, minutes, and seconds was either placed directly onto the video by a VCR or was added to the video in post-processing. The time placed on video was accurate to only a few tenths of a second. Sub-field accuracy (<17 ms) was obtained by estimating the time of the LED transition by implementing a procedure similar to that detailed in B.4.2.

A new technique was employed in 1997 to obtain normal-speed video timing. Horita GPT-50 units were used to place GPS information directly onto the video signals. The Horita units were specially modified by the manufacturer to insert a white vertical stripe onto the left side of the video image in response to a GPS-based pulse.

Figure B.2 shows 3 video fields extracted from a normal-speed video sequence around the time of a sprite event. The Horita GPT-50 inserted a vertical stripe at the left side of the middle image. The top of the stripe corresponds with the exact moment in which the onset of a second occurred according to GPS timing. By examining where in the video field the top of the stripe appears, one could theoretically determine the exact timing of the video to within the time period required to scan one line (<100 μs). In practice, however, such precision has not been achieved since the output timing characteristics of the video camera were not known precisely.

An image field is not converted to a video signal until after the light integration period is over. Consequently, the vertical stripe will always appear in a frame prior to the one in which the transition actually takes place. The length of time it takes to output a video field as a video signal after the start of light-integration is always at least the duration of a video field; 1000 ms/60 = 16.7 ms. However, there are

Figure B.2: Individual fields of a digitized normal-speed video sequence. The vertical stripe in the middle image was placed on the video signal at the moment of a second transition. The time shown at the top was the calibrated start time of light integration for the video image, while the time in the lower left is an approximate time updated by the GPT-50 every second. The light integration period actually preceded the second transition because images were not output to the video signal until after the light integration interval was over.

additional delays on the order of a few milliseconds. To determine the actual delay, light from return strokes within the camera's field of view was used. Because the light output from a lightning discharge increases many fold during the return stroke process, return strokes are easy to detect on video. The actual time of the return strokes could be determined precisely from the recorded sferics data. By examining many return strokes, the delay for the placement of the vertical stripe into a video image relative to the start time of light integration for the video image was determined to be 20 ms with an uncertainty of approximately 1 ms. Such precision was adequate for most normal-speed sprite observations.

B.4.2 High-speed video

The high-speed video timing was calibrated in a way similar to that originally used for the normal-speed video: with an LED in the field of view. The LED was connected through a resistor to the GPS-based binary coded decimal (BCD) 100 ms bit. The LED would be on during odd hundred millisecond intervals and off for even intervals. The time of a sprite event within the normal-speed video was used to determine which odd or even 100 ms block was being observed in the high-speed video sequence.

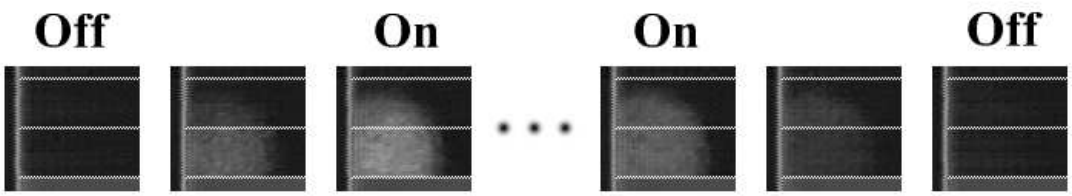

Figure B.3: Both the off⇒on LED transition as well as the subsequent on⇒off LED transition are shown for a 2000 frame-per-second sequence. The exact time of the transition within a frame can be estimated by comparing the relative brightness of the LED to when it was on throughout the frame. The horizontal white lines denote block boundaries and hence separate regions with different start and end times of integration.

Sub-frame accuracy timing was obtained by examining the brightness of the LED during an on/off transition and comparing this brightness with that when it was on for an entire frame. An LED which was observed to be relatively dim during an on⇒off transition must have changed state during the earlier part of the frame interval. However, a relatively dim LED during an off⇒on transition indicates that the LED turned on in the latter part of the frame interval, etc.

In order to calculate the time of the transitions, an average LED intensity was determined before, during, and after an LED transition. This procedure was complicated by the fact that the high-speed video frame is not light-integrated simultaneously. Instead, the high-speed video frame is integrated in blocks starting from the top, as explained in Section A.1. Any measurement of intensity had to be confined to within the same block.

Table B.1 shows the timing calibration procedure which was used for the 4:37:05 UT sprite event on October 6, 1997. The sprite event occurred between the LED transitions shown in Figure B.3. Calculations were performed for both the off⇒on and on⇒off transitions since the 8-bit grayscale in the digitized image may not have been linearly proportional to actual light intensity. By using both transitions, any systematic error in the intensity estimate was minimized.

The timing calibration procedure was also performed for all other high speed video sequences shown in this dissertation.

Timing calculation for Figure B.3							
Transition	Block index	LED region	LED intensity [0-255] Before	During	After	Calculation	Time Offset
off⇒on	4	top	33.2	60.7	106.2	$0.5(\frac{4}{6}+\frac{106.2-60.7}{106.2-33.2})=$	.645 ms
	5	center	31.3	89.5	139.6	$0.5(\frac{5}{6}+\frac{139.6-89.5}{139.6-31.3})=$	.648 ms
on⇒off	4	top	87.2	61.8	36.0	$0.5(\frac{4}{6}+\frac{61.8-36.0}{87.2-36.0})=$	.585 ms
	5	center	97.8	53.6	34.3	$0.5(\frac{5}{6}+\frac{53.6-34.3}{97.8-34.3})=$	.569 ms
						Average time offset: .612±.041 ms	

Table B.1: The high-speed video timing calibration procedure is shown here for the LED transitions in Figure B.3. The LED intensities are 9×9 pixel averages of the 8-bit grayscale intensities within the respective LED regions. The time offset corresponds to the time elapsed for the LED transition relative to the start of light integration for the top block at index 0 during the LED transition frame.

B.5 Refractive corrections

The index of refraction of air is not precisely unity, but is slightly larger than unity. A non-unitary refractive index for air will cause light entering the atmosphere to bend, much like light bends when it enters a higher refractive index substance such as water. The steeper the incidence angle relative to the surface normal, the more light is refracted. The refraction of light can have a dramatic influence on the apparent positions of stars at low elevation angles. In order to properly align a star field (see Section B.3.1) at low elevation angles, the refractive bending of light must be incorporated into the calculated apparent star positions.

Sprites are at a high enough altitude and low enough air density that they can be considered external to the atmosphere in refraction calculations. Thus, the atmosphere will bend the light from sprites in essentially the same way that it does for the star field behind the sprites.

The refractive index of air, minus one, is proportional to the density of air. At 600 nm, the equation for the refractive index of dry air as a function of air density is [*Weast*, 1987,p. E-320]:

$$n_i = 1.0 + 0.0002763(\frac{\rho_i}{\rho_o}) \tag{B.1}$$

where n_i is the refractive index for air of density ρ_i and ρ_o is the density of air at sea level. The numerical coefficient of 0.0002763 is based upon a wavelength of 600 nm (red light). The multiplier will change slightly for other visible wavelengths. The refractive index also depends somewhat on the water content of the air. The high altitude and dry enviroment of Langmuir Laboratory did not require that a correction be made for moisture content. Such a correction would have been smaller than the resolving power of the instruments used.

A raytracing code was implemented to calculate the actual incident angle of starlight or "spritelight" for any given observed angle. A light-ray was propagated, or "traced", back up through the atmosphere starting at the observed angle. In this calculation, the Earth's atmosphere was approximated to a large number of discrete shells. Each shell had a refractive index corresponding to the average air density within the shell.

At each interface between shells, the angle of propagation changed slightly according to Snell's Law:

$$n_i \sin\theta_i = n_{i+1} \sin\theta_{i+1} \tag{B.2}$$

where within the ith shell, n_i is the index of refraction and θ_i is the light-ray angle relative to the $ith \Leftrightarrow (i+1)th$ interface normal.

Since only the angle relative to the interface normal changes, the azimuth angle will not change. Refraction therefore affects only the elevation angle.

The 1976 US Standard Atmosphere model (see Section 2.3.1) was used to determine the air density for a given height. An array of refractive indices was then formed by using Equation B.1 on a uniformly spaced array of heights extending from sea-level up to a maximum altitude of 40 km. Above 40 km altitude, the air is thin enough that refractive effects can be completely neglected.

The raytracing was started from the observation altitude, which for most sprite observations reported in this paper was about 3200 m above sea-level. The raytracing procedure was performed on each element of a uniformly spaced array of observed elevation angles. Some of the observed elevation angles were even slightly negative since the horizon as viewed from a mountain observation site can be at negative angles (this fact is particularly important for the October 6, 1997 sprites). The result of these lengthy calculations was an array of incident elevation angles. A lookup table was formed which allowed one to determine the observed elevation angle given an incident angle and vice versa. This lookup table is utilized by the sprite analysis

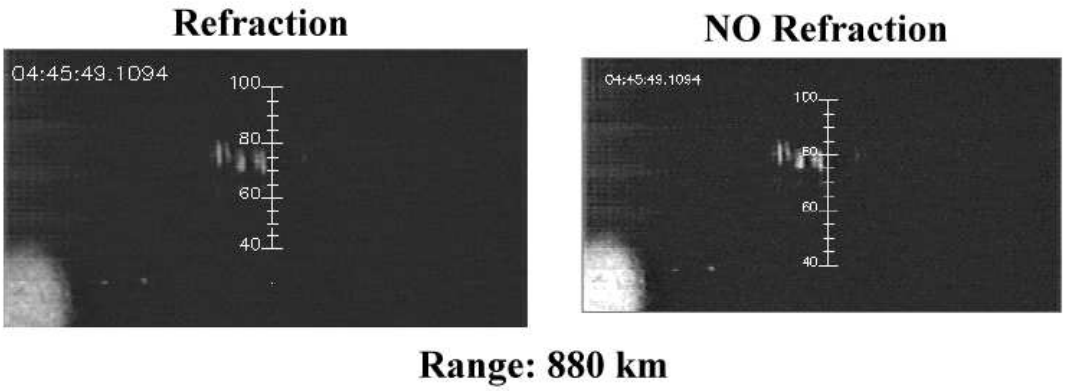

Figure B.4: The above comparison shows how significant the effect of refraction can be on height estimates. The heights shown on the vertical bar are in kilometers above a cloud-to-ground discharge at 880 km range. The height bar on the left was plotted with refractive effects included while that on the right neglects refraction. Ignoring refraction for this sprite image would have introduced a systematic error of 4-5 km in the height estimates.

software in both the calculations of observed stellar elevation angles as well as in the observed heights of sprites.

Figure B.4 shows how significant the effects of refraction can be for distant (low elevation angle) sprites. The camera orientation is identical for both cases and was properly determined by including the effects of refraction on star positions. The vertical bars in the images are height indicators in units of kilometers above the 880 km distant cloud-to-ground discharge which immediately preceeded the sprite event.

The vertical bar on the left in Figure B.4 was plotted with refraction taken into account. The vertical bar on the right was plotted without refractive effects. Comparing estimated heights for the same sprite features shows that ignoring refraction would have resulted in height estimates which were systematically 4-5 km too high. These systematic errors would increase for lower altitudes in a sprite event since refractive effects increase with decreasing elevation angle. (Note how the refracted vertical bar appears to be compressed at lower altitudes.)

Figure B.5: The slow antenna calibrator is shown above. The circular region in the center is the sensor plate. It is surrounded-by and flush-with a ground plate. This ensures that the electric field lines are undistorted in the region above the sensor.

B.6 Electric Field Calibration

B.6.1 Local Calibration

In principle, one could determine the relationship of the output voltage of the slow antenna to the vertical electric field by determining the gain of the antenna's charge amplifier, the area of the sensor plate, and the effective gain factor of the antenna. The first two quantities are readily obtained. However, it is very difficult to directly determine the antenna's geometrical gain factor since the electric field lines wrap around the grounded top hat and connect to the sensor plate in a complex way. The way to circumvent this difficulty is to calibrate another electric field antenna which has a much simpler geometrical arrangement and then calibrate the slow antenna by intercomparing data between the systems. This process is described below.

Figure B.5 shows a picture of Marx Brook's calibrator. This calibrator was used to calibrate the slow antenna in all of the field programs described in this dissertation. The ground "plane" surrounding the sensor in Figure B.5 ensures that the electric field will be undistorted above the sensor. Consequently, the gain factor of the calibrator antenna is equal to 1.

The simplest means of calibrating the calibrator was to apply a square wave of

known amplitude to a metallic plate spaced precisely 10 cm above the calibrator. By measuring the output voltage amplitude for a known electric field change amplitude, the electric field change of sferics could be determined from the change in output voltage (assuming no saturation).

Once the conversion factor between volts and volts/meter was known for the calibrator, the calibrator was placed outside in a flat area free from nearby obstructions. The electric field changes of sferic waveforms was recorded and compared with the voltage changes simultaneously observed on the slow antenna. The conversion factor of volts to volts/meter for the slow antenna could then be easily obtained. This intercomparison was repeated for the different gain settings of the slow antenna.

B.6.2 Absolute Calibration

The local calibration of the previous section enables the determination of the electric field at the instrument. This electric field, however, will be distorted if the conducting surface below and around the instrument is not planar. An uneven conducting ground can either amplify or reduce the measured electric field relative to that which would exist above a planar surface. The charge moment calculations based on the vertical static electric field (Section 3.5) and vertical ELF electric field (Section 4.1) assume that the field is measured above a flat surface. Thus, the amplification factor due to local topography must be calculated and removed before the charge moment can be calculated.

Kennedy Space Center, 1997

At the Kennedy Space Center (KSC) in 1997, the slow antenna instrument was placed on top of a building. The antenna's location was near the corner of the building, where the electric field was probably enhanced. The calibrator, however, was placed in an open level field away from the building. Thus, the local electric field calibration (Appendix B.6.1), which is based on calibrated electric field readings from the calibrator, should have been unaffected by the placement of the slow antenna. Unfortunately, the calibrator's calibration data for KSC was lost, making it impossible to reliably determine the electric field amplitude of sferics recorded by the calibrator.

The op-amp for the calibrator was temporarily replaced at KSC since the previous op-amp had burned out. The replacement op-amp was obtained on short notice and was not identical to the type of op-amp normally used. Thus, the data obtained at

other sites (with other op-amps) for the calibrator's V/m range could not be used for the KSC data. The net effect is that the local electric field calibration could not be performed on the KSC data. An independent means of determining the electric field was necessary.

The time, location, and peak-current of CG strokes is recorded by the National Lightning Detection Network, which is operated by Global Atmospherics Inc. [*Cummins et al.*, 1998]. If the ground can be assumed to be a perfect conductor at the dominant frequency of the return stroke (∼10 kHz), then the peak-current, I_p, is related to the peak electric field, E_p, by [*Uman et al.*, 1975; *Orville*, 1991]:

$$E_p = \frac{I_p V_{rs}}{2 \pi r \epsilon_o c^2} \tag{B.3}$$

where V_{rs} is the velocity of the return stroke ($\sim 1.2 \times 10^8$ m/s [*Idone and Orville*, 1982]), r is the distance between the return stroke and the electric field meter, ϵ_o is the permittivity of free space, and c is the velocity of light.

The range-normalized signal strength (S_{RN}) which is reported by the NLDN in "LLP units" is related to the raw signal strength (S) recorded at the sensor by the following signal propagation model [*Cummins et al.*, 1998]:

$$S_{RN} = C\, S \left(\frac{r}{l}\right)^p e^{\left(\frac{r-l}{A}\right)} \tag{B.4}$$

where r is the range in kilometers, l is the normalization range (100 km), p is an attenuation exponent, A is the e-folding length for attenuation, and C is a constant. Currently, the NLDN signal strengths are based on $p = 1.13$ and $A = 10^5$ km [*Cummins et al.*, 1998].

The peak current is determined from NLDN data by the following relationship:

$$I_p = \frac{S_{RN}}{5.4} \tag{B.5}$$

Substituting Equation B.5 into Equation B.3 for $r = 100$ km (the normalization range) yields the result that one LLP unit of signal strength would produce a field change of 0.045 V/m at 100 km range. Assuming that $S = E_p$, then $C = 1/0.045$ in Equation B.4. Solving for E_p:

$$E_p = 0.045\, S_{RN} \left(\frac{100}{r}\right)^{1.13} e^{\left(\frac{100-r}{1 \times 10^5}\right)} \tag{B.6}$$

where r is in units of kilometers.

Fast Antenna Calibration on June 22, 1997 at KSC					
Time [UT]	S_{RN} [LLP]	Range [km]	E_p [V/m]	Digital units	Number of digital units per V/m
1:39:55.845158	−120.0	83	−6.64	−1221	183.9
1:41:19.120782	−145.9	83	−8.07	−1556	194.1
1:41:33.758866	−105.5	74	−6.68	−1206	180.5
1:41:49.389430	−65.6	81	−3.77	−620	164.4
1:42:21.406597	−81.6	83	−4.54	−775	170.7
1:42:40.669062	−116.5	87	−6.13	−1191	194.3
1:44:33.520315	−99.3	119	−3.67	−671	182.8
1:44:59.627920	+55.0	93	+2.68	+500	186.6
					Average: 182±10 units/V/m

Table B.2: Several "CG" strokes recorded by the NLDN on June 22, 1997 were used to calibrate the fast antenna data. For each stroke, the LLP signal strength (S_{RN}) and range (r) were used to calculate a predicted peak electric field (E_p). The change in digital units of recorded data (12-bit: 0–4095) produced by the electric field change of amplitude E_p was used to calculate the number of digital units which corresponded to a 1 V/m field change.

The values of p and A used to derive Equation B.6 are based on data collected in Florida and may not be valid for other regions. Furthermore, Equation B.6 should only be used to predict E_p between about 50 and 200 km range (*K. Cummins,* private communication, 1999). The attenuation factors at other ranges may be different.

Table B.2 shows the electric field calibration which was used for the KSC data. Several strokes near the optimum 100 km normalization range occurred around the time of the 1:42:57 UT sprite-producing dicharge which was analyzed in Section 3.6. The LLP signal strengths reported by the NLDN were used to calculate a peak electric field, E_p, at the range of the electric field meter from the stroke. A change in the fast antenna electric field data, recorded as 12-bit values (0–4095), was produced by each stroke. The average ratio of the changes in digital units to the E_p values showed that a field change of 1 V/m produced a change of 182±10 digital units in the fast antenna data. Thus, the full-scale range of the recorded fast-antenna data was $4096/(182 \pm 10) = 22.5 \pm 1.3$ V/m.

On June 22, 1997, the fast antenna was operated in a 10x mode of amplification

relative to the slow antenna. The slow antenna data was also digitally sampled with 12-bit resolution. Since the 12-bit analog-to-digital converters for the slow and fast antenna data have nearly identical full-scale input voltage ranges, a 22.5 ± 1.3 V/m range on the fast antenna translated into a 225 ± 13 V/m full-scale range on the slow antenna.

Langmuir Laboratory, 1997

Electric and magnetic field data was acquired on the Magdalena Ridge at Langmuir Laboratory in 1997. The electric field would have been significantly enhanced on the ridge. The NLDN data will be used to determine the amount of electric field enhancement caused by the ridge and to properly calibrate the magnetic field instrument.

The magnetic field instrument was borrowed from Chris Barrington-Leigh of Stanford University. The magnetic field sensor consisted of a wire which was looped multiple times around the perphery of a square frame. The absolute sensitivity of the wire-loop and amplifier was calibrated. It was found that a change of 1.5 nT in the magnetic field component normal to the plane of the wire loop produced an output of ~ 1 V. However, significant errors may exist in the calibration procedure which was used in 1997 (*C. Barrington-Leigh,* private communication, 1998).

A well known result from electrodynamics is that at sufficient distances from an electromagnetic source, the magnetic field is related to the electric field by the simple relationship, $B = E/c$. Substituting this relationship into Equation B.3 gives:

$$B_p = \frac{\mu_o \, I_p \, V_{rs}}{2 \, \pi \, r \, c} \tag{B.7}$$

where B_p is the peak magnetic field and μ_o is the free-space permeability ($\mu_o \epsilon_o = 1/c^2$).

Near the ground, the electric field will be vertical while the magnetic field will be tangential to a circle centered on the current source. The magnetic field which is measured by the instrument is the component which is normal to the plane of the loop. B_p is related to the measured peak magnetic field, B_{pm}, by the trigonometric relationship:

$$B_p = \frac{B_{pm}}{\sin\left(\theta_l - \theta_s\right)} \tag{B.8}$$

where θ_l is the azimuth of the normal to the plane of the loop and θ_s is the azimuth to the source current. The null in sensitivity ($B_{pm} \rightarrow 0$) occurs when these azimuths

are either identical or 180° apart.

The θ_l value could have been determined from a compass, but this was not done accurately. The loop orientation can be found accurately by determining where θ_l produces measured B_p values which are consistent with the predicted B_p values.

Figure B.6 shows the standard deviation of the ratio of B_p calculated from Equation B.8 based on measured B_{pm} values and the θ_s values provided by NLDN to B_p calculated from Equation B.7 based on the NLDN I_p and r values. The standard deviation of the ratio is shown as a function of θ_l for the three different days on which high-speed video of sprites was obtained: October 3 (blue), October 6 (red), and October 7 (green) 1997. The agreement between the magnetic field values calculated by the two techniques increases as the standard deviation decreases. The minimum standard deviation of the ratio near $\theta_l = 20°$ azimuth corresponds to the orientation of the normal to the plane of the loop on all three days. The October 3 and 7 data is particularly sensitive to loop orientation since there were storms near one of the two nulls in loop sensitivity on both days, albeit for a different null on each day.

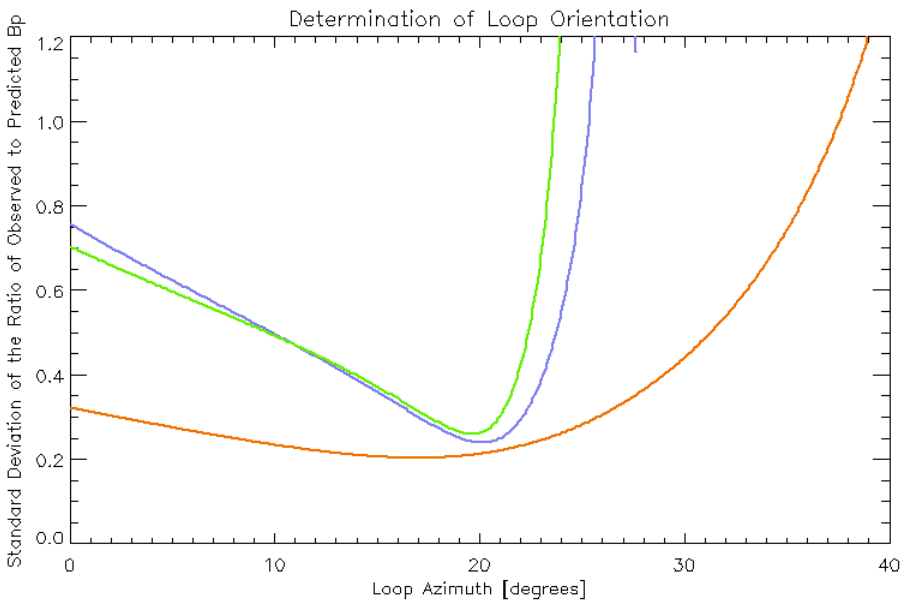

Figure B.6: The standard deviation of the ratio of the peak magnetic field, B_p, calculated from measurements to B_p calculated from NLDN data for three different days: October 3 (blue), October 6 (red), and October 7 (green) 1997. The minimum near 20° azimuth corresponds to the orientation of the normal to the plane of the loop on all three days.

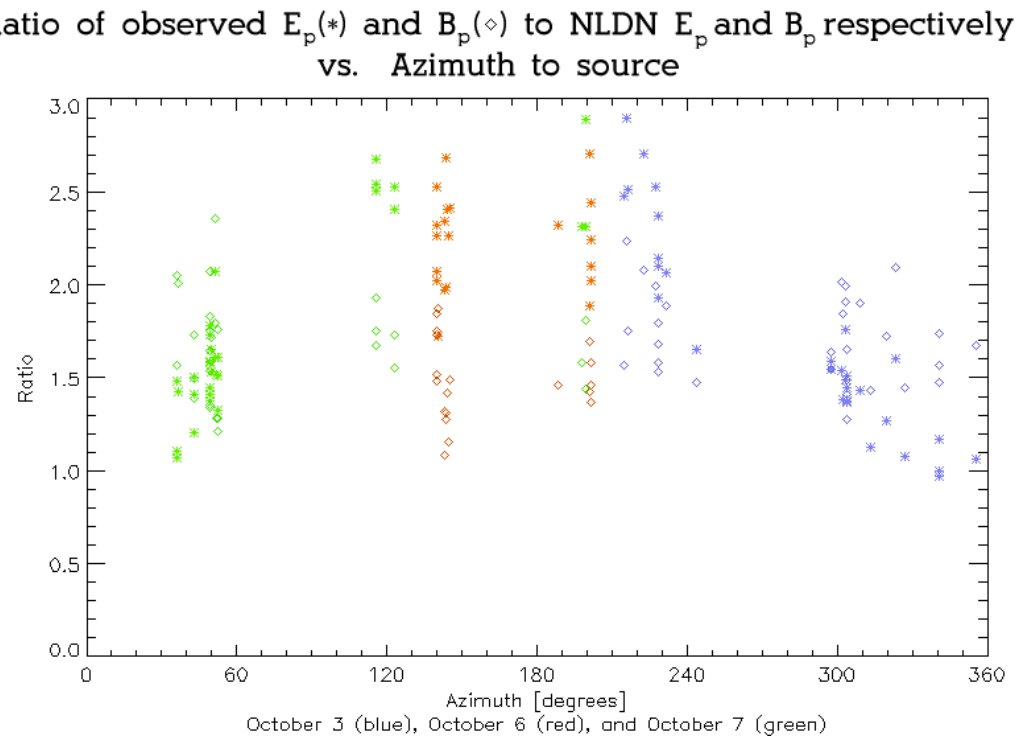

Figure B.7: The ratio of the observed E_p and B_p values to the E_p and B_p values calculated from NLDN data respectively, is shown as a function of source azimuth. The observed B_p values are about 1.6 times greater than predicted from NLDN data for all source azimuths. The observed E_p values are also enhanced over the values predicted from NLDN data, but the enhancement factor is a function of source azimuth.

Equations B.7 and B.8 were used to calculate the expected B_p values based on NLDN data and a loop orientation of 20°. Equation B.3 was used to calculate the expected E_p values based on NLDN data. Figure B.7 shows the ratio of the observed E_p and B_p values to the E_p and B_p values calculated from NLDN data, respectively, as a function of azimuth to the stroke. The observed B_p values are about 1.6 times greater than predicted and this enhancement factor appears to be independent of the azimuth to the source.

A new calibration factor of 1.5/1.6 = 0.94 nT/V was used to convert digitized magnetic data (with a known conversion factor between digital units and volts) to corresponding magnetic field values. The charge moment change calculations reported in Chapter 5 were based on the 0.94 nT/V conversion factor. The net effect of the NLDN-based calibration was to reduce the calculated charge moment values by about

40% from those based on the calibration of the magnetic field instrument.

No attempt was made to account for attenuation (see Equation B.4) in the calculations, since the attenuation exponents for the region around Langmuir are not known. However, NLDN strokes between 50 and 200 km range were analyzed using the Florida-based attenuation factors to see how including attenuation might effect the calibration. It was found that the observed B_p values were about 1.85 times greater than the predicted B_p values, an enhancement which is only 16% greater than the enhancement which was calculated without any attenuation.

The observed E_p values were roughly a factor of two greater than the E_p values based on NLDN data. The electric field enhancement was expected since the electric field meter was on a mountain ridge. However, the variation of the enhancement factor with source azimuth was not expected. It is speculated that this variation may be due to the presence of nearby metallic trailers and other conductive obstructions. The magnetic loop antenna was placed in an open field further away from the balloon hangar, so it would not have been subject to the same complications.

Langmuir Laboratory, 1998

NLDN data with precise timing and LLP signal strengths was not available in 1998. Also, the electric field meter was placed at a different location relative to 1997. The field meter was situated on top of the balloon hangar where there were fewer metallic obstructions which could produce an azimuthal dependency in sensitivity. Also, the field meter was placed away from the edges of the hangar so that an electric field enhancement due to the building would be minimized.

Distant sferics recorded by the electric field meter at Langmuir were intercompared with the same sferic events recorded by an electric field meter at Marx Brook's residency in Socorro. It was found that the electric field recorded on the ridge at Langmuir was systematically 1.93 ± 0.10 times greater than that recorded in Socorro on relatively level terrain. The electric field recordings of the daytime sprite-producing discharges and daytime sprites were first reduced by this enhancement factor before the charge moment calculations were performed (see Chapter 4).

Appendix C

Effect of Ionosphere on Static Field Measurements

It was shown in Section 2.5.1 that charge images due to the presence of the ionosphere increased the electric field above the source charge. It was also shown that the total number of images in a static electric field calculation was infinite, though the electric field rapidly converged with increasing image index to a final value at altitudes where sprites were likely to initiate. In this section, the effect of ionospheric images on static electric field observations near the ground at some distance from the source will be examined. The image index notation will be the same as in Figure 2.7a.

The distance to the estimated charge removal center of the sprite-producing discharges listed in Table 3.1 was about 80 km. Figure C.1 shows the convergence of the calculated electric field at 80 km range to a "final" electric field value as a function of the image index. Unlike the electric field at high altitude (see Figure 2.7b), the electric field at ground level is decreased by the presence of the ionosphere.

The calculated electric field converges to a final electric field value in Figure C.1, but the rate of convergence at a range of 80 km at ground level is slower than the rate of convergence at an altitude of 78 km MSL above the discharge (see Figure 2.7b). However, one should not use a large summation when attempting to determine a charge moment from an observed electric field since the images are not set up instantaneously. Rather, each successive image is delayed by at least the light propagation time between the ground and the ionosphere ($\Delta t \simeq 81/300 = 0.27$ ms).

In order to calculate the charge moments in Table 3.1 at delays of 1 and 4 ms after the return stroke, the product of the number of images with the light propagation time between the ground and ionosphere was not allowed to be greater than the

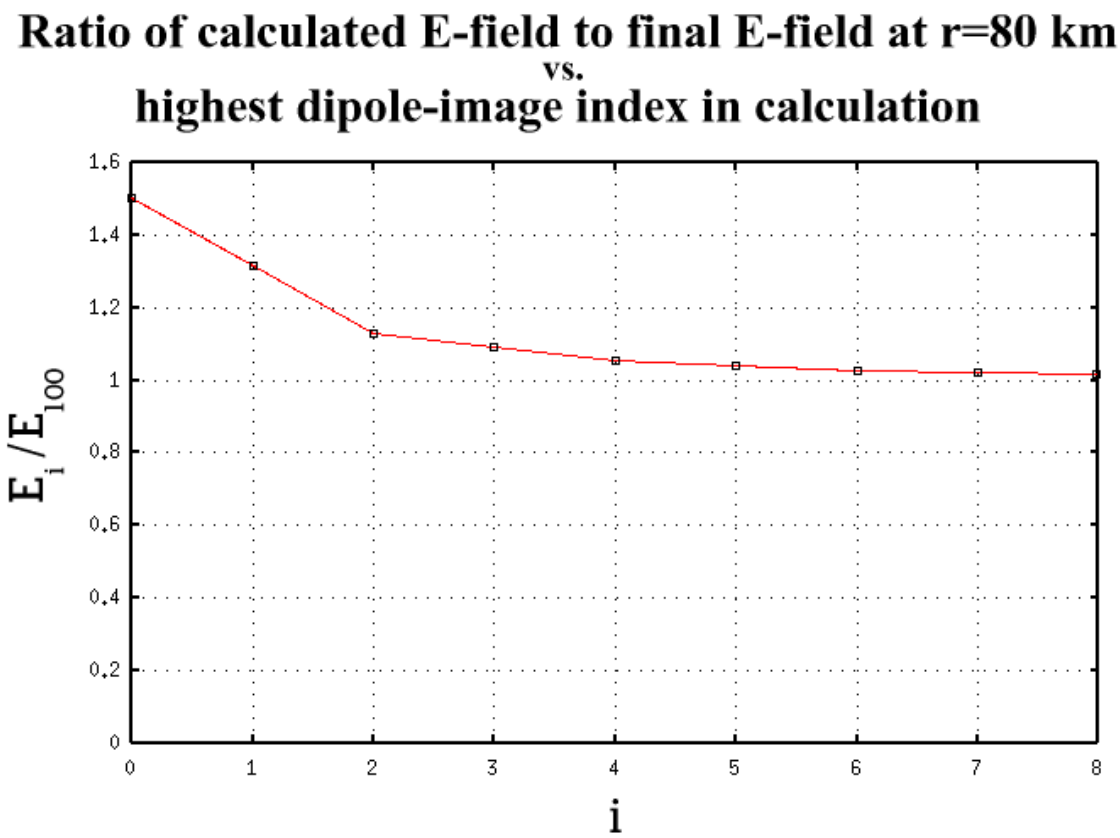

Figure C.1: The electric field is calculated at ground-level ($Z = 0$ km) at a range, r, of 80 km from the source charge. The rate of convergence of the calculated electric field to a "final" electric field value is shown as a function of the number of successive image pairs included in the calculation (with $i = 0$ corresponding to a calculation based only on the source and its below-ground image). The "final" electric field was calculated for a summation up to $i = 100$.

post return stroke delays. To complicate matters, the charge moment of the sprite-producing discharges increased throughout the interval after the return stroke instead of being "suddenly" introduced at $t = 0$. Thus, the number of images used in the static field calculation had to reflect the fact that some of the quasistatic electric field change might have occurred with less time for images to form relative to earlier portions of the field change. For the 1 ms delays, the highest image index included in the charge moment calculation shown in Table 3.1 was 3. The highest image index for the 4 ms delays was 7.

Near the source charge the effect of the ionosphere can be neglected since the electric field from the charge will dominate. As the range to the source is increased, the effect of the ionosphere images will become increasingly important. The ratio of the electric field calculated without the presence of an ionosphere, E_0, to the "final" electric field, E_{100}, is shown as a function of range in Figure C.2. At 40 km range, the ionosphere only decreases the static electric field by at most 7%. At 100 km range, however, the ionosphere reduces the static electric field by about a factor of two.

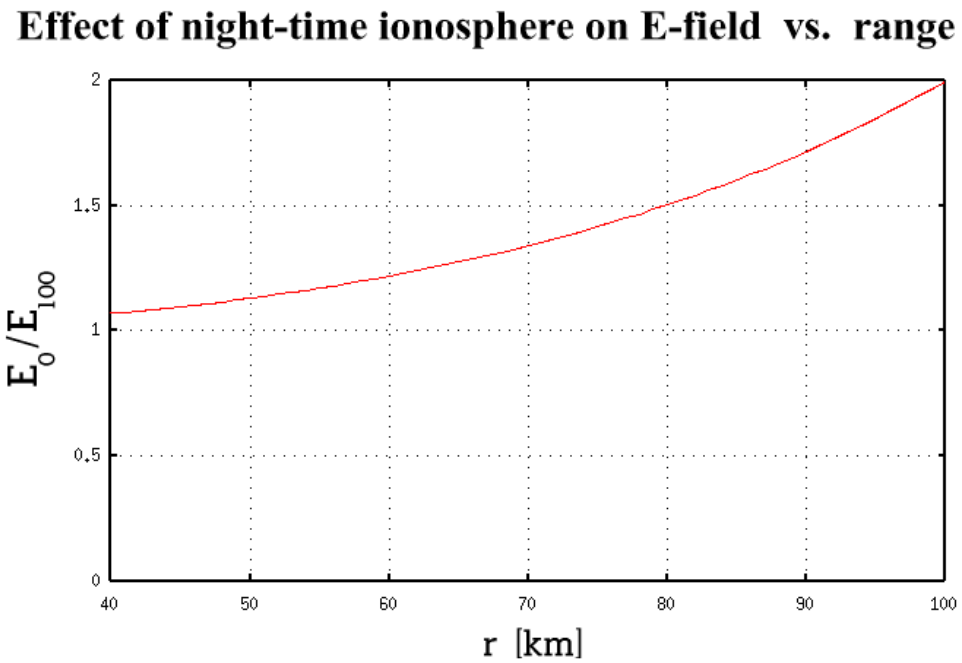

Figure C.2: The ratio of the electric field without the presence of the ionosphere to the field calculated with an ionosphere at $Z = 81$ km (night-time) is shown as a function of range.

Bibliography

Allen, N. L., and A. Ghaffar, The conditions required for the propagation of a cathode-directed positive streamer in air, *J. Phys. D: Appl. Phys.*, *28*, 331–337, 1995.

Armstrong, R. A., J. A. Shorter, M. J. Taylor, D. M. Suszcynsky, W. A. Lyons, and L. S. Jeong, Photometric measurements in the SPRITES '95 & '96 campaigns of nitrogen second positive (399.8 nm) and first negative (427.8 nm) emissions, *J. Atmos. Sol. Terr. Phys.*, *60*, 787–799, 1998.

Barrington-Leigh, C. P., and U. S. Inan, Elves triggered by positive and negative lightning discharges, *Geophys. Res. Lett.*, *26*, 683–686, 1999.

Barrington-Leigh, C. P., U. S. Inan, M. Stanley, and S. Cummer, Sprites directly triggered by negative lightning discharges, *Geophys. Res. Lett.*, *26*, 3605–3608, 1999.

Barrington-Leigh, C. P., U. S. Inan, and M. Stanley, Identification of sprites and elves with intensified video and broadband array photometry, *J. Geophys. Res.*, 2000, in review.

Bazelyan, E. M., and Y. P. Raizer, *Spark Discharge*, CRC Press, Boca Raton, Florida, 1997.

Bell, T. F., V. P. Pasko, and U. S. Inan, Runaway electrons as a source of Red Sprites in the mesosphere, *Geophys. Res. Lett.*, *22*, 2127–2130, 1995.

Bell, T. F., S. C. Reising, and U. S. Inan, Intense continuing currents following positive cloud-to-ground lightning associated with red sprites, *Geophys. Res. Lett.*, *25*, 1285–1288, 1998.

Berger, K., Methods and results of research on lightning on Mount San Salvatore 1963-1971, *Bull. ASE*, *63*, 1403–1422, 1972.

Boccippio, D. J., E. R. Williams, S. J. Heckman, W. A. Lyons, and I. Baker, Sprites, ELF transients and positive ground strokes, *Science*, *269*, 1088–1091, 1995.

Boccippio, D. J., S. Heckman, and S. J. Goodman, A diagnostic analysis of the Kennedy Space Center LDAR network, in *Proc. 11th Int. Conf. on Atmos. Elec.*, pp. 254–257, Guntersville, Alabama, 1999.

Boeck, W. L., O. H. Vaughan, R. Blakeslee, B. Vonnegut, and M. Brook, Lightning induced brightening in the airglow layer, *Geophys. Res. Lett.*, *19*, 99–102, 1992.

Boeck, W. L., O. H. Vaughan, R. J. Blakeslee, B. Vonnegut, M. Brook, and J. McKune, Observations of lightning in the stratosphere, *J. Geophys. Res.*, *100*, 1465–1475, 1995.

Brook, M., N. Kitagawa, and E. J. Workman, Quantitative study of strokes and continuing currents in lightning discharges to ground, *J. Geophys. Res.*, *67*, 649–659, 1962.

Brook, M., M. Nakano, and P. Krehbiel, The electrical structure of the Hokuriku winter thunderstorms, *J. Geophys. Res.*, *87*, 1207–1215, 1982.

Brook, M., M. Stanley, P. Krehbiel, W. Rison, C. B. Moore, C. Barrington-Leigh, D. Suszcynsky, T. Nelson, and W. Lyons, Correlated electric field, video, and photometric evidence of charge transfer within sprites, in *Eos Trans. AGU*, vol. 78 of *Fall Meet. Suppl.*, p. F82, AGU, 1997.

Cummer, S. A., and U. S. Inan, Measurements of charge transfer in sprite-producing lightning using ELF radio atmospherics, *Geophys. Res. Lett.*, *24*, 1731–1734, 1997.

Cummer, S. A., and U. S. Inan, Modeling ELF radio atmospheric propagation and extracting lightning currents from ELF observations, *Radio Science*, *35*, 385–394, 2000.

Cummer, S. A., and M. Stanley, Submillisecond resolution lightning currents and sprite development: observations and implications, *Geophys. Res. Lett.*, *26*, 3205–3208, 1999.

Cummer, S. A., U. S. Inan, T. F. Bell, and C. P. Barrington-Leigh, ELF radiation produced by electrical currents in sprites, *Geophys. Res. Lett.*, *25*, 1281–1284, 1998.

Cummins, K. L., M. J. Murphy, E. A. Bardo, W. L. Hiscox, R. B. Pyle, and A. E. Pifer, A combined TOA/MDF technology upgrade of the U.S. National Lightning Detection Network, *J. Geophys. Res.*, *103*, 9035–9044, 1998.

Dhali, S. K., and P. F. Williams, Numerical simulation of streamer propagation in nitrogen at atmospheric pressure, *Phys. Rev. A*, *31*, 1219–1221, 1985.

Farrell, W. M., and M. D. Desch, Cloud-to-stratosphere lightning discharges: A radio emission model, *Geophys. Res. Lett.*, *19*, 665–668, 1992.

Fernsler, R. F., and H. L. Rowland, Models of lightning-produced sprites and elves, *J. Geophys. Res.*, *101*, 29,653–29,662, 1996.

Fisher, R. J., Characteristics of the positive lightning flash, *Sandia Report*, 1988, SAND87-2615.

Fishman, J., et al., Discovery of intense gamma-ray flashes of atmospheric origin, *Science*, *264*, 1313–1316, 1994.

Franz, R. C., R. J. Nemzek, and J. R. Winckler, Television image of a large electrical discharge above a thunderstorm system, *Science*, *249*, 48–51, 1990.

Fukunishi, H., Y. Takahashi, M. Kubota, K. Sakanoi, U. S. Inan, and W. A. Lyons, Elves: Lightning-induced transient luminous events in the lower ionosphere, *Geophys. Res. Lett.*, *23*, 2157–2160, 1996.

Greifinger, C., and P. Greifinger, Transient ULF electric and magnetic fields following a lightning discharge, *J. Geophys. Res.*, *81*, 2237–2247, 1976.

Griffiths, R. F., and C. T. Phelps, The effects of air pressure and water vapour content on the propagation of positive corona streamers, and their implications to lightning initiation, *Quart. J. R. Met. Soc.*, *102*, 419–426, 1976.

Hale, L. C., Coupling of ELF/ULF energy from lightning and MeV particles to the middle atmosphere, ionosphere, and global circuit, *J. Geophys. Res.*, *99*, 21,089–21,096,, 1994.

Hampton, D. L., M. J. Heavner, E. M. Wescott, and D. D. Sentman, Optical spectral characteristics of sprites, *Geophys. Res. Lett.*, *23*, 89–92, 1996.

Hayenga, C. O., and J. W. Warwick, Two-dimensional interferometric positions of VHF lightning sources, *J. Geophys. Res.*, *86*, 7451–7462, 1981.

Holzworth, R. H., M. C. Kelley, C. L. Siefring, L. C. Hale, and J. D. Mitchell, Electrical measurements in the atmosphere and the ionosphere over an active thunderstorm, 2. direct current electric fields and conductivity, *J. Geophys. Res.*, *90*, 9824–9830, 1985.

Houze, R. A. J., B. F. Smull, and P. Dodge, Mesoscale organization of springtime rainstorms in Oklahoma, *Monthly Weather Review*, *118*, 613–654, 1990.

Huang, E., E. Williams, R. Boldi, S. Heckman, W. Lyons, M. Taylor, T. Nelson, and C. Wong, Criteria for sprites and elves based on Schumann resonance observations, *J. Geophys. Res.*, *104*, 16,943–16,964, 1999.

Idone, V. P., and R. E. Orville, Lightning return stroke velocities in the thunderstorm research international program (trip), *J. Geophys. Res.*, *87*, 4903–4915, 1982.

Inan, U. S., T. F. Bell, and J. V. Rodriguez, Heating and ionization of the lower ionosphere by lightning, *Geophys. Res. Lett.*, *18*, 705–708, 1991.

Inan, U. S., C. Barrington-Leigh, S. Hansen, V. S. Glukhov, T. F. Bell, and R. Rairden, Rapid lateral expansion of optical luminosity in lightning-induced ionospheric flashes referred to as "elves", *Geophys. Res. Lett.*, *24*, 583–586, 1997.

Krehbiel, P., X.-M. Shao, M. Stanley, G. Gray, S. McCrary, R. Scott, J. Lopez, C. Rhodes, and D. Holden, Interferometer observations of natural and triggered lightning at Langmuir Laboratory, in *Eos Trans. AGU*, vol. 75 of *Fall Meeting Supplement*, p. 99, AGU, 1994.

Krehbiel, P. R., An analysis of the electric field change produced by lightning, Ph.D. thesis, University of Manchester, 1981.

Krehbiel, P. R., The electrical structure of thunderstorms, in *The Earth's Electrical Environment*, Studies in Geophysics, chap. 8, pp. 90–113, Nat. Acad. Press, Washington D.C., 1986.

Krehbiel, P. R., M. Brook, and R. A. McCrory, An analysis of the charge structure of lightning discharges to ground, *J. Geophys. Res.*, *84*, 2432–2456, 1979.

Krehbiel, P. R., X.-M. Shao, and E. R. Williams, On the ability of positive CG lightning to initiate red sprites, in *Proc. 10th Int. Conf. on Atmos. Elec.*, Osaka, Japan, 1996.

Krehbiel, P. R., R. J. Thomas, W. Rison, T. Hamlin, J. Harlin, and M. Davis, GPS-based mapping system reveals lightning inside storms, *EOS*, *81*, 21–22,25, 2000.

Loeb, L. B., and J. M. Meek, The mechanism of spark discharge in air at atmospheric pressure. II, *J. Appl. Phys.*, *11*, 459–474, 1940.

Lyons, W. A., Characteristics of luminous structures in the stratosphere above thunderstorms as imaged by low-light video, *Geophys. Res. Lett.*, *21*, 875–878, 1994.

Lyons, W. A., Sprite observations above the U.S. High Plains in relation to their parent thunderstorm systems, *J. Geophys. Res.*, *101*, 29,641–29,652, 1996.

Lyons, W. A., T. E. Nelson, R. A. Armstrong, E. R. Williams, D. M. Suszcynsky, R. Strabley, M. Taylor, and L. Gardner, Characteristics of thunderstorms and lightning flashes which produce mesospheric transient luminous events, in *Proc. 11th Int. Conf. on Atmos. Elec.*, pp. 84–87, Guntersville, Alabama, 1999.

MacGorman, D. R., and W. D. Rust, *The Electrical Nature of Storms*, Oxford University Press, New York, 1998.

Mach, D. M., and W. D. Rust, Two-dimensional velocity, optical risetime, and peak current estimates for natural positive lightning return strokes, *J. Geophys. Res.*, *98*, 2635–2638, 1993.

Maier, L., C. Lennon, T. Britt, and S. Schaefer, Lightning Detection and Ranging (LDAR) system performance analysis, in *Proc. 6th Conf. on Aviation Weather Systems*, American Meteorological Society, Dallas, Texas, 1995a.

Maier, L., C. Lennon, P. Krehbiel, M. Stanley, and M. Robison, Comparison of lightning and radar observations from the KSC LDAR and NEXRAD radar systems, in *27th Conference on Radar Meteorology*, pp. 648–650, American Meteorological Society, Vail, Colorado, 1995b.

Marshall, L. H., L. C. Hale, C. L. Croskey, and W. A. Lyons, Electromagnetics of sprite- and elve-associated sferics, *J. Atmos. Sol. Terr. Phys.*, *60*, 771–786, 1998.

Marshall, T. C., and W. D. Rust, Two types of vertical electrical structures in stratiform precipitation regions of mesoscale convective systems, *Bull. Amer. Meteor. Soc.*, *74*, 2159–2170, 1993.

Marshall, T. C., W. D. Rust, W. P. Winn, and K. E. Gilbert, Electrical structure in two thunderstorm anvil clouds, *J. Geophys. Res.*, *94*, 2171–2181, 1989.

Marshall, T. C., M. Stolzenburg, and W. D. Rust, Electric field measurements above mesoscale convective systems, *J. Geophys. Res.*, *101*, 6979–6996, 1996.

Mazur, V., Triggered lightning strikes to aircraft and natural intracloud discharges, *J. Geophys. Res.*, *94*, 3311–3325, 1989.

Mazur, V., and L. H. Ruhnke, Common physical processes in natural and artificially triggered lightning, *J. Geophys. Res.*, *98*, 12,913–12,930, 1993.

Mazur, V., X.-M. Shao, and P. R. Krehbiel, "Spider" lightning in intracloud and positive cloud-to-ground flashes, *J. Geophys. Res.*, *103*, 19,811–19,822, 1998.

Mende, S. B., R. L. Rairden, G. R. Swenson, and W. A. Lyons, Sprite spectra: N_2 1 PG band identification, *Geophys. Res. Lett.*, *22*, 2633–2636, 1995.

Mende, S. B., R. L. Rairden, H. T. Su, R. R. Hsu, T. H. Allin, T. Neubert, E. A. Gerken, and U. S. Inan, Coordinated observations of sprite morphology during the 1999 sprite campaign, in *EOS Trans. AGU*, vol. 80 of *Fall Meeting Supplement*, p. F225, AGU, 1999.

Ogawa, T., and M. Brook, The mechanism of the intracloud lightning discharge, *J. Geophys. Res.*, *69*, 5141–5150, 1964.

Orville, R. E., Calibration of a magnetic direction finding network using measured triggered lightning return stroke peak currents, *J. Geophys. Res.*, *96*, 17,135–17,142, 1991.

Pasko, V. P., U. S. Inan, Y. N. Taranenko, and T. F. Bell, Heating, ionization, and upward discharges in the mesosphere due to intense quasi-electrostatic thundercloud fields, *Geophys. Res. Lett.*, *22*, 365–368, 1995.

Pasko, V. P., U. S. Inan, and T. F. Bell, Sprites as luminous columns of ionization produced by quasi-electrostatic thundercloud fields, *Geophys. Res. Lett.*, *23*, 649–652, 1996.

Pasko, V. P., U. S. Inan, and T. F. Bell, Sprites as evidence of vertical gravity wave structures above mesoscale thunderstorms, *Geophys. Res. Lett.*, *24*, 1735–1738, 1997a.

Pasko, V. P., U. S. Inan, T. F. Bell, and Y. N. Taranenko, Sprites produced by quasi-electrostatic heating and ionization in the lower ionosphere, *J. Geophys. Res.*, *102*, 4529–4561, 1997b.

Pasko, V. P., U. S. Inan, and T. F. Bell, Spatial structure of sprites, *Geophys. Res. Lett.*, *25*, 2123–2126, 1998a.

Pasko, V. P., U. S. Inan, T. F. Bell, and S. C. Reising, Mechanism of ELF radiation from sprites, *Geophys. Res. Lett.*, *25*, 3493–3496, 1998b.

Pasko, V. P., U. S. Inan, and T. F. Bell, Mesospheric electric field transients due to tropospheric lightning discharges, *Geophys. Res. Lett.*, *26*, 1247–1250, 1999.

Pasko, V. P., U. S. Inan, and T. F. Bell, Fractal structure of sprites, *Geophys. Res. Lett.*, *27*, 497–500, 2000.

Phelps, C. T., Positive streamer system intensification and its possible role in lightning initiation, *J. Atmos. Terr. Phys.*, *36*, 103–111, 1974.

Pierce, E. T., Electrostatic field-changes due to lightning discharges, *Quart. J. Roy. Meteorol. Soc.*, *81*, 211–228, 1955.

Raether, H., *Electron Avalanches and Breakdown in Gases*, Butterworths Advanced Physics Series, Butterworth Inc., Washington, D.C., 1964.

Rairden, R. L., and S. B. Mende, Time resolved sprite imagery, *Geophys. Res. Lett.*, *22*, 3465–3468, 1995.

Raizer, Y. P., G. M. Milikh, M. N. Schneider, and S. V. Novakovski, Long streamer in the upper atmosphere above thundercloud, *J. Phys. D: Appl. Phys.*, *31*, 3255–3264, 1998.

Rawer, K., D. Bilitza, and S. Ramakrishnan, Goals and status of the International Reference Ionosphere, *Rev. Geophys. Space Sci.*, *16*, 177–181, 1978.

Reid, G. C., Electrical structure of the middle atmosphere, in *The Earth's Electrical Environment*, Studies in Geophysics, chap. 13, pp. 183–194, Nat. Acad. Press, Washington D.C., 1986.

Reising, S. C., U. S. Inan, T. F. Bell, and W. A. Lyons, Evidence for continuing currents in sprite-producing lightning flashes, *Geophys. Res. Lett.*, *23*, 3639–3642, 1996.

Reising, S. C., U. S. Inan, and T. F. Bell, ELF sferic energy as a proxy indicator for sprite occurrence, *Geophys. Res. Lett.*, *26*, 987–990, 1999.

Rhodes, C. T., X. M. Shao, P. R. Krehbiel, R. J. Thomas, and C. O. Hayenga, Observations of lightning phenomena using radio interferometry, *J. Geophys. Res.*, *99*, 13,059–13,082, 1994.

Richard, P., and G. Auffray, VHF-UHF interferometric measurements, applications to lightning discharge mapping, *Radio Science*, *20*, 171–192, 1985.

Rison, W., R. J. Thomas, P. R. Krehbiel, T. Hamlin, and J. Harlin, A GPS-based three-dimensional lightning mapping system: Initial observations in central New Mexico, *Geophys. Res. Lett.*, *26*, 3573–3576, 1999.

Rodger, C. J., Red sprites, upward lightning, and VLF perturbations, *Rev. Geophys.*, *37*, 317–336, 1999.

Roussel-Dupré, R. A., and A. V. Gurevich, On runaway breakdown and upward propagating discharges, *J. Geophys. Res.*, *101*, 2297, 1996.

Sentman, D. D., and E. M. Wescott, Observations of upper atmospheric optical flashes recorded from an aircraft, *Geophys. Res. Lett.*, *20*, 2857–2860, 1993.

Sentman, D. D., E. M. Wescott, D. L. Osborne, D. L. Hampton, and M. J. Heavner, Preliminary results from the Sprites94 aircraft campaign: 1. Red sprites, *Geophys. Res. Lett.*, *22*, 1205–1208, 1995.

Sentman, D. D., E. M. Wescott, H. C. Stenbaek-Nielsen, M. J. Heavner, D. R. Moudry, and F. T. S. Sabbas, Observations of gravity waves associated with a sprite-producing storm, in *Eos Trans. AGU*, vol. 80 of *Fall Meeting Supplement*, p. F227, AGU, 1999.

Shao, X.-M., Development and structure of lightning discharge observed by VHF radio interferometer, Ph.D. thesis, New Mexico Institute of Mining and Technology, 1994.

Shao, X. M., and P. R. Krehbiel, The spatial and temporal development of intracloud lightning, *J. Geophys. Res.*, *101*, 26,641–26,668, 1996.

Shao, X. M., M. Stanley, P. Krehbiel, W. Rison, G. Gray, and V. Mazur, Results of observations with the New Mexico Tech VHF lightning interferometer, in *Proc. 10th Int. Conf. on Atmos. Elec.*, pp. 317–320, Osaka, Japan, 1996.

Stanley, M., P. Krehbiel, L. Maier, and C. Lennon, Comparison of lightning observations from the KSC LDAR system with NEXRAD radar observations, in *Proc. 10th Int. Conf. on Atmos. Elec.*, pp. 224–227, Osaka, Japan, 1996a.

Stanley, M., P. Krehbiel, W. Rison, C. Moore, M. Brook, and O. H. Vaughan, Observations of sprites and jets from Langmuir Laboratory, New Mexico, in *EOS Trans. AGU*, vol. 77 of *Fall Meeting Supplement*, p. F69, AGU, 1996b.

Stanley, M., P. Krehbiel, M. Brook, C. Moore, W. Rison, and B. Abrahams, High speed video of initial sprite development, *Geophys. Res. Lett.*, *26*, 3201–3204, 1999.

Stanley, M., M. Brook, P. Krehbiel, and S. A. Cummer, Detection of daytime sprites via a unique sprite ELF signature, *Geophys. Res. Lett.*, *27*, 871–874, 2000.

Stanley, M., et al., A 47-stroke triggered lightning discharge, in *Eos Trans. AGU*, vol. 75 of *Fall Meeting Supplement*, p. 104, AGU, 1994.

Stolzenburg, M., T. C. Marshall, W. D. Rust, and B. F. Small, Horizontal distribution of electrical and meteorological conditions across the stratiform region of a mesoscale convective system, *Mon. Weather Rev.*, *122*, 1777–1797, 1994.

Sukhorukov, A. I., and P. Stubbe, On ELF pulses from remote lightnings triggering sprites, *Geophys. Res. Lett.*, *24*, 1639–1642, 1997.

Suszcynsky, D. M., R. Roussel-Dupré, W. A. Lyons, and R. A. Armstrong, Blue-light imagery and photometry of sprites, *J. Atmos. Sol. Terr. Phys.*, *60*, 801–809, 1998.

Taranenko, Y., and R. Roussel-Dupré, High altitude discharges and gamma-ray flashes: A manifestation of runaway air breakdown, *Geophys. Res. Lett.*, *23*, 571–574, 1996.

Taranenko, Y. N., U. S. Inan, and T. F. Bell, Optical signatures of lightning-induced heating of the D region, *Geophys. Res. Lett.*, *19*, 1815–1818, 1992.

Taranenko, Y. N., U. S. Inan, and T. F. Bell, The interaction with the lower ionosphere of electromagnetic pulses from lightning: Excitation of optical emissions, *Geophys. Res. Lett.*, *20*, 2675–2678, 1993.

Thomas, R. J., P. R. Krehbiel, W. Rison, T. Hamlin, J. Harlin, and D. Shown, VHF source powers radiated by lightning discharges, *Geophys. Res. Lett.*, 2000, in press.

Uman, M. A., *The Lightning Discharge*, vol. 39 of *International Geophysics Series*, Academic Press, Orlando, 1987.

Uman, M. A., D. K. McLain, and E. P. Krider, The electromagnetic radiation from a finite antenna, *Am. J. Phys.*, *43*, 33–38, 1975.

Valdivia, J. A., G. M. Milikh, and K. Papadopoulos, Model of red sprites due to intracloud fractal lightning discharges, *Radio Science*, *33*, 1655–1668, 1998.

Vaughan, O. H., and B. Vonnegut, Recent observations of lighning discharges from the top of a thundercloud into the clear air above, *J. Geophys. Res.*, *94*, 13,179–13,182, 1989.

Vaughan, O. H., R. Blakeslee, W. L. Boeck, B. Vonnegut, M. Brook, and J. McKune, A cloud-to-space lightning as recorded by the Space Shuttle payload-bay TV cameras, *Mon. Weather Rev.*, *120*, 1459–1461, 1992.

Vonnegut, B., Cloud-to-stratosphere lightning, *Weather*, *35*, 59–60, 1980.

Weast, R. C., *CRC Handbook of Chemistry and Physics*, 1st student ed., CRC Press, Boca Raton, Florida, 1987.

Wescott, E. M., D. Sentman, D. Osborne, D. Hampton, and M. Heavner, Preliminary results from the Sprites94 aircraft campaign: 2. Blue jets, *Geophys. Res. Lett.*, *22*, 1209–1212, 1995.

Wescott, E. M., D. D. Sentman, M. J. Heavner, D. L. Hampton, D. L. Osborne, and O. H. Vaughan, Blue starters: Brief upward discharges from an intense Arkansas thunderstorm, *Geophys. Res. Lett.*, *23*, 2153–2156, 1996.

Wescott, E. M., D. D. Sentman, M. J. Heavner, D. L. Hampton, W. A. Lyons, and T. Nelson, Observations of 'columniform' sprites, *J. Atmos. Sol. Terr. Phys.*, *60*, 733–740, 1998.

Williams, E. R., The positive charge reservoir for sprite-producing lightning, *J. Atmos. Sol. Terr. Phys.*, *60*, 689–692, 1998.

Williams, E. R., C. M. Cooke, and K. A. Wright, Electrical discharge propagation in and around space charge clouds, *J. Geophys. Res.*, *90*, 6059–6070, 1985.

Wilson, C. T. R., The electric field of a thundercloud and some of its effects, *Proc. Phys. Soc. London*, *37*, 32D–37D, 1925.

Wilson, C. T. R., A theory of thundercloud electricity, *Proc. R. Soc. London, Ser. A*, *236*, 297–317, 1956.

Winckler, J. R., Further observations of cloud-ionosphere electrical discharges above thunderstorms, *J. Geophys. Res.*, *100*, 14,335–14,345, 1995.

Winckler, J. R., W. A. Lyons, T. E. Nelson, and R. J. Nemzek, New high-resolution ground-based studies of sprites, *J. Geophys. Res.*, *101*, 6997–7004, 1996.

Yukhimuk, V., R. A. Roussel-Dupré, E. M. D. Symbalisty, and Y. Taranenko, Optical characteristics of Red Sprites produced by runaway air breakdown, *J. Geophys. Res.*, *103*, 11,473–11,482, 1998.